NORTHWESTERN UNIVERSITY

SiO_2 Deposition on Metal Oxides to Tune Catalytic Reaction Behavior

A DISSERTATION

SUBMITTED TO THE GRADUATE SCHOOL

IN PARTIAL FULFILLMENT OF THE REQUIREMENTS

for the degree

DOCTOR OF PHILOSOPHY

Field of Chemical and Biological Engineering

By

M. Alexander Ardagh

EVANSTON, ILLINOIS

September 2018

Abstract

SiO_2 Deposition on Metal Oxides to Tune Catalytic Reaction Behavior

Alex Ardagh

Mixed oxides including SiO_2 and supported oxides on SiO_2 comprise the majority of heterogeneous catalysts employed in the chemical industry. SiO_2-Al_2O_3 and microporous, crystalline variants called zeolites have been used widely since the 1960s in petroleum processing, commodity chemical production, and fine chemical synthesis [1]. SiO_2 supported TiOx catalysts TS-1 and nonporous Ti-SiO_2 were patented in the 1970s and have been used since in alkene oxidation and ketone ammoxidation processes [2-3]. Regardless of catalyst type, the prevailing synthetic approach has been to rely on black box sol-gel processes to synthesize the catalyst structure and active sites in one pot. This dissertation supports an alternative approach where sol-gel deposition of SiO_2 is used to tune active site identity and sterics while confining catalytic sites to the external surface of the catalyst.

Preliminary work was conducted to develop a controlled, tunable, liquid phase SiO_2 deposition technique on bulk metal oxides. NanoDur Al_2O_3 and Evonik P25 TiO_2 were used as example nonporous substrates for SiO_2 deposition. The deposition technique was found to result in ~0.4 nm/cycle SiO_2 growth, conformal to the surface of the support [4]. Grafting of a carbonaceous template, 4-tert-Butylcalixarene, before SiO_2 deposition allowed for nanocavity formation in the resulting overcoat. Higher external surface area was observed, which corresponds to nanocavity walls. A high heating ramp rate during calcination posttreatment was found to impart microporosity on the overcoat [4].

Then, the SiO_2 deposition technique was extended to supported Lewis acid catalysts to enact confinement around external surface sites. Liquid phase limonene oxidation was identified as a reaction that probes for acid site strength and steric effects. The reaction network and kinetics were explored using Ti, Nb, and Ta supported on wide pore SiO_2. Calixarene and other bulky templates Cp and Cp* were used to synthesize predominantly site isolated, extraframework $O_3MO(H)$ on SiO_2 using a surface loading of ~0.20 M/nm^2. In a test of oxidation activity, direct selectivity, and external regioselectivity, the use of Ti-SiO_2 with anhydrous tert butyl hydroperoxide (TBHP) showed promise with high activity (58 hr^{-1}), direct selectivity (95 mol %), and low external regioselectivity (25 mol %) to limonene 8,9-oxide. I hypothesized that templated SiO_2 deposition on Cp*Ti-SiO_2 would increase oxidation rate and regioselectivity.

An in depth investigation was conducted using SiO_2 overcoated Ti-SiO_2 along with conventional mesoporous material Ti-SBA-15 and zeolite Ti-Beta. These 7 catalysts seemed to possess nominally similar TiOx sites because their DRUV-vis spectra and Ti K-edge XANES spectra result in similar indirect edge energies (3.5-4.5 eV) and average coordination numbers (4.2-4.6). However, their limonene oxidation activity spans a wide range of values between 14-60 hr^{-1}. In-situ titration with phosphonic acids per prior work from the group did not resolve differences in oxidation rate. Then, limonene adsorption behavior was assessed using a literature GCMS SIM mode analysis which tracked ions with m/z = 68, 93, and 67 [5]. One SiO_2 overcoated Ti-SiO_2 material was found to strongly bind limonene (ΔH_{ads} = -39 kJ/mol) and thus have the lowest apparent activation enthalpy (9 kJ/mol). It was the top performer under industry conditions which require large catalyst particle sizes and low processing temperatures. These materials can find future use in contaminant removal and conversion of bulky reactants.

Acknowledgements

I thank my advisor, Justin Notestein, for his advice and guidance throughout the course of my PhD. His limitless patience and persistence for more and higher quality data have led to the level of experimental work that you will see below. My lab mentors Zhenyu Bo, Neil Schweitzer, and Nick Thornburg deserve huge credit for teaching me the ways of materials synthesis, physical and active site characterization, and liquid phase reaction studies. Without their help, I would still be stuck on the first step of my first project. I thank Daniel Bregante and the Flaherty group at the University of Illinois at Urbana-Champaign, who have graciously complied with our requests for the synthesis of Ti-Beta and other Lewis acid substituted Beta. I am sure the Notestein group will figure out the synthesis someday guys!

I thank the managers of the state of the art user facilities at Northwestern including Yuyang Wu (IMSERC NMR), Christos Malliakas (IMSERC XRD), Jerry Carsello (J. B. Cohen Facility XRD), and Keith MacRenaris (QBIC ICP). In addition, I thank Qing Ma (Argonne) and Louisa Savereide who helped me set up for Ti K-edge XANES. Your patience and careful explanation in the face of sleep deprivation was extremely appreciated. A special thanks to Scott Nauert for constant discussion on seemingly unexplainable catalytic phenomena and for letting me nearly destroy his gas chromatograph (GC) in order to obtain vital triisopropylbenzene cracking reaction data. Finally, I thank my PhD committee (Linda Broadbelt, Neil Schweitzer, and Peter Stair) for demanding constant improvement and for leading me to develop a much more polished presentation style that will sell my science for years to come.

Dedication

I dedicate this work to my family, who supported me through the ups and downs of the PhD life. This is especially dedicated to my parents Curt and Phyllis Ardagh who have patiently supported me as I navigate a career in academia. I dedicate this in part to my partner, Stacey Chin, whose companionship and love has made the final 2 years of my PhD enjoyable. I wish her the best in finishing up her own PhD in the Stupp group at Northwestern and hope that she can join me elsewhere soon!

Table of Contents

List of Figures

List of Tables

Chapter 1. Introduction and Motivations

Section 1.1 Heterogeneous Catalysts in Industry

Catalysts were first used in the 1740s by English physician John Roebuck to produce sulfuric acid during hobbyist experiments [18]. In general, the first catalysts were homogeneous Brønsted or Lewis acids and bases. These chemicals readily yield the desired product, but oftentimes they could not be reused due to chemical separation difficulties. Distillation can be used to separate the catalyst from the product mixture, but high temperatures required may lead to deactivation. This reuse issue led to the development of solid heterogeneous catalysts in the late 1800s and early 1900s. Early heterogeneous catalysts typically consisted of precious metals, metal oxides, or mixtures of the two. Amorphous aluminosilicates (SiO_2-Al_2O_3) were especially widely used due to their low cost, high availability, and strong Brønsted acidity. Industrial researchers continued to explore better heterogeneous catalysts, and synthetic zeolites were discovered in the late 1950s [1]. Zeolites, microporous (pore size < 2 nm) crystalline aluminosilicates, are now widely used in chemical industrial processes after coming to prominence in the 1960s. These materials have high hydrothermal stability, strong Brønsted acid sites, and shape selective behaviors in catalytic reactions. Their primary applications were in petroleum processing as their shape selectivity allowed for the production of desired gasoline grade products.

However, as the chemical industries look to use alternative feedstock reactants such as biomass, bitumen (tar sands), and natural gas; there is a large opportunity for new catalysts to emerge as the best option for industrial processing. Petroleum companies such as ConocoPhilips,

ExxonMobil, and Shell are interested in utilizing tar sands for energy security reasons and to counteract the pricing power of OPEC [19]. The bitumen contains heavy polyaromatics with molecular weights up to 15,000 that will need to undergo catalytic cracking to produce conventional oil products [20]. Zeolitic catalysts often suffer from deactivation by large polyaromatics as they can form solid carbon (coke) in the zeolite channels or block the zeolite pore mouth thus blocking access to the zeolite active sites. Amorphous silica alumina (ASA) materials can work with less observed deactivation but then control over catalytic activity is reduced due to the way that ASAs are made. Since liquid phase co-gelation is typically used in ASA synthesis, the mixed oxide may contain separated bulk phases of Al_2O_3 and SiO_2 as well as intimately mixed SiO_2-Al_2O_3. Any new catalyst design will need to undergo rigorous development including steps shown in Figure 1.1 [6].

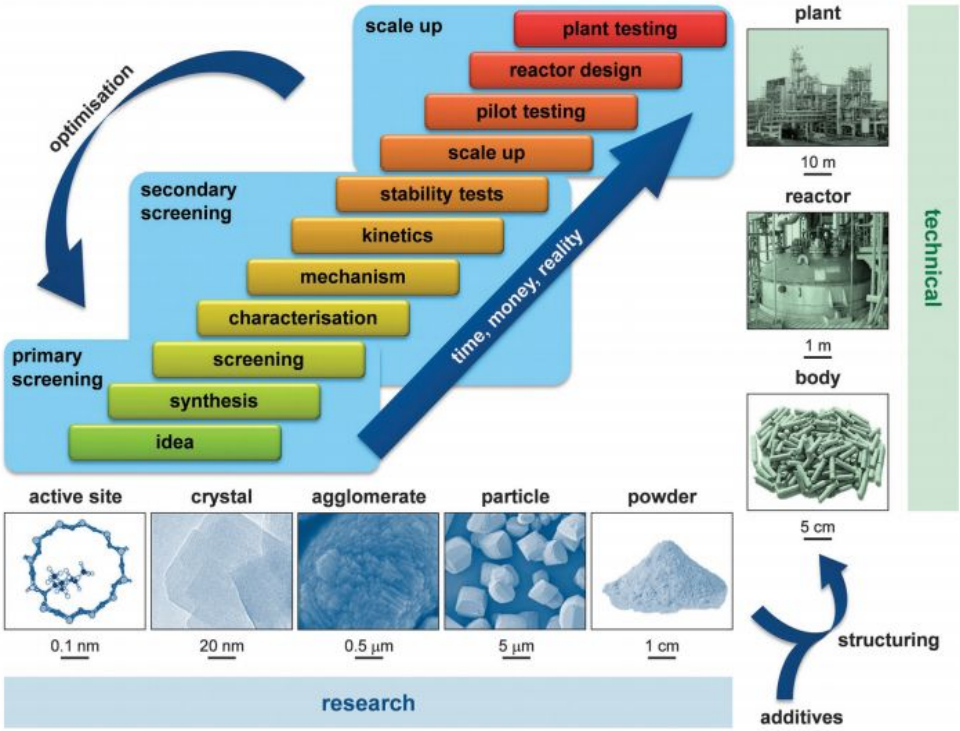

Figure 1.1 Sequence of tasks needed to complete catalyst development. A key transition here is to translate promising catalysts with high intrinsic performance into an industrial catalyst usable in a reactor. Successful technologies deliver enhanced performance at multiple length scales from the active site to industrial production [6].

An alternative to sol-gel synthesis methods is core-shell oxide nanoparticles, where one oxide phase is deposited out of a liquid solution or the vapor onto nanoparticles of the other oxide. This structure allows for surface sensitive characterization techniques to be used and it confines the intimately mixed layer to the surface of the oxide, which guarantees that reactant molecules interact with the mixed phase before interaction with the bulk support phase. Regarding SiO_2-Al_2O_3, both possible variants, SiO_2 on Al_2O_3 and Al_2O_3 on SiO_2, have been synthesized in several ways. Chemical vapor deposition (CVD), atomic layer deposition (ALD), and chemical liquid deposition (CLD) have been previously shown to work in forming the core-shell structure [21-23]. Solid acid materials synthesized in this way have been shown to be less active than conventional ASA for Brønsted acid probe reactions such as catalytic cracking, alkene isomerization, and alcohol dehydration [14, 24-25]. This has led to detailed characterization studies that use benzaldehyde-ammonia titration (BAT), infrared spectroscopy (DRIFTS), ammonia (NH_3) temperature programmed desorption (TPD), and solid state NMR in order to determine the number and type of active sites [7, 26-27].

Detailed studies have shown that SiO_2 and Al_2O_3 precursors graft onto surface sites that encourage the formation of strong interfacial binding, via bonding to tetrahedral Al and Si respectively as shown in Figure 1.2 [7]. SiO_2 deposition on Al_2O_3 leads to the formation of Brønsted sites initially but these are covered up upon further SiO_2 deposition. Conversely, Al_2O_3 deposition on SiO_2 goes through a maximum in Brønsted site density which is then supplanted

by the formation of Al^{IV} Lewis sites [7, 28]. Intrinsically, the majority of these Brønsted sites are different than the bridging hydroxyl in zeolites and ASA [28-29]. A confounding factor that may explain differences in acidity between zeolites and these amorphous materials is confinement effects. Confinement effects occur when the steric environment and pore structure of the active site stabilizes reactant molecules or transition states, this stabilization leads to higher rates and adsorption uptakes [30]. In zeolites, the cage structure around the active site can impart confinement effects during reaction. Unfortunately, researchers working on core-shell ASA particles have yet to incorporate confinement effects around surface Brønsted sites. One can imagine using carbonaceous templates, similar to zeolite structure directing agents, and depositing oxides to form active sites in a templated environment. Another method is to functionalize the template, which has been done in the case of Lewis acid transition metals such as Ti, Zr, and Nb [31-32]. Lewis acid catalysts with engineered active site environments are discussed next.

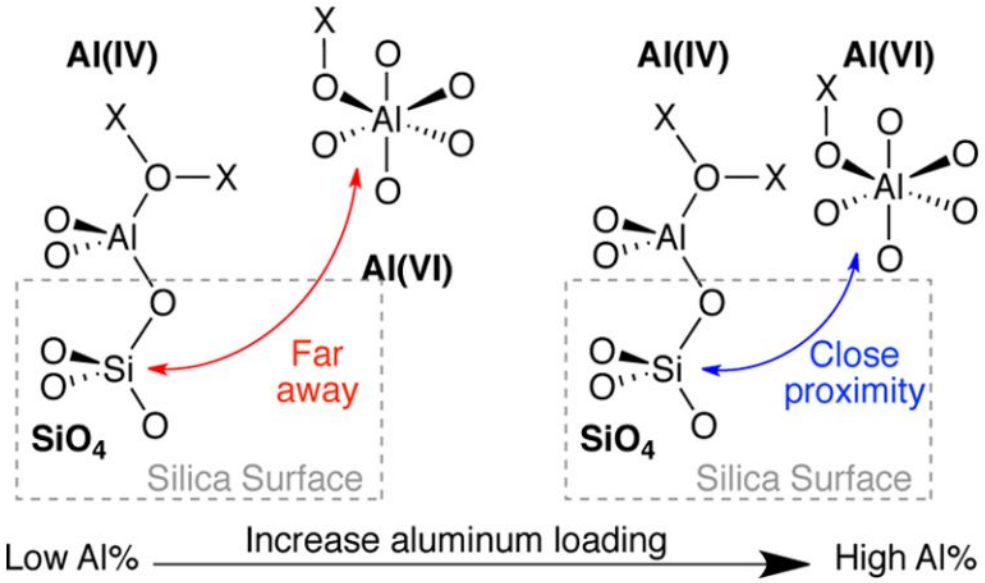

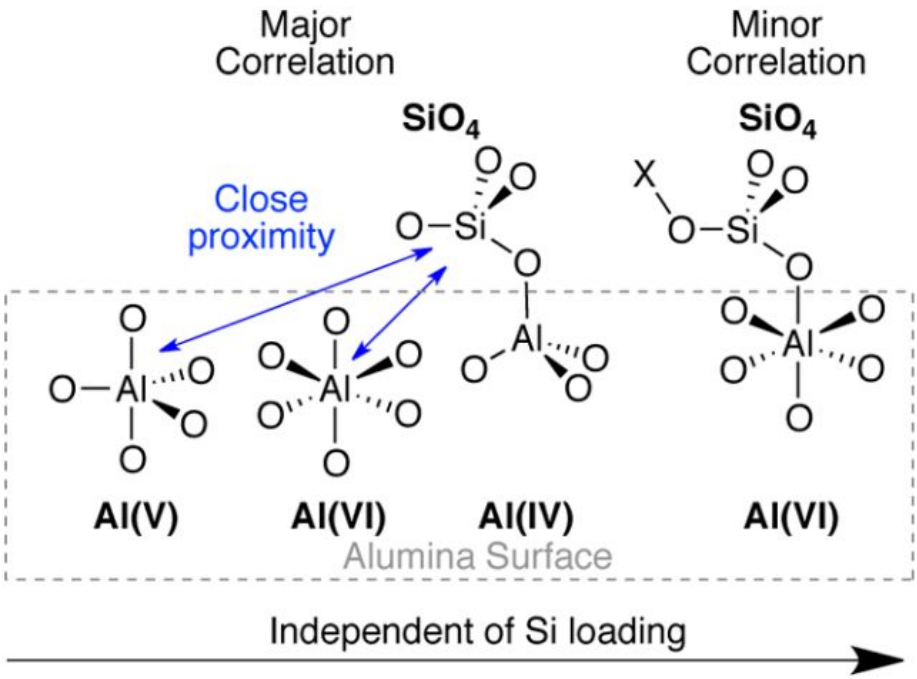

Figure 1.2 Representations of top) $AlOx/SiO_2$ and bottom) $SiOx/Al_2O_3$ interfaces depicting bonding between tetrahedral Al and Si with octahedral Al near interfacial sites [7].

Section 1.2 SiO_2 Supported Lewis Acids

Traditional zeolites contain Si and Al atoms interlocked into a 3D crystalline framework because the co-gelation of mixtures of Si and Al precursors is well studied. These materials can act as Brønsted or Lewis acid catalysts and have been shown to be active in catalytic cracking, alkane isomerization, epoxide ring opening, and many other reactions [24-26, 33]. For the production of fine chemicals, metals other than Al have found use, with Ti being the predominant Lewis acid site choice. To that end, Enichem and Shell separately developed the first Lewis acidic Ti-SiO_2 catalysts in the 1970s [2-3]. Enichem patented titania silicalite 1 (TS-1), which is a Ti-SiO_2 that is isomorphous with zeolite ZSM-5 (MFI), for the ammoxidation of ketones. Shell developed a nonporous Ti-SiO_2 catalyst for the epoxidation of olefins with

organic hydroperoxides. Since then, researchers have found that undercoordinated Lewis acid sites comprised of Group IV, V, VI, XIII, and XIV metals have high activity and selectivity in various oxidation reactions [34-36].

Alkene oxidation has been especially studied over this class of materials because it is the first step towards making polymers, plastics, and many consumer products [37-40]. Large chemical companies like Dow and BASF produce 2 rail cars per hour of product based on a liquid phase process [8]. Dow and BASF piloted propylene epoxidation with aqueous H_2O_2 using an SiO_2 supported Ti catalyst in 2006 [8]. H_2O_2 is a preferred oxidant because its use results in the formation of water, which is a benign co-product for the epoxide. Further improvements to this process are being conducted in a collaboration between Chevron, University of California Berkeley, and the National Science Foundation (NSF). There, researchers use delamination on synthesized boron substituted zeolites to make a 2D zeolite material with more external surface area. They then remove framework boron with strong acid and graft isolated O_3TiOH onto the SiO_2 surface, resulting in a more active and stable catalyst than industry standard TS-1 [36, 41]. Regardless of these successes, the understanding of how Lewis acid catalyst design affects alkene oxidation still has a long way to go. For example, researchers in the 1990s discovered that entire classes of catalysts used for alkene oxidation were actually trojan horses. This means that the support oxide carries the Lewis acid site into the reactor, but the active metal leeches off the surface under reaction conditions and continues to catalyze the reaction in the homogeneous phase [42-43]. Leeching phenomena are especially important for SiO_2 supported vanadium and the Group VI metals.

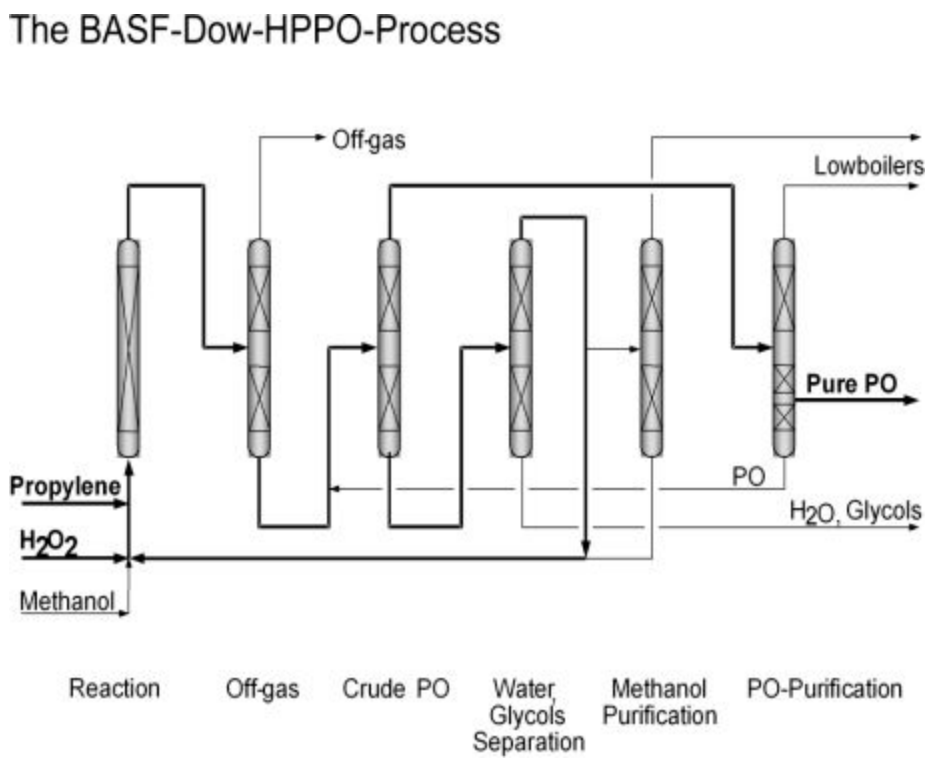

Figure 1.3 Process flow diagram for BASF-Dow-Solvay HPPO process that began operation in early 2008. Combined production capacity for this and several other similar plants approaches 2 rail cars per hour of propylene glycol [8].

Attempts at rational design of these catalysts has focused on controlling the surface density of the metal, precursor effects, and support effects. The dispersion of one Lewis acid metal, vanadium, was studied on various oxide supports including SiO_2, Al_2O_3, TiO_2, ZrO_2, and Nb_2O_5. VOx are important active sites for the oxidative dehydrogenation (ODH) of propane to propylene [44-45]. Researchers found that V_2O_5 dispersion on different oxide surfaces depends on the reactivity of surface hydroxyl groups. On SiO_2, VOx forms a full monolayer and 3D crystallites at much lower surface densities than on the other oxide materials due to the weak reactivity of surface silanols [45-46]. This has been alleviated in part by a discovery that doping SiO_2 with alkali cations like Na^+ leads to enhanced dispersion [46]. Furthermore, catalytic

activity and selectivity has been shown to be a big function of surface loading of the oxide. In the case of VOx, the optimal surface loading has shown to be just above a monolayer. However, for alkene oxidation, isolated MOx species have been repeatedly demonstrated to be the most active and selective for oxidation using SiO_2, zeolites, mesoporous materials, and metal organic frameworks (MOFs) as supports [35, 47-48].

Precursor effects and deposition techniques have been shown to be critical for Lewis acid (Ti and Nb) deposition onto SiO_2 [9, 49]. Alkoxide precursors such as ethoxides and isopropoxides tend to form agglomerated structures and 2D oligomers even at low surface loadings. Metal chlorides disperse much better but their volatility and self reactivity is a concern because chlorides readily form HCl upon contact with even trace moisture in the air. Commercially available cyclopentadienyl (Cp) metal complexes are the traditional precursor of choice for deposition when isolated sites are preferred. These complexes have been shown to deposit and form a O_3M-Cp surface complex that is air and moisture stable [50-51]. The pentahapto bond between the metal and the conjugated Cp ring is strong enough to maintain ligand connection, thus ensuring steric separation between neighboring metal precursor molecules. Furthermore, our group and others have developed synthetic methods to produce bulkier metal complexes, i.e. metallocalixarenes [31-32]. Their deposition on SiO_2 ensures even greater dispersion due to the calixarene being twice as wide as Cp. When all of the aforementioned metal deposition routes are employed and the resulting catalysts probed with alkene oxidation reactions, the bulky metallocalixarene and Cp complexes lead to more active catalysts on a per metal basis.

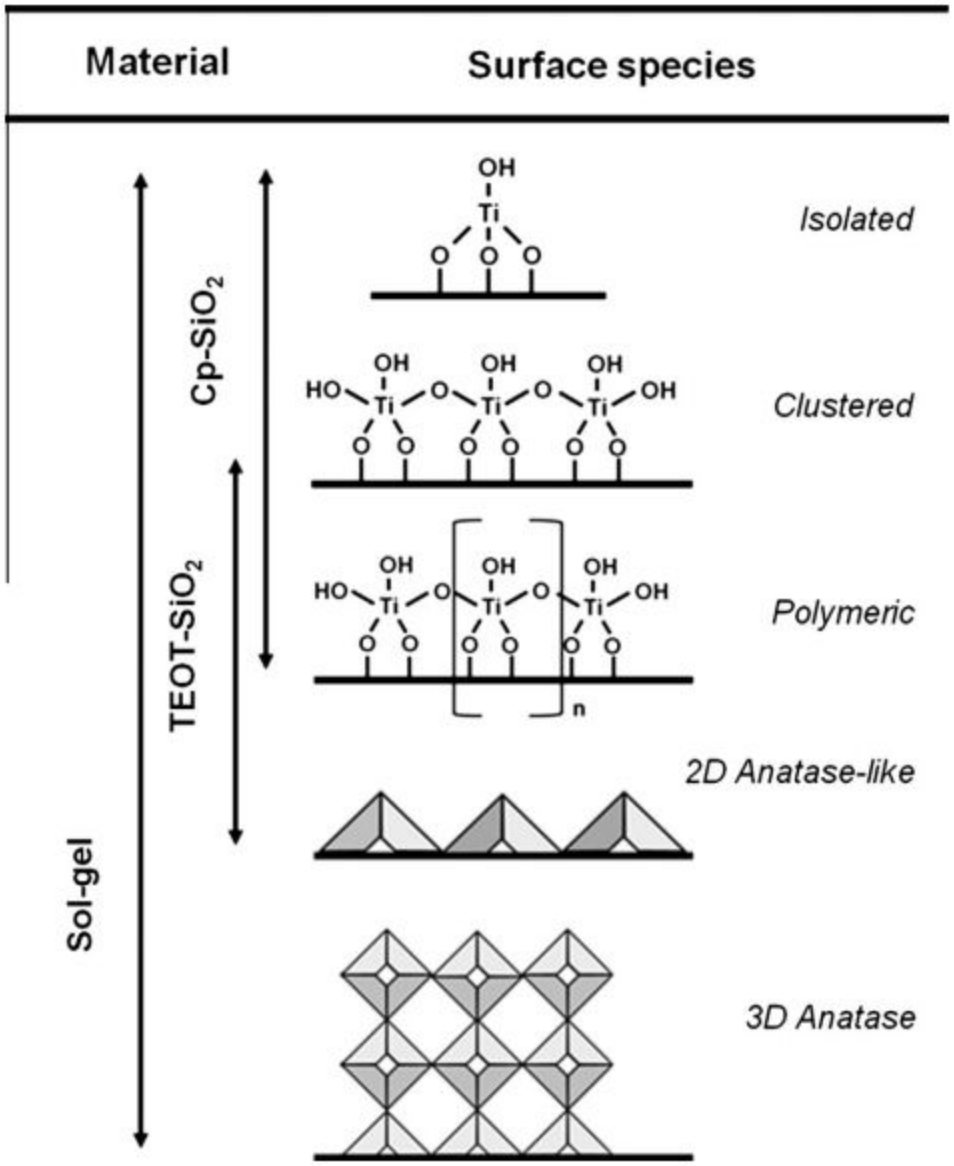

Figure 1.4 Precursor effects on TiOx nuclearity after deposition on mesoporous SiO_2. Bulky, air and moisture-stable templates such as calixarene, Cp*, and Cp lead to isolated O_3TiOH active for alkene oxidation reactions [9].

An alternative approach to synthesizing highly dispersed lewis acids is related to the earlier section on zeolite synthesis. Use of Ti precursors in the zeolite mixture was achieved in the late 1980s and 1990s, this lead to highly dispersed framework Ti incorporation into zeolites

TS-1 (MFI), Ti-Beta (BEA), and mesoporous materials Ti-MCM-41 and Ti-SBA-15 [52-55]. These catalysts have proven to be more active and selective than their nonporous grafted counterparts in alkene oxidation probe reactions. For example, TS-1, Ti-Beta, and Ti-MCM-41 were separately compared to Ti-SiO_2 in the oxidation of linear 1-octene, cyclohexene, and bulky norbornene [54, 56]. Differences in reactivity were attributed to sieving by the zeolite channel size. However, catalyst Ti-Beta was observed to have higher oxidation activity for cyclohexene than 1-octene, which indicates that there a more complicated phenomena at work. In addition, although these compare favorably with SiO_2 supported Ti catalysts, their surface loadings are very different, meaning that the oxidation rate per metal may be the same or even higher for the nonporous catalyst. Even so, rates on a per metal basis are not legitimate turnover frequencies (TOF) because not all metal sites are active. Typical metal and metal oxide catalysts only contain 10-70 % active metal [57-59]. Therefore, our group and others have developed site counting methods in order to obtain intrinsic oxidation TOFs.

Phosphonic acid titrants can be used in order to remove Lewis acid reactivity. Phosphonic acids were shown to selectively graft to TiO_2 domains instead of SiO_2 when the titrants were exposed to mixed TiO_2-SiO_2 oxides [9, 60]. This modification has been demonstrated to decrease oxidation activity by preventing the activation of hydrogen peroxide or organic hydroperoxides. Therefore, one can measure initial oxidation rate as a function of added phosphonic acid and observe the decrease in oxidation rate. This was done in the liquid phase oxidation of cyclooctene and cyclohexene with H_2O_2, with initial oxidation rates decreasing linearly for Group IV metals until reaching zero [49, 61-63]. An open question for this titration technique is whether the preferred titrant, bulky phenylphosphonic acid (PPA, 0.65 nm kinetic diameter) can

effectively titrate zeolite TS-1 and Ti-Beta framework Ti sites. The next section discusses the effects of pore size and diffusion limitations on apparent alkene oxidation activity and selectivity.

Section 1.3 Pore Size and Diffusion Limitations

A complete understanding of fluid flow phenomena and catalytic behavior by catalysis researchers led to the discovery of mass transport limitations on catalytic activity. The well known Weisz-Prater criterion and Madon-Boudart test allow for experimental verification of the absence of diffusion limitations [64-65]. Mass transfer limitations occur when the intrinsic rate of reaction is fast enough that the limiting step (or measured reaction rate) is either external mass transfer (diffusion from the bulk phase to the particle) or internal mass transfer (diffusion from the particle surface to the active site). Zeolites in particular suffer from internal diffusion limitations due to their small pore sizes (0.3-1 nm) and industrial requirements for large particle sizes (> 100 micron, often > 1 cm) [66]. Unfortunately, zeolite synthesis is a sol-gel method so the entire pore structure is formed in one step. This means that desired shape selective properties around the active site, i.e. the cage, are tethered to the extended pore. In addition to resulting in lower apparent catalytic rates, the interactions between pore size and crystal sizes can lead to negative effects on selectivity.

In one current example, the methanol to hydrocarbons or olefins (MTH/MTO) reaction selectivity is largely dependent on the crystal size of the SAPO-34 zeolite [17, 67-69]. Methanol is a readily abundant feedstock that could provide a biorenewable pathway to larger hydrocarbon molecules via the MTO reaction. As methanol reacts in the zeolite pores, a bulky pentamethylbenzene reaction center forms inside the pore [70]. If large crystals of SAPO-34 are

used, sequential reactions occur in the zeolite channels and time on stream stability is diminished as large coke molecules form. If smaller crystallites are used, ethylene and propylene are formed and these catalysts have a much longer time on stream stability [17, 67-69]. Therefore, diffusion related phenomena have unintended secondary consequences in cage-channel topologies prevalent in zeolites. Finally then, catalyst designs that remove the channel structure are important in order to understand intrinsic reaction behaviors, impart shape selective transformation on larger feedstock molecules, increase catalytic production rates, and improve time on stream stability.

Table 1.1 Effects of intracrystalline diffusion on MTO reaction performance over SAPO-34 zeolites. Shape selectivity and reaction behavior is not just a function of pore size but also zeolite crystal size [17].

Crystal size (μm)	Conversion of MeOH	Selectivity to DME	Selectivity to olefins	Interpretation
0.25	High	High	Low	No diffusion limitation on MeOH or DME
0.4/0.5	High	Medium	High	Diffusion limitationon DME
2.5	Low	Low	Low	Diffusion limitation on both MeOH and DME

One class of materials that addressed some of these issues is hierarchical zeolites. The first synthetic methods involved desilication using highly basic aqueous solutions on synthesized zeolites [71-73]. When part of the SiO_2 framework is removed, large irregular mesopores are formed. These molecular “highways” allow for transport to smaller fully intact zeolite crystals. Another route to increasing accessibility to the active site was demonstrated with the well known Lewis acid zeolite TS-1. The zeolite was synthesized hierarchically via carbon templating [74]. This involves suspending a carbon sieve in solution, crystallizing the TS-1 zeolite around the sieve, and then calcination to remove the carbon and leave behind mesopores. The catalyst was tested in the liquid phase oxidation of benzothiophene (BT), which is a common model

compound for sulfur contaminants in petroleum feedstocks [74-75]. The traditional TS-1 catalyst had low activity and was blocked by deactivation as evidenced by a decrease to zero rate after ~50 % conversion. However, the hierarchical TS-1 proceeded quickly to 100 % conversion [74]. Although this worked for the small BT molecule, the implementation of shape selectivity for bulky molecules is poor because there are still extended microporous channel regions in the zeolite that prevent access to the active site.

In this case; mesoporous, macroporous, and nonporous materials with similar chemical composition to zeolites have been synthesized. For example, the so-gel synthesis of MCM-41 and SBA-15 mesoporous materials results in Al or Lewis acid metal incorporation into the walls/SiO_2 framework. Because their pore sizes are > 2 nm, metals can also be grafted onto the surface of the pure SiO_2 sieve [76-77]. However, as mentioned earlier, these materials are typically less active and selective than their zeolite analogs. This is potentially due to the lack of local confinement, as mesoporous channels are too wide to provide stabilizing van der Waals interactions with reactant molecules. Since the chemical industry is looking to process molecules in the micropore size region (i.e. 0.7-1.2 nm), mesoporous materials are not quite suitable. Furthermore, a confounding issue in interpreting catalytic behavior of SBA-15 is that there are mesoporous and microporous regimes, which may lead to internal diffusion limitations or different catalytic behaviors [78].

Therefore, a synthetic method that can address these issues in full is still urgently needed. One idea that has found recent traction is to build in zeolite cage type structures on non-transport limited catalytic supports. These can be wide mesoporous (> 10 nm), macroporous, or nonporous materials. Examples from the early 2000s include molecular imprinting of CVD SiO_2 overcoat

layers. Researchers grafted a template, nearly identical to the reactant of interest, to Rh or Ru active sites supported on nonporous SiO_2. They used CVD to deposit SiO_2 layers around the molecular template and removed the template at high temperature. Enhanced shape selectivity was demonstrated in the vapor phase hydrogenation of various alkenes and the regioselective liquid phase oxidation of limonene [10]. Their limonene oxidation products consisted of >90 % of the sterically unhindered, kinetically disfavored limonene 8,9-oxide. This research is a primer for the following discussion on active site construction for supported materials.

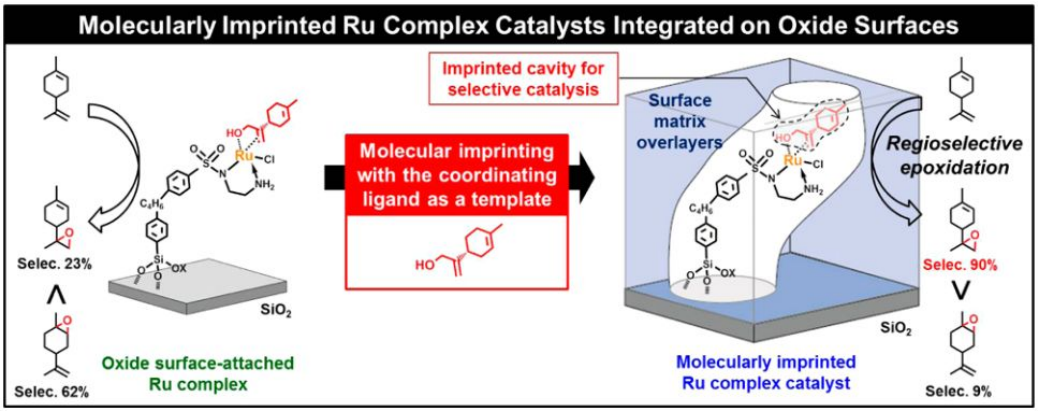

Figure 1.5 Molecularly imprinted Ru catalyst supported on SiO_2. Templating with limonene-10-ol, overcoating with SiO_2 CVD, and finally template removal leaves behind limonene shaped cavities ~0.73 nm wide. Regioselective limonene oxidation with O_2 changes towards the external limonene 8,9-oxide with ~90 mol % selectivity [10].

Section 1.4 Design and Synthesis of the Active Site

Active site design and materials synthesis for heterogeneous catalysts have evolved via two promising approaches. One pathway has focused on the holistic synthesis of the catalyst, which typically proceeds via a sol-gel mechanism with the zeolite synthesis route being one example. An increasingly popular alternative is to use SOMC (surface organometallic chemistry) on the surface of well defined oxide supports. Sol-gel synthesis has been discussed extensively in

prior sections but it is worth repeating that the technique is considered a black box process in that it yields the entire catalyst structure in one step. In order to separately design aspects of the active site, the chosen synthesis method must have separate steps for each design decisions. SOMC has been used extensively to deposit specific active site clusters on various supports [11]. These precursors may be purchased commercially or synthesized in house via reaction between a carbonaceous molecule and a reactive metal precursor. Template size and functional groups often lead to changes in active site behavior and dispersion on the support surface.

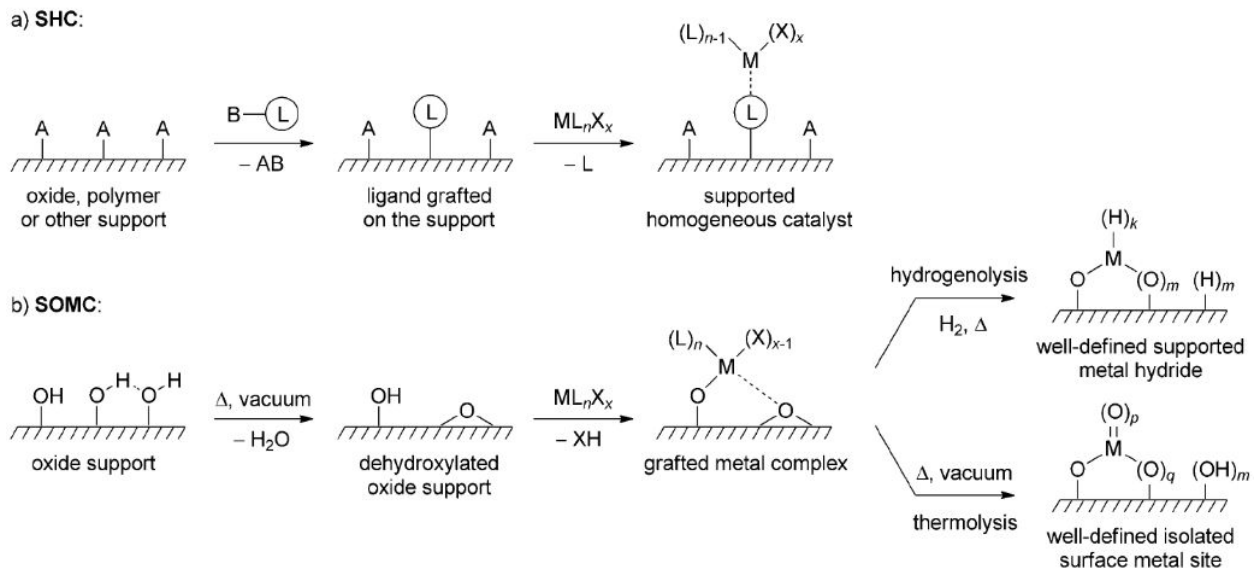

Figure 1.6 Key concepts and synthesis scheme for preparation of well defined supported catalysts via ligand attachment or direct bonding to the oxide. These allow for isolated, in-depth study of active sites present on industrial catalysts [11].

The thermolytic precursor route from the early 2000s was one of the first examples of successful SOMC. This method allowed for the controlled deposition of single site Ti and Ta via attachment to a siloxy ligand [79-80]. After calcination, the isolated Lewis acid metal was supported on amorphous SiO_2 as the siloxy ligand bonded to the surface. These materials had

distinctly higher activity and selectivity in alkene oxidation reactions with cyclohexene. However, this strategy did not allow for steric control because the template siloxy ligand joined the support upon calcination. The use of removable ligands, i.e. carbonaceous templates, is well known for sol-gel techniques but has rarely been exploited in SOMC strategies. Our group and others have synthesized bulky Lewis acid metallated calixarenes in order to deposit site isolated active sites for oxidation reactions [31-32, 49, 61-63]. One of the first attempts was to graft Calixarene-TiCl to SiO_2 and use the as-grafted complex for cyclohexene epoxidation. This Calixarene-Ti-SiO_2 catalyst was very fast, selective, and had an oxidation TOF that was invariant of the Ti surface loading, confirming site isolation [31].

Our group has furthered this by synthesizing metallocalixarenes containing each of the Group IV and V metals, with extensive experiments focused on Ta and Nb [49, 81]. Ta-SiO_2 and Nb-SiO_2 were found to be highly active and selective in alkene oxidation with H_2O_2. Others have tried to control active site sterics via incorporation within a framework vs grafting on surface. Each synthesis is conceptually simple but has an upper limit for metal incorporation above which oligomeric extraframework species begin to form. Ideally, all of these design options will lead to full control over the active site structure similar to the diversity of site sterics present in enzymes. Enzymes, nature's heterogeneous catalysts, combine specific chemoselective active sites with active site environments well fitted to the reactant. We want to replicate this behavior on metal oxide surfaces. In the next section, changes to the energetics and entropies of adsorption and reaction are discussed.

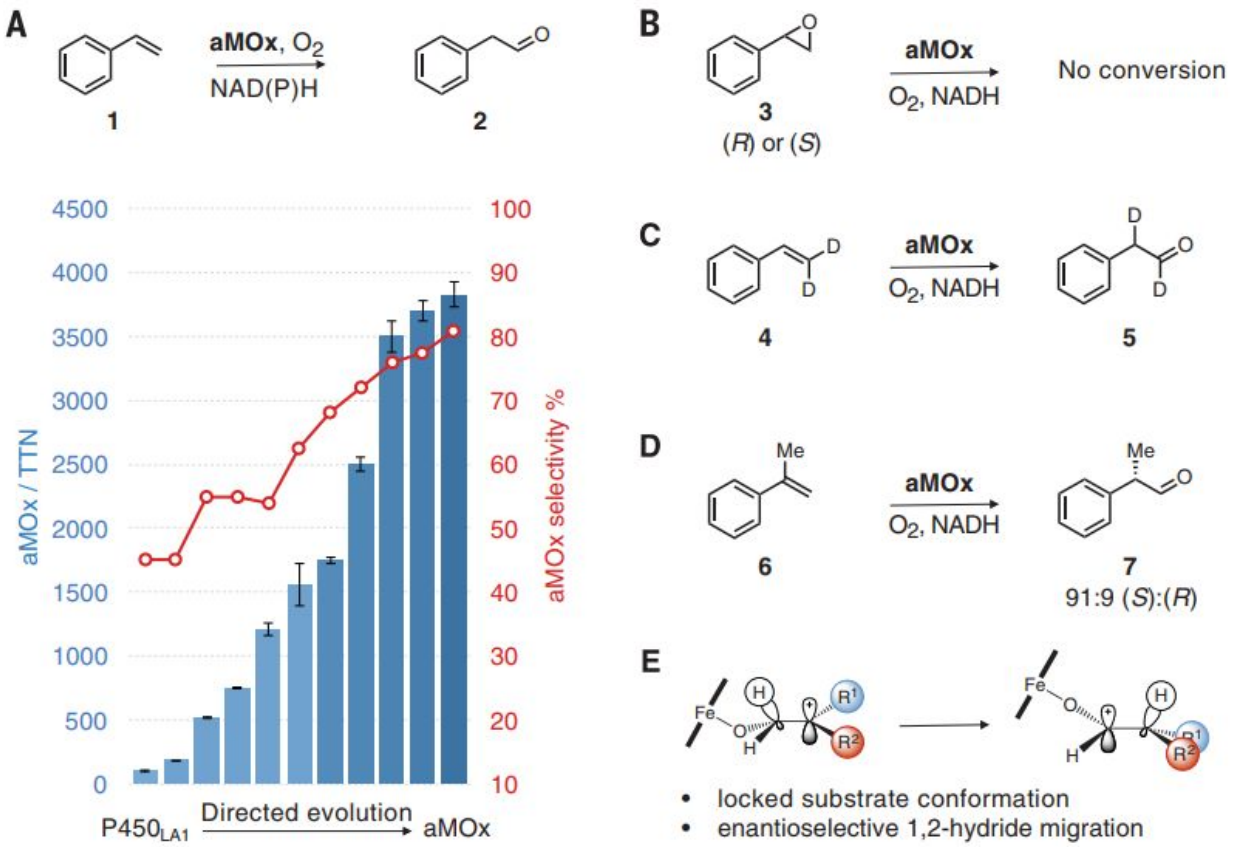

Figure 1.7 Directed evolution of wild type P450 enzyme leads to highly chemoselective styrene oxidation catalyst with over 80 mol % selectivity to phenylacetaldehyde. Similar active site environment modification on inorganic oxide catalysts can be used to enhance oxidation activity and selectivity [12].

Section 1.5 Adsorption and Energetics of Catalysis

Heterogeneous catalytic reactions usually proceed via Langmuir Hinshelwood or Eley Rideal mechanistic steps. Both mechanisms require reactant adsorption, surface reaction, and product desorption as elementary steps. The rate limiting (or rate controlling) step is determined by calculating the degree of rate control for all reaction steps for well studied mechanisms [82-84]. Typically adsorption and desorption are considered reversible unless the reactant is chemically activated by the catalyst. By combining the Arrhenius and Eyring equations for

kinetics with the equilibrium constant expression, one can see that catalytic behavior is entirely dependent on the entropies and energies of adsorption and reaction. Several combined computational and experimental studies on precious metal catalysts have shown that information on enthalpies of adsorption and activation enthalpies leads to the discovery and design of better catalysts [85-87]. These optimization attempts have been largely restricted to pure metal catalysts and focused on changing the active site identity.

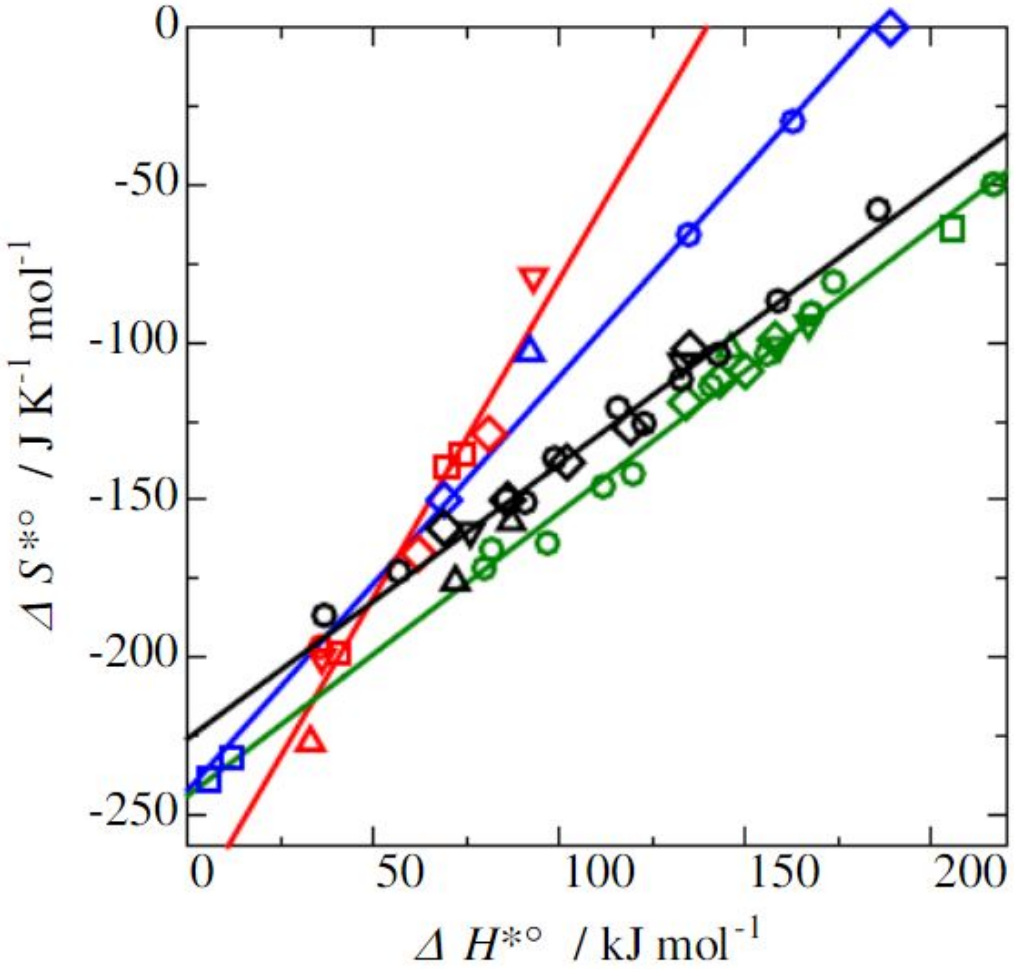

Figure 1.8 Plots of apparent activation entropy as a function of apparent activation enthalpy for propane and isobutane cracking (green), C4-C8 linear alkane and isopentane cracking (black), toluene disproportionation (blue), and cumene cracking (red) over various zeolites and ASA. Linear relationships indicate that adsorption affects the values [13].

A comparable study is sorely needed for assessing active site sterics on metal oxide catalysts because most industrial catalysts employ metal oxides as the active site or support. Support engineering allows for synthesis of an active site pocket similar to enzymes. Therefore, in order to bridge the gap between sol-gel black box active site design to stepwise designer catalysts, one must find a way to modify surface sterics. Adsorption properties including entropies/sterics have been previously modified in the literature by grafting bulky molecules onto the active site or modifying surface hydrophobicity. Another option for supported materials is to grow oxide layers on the surface to provide a rigid, confining environment around the active site.

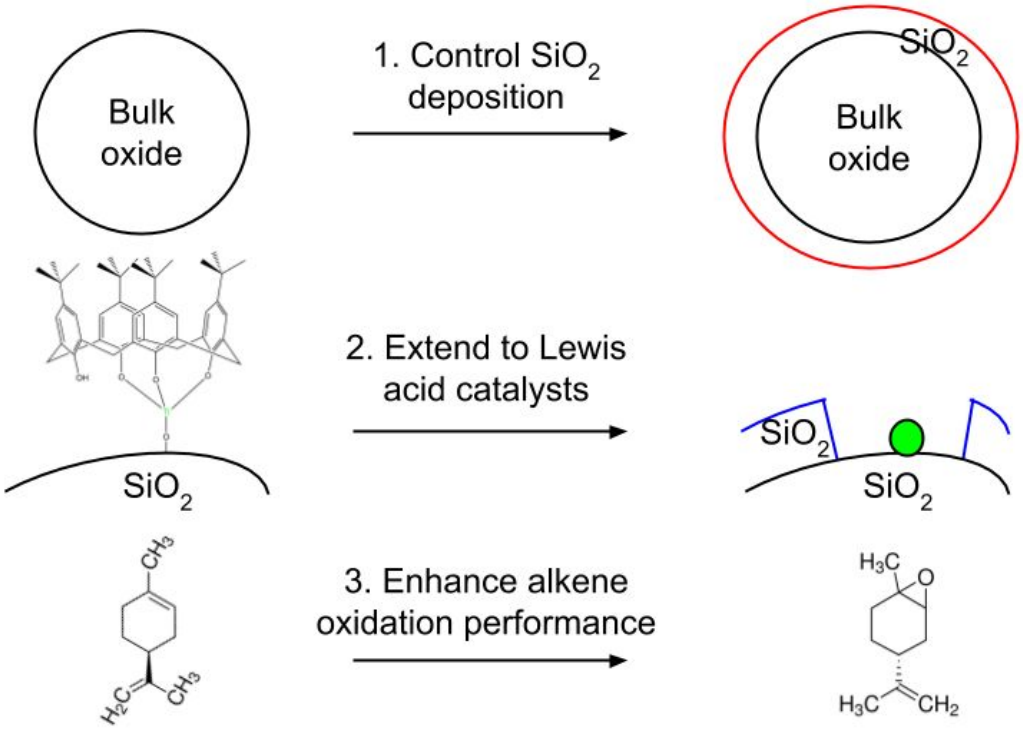

Figure 1.9 Experimental plan to implement enhanced performance in alkene oxidation via templated SiO_2 deposition on supported Lewis acid catalysts. Steps 1, 2, and 3 correspond to Chapters 3, 5, and 4 respectively.

Increased steric hindrance primarily decreases the entropy of adsorption but can affect adsorption enthalpies via van der Waals interactions between the surface and the reactant. Sterics changes can increase the adsorbent behavior for the material for the reactant if the catalyst environment is attuned to reactant molecular dimensions. This is conceptually distinct from changing metal site identity, which primarily decreases the apparent activation barrier for the reaction by changing the electronics of the transition state. In-depth investigation into reaction energetics requires well studied probe reactions, like alkene oxidation, where the rate limiting step is tunable by changing the bulk concentrations of the reactants. Therefore, this thesis will have the following objectives:

1. Demonstrate facile SiO_2 CLD overcoating of bulk oxide materials
2. Identify and use synthesis parameters to tune overcoat morphology
3. Graft and overcoat well defined, stable Lewis acid sites on SiO_2
4. Investigate effects on electronics and entropies of a probe reaction

Chapter 2. Synthesis of SiO_2 Overcoated Oxides

Section 2.1 Template Grafting

The formation of pores on mixed metal oxide materials was first achieved using sacrificial carbonaceous templates in zeolites. Typical template molecules are bulky ammonium chlorides or bromides which facilitate SiO_2 crystallization in the shape of cages and channels [88-90]. Templating onto existing nonporous or mesoporous materials works in a similar fashion except for different functional requirements for the template molecule. For non-metallated templates, the molecule must be rigid, have a defined crystal structure, and have functional groups (i.e. alcohols, carboxylic acids) that can react with the surface of the oxide. Metallated templates must have strong ligand-metal bonds and allow for multiple grafting points to the metal atom.

Templated bulk oxide materials were synthesized according to the following representative method [4, 91]. NanoArc Al_2O_3 (Alfa Aesar, 40 nm particle size, 34 m^2/g, 70 % delta phase, 30 % gamma phase, 99.5 %) was used as received in the synthesis process. 5 g of Al_2O_3 was added to an oven dried 250 mL round bottom flask. Then, 50 mL of freshly distilled anhydrous toluene (Sigma-Aldrich, ACS Reagent, ≥ 99.5 %) was added to a 50 mL centrifuge tube along with 100 mg of 4-tert-Butylcalix[4]arene (Sigma-Aldrich, 95 %) or 1-Adamantanecarboxylic acid (ACA, Sigma-Aldrich, 99 %). This mixture was sonicated until the fine white calixarene powder was fully dispersed into the toluene solvent. Finally, the mixture was added to the flask containing Al_2O_3 along with a teflon stir bar and a water cooled condenser was affixed on top of the flask. The mixture was stirred at 375 rpm for 4 h at toluene

reflux under flowing N_2 on a Schlenk line. Within 30 min, the suspension changed from a white color to a tan color, indicating that grafting has begun. After 4 h, stirring was stopped and the solid was recovered via vacuum filtration. Excess or physisorbed 4-tert-Butylcalix[4]arene was removed during vigorous washing with 200 mL toluene and 200 mL hexanes (Fisher Chemical, Certified ACS, ≥ 98.5 %). The recovered solid was allowed to dry in air overnight and then was used for thermogravimetric analysis (TGA), diffuse reflectance UV-visible spectroscopy (DRUV-vis), or SiO_2 overcoating.

A similar procedure was applied to other oxides including SiO_2 (Selecto, 6 nm pore size, 63-200 micron particle size, ~550 m^2/g), P25 TiO_2 (Sigma-Aldrich, nanopowder, 21 nm primary particle size, ~50 m^2/g, ≥ 99.5 % trace metals basis), niobic acid (CBMM, HY-340), silica-alumina (Sigma-Aldrich, catalyst support, grade 135, 6.5 % Al, 100 mesh particle size), and phosphotungstic acid hydrate (Sigma-Aldrich, reagent grade) to demonstrate that template grafting with calixarenes was generalizable to other metal oxides. Prior publications have detailed template grafting results on SiO_2 and TiO_2 [92-93]. Nb_2O_5 grafting proceeds with a stark color change from white to bright orange, indicative of Calix-O-Nb bond formation. CAUTION: dry niobic acid above 100 ^oC overnight before grafting, because otherwise surface water will boil vigorously during the grafting procedure. Phosphotungstic acid hydrate melts at ~95 ^oC, so grafting was performed at 60 ^oC. However, even at this low temperature, the polyoxometalate (POM) coked up with calixarene fragments as evidenced by the solution changing from a white to black color. POM acidity needs to be quenched via cation exchange if this procedure is to be attempted again.

Metallated templates were grafted using a similar method that was based on prior literature [32, 36, 50]. $TiCl_4$ (Strem Chemicals, 99 %), Cp_2TiCl_2 (Strem Chemicals, ≥ 99 %), Cp^*TiCl_3 (Strem Chemicals, 98 %), 4-tert-Butylcalix[4]arene-TiCl (synthesized using methoxy-calixarene and $TiCl_4$), Ti-TADDOLate (Sigma-Aldrich, 97 %), $NbCl_5$ (Strem Chemicals, ≥ 99 %), Cp_2NbCl_2 (Sigma-Aldrich, 95 %), 4-tert-Butylcalix[4]arene-NbCl (synthesized using calixarene and $NbCl_5$), $TaCl_5$ (Strem Chemicals, 99.9 %), Cp^*TaCl_4 (Strem Chemicals, 98 %), and 4-tert-Butylcalix[4]arene-TaCl (synthesized using calixarene and $TaCl_5$) were grafted to SiO_2 (Alfa Aesar, 15 nm pore size, 100-200 mesh particle size, ~375 m^2/g). SiO_2 was dried at 190 ^oC overnight using a Schlenk line vacuum pump to remove physisorbed water.

Typically, 20-25 g of dry SiO_2 were added to an oven dried 250 mL round bottom flask. 50-75 mL of freshly distilled anhydrous toluene was added to the flask along with a teflon stir bar. The mixture was allowed to stir at 500 rpm until suspension of SiO_2 in the toluene. Then, 750-1000 mg (equivalent of 0.20-0.22 Ti/nm^2 support) of Ti precursor was added and the solution was allowed to stir at 500 rpm under flowing N_2 on a Schlenk line. For 4-tert-Butylcalix[4]arene-TiCl, a water cooled condenser was added and the suspension was refluxed in toluene for 18 h. All others were grafted at RT for 4 h, with the color transferring from the solution to the solid after 15-30 min. Stirring was stopped and the solid was recovered via vacuum filtration. The solid was vigorously washed with 200 mL toluene and 200 mL hexanes to remove physisorbed Ti precursors. L-Ti-SiO_2 was allowed to dry in air overnight and then was subsequently stored in a desiccator until further use in DRUV-vis analysis, SiO_2 overcoating, or calcination.

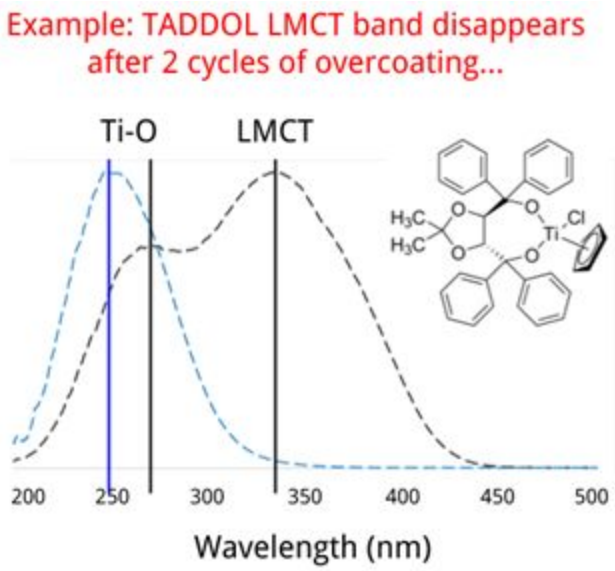

Figure 2.1 Ambient DRUV-vis spectra of as-made (black) and 2cPO (blue) Ti-TADDOLate supported on SiO_2.

Table 2.1 Ti ICP-OES results for as-made and 2cPO variants of various grafted L-Ti-SiO_2.

Precursor	As-made Ti content (M/nm^2)	2cPO Ti content (M/nm^2)
$TiCl_4$	0.17	0.14
Cp_2TiCl_2	0.21	0.20
Calix[4]arene-TiCl	0.19	0.13
Cp*$TiCl_3$	0.21	0.21
Ti-TADDOLate	0.22	0.15

One should note that template grafting proved to be difficult on fumed Al_2O_3 and SiO_2. This may be due to the known thickening properties of fumed oxides [94]. Although the grafting process did appear to proceed readily, vacuum filtration led to the formation of a thick gel disc that was resistant to drying, even after drying for seven days in air. We therefore decided against using fumed supports for bulk or mixed oxide catalysts in this work.

Several SiO_2 supports were tested before deciding on the use of the wide pore Alfa Aesar SiO_2. Snowtex ST-OL 40 (Nissan Chemical, 45 nm particle size), Ludox AS-40 (Sigma-Aldrich, 40 wt % suspension in H_2O, ~140 m^2/g, 22 nm particle size), and Aerosil OX 50 (Evonik, 50 m^2/g, ≥ 99.8 %) were tested as supports for grafting and overcoating. Aerosil OX 50 underwent successful grafting but the resulting powder retained a gel disc shape during vacuum filtration so it was removed from further testing. Both Snowtex and Ludox seemed to undergo grafting and overcoating without issue, however, trace elemental analysis using ICP-OES revealed a significant amount of Al and Na on Snowtex. Al can catalyze classical Lewis acid reactions when it is supported as extraframework species on the surface of SiO_2, so Snowtex was not used further [95]. We tried Ludox as the support for Ti, Nb, and Ta in alkene oxidation reactions but found that these catalysts have too low metal content. When the surface area is low and the surface metal loading has to be low, undesired homogeneous reactions can outperform catalytic activity and complicate analysis. Therefore, Ludox supported materials were discarded in favor of wide pore SiO_2.

Section 2.2 SiO_2 Deposition

Oxide deposition on 2D and 3D surfaces has been explored by materials science, chemistry, and chemical engineering researchers over the last 40 years. CVD and ALD routes have proven to be popular due to the ease of automation for the process and customizability to 2D or 3D substrates. CLD is a well known method to deposit metals and metal precursors but generally occurs in a less controlled way for oxides [21-23]. The use of an alkoxide Si precursor, tetraethyl orthosilicate (TEOS), is widespread for pore size manipulation on zeolites and modification with TEOS also leads to a decrease in external surface acidity [23]. This is useful

for reactions such as xylene isomerization where product selectivity to p-xylene is strongly dependent on confining acidity to the interior of the zeolite [96-98]. Here, we extend CLD TEOS deposition to bulk and mixed metal oxide materials to construct confined steric environments around our chosen active site.

In a representative procedure, 2-5 g of Al_2O_3 was added to a clean 500 mL HDPE bottle [4]. Then, an appropriate amount of ethanol (Decon Labs, 200 proof, ≥ 99.9 %) was added to suspend the powder in solution. This was found empirically to be 15 mL ethanol /g for Al_2O_3. Aqueous ammonium hydroxide (NH_4OH, Macron Fine Chemicals, ACS Reagent, 28-30 wt %) was added, until it comprised 15 vol % of the liquid solution, in order to activate surface hydroxyl groups as basic -M-O^-. CAUTION: 30 wt % NH_4OH fumes and must be used in a fume hood in order to avoid respiratory and eye irritation. The solid suspension was sonicated for 30 min in order to fully disperse the powder into solution and prevent particle agglomeration during the overcoat process.

Then, the appropriate amount of TEOS (Sigma-Aldrich, ≥ 99.0 %) was added corresponding to 1 TEOS molecule per 2 surface hydroxyl groups. Hydroxyl group densities were estimated based on prior literature on bulk oxide surfaces. In early versions of the method, additional NH_4OH was added with TEOS during each deposition cycle. Finally, the mixture was shaken on a gyratory plate at 200 rpm for 1 h. This constitutes the first cycle of SiO_2 overcoating. Subsequent deposition cycles included sonication, TEOS (and NH_4OH, early on) addition, and shaking. Between 0.1-20 cycles of TEOS were deposited on the oxide substrate. After overcoat deposition, the solid was recovered via vacuum filtration. The recovered solid was washed with

200 mL ethanol and 200 mL hexanes, then allowed to dry in air overnight. Solids were then used for study with DRUV-vis or heat treated via calcination.

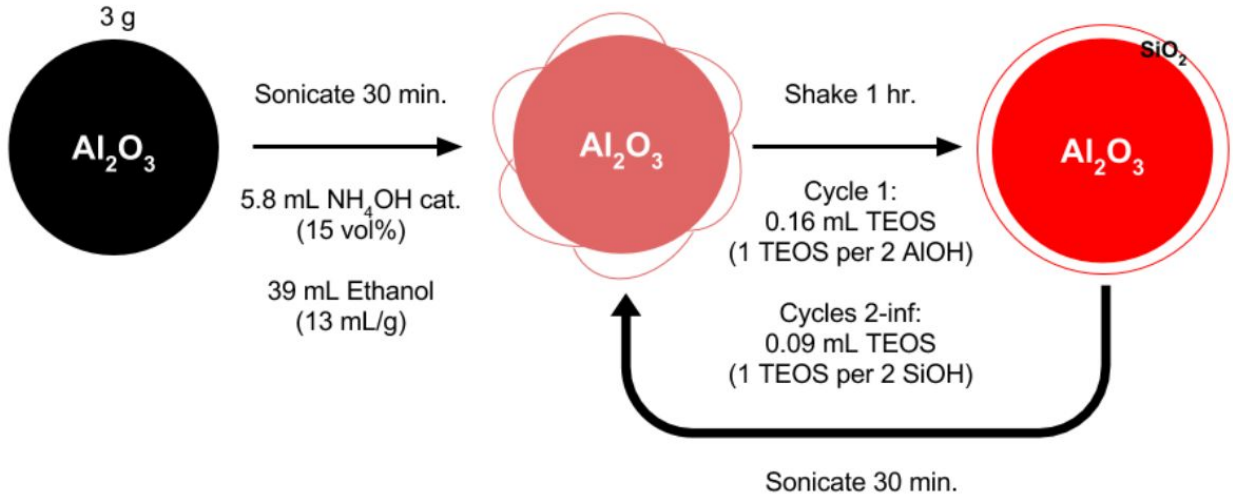

Figure 2.2 Liquid phase, sol-gel SiO_2 overcoat method for deposition on bulk oxide catalysts. The support oxide is sonicated in a basic ethanol solution to disperse particles and activate surface hydroxyl groups. 1 monolayer equivalent of TEOS is added and 1 h is allowed for the alkoxide precursors to polymerize and graft onto the support [4].

This procedure was heavily modified from a prior lab method to decrease SiO_2 surface roughness by decreasing the amount of NH_4OH added during synthesis. First synthesis attempts that involved NH_4OH addition with each deposition cycle led to the formation of large agglomerates of Al_2O_3 covered by an irregularly shaped SiO_2 shell. During a DRIFTS study of one overcoated material, crushing with a mortar and pestle led to the emergence of Al_2O_3 surface hydroxyl peaks. This finding led us to modify the procedure such that NH_4OH addition only occurs at the beginning.

The SiO_2 overcoating method was also applied to Calixarene-Al_2O_3, ACA-Al_2O_3, TiO_2, Calixarene-TiO_2, ACA-TiO_2, Nb_2O_5, Calix-Nb_2O_5, ACA-Nb_2O_5, SiO_2-Al_2O_3, Calixarene-ASA, ACA-ASA, Ti-SiO_2, CpTi-SiO_2, Cp*Ti-SiO_2, CalixTi-SiO_2, TADDOLate-Ti-SiO_2, Nb-SiO_2,

CpNb-SiO_2, CalixNb-SiO_2, Ta-SiO_2, Cp*Ta-SiO_2, and CalixTa-SiO_2. TGA of overcoated ACA templated materials revealed decreased mass loss compared to the original ACA-oxide material, so calixarene was employed as the template for bulk oxide materials. Inductively coupled plasma optical emission spectroscopy (ICP-OES) and DRUV-vis analysis of Cp, Calix, and TADDOLate templated materials also revealed lower metal and ligand content as compared to the original L-M-SiO_2 material, so Cp* was employed as the template for mixed oxide materials.

One should note that SiO_2 overcoating was shown to be ineffective on fumed Al_2O_3. This may be due to the known decreased surface hydroxylation of fumed materials as compared to sol-gel derived materials [99]. However, after vigorous rehydroxylation in refluxing water for 4 h, SiO_2 overcoating proceeded and the second oxide phase was observed with transmission electron microscopy (TEM).

Section 2.3 Posttreatment

All synthesized materials contain either carbonaceous template molecules or ethoxy capped silanols that needed to be removed to activate the catalyst. Heat treatment (calcination) conditions were chosen based on the thermal phase diagrams for bulk oxide supports or based on literature precedent for Lewis acid materials [100-102]. Al_2O_3 based materials were calcined at 650 ^oC for 4 h with a ramp rate between 3.5-20 ^oC/min. TiO_2 based materials were treated with ozone at 120 ^oC for 4 h in order to remove all carbon but prevent extensive restructuring or oxygen vacancy formation. Nb_2O_5 based materials were calcined at 500 ^oC for 4 h with a 3 ^oC/min ramp rate because it was found experimentally via TGA that a phase change/particle sintering occurs for niobic acid at ~525 ^oC. SiO_2-Al_2O_3 based materials were calcined at 450 ^oC

for 6 h with a 7.5 ºC/min ramp rate in order to avoid the gamma to delta Al_2O_3 phase change that begins at 450 ºC.

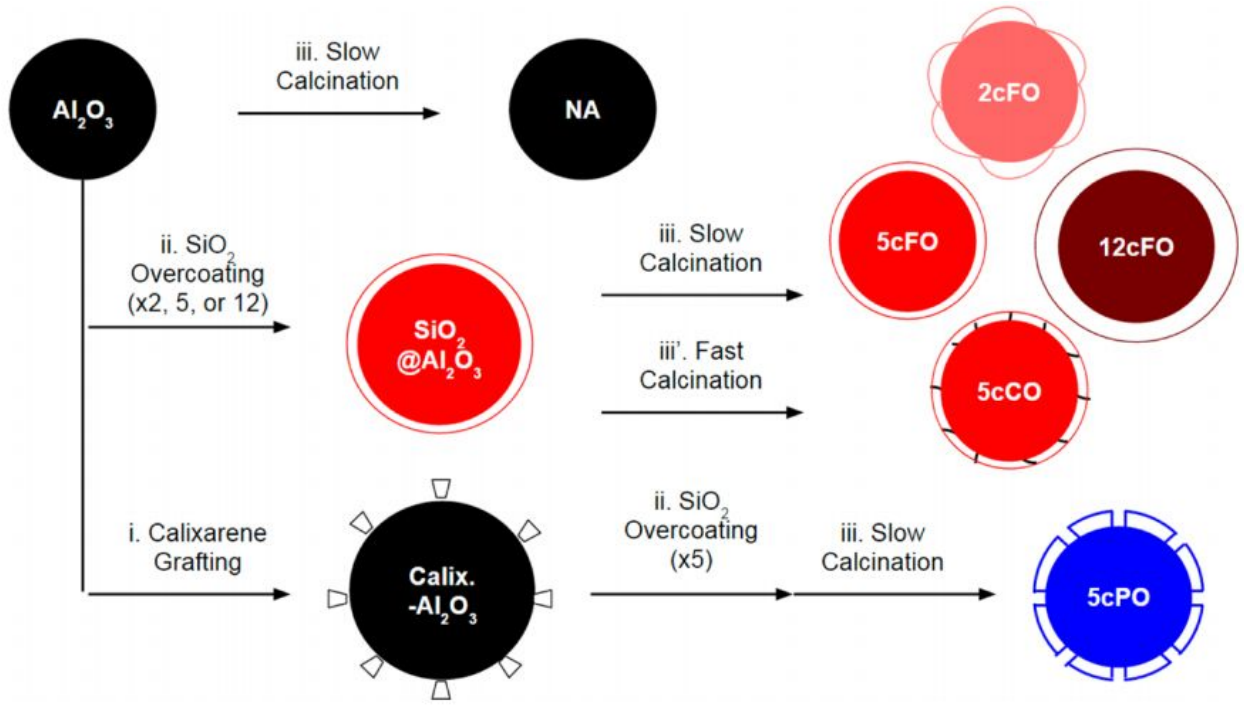

Figure 2.3 Synthesis scheme for SiO_2 overcoated Al_2O_3 catalysts. The effects of (i) SiO_2 overcoat thickness, (ii) calcination ramp rate, and (iii) carbonaceous template were assessed using this family of core-shell catalysts [4].

L-M-SiO_2 materials were all calcined at 550 ºC for 6 h with a 10 ºC/min ramp rate because this has been previously found to be the optimal calcination conditions for supported Lewis acid catalysts [100-101]. The loss of carbonaceous templates was verified with DRUV-vis, TGA, and the color change resulting in bleached white powders.

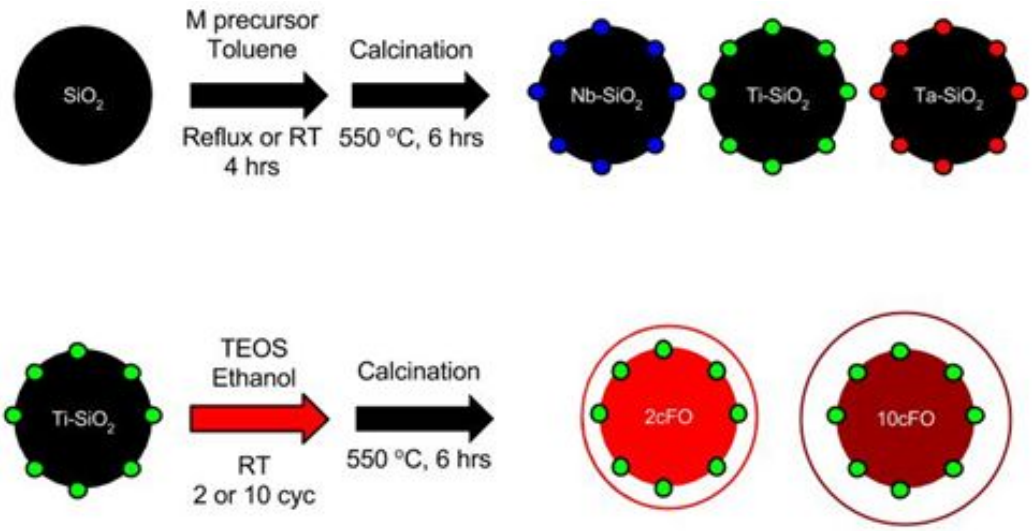

Figure 2.4 Synthesis scheme for site isolated, extraframework $O_3MO(H)$ supported on mesoporous SiO_2. Cp* or calixarene precursors were grafted at ~0.20 M/nm^2 from a toluene solution. Ti-SiO_2 was overcoated with 2 or 10 deposition cycles of SiO_2.

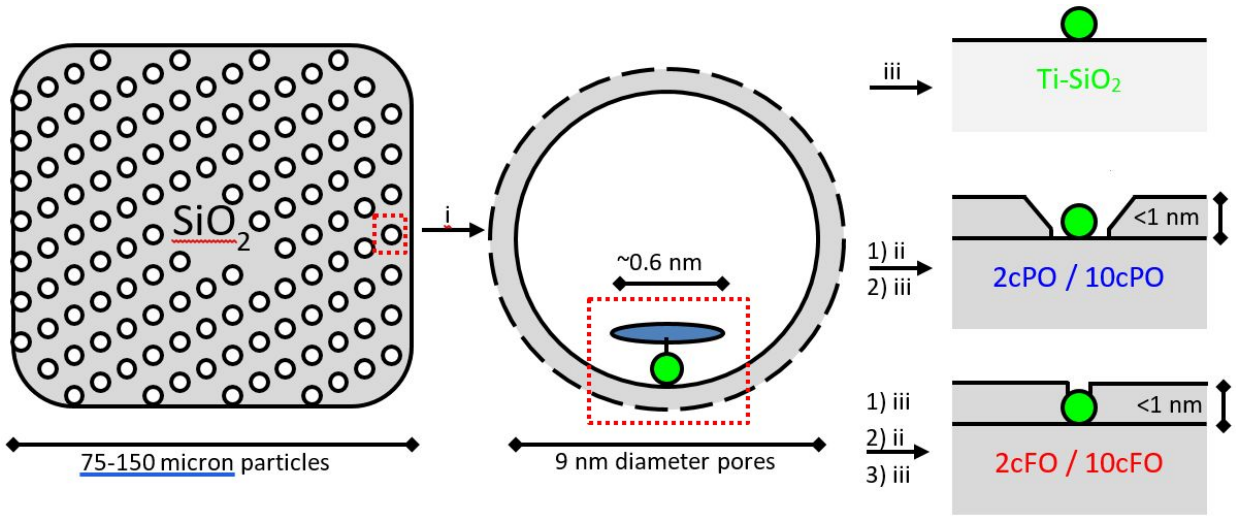

Figure 2.5 Ti-SiO_2 and SiO_2 overcoated catalysts beginning with micron sized support particles. i) Cp*$TiCl_3$ grafting at RT for 4 h, ii) liquid phase, sol gel SiO_2 overcoating, and iii) posttreatment via calcination at 550 ºC for 6 h. Green circles represent resulting TiOx species which can nominally represent site isolated, extraframework O_3TiOH or small TiOx oligomers.

Section 2.4 Control Materials

Control materials for Brønsted acid probe reactions were chosen as (i) the ASA from Sigma-Aldrich and (ii) zeolite H-Y (Zeolyst, CBV 780, SiO_2/Al_2O_3 = 80, 780 m^2/g). A high silica zeolite was chosen in order to study isolated Brønsted sites free from interactions that can occur when two sites are present in the same zeolite cage [103-104]. The ASA was synthesized via co-gelation so it may have varying degrees of mixing between SiO_2 and Al_2O_3. Selecto SiO_2 was used as a negative control to verify that bulk SiOH groups were inactive for the reaction. All materials were calcined using identical conditions to the Al_2O_3 based materials and were then used as positive controls in the catalytic cracking of 1,3,5-triisopropylbenzene (TIPB).

Control materials for Lewis acid probe reactions were chosen as (i) an in-framework mesoporous Ti-SBA-15 synthesized by former lab member Todd Eaton for a prior publication and (ii) zeolite Ti-Beta was obtained from the Flaherty group at the University of Illinois Urbana-Champaign [61, 105]. They synthesized this material via post synthetic ion exchange between a dealuminated commercial Beta (Zeolyst, CP814E, SiO_2/Al_2O_3 = 25, 680 m^2/g) and $TiCl_4$ in a dichloromethane solution. Both materials were calcined under identical conditions to the supported macroporous SiO_2 based materials and were then used as positive controls in the liquid phase oxidation of limonene with tert-butyl hydroperoxide (TBHP). Wide pore SiO_2 was used as a negative control to verify that the support was inactive for alkene oxidation.

Chapter 3. SiO_2 Deposition on Al_2O_3 for Tunable Brønsted Acid Catalysis

The research presented in this chapter was published in ACS Catalysis with Zhenyu Bo, Scott L. Nauert, and Justin M. Notestein [4].

Section 3.1 Brønsted Acid Catalysts

The grand challenges in Brønsted acid catalysis as identified by the DOE are to achieve controlled synthesis of catalytic materials with one type of active site and a designed active site environment [106]. Typical solid Brønsted acids consist of silica-aluminas with crystalline (zeolites) or amorphous (ASA) structure. Zeolites have proven incredibly useful in petroleum processing, commodity chemical production, and fine chemical synthesis since their prevalent use began in the 1960s [1]. ASA catalysts have historically been viewed as weaker Brønsted acid catalysts even though researchers recognized early on that zeolites and ASA possess the same active site, namely the bridging hydroxyl between Si and tetrahedral Al [28-29,107-108]. A nuanced discussion of acid strength needs focus on the synergy of three factors: (i) active site identity, (ii) active site density, and (iii) confinement effects. Over the past 30 years post-synthetic strategies have been the tool of choice for modification of zeolite and ASA reaction behavior.

The earliest methods developed to tune the acidity of strong Brønsted acid catalysts were dealumination via steaming with water or dissolution in strongly acidic nitric acid solutions [109-111]. This leads to significant leaching of framework Al and can result in redeposition as

extraframework Al species. There is then uniformly reduced active site density (sites/g) but stronger per site strength due to the removal of site-site interactions that occur if two sites are present in the close proximity. Another way to reduce acidity or switchover to primarily Lewis acid behavior is ion exchange of alkali cations to replace the bridging hydroxyl H^+ [112-113]. Commercial zeolites are available in NH_4^+ or Na^+ forms and all Group I and II elements have been screened for exchange properties into zeolites. This method reduces Brønsted acidity but keeps the Lewis acidity of framework Al intact.

The aspect of acidity that is unaddressed by these post-synthetic methods is confinement effects. Confinement leads to stronger adsorption of reactant molecules and/or decreased intrinsic activation barriers due to stabilizing van der Waals interactions with the surrounding oxide. The general approach for tuning the active site environment has been to synthesize entirely new materials with different pore sizes. For example, one can research microporous, mesoporous, and nonporous behavior by using zeolites, mesoporous materials, and core-shell ASA. Core-shell ASA offers unique opportunities for tunable acid site strength, acid site density, and active site environment via manipulating synthesis parameters. Prior attempts at this include CVD, ALD, and CLD of SiO_2 or Al_2O_3 precursors onto Al_2O_3 or SiO_2 respectively [7, 114-116]. These studies have led to great understanding of trends in active site identity and active site density but controllable catalyst design remains elusive for core-shell ASA.

In a recent example, SiO_2 was deposited on mesoporous Al_2O_3 using ALD to synthesize a weak Brønsted acid catalyst [115]. This material was shown to have increased activity in cyclohexanol dehydration as compared to the Al_2O_3 support. ALD with TEOS in this setup was limited to isolated SiOH groups because ALD was performed with water as the co-reactant

[115]. NH_3 or other basic vapor phase catalysts are need to encourage multilayer deposition of TEOS onto the oxide support [22]. Further findings by the same researchers show that surface acid sites and morphology is heavily dependent on post treatment calcination conditions [116]. Calcination under flowing air in a tube furnace was shown to generate site isolated SiOH regardless of the synthesis method whereas calcination under static air in a muffle furnace produces polymeric SiOx species [116]. The strong effects of posttreatment has also been studied on zeolites and ASA because accidental steaming can occur when the muffle furnace is used as water is easily trapped within zeolite micropores.

Therefore, in this work the objectives were to (i) achieve controlled CLD of SiO_2, (ii) find synthesis handles to tune SiO_2 overcoat morphology, and (iii) connect synthesis decisions to catalytic behavior in a Brønsted acid probe reaction. SiO_2 CLD was performed on Al_2O_3 nanoparticles with or without a carbonaceous template, followed by calcination using varying ramp rates to modify the overcoat morphology. Extensive physical and active site characterization was performed in order to assess the morphological changes to the support along with the identity and number of active sites. Finally, vapor phase TIPB cracking was performed to quantitatively assess the active site distribution and compare synthesized core-shell materials to ASA and industry standard zeolite Y. This synthesis-characterization-reaction study allows one to connect synthesis decisions to catalytic performance and make iterative changes to the catalyst design.

Section 3.2 Catalyst Characterization

Transmission electron microscopy (TEM) images were collected using the JEOL JEM-2100 FasTEM in the EPIC core facility at Northwestern university. Samples were prepared

by dispersing the solid into ethanol, sonicating the solution, and letting a single drop air dry onto a TEM grid. N_2 physisorption isotherms were collected at -196 ºC on a Micromeritics ASAP 2010 for previously dried materials. The materials were dried before physisorption via treatment under vacuum at 450 ºC overnight. BET surface areas were calculated using the Roquerol consistency criteria on the adsorption branch of the isotherm [117-118]. The BJH method was used to obtain the mesopore size distribution from the desorption branch of the isotherm. The t-plot (Al_2O_3, ASA, zeolite Y) or α_s plot (2cFO, 5cFO, 5cCO, 5cPO, 12cFO) was used to separate out the micropore and external surface areas [119]. To obtain lower pressure data points (< 1 torr), N_2 physisorption isotherms for 5cFO, 5cCO, and 5cPO were collected at -196 ºC on a Micromeritics 3Flex in the CleanCat core facility at Northwestern University. The NLDFT method (cylindrical pores) was used to calculate micropore size distributions from the adsorption branch of the isotherm.

Si and Al content was obtained for conventional ASA and zeolite Y materials. Briefly, 20-50 mg of material was loaded into a 15 mL centrifuge tube. 2-3 drops of concentrated HF (Macron Fine Chemicals, ACS Reagent, 48 %) were added to dissolve the solid. CAUTION: HF is a highly dangerous chemical and all contact with skin or eyes needs to be avoided. Minimum PPE for use includes silver shield gloves and goggles. For solids consisting mostly of Al_2O_3, treatment with concentrated HF was ineffective. We attempted stirring at RT in concentrated HNO_3 (Fisher Chemical, TraceMetal Grade, 67-70 wt %), stirring in refluxing HNO_3, and dissolution with 2-3 drops of concentrated KOH (Fisher Chemical, Certified ACS, ≥ 85.0 %). Dissolution did occur in refluxing HNO_3 but we never finished ICP-OES of Al_2O_3 based samples. Therefore, reported Si content for core-shell materials is based on the amount of TEOS

added during the overcoating procedure. Dissolved ASA and zeolite Y solids were compared to 1 blank and 5 diluted standards spanning 0-75 ppm Al (Sigma-Aldrich, TraceCERT, 1000 ppm Al in HNO_3) or Si (Sigma-Aldrich, TraceCERT, 1000 ppm Si in HNO_3, CAUTION: contains trace HF). ICP measurements were performed on the Thermo iCAP7600 ICP-OES in the QBIC facility at Northwestern University.

Quantification of carbonaceous calixarene and ACA templates was performed using TGA on a TA Instruments Q500. The O_2 flow rate was set to 90 sccm and N_2 to 10 sccm. 20-50 mg of materials was loaded into an alumina pan. The weight was allowed to equilibrate at RT for 20 min, then the temperature was ramped at 20 ^{o}C/min to 800 ^{o}C. High res mode was active so rapid mass loss triggered a slowing down of the ramp rate. Once the sample reached 800 ^{o}C, the weight was equilibrated for 10 min. Mass loss between ~300 ^{o}C and 800 ^{o}C was quantified and attributed to the template removal and desorption of surface hydroxyls. Surface hydroxyl loss was subtracted out by doing the same TGA run on the bare Al_2O_3 support. Templates were characterized via ambient DRUV-vis using a Shimadzu UV-3600 Plus UV-Vis-NIR Spectrophotometer. PTFE (Sigma-Aldrich, powder, 35 micron particle size) was used as the background and diluent. Samples were diluted by a factor of ~20 and measured from 200 nm to 800 nm.

Active site density (sites/g) were calculated using NH_3 temperature programmed desorption (TPD) on an AMI-200 instrument in the CleanCat core facility at Northwestern University. 80-120 mg of powder were packed on top of a small bed of quartz wool such that the TPD thermocouple was in position just above the powder surface. The catalyst was activated at 450 ^{o}C for 1 h with a 10 ^{o}C/min ramp rate using a 30 sccm stream of 10 % O_2 in He. Then, the

sample was allowed to cool to 100 ºC. 10 % NH_3 in He was pulsed in at 100 ºC using a 0.6 mL sample loop until no change was detected in the outgoing NH_3 TCD signal. Then, the chemisorbed NH_3 was desorbed under 30 sccm of an inert He purge stream while ramping the temperature to 450 ºC at 10 ºC/min. Duplicate trials were run for each catalyst to verify peak shape and desorption maxima.

Brønsted and Lewis acid site identity was performed using NH_3 DRIFTS on a Thermo Nicolet 6700 FTIR in the CleanCat core facility at Northwestern University. Freshly calcined catalysts were loaded into the diffuse reflectance cell and activated at 450 ºC under 120 sccm of Ar flow. The powder was cooled down to 100 ºC and equilibration was considered complete once the FTIR spectrum remained stable. Background spectra under Ar were obtained at 100, 215, 335, and 450 ºC. After obtaining backgrounds, the sample was again cooled down to 100 ºC. Then, 80 sccm of 1 % NH_3 in He was flowed over the sample at 100 ºC until the spectrum remained stable. Inert Ar at 120 sccm was used to purge physisorbed NH_3 and difference spectra were recorded at 100, 215, 335, and 450 ºC with 30 min allowed at each temperature to equilibrate desorption.

Pyridine DRIFTS spectra were collected using a Nicolet Nexus 670 FTIR in the Kung lab. Freshly calcined catalysts were loaded into the diffuse reflectance cell and activated at 400 ºC under 40 sccm of He flow. The powder was cooled down to 150 ºC and equilibration was considered complete once the FTIR spectrum remained stable. Background spectra under He were obtained at 150, 235, 315, and 400 ºC. After collecting backgrounds, the sample was again cooled down to 150 ºC. 2-3 drops of anhydrous pyridine (Sigma-Aldrich, 98 %) were added to a quartz wool bed inside an oven dried glass u-tube. The u-tube was connected to two Ultra-Torr

fittings and He flow was switched to flow through the u-tube and over the sample at 150 ^{o}C until the adsorbed pyridine spectrum remained stable. Then, He flow was switched back to bypass the u-tube. Difference spectra were recorded at 150, 235, 315, and 400 ^{o}C with 30 min allowed at each temperature to equilibrate desorption.

Al coordination was obtained via ^{27}Al DP and ^{1}H-^{27}Al CP/MAS solid state NMR performed on the Varian Solids 400 MHz VNMRS instrument in the IMSERC user facility at Northwestern university. Crystalline aluminum nitrate nonahydrate (Sigma-Aldrich, 99.997 % trace metals basis) was used as the ^{27}Al standard and its chemical shift was set to 0 ppm. Freshly calcined materials were loaded into 5 mm zirconia rotors and NMR spectra were obtained while spinning at 10,000 rpm. The recycle delay was 1.0 s and the contact time was 0.5 ms. 16 scans were taken and all reported data are averages of these scans. Si coordination data via ^{29}Si DP and ^{1}H-^{29}Si CP/MAS solid state NMR was attempted on the solids 400 instrument. However, after allowing SiO_2 overcoated samples to run for 24 h or ~4,500 scans, no signal was observed. Future studies where NMR is necessary to characterize the Si coordination will require the use of DNP NMR at the Iowa State facility [115-116].

Triphenylphosphine oxide (TPPO, Sigma-Aldrich, 98 %) was adsorbed onto 5cFO, 5cCO, and 5cPO catalysts for probing acid sites using ^{31}P solid state NMR on the Solids 400 instrument in the IMSERC facility at Northwestern university. 250 mg catalyst were shaken overnight at RT and 200 rpm in 10 mL of a THF (Sigma-Aldrich, inhibitor-free, for HPLC, ≥ 99.9 %) solution containing 10-fold excess TPPO (per total acidity as found using NH_3 TPD). Solids were recovered via vacuum filtration and washed with 2 x 50 mL of THF. Samples were then dried at RT under vacuum on a Schlenk line for 4 h until use in the NMR experiment. ^{31}P

DP and ^{1}H-^{31}P CP solid state NMR experiments were performed, with the CP experiment giving no signal after 10,000 scans. All shifts were referenced to 85 % H_3PO_4 and this standard was set to 0 ppm.

Section 3.3 Catalytic Cracking of TIPB

TIPB (Sigma-Aldrich, 95 %) cracking was performed in the vapor phase using a syringe feed pump attached in-line before a u-tube glass reactor. 10-100 mg of catalyst was loaded and diluted to a total of 250 mg with sand (BDH Chemicals, 30-40 mesh). All catalysts were sieved below 325 mesh particle size before use in the reaction. He was used as a carrier gas and was typically flowed over the catalyst bed at 40-50 sccm. The catalyst was activated in 50 Nccm of He at 250 ^{o}C for 1 h before use in the reaction. Then, the catalyst bed temperature was increased to 450 ^{o}C and allowed to equilibrate for 15-30 min. The syringe pump was turned on with the flow rate set at 0.2 mL/h in order to maintain steady evaporation. CAUTION: TIPB is a very high boiling liquid so all metal lines need to be traced with the temperature set above 165 ^{o}C.

Catalytic cracking rates were measured using an online HP Agilent 6890 GC-FID with a HP-INNOWax column attached. Standards for major reaction products 1,3-Diisopropylbenzene (Sigma-Aldrich, 96 %), 1,4-Diisopropylbenzene (Sigma-Aldrich, 97 %), Cumene (Sigma-Aldrich, 98 %), and Benzene (Sigma-Aldrich, ≥ 99.9 %) were injected manually in order to obtain retention times. Integration and quantification was performed using the carbon number method with TIPB being 15, DIPBs being 12, cumene being 9, and benzene being 6. This method is accurate for products who all belong to the same chemical family [120].

Mass balances closed to within 85-105 % on the basis of TIPB consumed vs products formed when including the 4 expected products. The syringe pump setup was found to deliver

steady TIPB flow with a standard error of 5 %. Other observed products were likely structural isomers formed due to isomerization on the benzyl ring or within the isopropyl group. Time on stream data was obtained for 2 h with negligible deactivation occurring under these conditions. TGA and DRUV-vis were employed on some post reaction catalyst samples when color change was observed. Internal and external mass transfer limitations were assessed with the Weisz-Prater criterion and by varying W/F while keeping W constant at 100 mg. These two tests demonstrated that diffusion limitations were negligible until ~70 % conversion for Al_2O_3 based catalysts.

Section 3.4 Results and Discussion

Section 3.4.1 Physical Characterization

Our group and many others have demonstrated surface modification of metal oxides using CLD, CVD, and ALD with metal precursors [7, 21-23, 91, 93, 115-116]. Although the SiO_2 overcoats synthesized in this work may be achievable via ALD, the CLD method used here enables the production of large quantities of material (10-25 g), allows for the use of standard lab equipment, and does not require air sensitive metal precursors. All physical characterization results for Al_2O_3, five SiO_2 overcoated variants, ASA, and zeolite Y are collected in Table 3.1. Figure 3.1 demonstrates that five TEOS deposition cycles (5cFO) leads to the formation of a thin, conformal SiO_2 overcoat with a thickness ~2 nm. A material that underwent twelve deposition cycles (12cFO) has a thicker overcoat of 5 nm and interstitial growth between Al_2O_3 particles. It is clear from this image that particle agglomeration becomes significant during higher deposition cycles.

Table 3.1 Physical characterization for SiO_2-Al_2O_3 core-shell catalysts and the Al_2O_3 support.

			surface area (m^2/g)		
material	SiO_2 (wt %)[a]	shell thickness (nm)	external	micropore	total
NA			36	0	36
2cFO	3.2	n.d.	36	0	36
5cFO	6.2	2	34	6	40
5cCO	6.2	2	22	18	40
12cFO	11.7	5	0	30	30
5cPO	6.2	3	46	6	52

[a]calculated based on TEOS added during SiO_2 overcoating

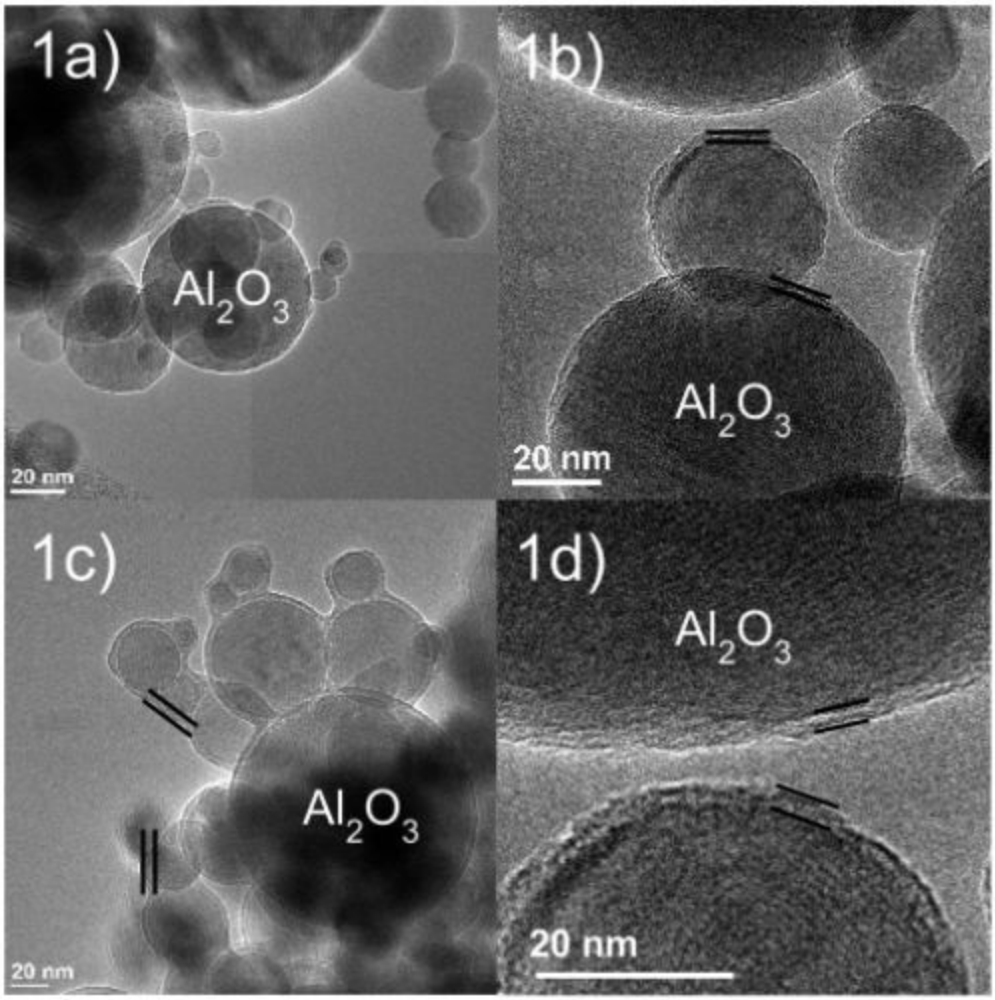
1a)
Al_2O_3
20 nm
1b)
Al_2O_3
20 nm
1c)
Al_2O_3
20 nm
1d)
Al_2O_3
20 nm

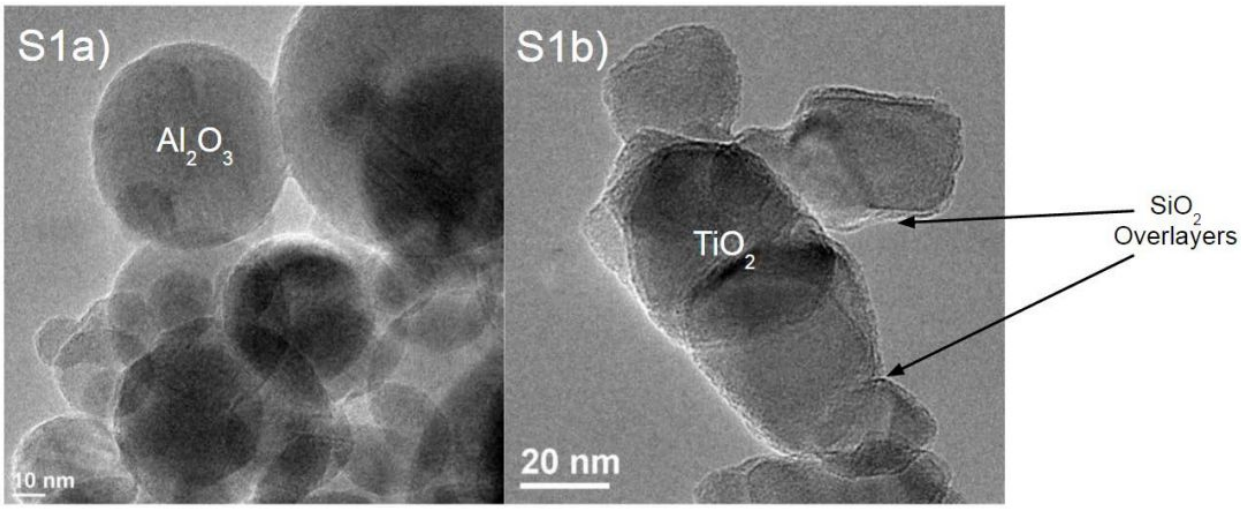
S1a)
Al_2O_3
10 nm
S1b)
TiO_2
20 nm
SiO_2
Overlayers

Figure 3.1 TEM images of SiO_2 overcoated catalysts and the bare Al_2O_3 support. 1a) Al_2O_3, 1b) 5cFO, 1c) 12cFO, 1d) zoomed-in 5cFO, S1a) 2cFO, and S1b) 5cFO-TiO_2 (Evonik P25).

With an average deposition rate of 0.4 nm/cycle, this method deposits 1.4 monolayers SiO_2/cycle [121]. This is likely due to the use of hydroxyl density for determining the TEOS added during each deposition cycle. As suggested by others researchers recently, projected van der Waals diameter of the TEOS precursor is likely a better way to determine monolayer addition amounts for TEOS [122-123]. Rough calculations show that a steric monolayer of TEOS would involve a factor of 1.4 less TEOS added per cycle. Anyway, a broad visual survey of the SiO_2 overcoated samples revealed no bulk SiO_2 particle formation. Although not used further in this study, SiO_2 overcoating was performed on Evonik P25 TiO_2 to demonstrate that the overcoat is extendable to other oxides. Similar thickness and conformal nature were observed for these materials as shown in Figure 3.1.

Our group previously developed a method to create 1-2 nm sized pores on the surface of nonporous oxides by grafting carbonaceous templates on TiO_2, depositing Al_2O_3 via ALD or SiO_2 via CLD, and removing the templates using ozone [93, 124]. These thin, cavity containing overlayers allowed for shape selective sieving of reactant molecules for photocatalysis with TiO_2 and the controlled deposition of small Ag nanoparticles on limited TiO_2 domains. In this study, calixarene was used similarly to prevent complete coverage of the Al_2O_3 support and leave behind interfacial sites between Al_2O_3 and SiO_2. The calixarene-Al_2O_3 material was synthesized with a surface loading of 0.30 calix/nm^2 as found by TGA shown in Figure 3.2. Using a simple 2D geometric model where calixarene is packed upper rim to upper rim (1.4 nm diameter),

calixarenes cover 45 % of the Al_2O_3 surface at maximum loading. These values were taken to be the density of exposed domains after calcination.

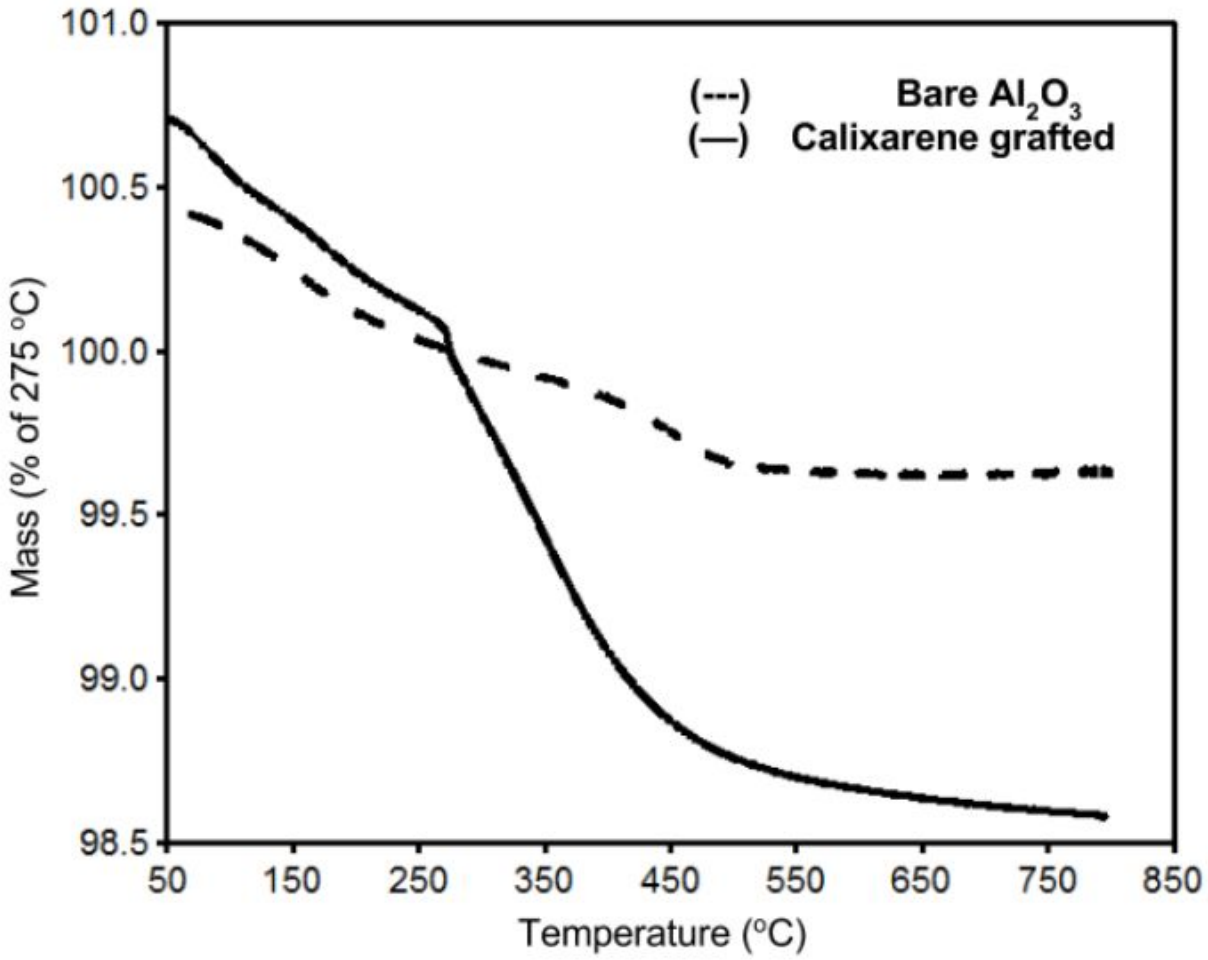

Figure 3.2 Representative TGA curves for the Al_2O_3 support and a variant loaded with 0.30 calixarene/nm^2. Mass loss between 300-800 °C was measured for both materials and the difference between their mass losses was assumed to be due to calixarene decomposition.

N_2 physisorption experiments and BET method analyses were performed to assess surface morphology changes due to overcoating, calcination conditions, and the calixarene template. N_2 physisorption isotherms at -196 °C, α_s plots, and pore size distributions are shown in Figures 3.3 and 3.4. The Al_2O_3 support has a Type III isotherm typical for nonporous materials

and its external surface area is 34 m^2/g [125]. Materials with intact SiO_2 overcoats (xcFO) have Type I isotherms with this Type I character increasing as more SiO_2 is deposited [125]. This indicates the formation of microporous regions on the surface. 2cFO shows little changes but 5cFO, 5cCO, and 12cFO show a decrease in external surface area compensated by an increase in micropore surface area. 12cFO has almost entirely micropore surface area which is due to the formation of a loosely packed SiO_2 shell. The loss of external surface area is mostly due to agglomeration as observed by TEM imaging.

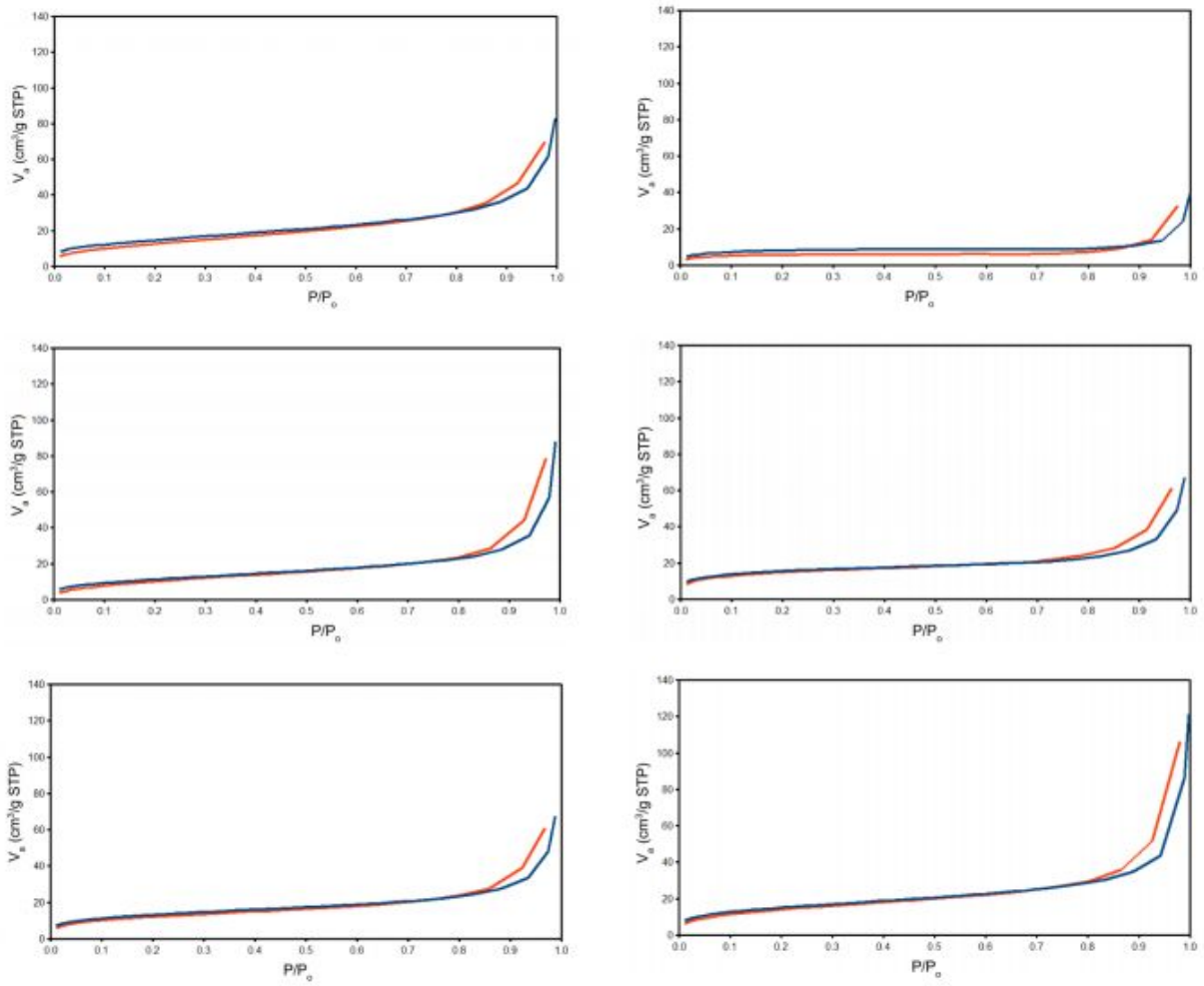

Figure 3.3 N_2 physisorption isotherms obtained at -196 ºC for synthesized SiO_2-Al_2O_3 core-shell materials. The adsorption branch is shown in blue and the desorption branch is shown in orange.

The surface areas for the Al_2O_3 support (top left), 2cFO (mid left), 5cFO (bottom left), 12cFO (top right), 5cCO (mid right), and 5cPO (bottom right) were derived from this data.

Differences among the materials in terms of micropore surface area demonstrates the large effects of calcination ramp rate on surface morphology. 5cFO, which was calcined with a 3.5 ^{o}C/min ramp rate, has 6 m^2/g micropore surface area whereas 5cCO, calcined with a much more aggressive 20 ^{o}C/min ramp rate, has 18 m^2/g. This is interpreted as the formation of cracks in the SiO_2 overcoat. This has been demonstrated previously for some bulk oxide materials and the phenomena is attributed to rapid hydroxyl condensation and water evaporation leading to the formation of irregular micropore structures [126-128]. 5cPO exhibits a distinct increase in external surface area rather than micropore surface area, up to 46 m^2/g, which is a 35 % increase. The calixarene template thus influenced the morphology of the partial SiO_2 overcoat by leaving behind nanocavity walls that will contribute to external surface area.

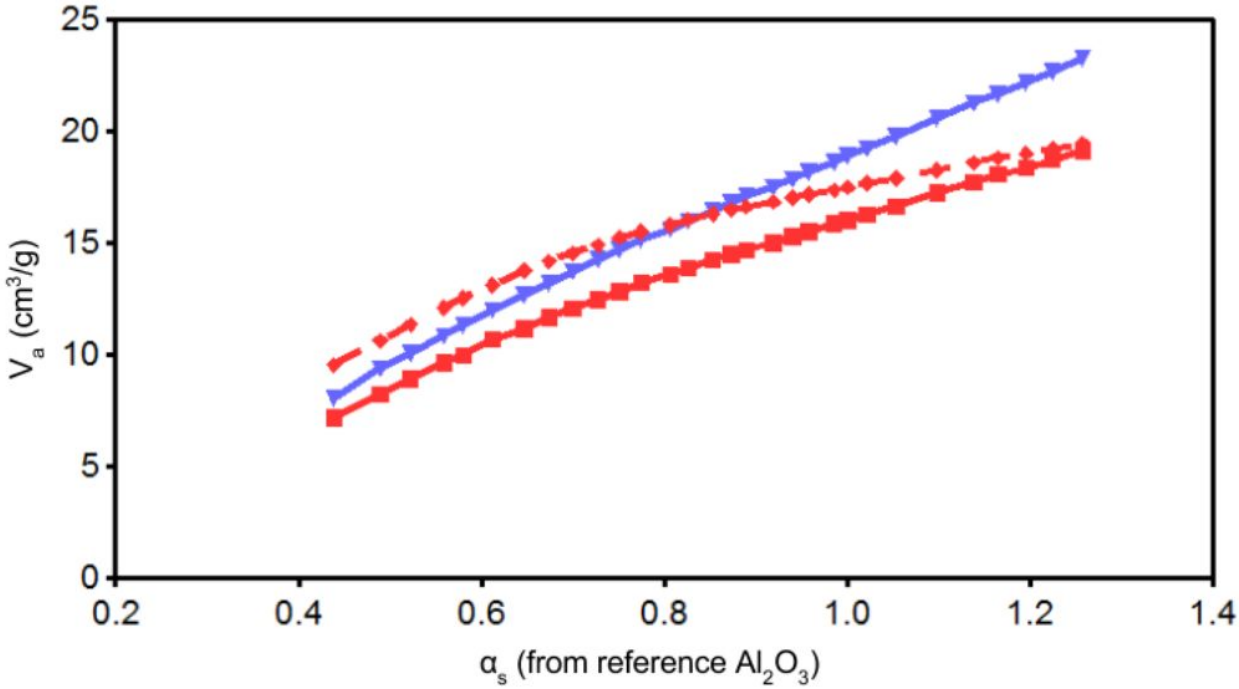

Figure 3.4 N_2 physisorption α_s plot for 5cFO (red), 5cCO (dashed red), and 5cPO (blue). The Al_2O_3 support was used as the reference. The external surface area regime for each material was used because the reference only possesses external surface area. Micropore surface area was calculated as the difference between total BET and external surface area.

The micropore size distribution seen in Figure 3.4 suggests that surface micropores are on the order of ~0.5 nm. However, caution is urged in interpretation because the pore volume is very low on these materials. The pore volume is orders of magnitude lower than mesoporous materials and zeolites because porosity is confined to the 2 nm thick SiO_2 shell rather than extending throughout the particle. In summary, several synthesis parameters have been identified for tuning SiO_2 overcoat morphology. Deposition cycle count, calcination ramp rate, and template grafting show distinct influences on the resulting material.

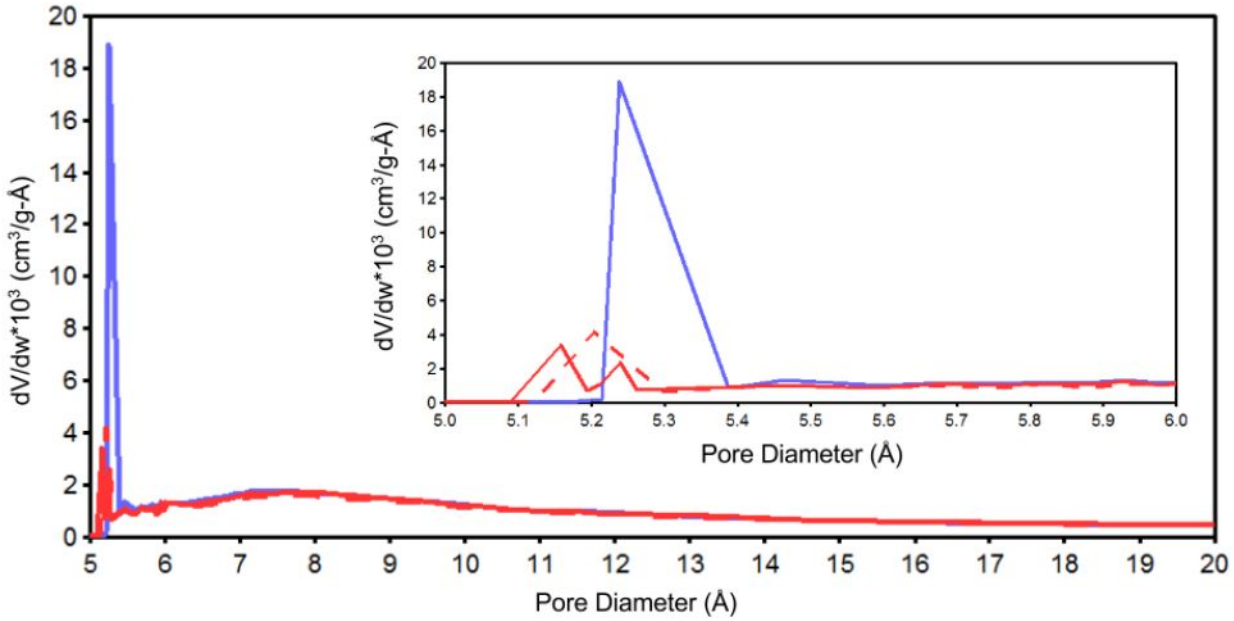

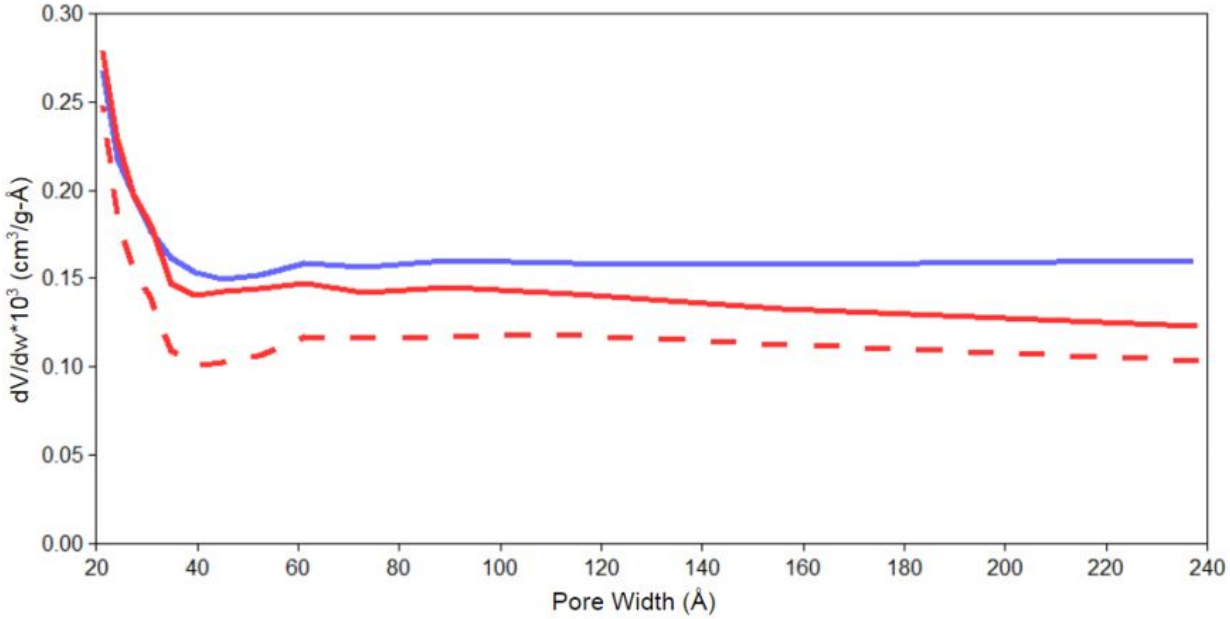

Figure 3.5 top, a) micropore size distribution based on the Saito-Foley modification of the Horvath-Kawazoe method from N_2 physisorption data obtained at -196 ºC. 5cFO (red), 5cCO (dashed red), and 5cPO (blue) are shown. The inset shows the curves from 0.5-0.6 nm. Caution is urged in overinterpretation because the total pore volumes for each material are <0.015 cm^3/g. **bottom, b)** mesopore size distribution based on the BJH method (Kelvin model) from N_2 physisorption data obtained at -196 ºC. 5cFO (red), 5cCO (dashed red), and 5cPO (blue) are shown. Note that the primary particle size for all materials is 40-50 nm.

Section 3.4.2 Acid Site Characterization

After quantifying the effects of templating on the SiO_2 overcoated materials, we characterized the resulting active sites using basic probe molecules. Vapor phase NH_3 has been widely used to identify and quantify acid sites throughout various catalysts structures [24, 129-130]. Due to its nonspecific and high reactivity with surface hydroxyl groups through hydrogen bonding and coordinating bonds, it typically provides an overestimate of catalyst acidity (sites/g). However, a benefit of its use is that its small kinetic diameter of 0.26 nm allows it to access nearly all sites even in microporous zeolites [24, 131-133]. Figure 3.6 shows NH_3

TPD curves for Selecto SiO_2, the Al_2O_3 support, 5cFO, 5cCO, and 5cPO along with total acid site counts.

There is a clear shift in site density down from the Al_2O_3 support to the overcoated materials, with the value dropping from 0.31 to 0.13 mmol/g for 5cFO. On Al_2O_3 catalysts, the peak at 360 °C has previously been attributed to Lewis acidic tetrahedral Al (Al^{IV}), and this peak is suppressed after SiO_2 deposition [134]. This indicates that the TEOS deposition is unselective during overcoating, with most sites blanketed by SiO_2. However, there is evidence for the formation of strong acid sites due to the emergence of a peak at 450 °C for 5cCO. While we cannot assign an exact active site structure based on this study, zeolites and ASA have peaks in the regime corresponding to Brønsted acid sites [135-137]. All of the curves are distinctly different than that for Selecto SiO_2, which has a small broad peak in the weak hydroxyl region. SiO_2 is well known to be weakly Brønsted acidic and inactive in most reactions.

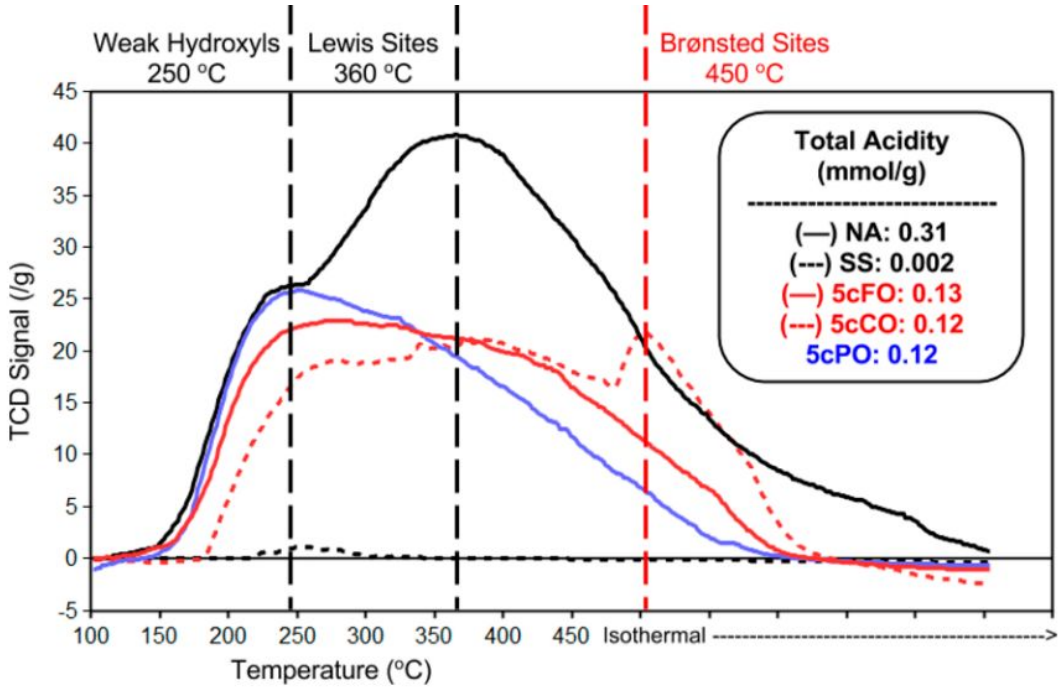

Figure 3.6 NH_3 TPD curves for SiO_2-Al_2O_3 core-shell materials, the Al_2O_3 support (NA), and Selecto SiO_2 (SS). An isothermal step was started at 450 ºC and continued for ~30 min as the TCD signal returned to 0. Site assignments were made retroactively based on NH_3 DRIFTS, pyridine DRIFTS, and TIPB cracking performance.

Although similar numbers of total acid sites exist on all 5c overcoated materials, the desorption temperatures are different, implying a different active site distribution. Since the Al_2O_3 surface is totally covered for 5cFO, the acid sites are likely perturbed silanols of the form Al-O-Si-OH. Sites of this type have been proposed to be present on external zeolite surfaces and ASA, and are related to the formation of pseudo bridging hydroxyls on amorphous surfaces [138-141]. The high temperature feature for 5cCO indicates that it possesses a subset of sites distinctly stronger than those on 5cFO and 5cPO. Further characterization and reaction probes provide evidence for interfacial strong Brønsted acid sites in the cracked 5cCO SiO_2 overcoat. To complete a cursory analysis, the fraction of strong sites (Tdes > 300 ºC) vs weak sites (Tdes < 300 ºC) changes significantly upon SiO_2 overcoating. The Al_2O_3 support has nearly 4 times the high temperature sites of 5cFO (0.22 vs 0.06 mmol/g), implying that TEOS deposition results primarily in the formation of weak acid sites. Therefore, SiO_2 overcoated Al_2O_3 has several orders of magnitude more acid sites than bulk SiO_2 but possesses distinct acidity different from the Al_2O_3 support.

In order to identify and differentiate surface acid sites, FTIR studies were performed using vapor phase NH_3. Figure 3.8 shows the hydroxyl region of the difference spectra, which consists of negative peaks corresponding to OH interactions with NH_3, and the amine region, which consists of positive peaks corresponding to new interactions with the surface. Figure 3.7 and Table 3.2 contain the full NH_3 DRIFTS difference spectra along with peak assignments for

the amine region. The hydroxyl region has eight total peaks, with four contributions from the Al_2O_3 and four contributions from the SiO_2. Since the Al_2O_3 is a mixed delta/gamma phase, the surface hydroxyls are expected to take on gamma phase character [142]. TEOS deposition fully covers the basic isolated OH groups on Al^{IV} (3787 cm^{-1}), octahedral Al (Al^{VI}, 3768 cm^{-1}), and the bulk hydroxyl at 3671 cm^{-1} [143-145]. One aluminol at 3730 cm^{-1}, the most reactive according to prior research, remains as a shoulder feature despite the overcoat, especially for the templated 5cPO catalyst [143-145]. This strongly suggests that the calixarene template protected these hydroxyls during SiO_2 deposition.

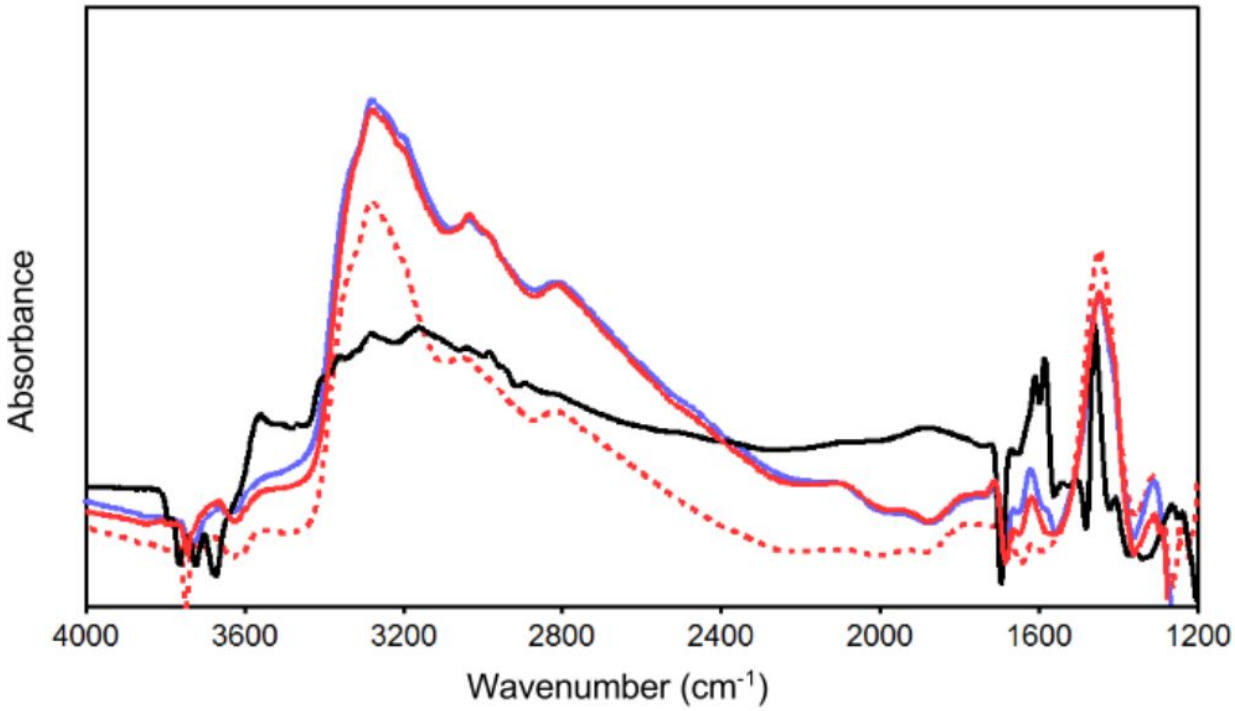

Figure 3.7 Complete DRIFTS NH_3 chemisorption spectra obtained at 100 °C for the Al_2O_3 support (black), 5cFO (red), 5cCO (dashed red), and 5cPO (blue).

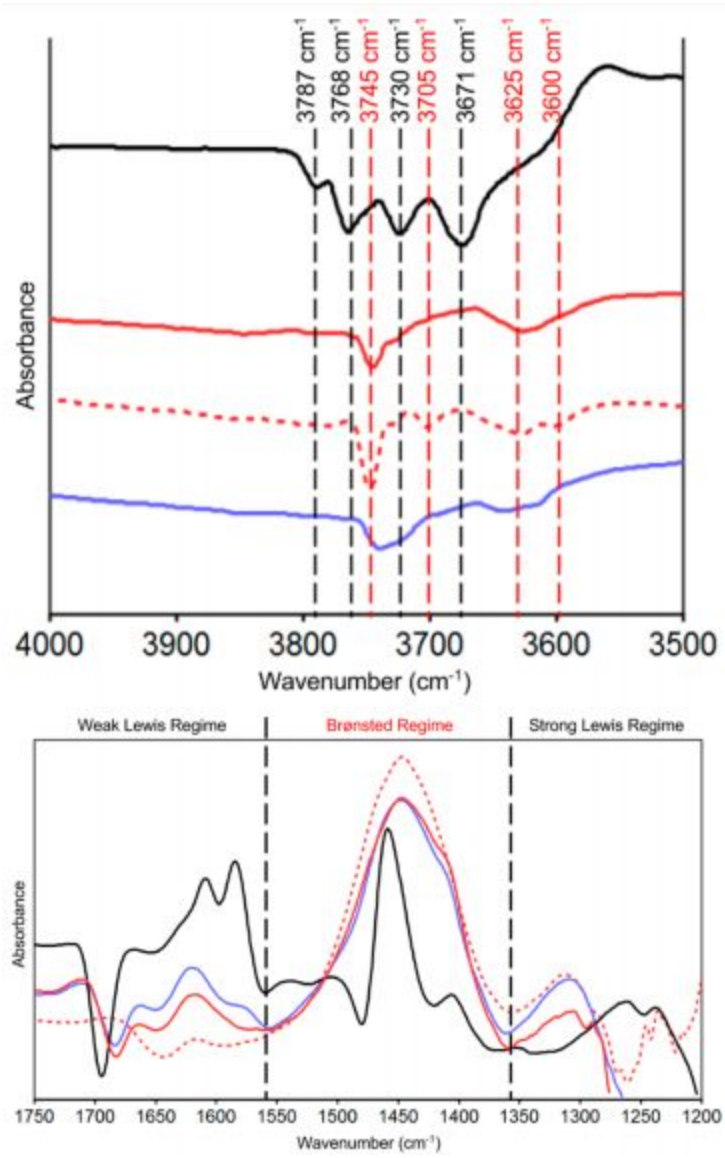

Figure 3.8 top, a) hydroxyl stretching region and **bottom, b)** amine stretching and bending region of DRIFTS NH_3 chemisorption spectra obtained at 100 ºC for the Al_2O_3 support (black), 5cFO (red), 5cCO (dashed red), and 5cPO (blue).

Table 3.2 NH_3 DRIFTS amine stretching and bending region assignments for Al_2O_3 and SiO_2-Al_2O_3 [108, 146-147].

WAVELENGTH (CM^{-1})	VIBRATIONAL MODE
1232	Al^{VI}---NH_3 symmetric deformation
1258	Al^{IV}---NH_3 symmetric deformation
1287	SiO_2 perturbed 1232 band
1306	SiO_2 perturbed 1258 band
1405	NH_4^+---NH_3 interaction
1440	NH_4^+ on Si-O^-
1455	NH_4^+ on Al-O^-
1501	Al^{IV}---NH_2 deformation
1537	Al^{VI}---NH_2 deformation
1578	H bonding interactions
1583	H bonding interactions
1605	Al---NH_3 asymmetric deformation
1620	SiO_2 perturbed 1605 band
1664	O---NH_3 coordination
1668	O---NH_3 coordination
1710	O---NH_3 coordination

All SiO_2 overcoated materials show a strong signal at 3745 cm^{-1}, which corresponds to the generation of isolated SiOH [138-141]. This hydroxyl was expected to be prevalent due to high temperature calcination at 650 ^oC and the thinness of the SiO_2 layer. Interestingly, there is a weak feature in the 3725-3730 cm^{-1} region for 5cFO and 5cCO. This may correspond to the aforementioned aluminol or the perturbed silanol Al-O-Si-OH [138-141, 143-145]. Unfortunately, no definitive peaks appear in the bridging hydroxyl region 3550-3700 cm^{-1} for

5cPO. Therefore, there are unlikely to be interfacial sites between Al_2O_3 and SiO_2 on this material. Although there are weak features in the 5cFO and 5cPO spectra at 3625 cm^{-1}, further characterization and reaction studies prove this to be unassignable to strong Brønsted acid sites. However, the 5cCO catalyst DRIFTS spectra possesses three unique peaks. The hydroxyl at 3705 cm^{-1} is assigned as bridging AlOH or hydrogen bonded micropore SiOH [138-141, 143-145]. This extra peak lends support to surface roughening and a cracked overcoat as observed from the N_2 physisorption isotherm. Peaks at 3600 and 3625 cm^{-1} can indicate bridinging Al-OH-Si hydroxyls which are the strong Brønsted acid sites present in zeolites and ASA [138-141]. These correlate with the high temperature NH_3 desorption peak observed for 5cCO. Surface roughening has then led to the formation of interfacial sites, and unlike 5cPO, surface SiOH can interact with underlying Al^{IV}.

The amine stretching and bending IR region provides information on catalyst acidity and allows for distinction between Lewis and Brønsted acid site chemisorption of NH_3. In the zeolite and ASA literature, commonly cited peaks occur at 1260 cm^{-1} (strong Lewis sites), 1450 cm^{-1} (Brønsted sites), and 1620 cm^{-1} (weak Lewis sites or framework O) [138-141, 143-145]. The spectra for Al_2O_3 supported materials contain all three peaks and further substructure, but for the purposes of Brønsted:Lewis (B:L) ratio analysis, broad regions were defined to categorize different sites with similar character [108, 132, 146]. After integration of the spectra using midpoint Riemann summation in excel, the B:L peak area ratio increases from 0.68 for Al_2O_3 to 1.32 for 5cPO, 1.67 for 5cFO, and 2.17 for 5cCO. This calculation correlates well with an increase in the Brønsted acid peak area and unselective attenuation of Lewis acid peaks for SiO_2 overcoated materials. These spectra combined with TPD analysis indicate that SiO_2 deposition

quenches surface Al Lewis acid sites and generates SiOH capable of protonating vapor phase NH_3. The DRIFTS spectra indicate that the preferred grafting mode for calixarene is not on Lewis acid sites. The small increase in Lewis peak area for 5cPO and 5cCO is due to microporosity that allows access to the underlying surface. A marked difference in acidity is not observed for 5cFO and 5cPO, meaning that the primary difference between these two is likely due to less surface SiOH content for 5cPO (sites/m^2).

Both NH_3 chemisorption studies demonstrate that surface acidity changes upon TEOS deposition and that Lewis acid sites are covered up during the deposition. ^{1}H-^{27}Al CP/MAS solid state NMR was attempted with the goal of analyzing changes in surface Al distribution due to modification with SiO_2. The samples were pretreated under vacuum at 120 ^{o}C to remove physisorbed water. NMR spectra for the Al_2O_3 support, 5cFO, and 5cPO are shown in Figure 3.9. All spectra contain two peaks, one for Al^{IV} at 11 ppm and Al^{VI} at 63 ppm [147-149]. No significant differences in tetrahedral:octahedral ratio were observed among these materials because the vast majority of Al atoms are in the core of the particle. Attempts at ^{29}Si-^{27}Al HSQC and other ^{29}Si solid state NMR studies were inconclusive due to no signal being observed even after 10,000 scans, from the low loadings of Si on the support. A dedicated NMR investigation into these materials with surface sensitive ^{29}Si DNP NMR will help verify proposed surface species [115-116].

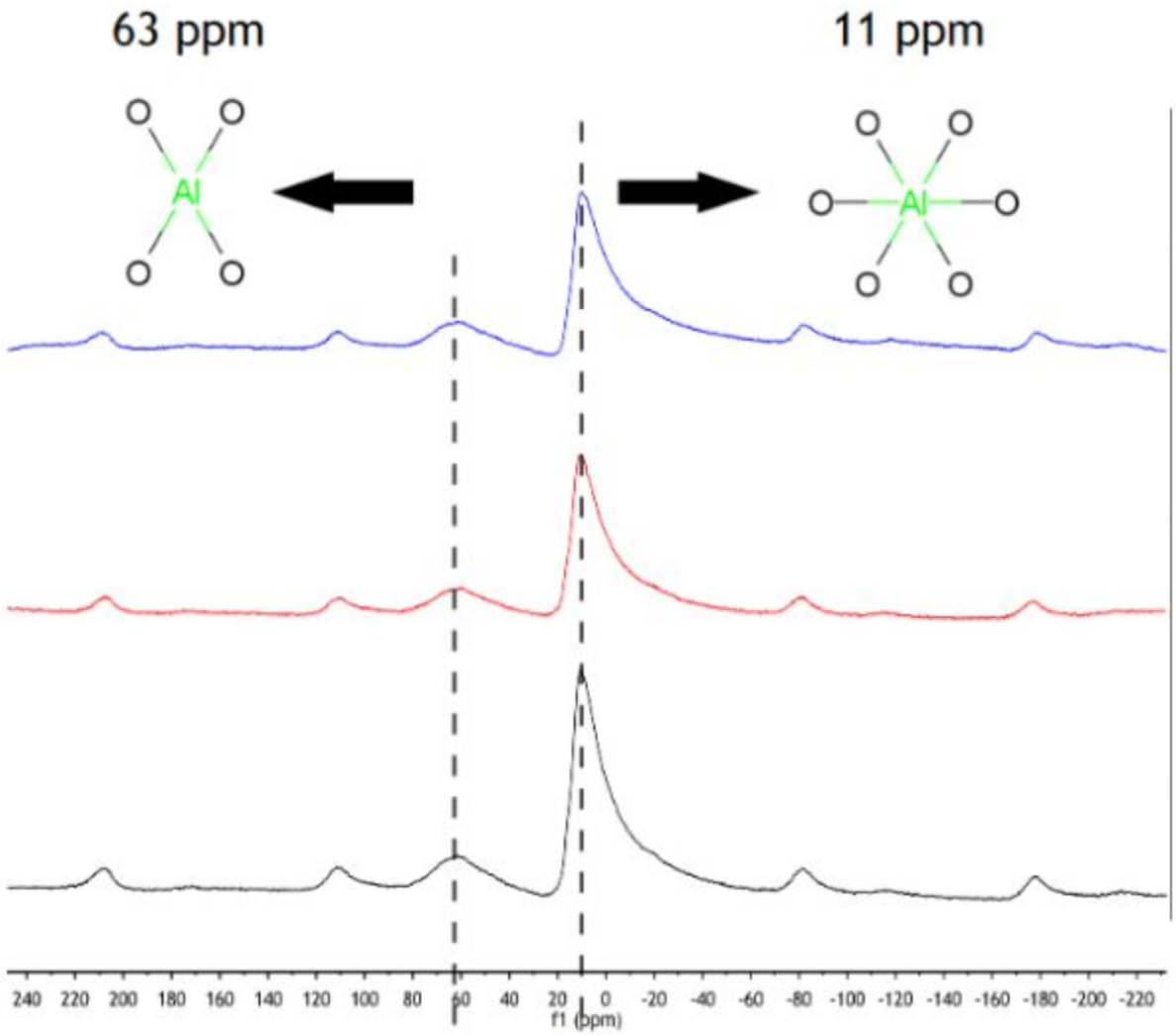

Figure 3.9 ^{1}H-^{27}Al CP-MAS solid state NMR spectra for the Al_2O_3 support (black), 5cFO (red), and 5cPO (blue). The octahedral:tetrahedral ratio varies slightly from 3:1 for Al_2O_3 to 4:1 for 5cFO. No marked peak shift were observed.

Pyridine is a more selective basic probe for analysis of strong surface acid sites that may be competent for catalytic reactions. Therefore, to complement the NH_3 chemisorption studies, a DRIFTS study was performed using pyridine. The hydroxyl and amine regions are shown in Figure 3.11. Immediately a stark contrast in the hydroxyl region is noticed as less hydroxyl groups are capable of interaction with pyridine than NH_3. The Al_2O_3 peaks reduced down to two,

with the reactive aluminol at 3730 cm^{-1} and bulk hydroxyl at 3671 cm^{-1} capable of interacting with pyridine. All SiO_2 overcoated materials display a peak at 3745 cm^{-1} which again correspond to isolated silanols. There is still distinct substructure to this peak for 5cPO, indicating the remaining aluminol at 3730 cm^{-1}. This finding further supports the proposed protection of this hydroxyl by calixarene from SiO_2 overcoating.

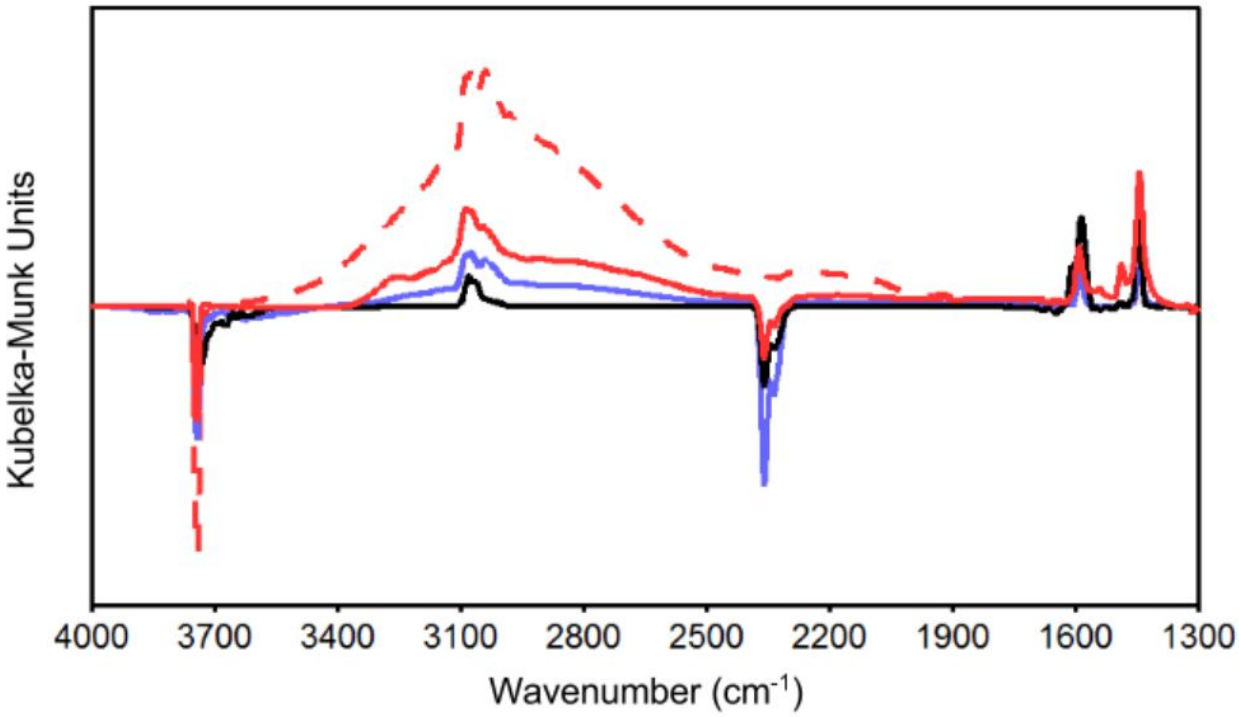

Figure 3.10 Complete DRIFTS pyridine chemisorption spectra at 150 °C for Al_2O_3 (black), 5cFO (red), 5cCO (dashed red), and 5cPO (blue).

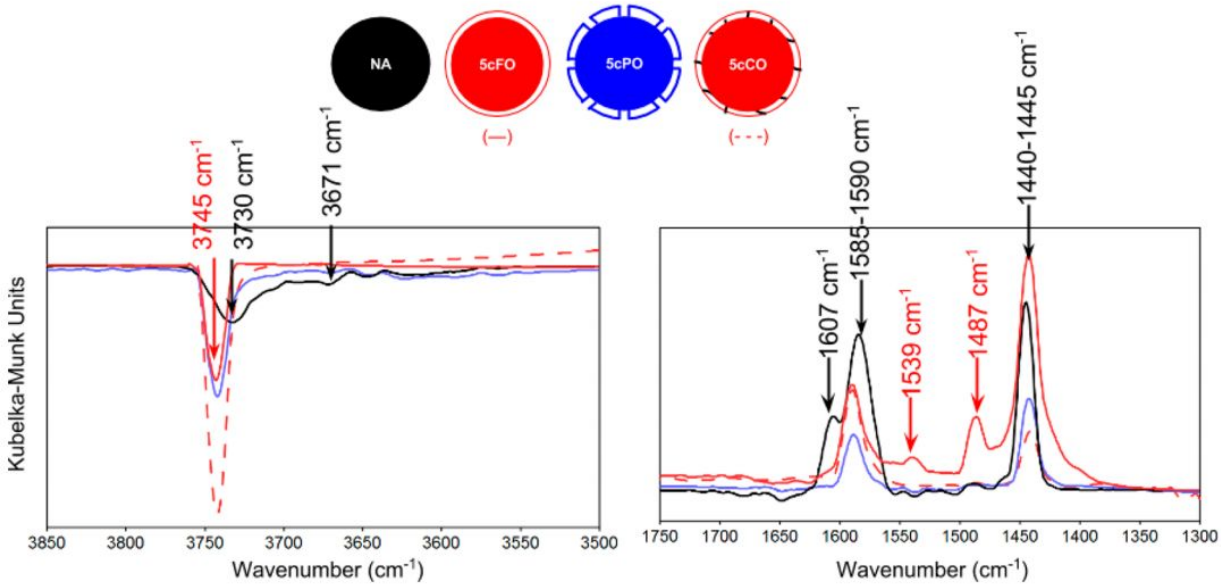

Figure 3.11 left, a) hydroxyl stretching region and **right, b)** pyridine stretching and bending region for DRIFTS pyridine chemisorption spectra at 150 ºC for Al_2O_3 (black), 5cFO (red), 5cPO (blue), and 5cCO (dashed red).

More importantly concerning catalyst acidity, the ring stretching region provides further insight into the Brønsted and Lewis acidity of the catalysts and types of Lewis sites present. The Al_2O_3 support has three peaks corresponding to coordinating interactions or Lewis acid sites. Peaks at 1607 cm^{-1} and 1585 cm^{-1} are indicative of Al^{IV} and Al^{VI} respectively [150-152]. The peak at 1445 cm^{-1} merely indicates any coordinating interactions which can be via surface hydroxyls or Lewis acid sites [150, 152]. This demonstrates that the two aluminols merely coordinate pyridine during chemisorption. Interestingly, distinct Brønsted acid character is observed on the 5cFO material [150-152]. Peaks at 1539 cm^{-1} and 1487 cm^{-1} are strong indicators of protonated pyridinium ions. This means that a fraction of the perturbed Al-O-Si-OH are capable of protonating vapor phase pyridine and may be competent for Brønsted acid catalyzed reactions. Since 5cFO possesses SiOH in a confined environment near framework SiO_4, pyridine

may activate the bridging Si-OH-Si observed on ASA in prior studies [28-29, 114, 141]. Peaks at 1590 cm^{-1} and 1440 cm^{-1} correspond to weakly coordinating H bonding modes.

5cCO and 5cPO spectra do not possess the Brønsted acid peak at 1540 cm^{-1}, indicating that there are no accessible Brønsted sites on the surface. Since pyridine has a kinetic diameter of 0.6 nm, it is unlikely that it can interact with micropore Brønsted sites [132]. However, if 5cPO possessed such sites, they should be accessible because not much microporosity was detected on the surface during N_2 physisorption. Based on surface acidity characterization, 5cPO only has weak H bonding hydroxyls on the surface. The predominant hydroxyls contribute to the Lewis acid peak at 1440 cm^{-1}, and therefore the acid site distribution is very different from that of crystalline zeolites and closer to that of ASA.

Section 3.4.3 1,3,5-TIPB Catalytic Cracking

A wide range of probe reactions are available to assess Brønsted acidity including alcohol dehydration, alkene isomerization, and catalytic cracking [24-26]. Ultimately, considering the wide range of acid sites present and prevalent industrial uses for zeolites and ASA, the cracking of bulky TIPB was chosen. Typically, this reaction has been used to probe external acidity for zeolites and accessibility of strong Brønsted acid sites [153-156]. In Figure 3.12, the major products and reaction pathways are shown for TIPB conversion over ASA catalysts at high temperature. The desirable Brønsted acid catalyzed pathway involves three successive dealkylation steps. At each step, one molecule of propylene is produced and the activation enthalpy for subsequent dealkylation increases. Side reactions including transalkylation, side chain isomerization, and coking are possible and have previously been observed over other catalysts [14-16 , 153-156].

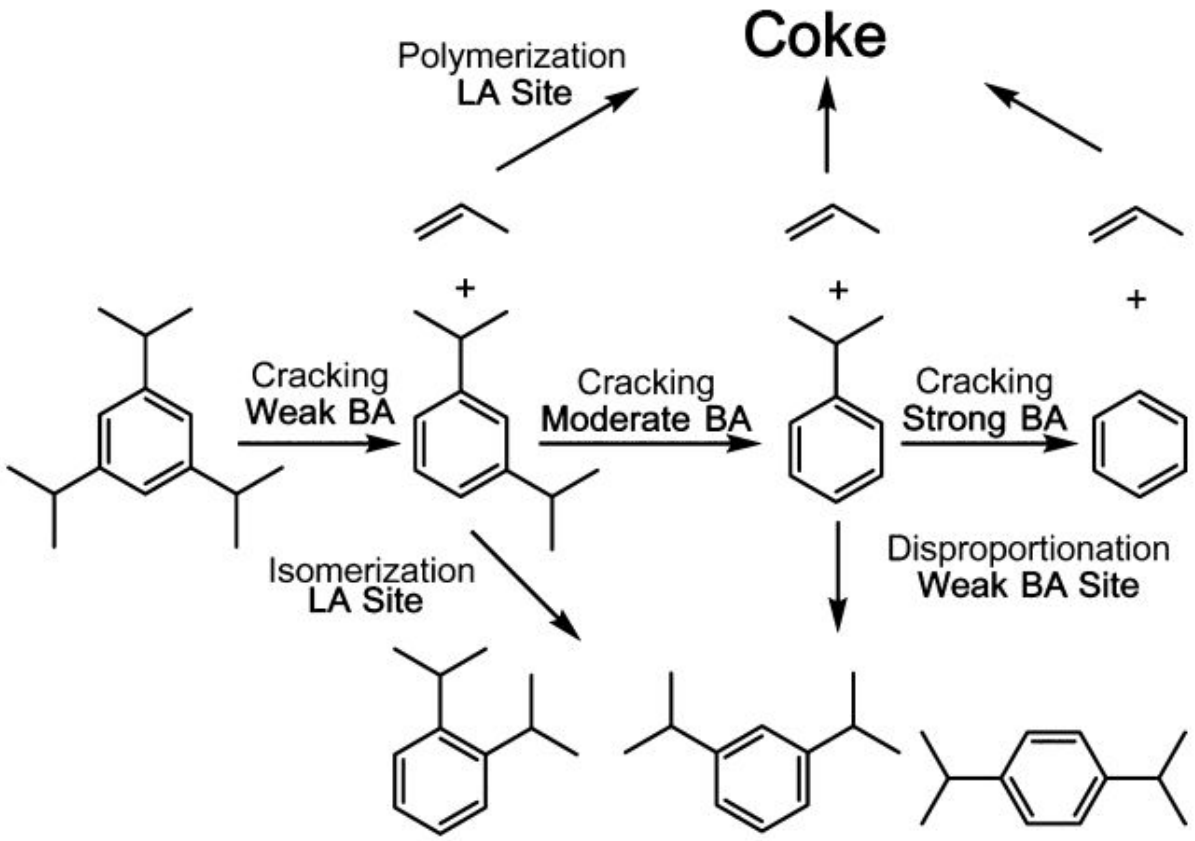

Figure 3.12 Reaction network over SiO_2-Al_2O_3 for the catalytic cracking of TIPB [14-16, 153-156]. Side reactions not shown here include side chain isomerization and transalkylation.

Due to the variety of catalytic pathways and wide distribution of reaction products, a rich amount of information can be culled from reaction results. The conversion was quantified in order to assess catalytically competent acidity on the surface of these catalysts. The conversion results are shown in Figures 3.15 and 3.16. Values are normalized to surface area because we considered the entire surface to be active for the reaction as standard for mixed oxide Brønsted acids. In this measure, SiO_2 overcoated materials perform highly compared to the Al_2O_3 support. Perturbed silanols in the thin overcoat are then strong enough to dealkylate TIPB. Upon comparison to selecto SiO_2 gel and quartz sand, it is clear that overcoat SiOH are of a different

nature than bulk silanols. The 5cPO catalyst was unremarkable when compared with the non-templated 5cFO, demonstrated conclusively that unique acidity is not formed here. However, 5cCO demonstrates pronounced higher activity than the other overcoated catalysts, confirming results from acid site characterization that this catalyst possesses strong Brønsted acid sites.

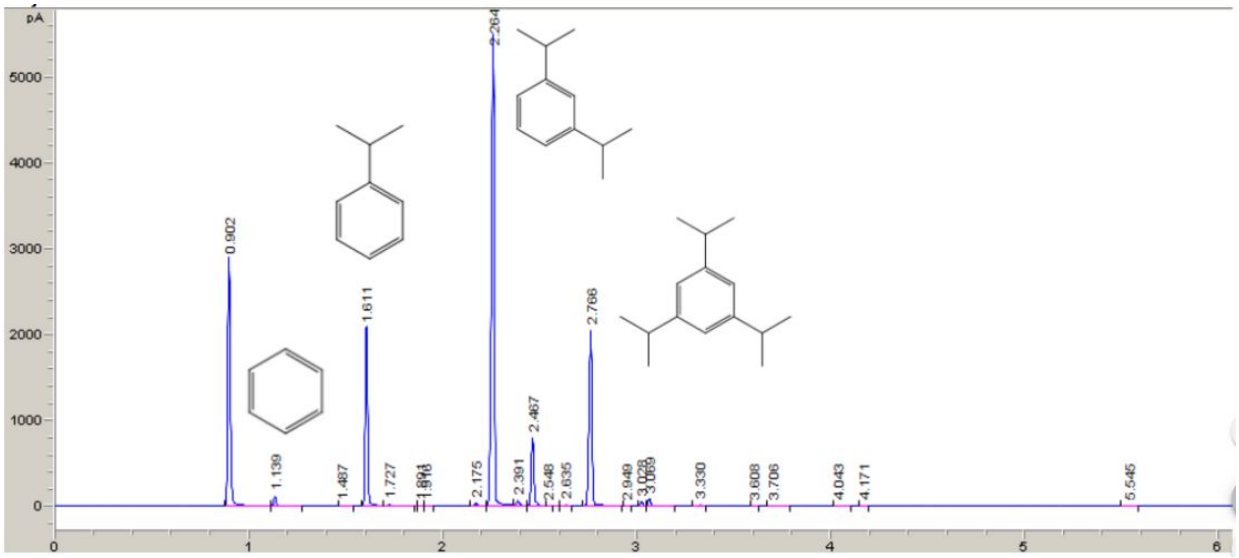

Figure 3.13 Sample GC-FID chromatogram for TIPB cracking product analysis. Primary cracking pathway species including 1,3-DIPB (2.26 min), 1,4-DIPB (2.77 min), cumene (1.61 min), and benzene (1.14 min) are identified here. The x-axis corresponds to the GC retention time in min.

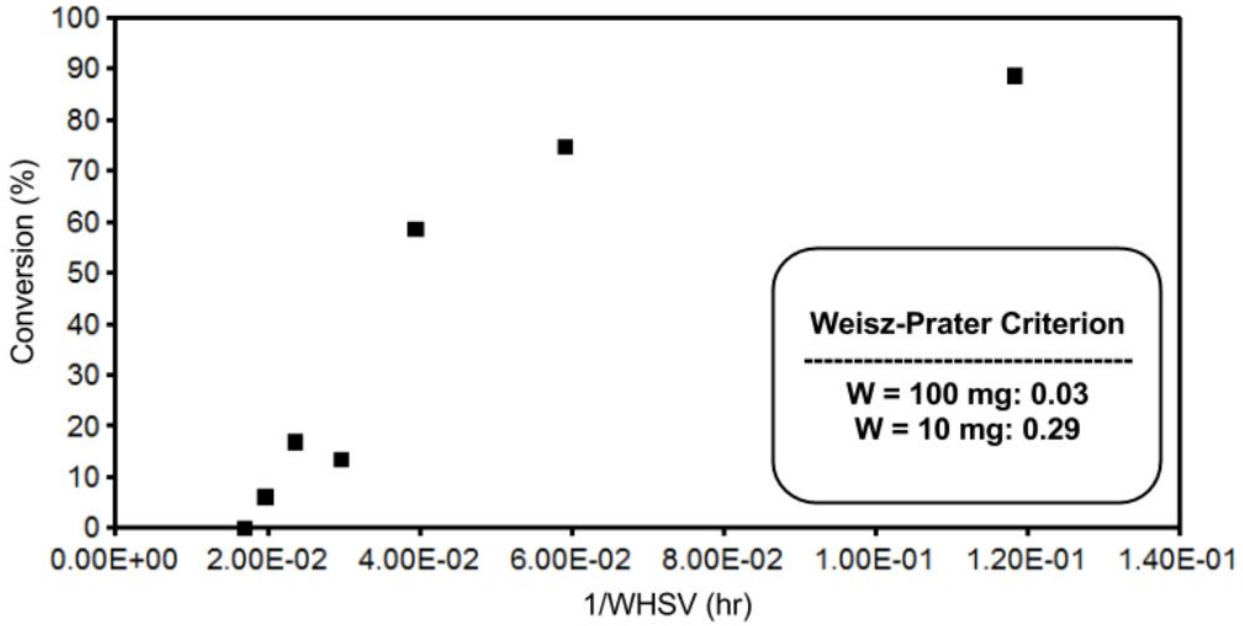

Figure 3.14 External diffusion testing on 5cFO indicates that the reaction is not diffusion limited below 70 % conversion. The Weisz-Prater criterion was calculated for the case of 100 % conversion and the requirement of < 0.6 for 1st order reactions is met. This suggests that internal pore diffusion would not be limiting even if the pores extended into the bulk of the material, instead of the < 5 nm thick SiO_2 shell here.

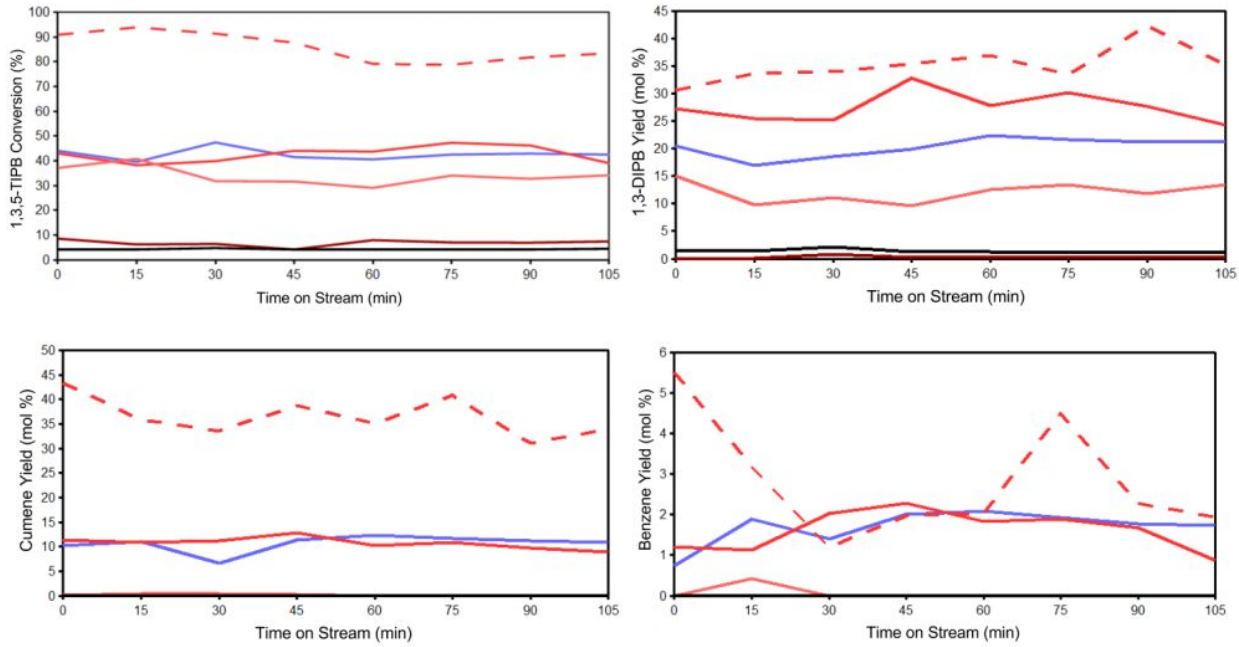

Figure 3.15 Time on stream data for high conversion TIPB cracking runs. See Section 3.3 for reaction conditions. Catalysts shown include Al_2O_3 (black, near 0), 12cFO (maroon, near 0), 2cFO (pink, no substantial benzene), 5cFO (red), 5cCO (dashed red), and 5cPO (blue).

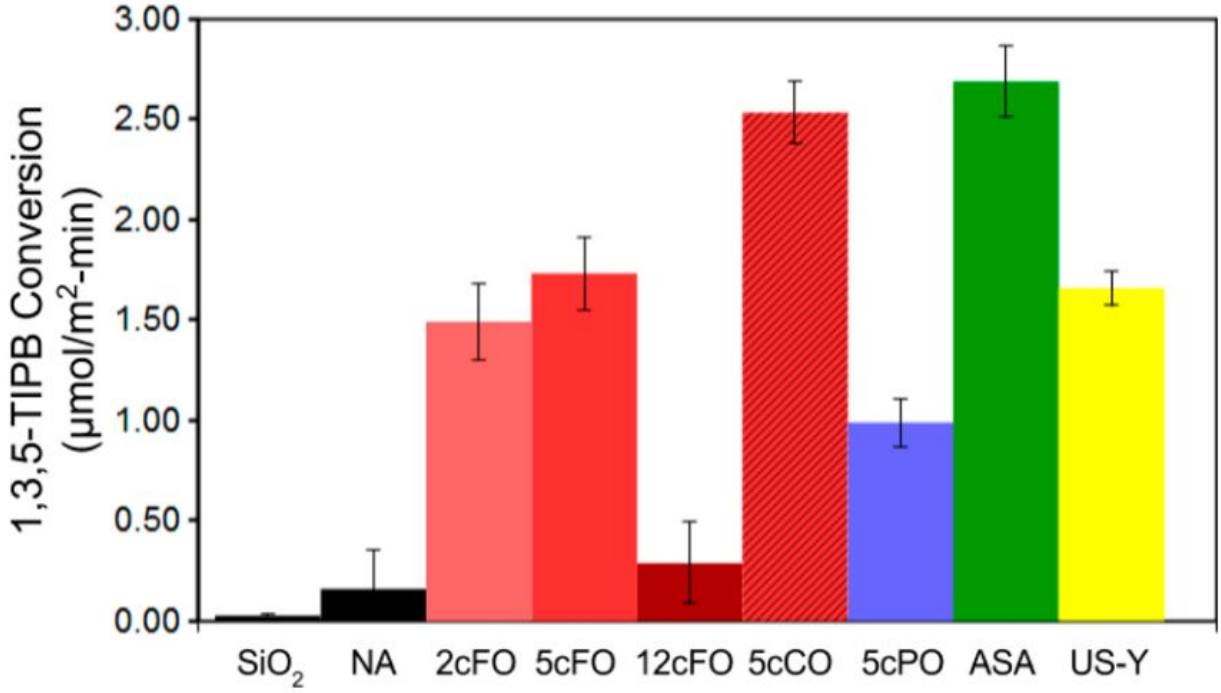

Figure 3.16 TIPB cracking conversion rate at 450 ºC. Values are average over 2 h TOS with a 1.69 h^{-1} WHSV for SiO_2-Al_2O_3 core-shell catalysts. All catalyst loadings were 100 mg except for ASA and US-Y which were 10 mg. Conversion rate was normalized by total BET surface area.

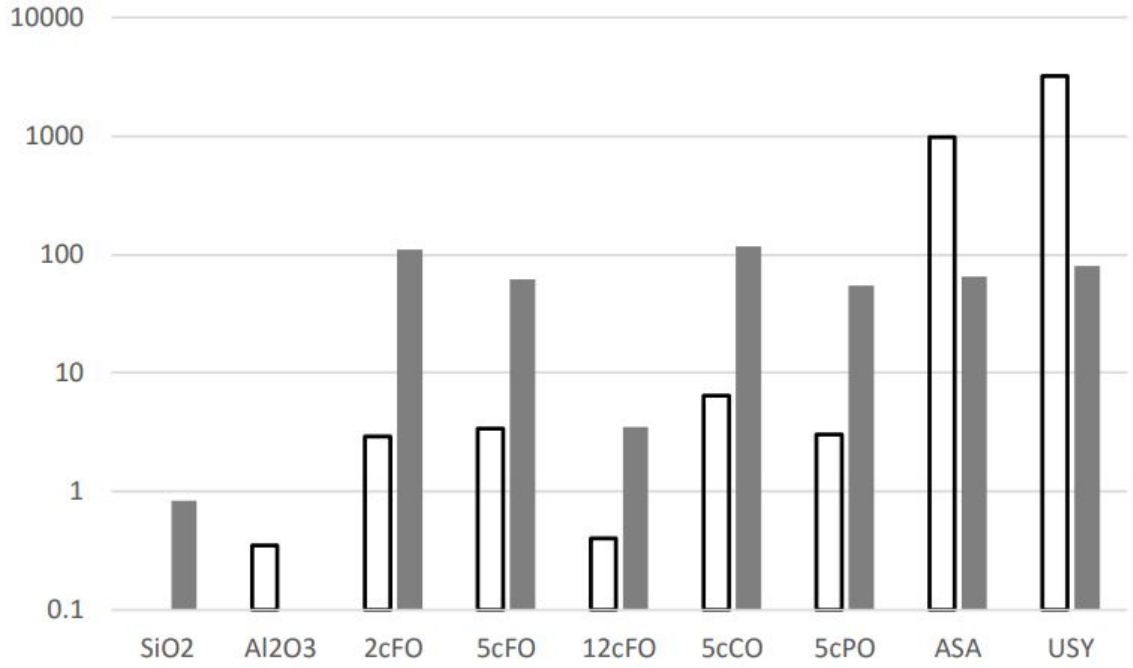

Figure 3.17 TIPB cracking conversion rate (a.u.) at 450 ºC normalized by total Si (filled) or Al (empty) content. Neither a Si or Al atom basis is an apt comparison between experimental

materials, ASA, and US-Y because the latter consist of Al incorporated within amorphous or crystalline SiO_2 while the experimental materials have a SiO_2 shell completely covering Al_2O_3.

Since increased acidity was generated by grafting SiOH onto the Al_2O_3 surface, there should be an optimal overcoat thickness between SiOH and the surface to maximize Brønsted acidity. At the extremes, low Si content will lead to the formation of isolated islands of perturbed SiOH [115-116]. The opposite should occur for high cycle counts where the overcoat should take on bulk SiO_2 behavior and not show influence from the underlying support. Figures 3.15 and 3.16 show that even the 2 cycle material (2cFO) has enhanced activity compared with Al_2O_3, in contrast 12cFO conversion is lower and similar to Al_2O_3 and SiO_2. Further insight into the acid site distribution of 5cFO and 5cCO was acquired by analyzing the product distribution. To differentiate Lewis and Brønsted acid activity, the appearance of certain products was assigned to that acid type. We define cracking pathway selectivity as (DIPBs + Cumene + Benzene)/(TIPB conversion). Although the side products mentioned in Figure 3.12 were individually present in small amounts, their sum contribution is important to designate behavior aside from cracking. With all reactions held to the differential regime (< 10% conversion, 10 mg catalyst), the selectivity towards cracking products is shown in Figure 3.18.

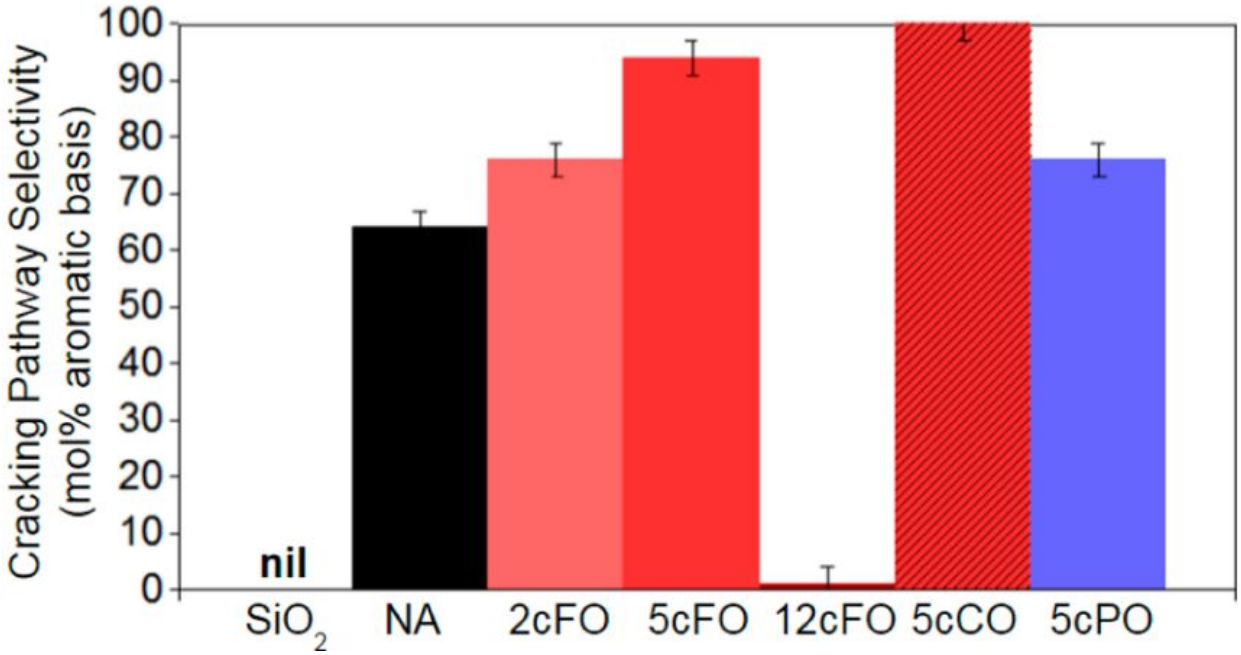

Figure 3.18 Cracking pathway selectivity during TIPB cracking at 450 °C. Values are averaged over 2 h TOS, 16.9 h^{-1} WHSV for SiO_2-Al_2O_3 core-shell catalysts, and conversion held to < 10 %. All catalyst loadings were 10 mg.

Al_2O_3 on its own has 60 % selectivity to dealkylation. However, 5c overcoated materials have higher selectivity as expected from their increased B:L ratio calculated from NH_3 DRIFTS. Detrimental Lewis acid behavior from the surface was quenched and modified to be productive towards the cracking pathway. Bulk SiO_2 and 12cFO only were able to catalyze side chain isomerization of TIPB and provide surfaces for polymerization to occur. Finally, Figure 3.19 shows the cracking product distribution for the most active of the synthesized catalysts, 5cCO, compared to ASA and US-Y. Only zeolites and very few ASA have demonstrated sufficiently strong acidity to dealkylate TIPB all the way down to benzene [14-16, 153-156]. The cracked overcoat material 5cCO demonstrated primarily moderate acidity but some strong acidity as evidenced by the formation of benzene in its product mixture. On a surface area basis, 5cCO

compares well with ASA but the industry standard US-Y remains more active towards deep cracking products. This difference in apparent acid strength may be due to confinement effects rather than stronger intrinsic acidity [13]. Therefore, we have demonstrated that we can replicate the catalytic behavior of ASA in two well controlled synthesis steps. These moderate Brønsted acid catalysts may prove useful in hydrocarbon processing of bulky substituted polyaromatics.

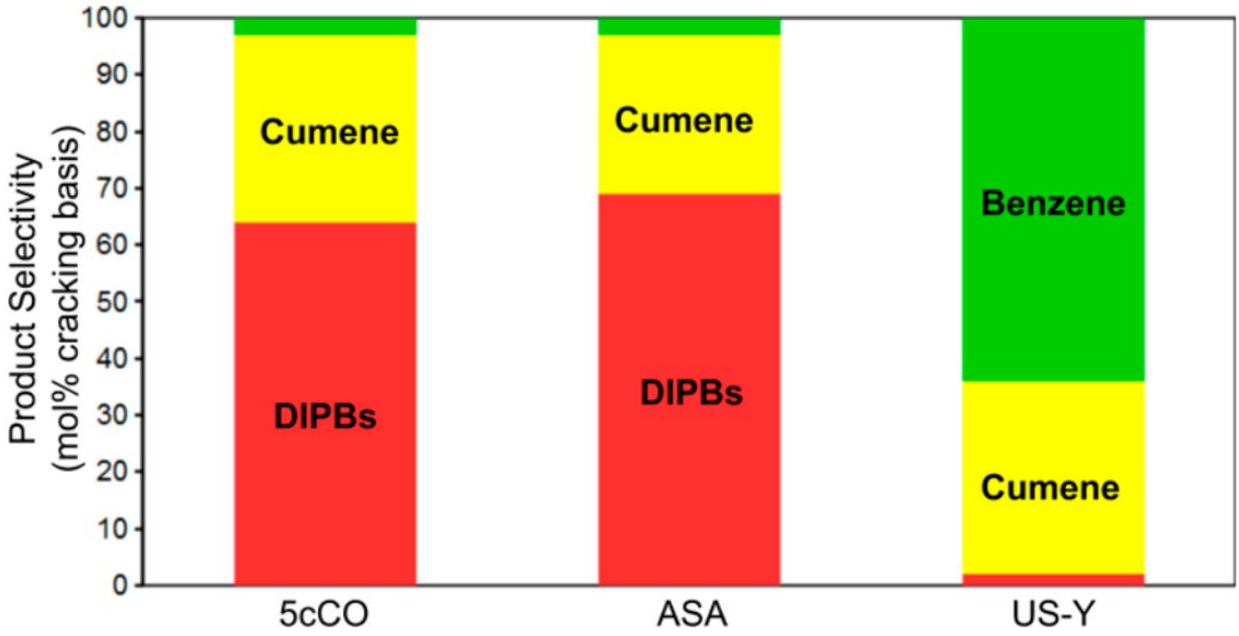

Figure 3.19 Product selectivity amongst cracking pathway products for TIPB cracking at 450 ºC. Values are averaged over 2 h TOS and conditions correspond to those for Figure 3.17.

Section 3.5 Conclusions on SiO_2 Overcoated Al_2O_3

In this work, Brønsted acidity sufficient to crack alkyl benzenes was demonstrated to be generated on core-shell SiO_2 overcoated Al_2O_3 catalysts. The use of a calixarene template proved to preserve the most reactive support Al_2O_3 hydroxyl but it did not lead to unique reactivity as compared to similarly overcoated materials. Thicker SiO_2 overcoats led to a largely inactive material as expected. In contrast, cracking the overcoat by rapid heating during calcination led to

enhanced reactivity. The exact structure of the active sites present on these materials will require additional investigation by DNP ^{29}Si NMR to rule out alternative explanations for acid site generation including Al migration into the overcoat [115-116]. Others have similarly claimed the generation of moderate Brønsted acidity via proximity between SiOH and Al^{IV}. This has been observed for isolated silanols present on the external surface of zeolites ZSM-5 and Beta [138-140]. Regardless of the mechanism of acid site formation, the 5cCO material possesses strong Brønsted acid sites and displays behavior identical to that of conventionally prepared ASA. The benefits of these overcoated materials are (i) a highly tunable synthesis pathway that allows for material optimization, (ii) a shallow active region that should limit intraparticle diffusion limitations, and (iii) a shifted distribution of active sites to stronger reactivity. Future materials development will head towards varying the carbonaceous template and composition of the oxide support.

Future work on materials with varying composition will need to use NH_3 TPD, NH_3 DRIFTS, pyridine DRIFTS, in-situ titration with substituted pyridines, and ^{31}P solid state NMR of adsorbed phosphine oxides to help identify the active sites on these catalysts. Rates per active Si or heteroatom are needed to truly compare across the material set and allow for TOF measurement. A qualitative understanding of the active site will help with catalyst synthesis and design so that proper metal precursors can be employed. Although we can postulate the presence of perturbed silanols and MOx dimers, a definitive identification is needed to extend these catalysts to other reaction systems while maintaining high performance.

Chapter 4. Limonene Oxidation Kinetics over M-SiO_2

Section 4.1 Biorenewable Polymer Production

Alkene oxidation serves as the first step towards the formation of many desirable polymers and plastics used in everyday consumer products [34, 37-40]. The current processes and feedstocks can easily be improved to more environmentally friendly options if new catalysts are designed for their use. One example is the use of limonene as a biorenewable feedstock for poly limonene carbonate production [157-158]. Limonene is readily extracted from citrus fruit skins and peels. Over 9 million tons of citrus rinds are wasted each year due to harvest losses, superficial issues, or rotting by neglect [159]. Citrus peels contain valuable chemical precursors including limonene and sugars. Furthermore, researchers have discovered that limonene 1,2-oxide, the primary limonene oxidation product, can be easily copolymerized with CO_2 using a homogeneous Zn based catalyst [157-158]. This polymerization reaction is susceptible to product issues if the limonene 1,2-oxide is mixed with other oxygenates such as limonene diepoxide or limonene based alcohols [157]. Therefore, selective oxidation and facile production of limonene 1,2-oxide is key to further scale up biorenewable plastics. Alternatively, if the catalyst can be tuned to selectively produce limonene 8,9-oxide, different copolymers could readily be synthesized.

Many researchers have performed limonene oxidation with O_2, H_2O_2, and organic hydroperoxides over POMs, bulk oxides, supported metal catalysts, and supported metal oxide catalysts [10, 51, 160-164]. The best selectivity and activity to limonene 1,2-oxide is typically observed for organic hydroperoxides when used with Ti supported on SiO_2. Interestingly, some

cases of selective formation of the kinetically unfavorable limonene 8,9-oxide has been reported [10, 51]. One case involved SiO_2 overcoated Ru-SiO_2 templated with limonene-10-ol. Its oxidation regioselectivity switched from favoring the 1,2-oxide (1:3 exo:endo) to favoring the 8,9-oxide (9:1 exo:endo) after SiO_2 overcoating [10]. Alternatively, Nb supported on SiO_2 has been shown to selectively produce the 8,9-oxide when polar acetonitrile solvent is used [51, 165]. This has been proposed to take place via a solvent oxidation mechanism or due to active site sterics [51, 165]. Not much concrete evidence has been put forth to explain regioselectivity differences between Ti and Nb based catalysts.

A confounding factor in oxidation kinetics is the competition between direct epoxidation and radical allylic oxidation which is well known for cyclohexene. With cyclohexene, the expected product cyclohexane oxide is formed in addition to unexpected products cyclohexenol and cyclohexenone [32, 62]. This is more problematic for the limonene reactant because its double bonds are more reactive for both oxidation pathways. Therefore, direct vs radical oxidation selectivity is important because alcohol byproducts affect the further use of the oxide products. The goal of this preliminary study then was to understand limonene oxidation mechanistically. Reaction behavior was tuned via changing (i) metal identity, (ii) oxidant identity, (iii) reactant concentrations, (iv) temperatures, and (v) the catalyst support.

Section 4.2 Catalyst Characterization

N_2 physisorption isotherms were obtained at -196 ^{o}C for all catalysts using a Micromeritics 2010 ASAP instrument. All materials were dried previously at 450 ^{o}C under vacuum overnight to remove physisorbed water. BET surface areas were obtained by applying the Rouquerol consistency criteria to the adsorption branch of the isotherm [117-118]. The t-plot

(M-SiO_2, M-BEA, M-SBA-15) or the α_s plot (2cFO, 2cPO, 10cFO, 10cPO) was applied to separate out micropore and external surface areas. The BJH method was used on the desorption branch of the N_2 isotherm to obtain mesopore size distributions. Areas are tabulated as divided by total mass or the mass of the original support before SiO_2 overcoating.

Ambient DRUV-vis spectra were obtained for all catalysts as-synthesized and freshly calcined. Spectra were obtained from 200-800 nm with PTFE as the perfect reflector, background, and diluent. Edge energies were calculated using the corresponding indirect Tauc plot for each material's DRUV-vis spectrum [166]. Ti, Nb, and Ta content were measured using ICP-OES in the QBIC core facility at Northwestern university. Materials were dissolved using 2-3 drops of concentrated HF and this was diluted to 11 mL total volume with 1 wt % HNO_3. ICP standards for Ti, Ta, and Nb were developed by diluting know standards (Sigma-Aldrich, TraceCERT, 1000 ppm metal in HNO_3, CAUTION: contains trace HF) down to make 5 standards and 1 blank between 0-75 ppm metal content.

Section 4.3 Limonene Oxidation Kinetics

Limonene oxidation kinetics were collected by running the reaction in 20 mL glass vial reactors. Reaction conditions were used based on prior literature for epoxidation with various M-SiO_2 catalysts. Catalysts were repetitively ground with mortar and pestle then passed through a 325 mesh sieve before use in catalytic reactions. A typical run used 20-50 mg of freshly calcined catalyst along with 4.6 mL of acetonitrile (Sigma-Aldrich, HPLC Plus, ≥ 99.9 %). Then, 0.16 mL limonene (Sigma-Aldrich, 97 %) was added to the vial. Limonene was filtered over a column of neutral Al_2O_3 (Fisher Chemical, 60-325 mesh) immediately before use. The vial was shaken to mix thoroughly on a Glas-Col digital mixer at 800 rpm for 30 min. Finally, 0.2 mL

TBHP (Sigma-Aldrich, ~5.5 M in decane, over molecular sieve 4 Å) or 0.12 mL H_2O_2 (Sigma-Aldrich, 50 wt % in H_2O, stabilized) was added to the vial. The timer was started when TBHP or H_2O_2 was added and time points were typically taken at 0, 5, 10, 15, 30, 60, 120, 360, and 1440 min. Samples containing H_2O_2 were quenched with Ag powder (Alfa-Aesar, -120+325 mesh, atomized, 99 % metals basis) to prevent overoxidation during analysis [32].

Runs at sub ambient temperatures were conducted in the same way but with a propylene glycol (Sigma-Aldrich, ≥ 99.5 %, FCC, FG) cooled chiller block attached to the shaker plate. Catalyst loading was varied between 10-500 mg to assess the effects of metal concentration. This set of reactions was used to assess the relative effects of heterogeneous and homogeneous reaction. [Limonene] and [TBHP] were varied between 0.2-2.2 M, keeping one or the other species at 0.2 M. In the case of increased concentration, acetonitrile volume was removed in order to keep total volume constant at 4.96 mL.

Homogeneous background reactions were slow with a blank reactor resulting in ~2-3 % limonene conversion after 6 h and selectivity being to allylic oxidation products. Mass balances closed to >87 % by quantifying limonene, limonene 1,2-epoxide, limonene 8,9-epoxide, limonene diepoxide, limonene 1,2-diol, limonene 8,9-diol, carveol, carvone, perillyl alcohol, perillyl aldehyde, and structural isomers of these compounds. Product concentrations were compared to the amount of consumed limonene reactant. Known standards were created of most products with calibration curves on the Shimadzu 2010 GC-FID consisting of 1 blank and 5 standards spanning 0-0.2 M. The calibration factors for structural isomers unavailable commercially were assumed to be identical to known isomers. Typical runs were quantified using a Shimadzu GC-2010 with a FID and a ZB-624 column. Product identification, retention

time calculation, and discovery of structural isomer production were performed on a Shimadzu GCMS-QP2010 equipped with a ZB-624 column. Some runs were performed with a low GC injection temperature (90 ^{o}C) in order to quantify TBHP consumption. Initial rates were calculated from limonene concentration data over the first 15 min of reaction. The standard error for initial rates was 15 % based on triplicate runs of different material batches.

Some Ti-SiO_2 catalysts were tested in recycle runs by recovering the catalyst after 6 h of reaction. The recovered catalyst was washed with two 50 mL portions of methanol (Sigma-Aldrich, HPLC Plus, ≥ 99.9 %), dried overnight in a glass oven at 120 ^{o}C, and then calcined at 550 ^{o}C as before. The recovered and recalcined catalysts were separately used to obtain DRUV-vis spectra.

Section 4.4 Kinetics Analysis and Reaction Network

A lumped parameter reaction network was used to describe limonene oxidation over M-SiO_2. Limonene oxidation typically proceeds via an Eley-Rideal mechanism to form limonene 1,2-oxide and limonene 8,9-oxide [10, 51, 160-164]. Limonene 1,2-oxide can react further to form dihydrocarvone via isomerization, limonene 1,2-diol via hydrolysis, and limonene dioxide via overoxidation [160-164]. Limonene 8,9-oxide can similarly react further to form limonene 8,9-diol and limonene dioxide. Peroxide decomposition occurs in parallel especially under high oxidant conditions or over known peroxide decomposition catalysts including Nb and Ta-SiO_2. With an oxidant such as TBHP, decomposition products include catalyst poisons H_2O and TBOH or potentially radical species including *OH and t-BuO* [167]. These radicals and metal based radicals (i.e. superoxides) can abstract H atoms from limonene and lead to the production of

alcohols and carbonyl species. Assuming the presence of parallel internal oxidation, terminal oxidation, and allylic oxidation pathways, limonene consumption can be expressed as:

$$d[L]/dt = -R_I - R_E - R_R \quad (4.1)$$

Product selectivity is therefore critically dependent on the kinetics of competing oxidation pathways shown in Figure 4.1. We can define direct epoxidation selectivity and oxide regioselectivity from product concentrations as follows:

$$DS = \textit{sum of epoxides and dihydrocarvone / limonene consumed} \quad (4.2)$$

$$RS = \textit{sum of limonene } 8,9-\textit{oxide and } 8,9-\textit{diol / sum of direct oxidation products} \quad (4.3)$$

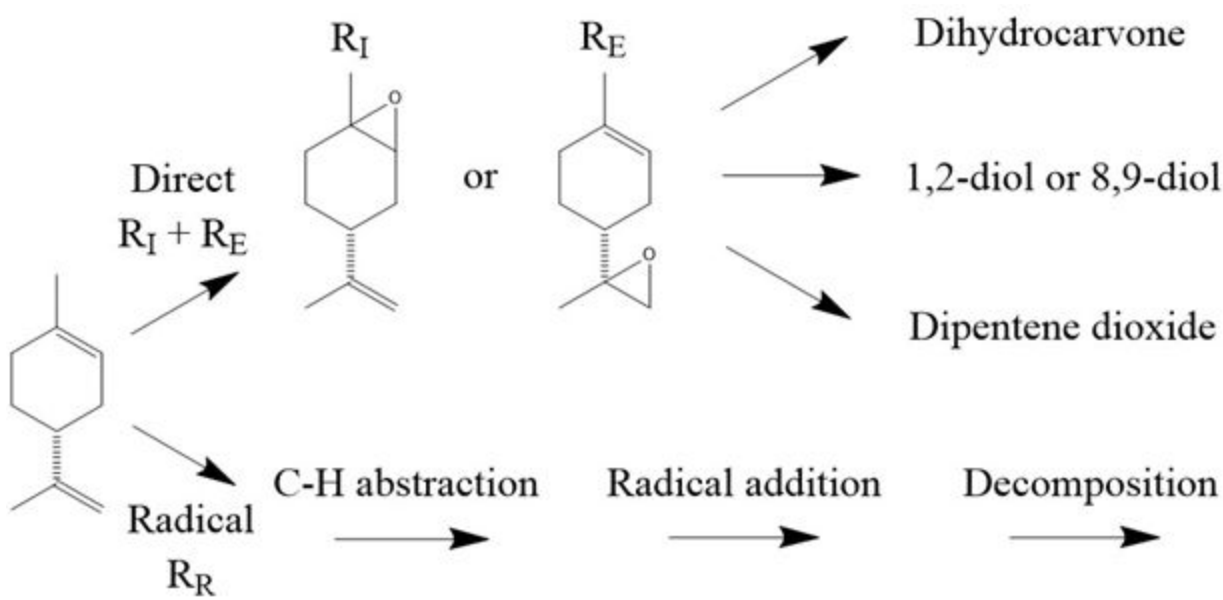

Figure 4.1 Limonene oxidation reaction network over M-SiO_2 [10, 51, 160-164, 167]. Radical oxidation steps are further detailed in Figures 4.2, 4.3, and 4.4.

Two potential bimolecular hydroperoxide decomposition pathways lead to the formation of an alcohol and either an epoxide or carbonyl species via catalyzed oxidation or decomposition pathways. However, direct decomposition of the hydroperoxide to water and a carbonyl species

is possible especially in the presence of radicals HO* and t-BuO*. In theory, fragmentation of the limonene skeleton is possible if hydroperoxides are formed on the attached propyl group, but no C7 species were observed during GC-MS analysis of select reaction vials. Initial selectivities are reported by extrapolating the overall selectivity at low conversion (< 10 %) back to t = 0. Substituting internal, external, and radical oxidation rates in Equation 4.1 into the definitions of overall selectivity in Equations 4.2 and 4.3 gives the instantaneous selectivity as a function of rates:

$$S_D = (R_I + R_E) / (R_I + R_E + R_R) \tag{4.4}$$

$$S_E = R_E / (R_I + R_E) \tag{4.5}$$

Radical allylic oxidation proceeds via a three step mechanism: (i) allylic C-H activation, (ii) addition of a solution species to the radical, (iii) decomposition or oxidation to yield non-radical products. Due to the quantity and variety of allylic C-H bonds available on limonene, this radical pathway yields 10 unique primary products and may contribute to the limonene oxide pool if hydroperoxide species transfer oxygen to limonene.

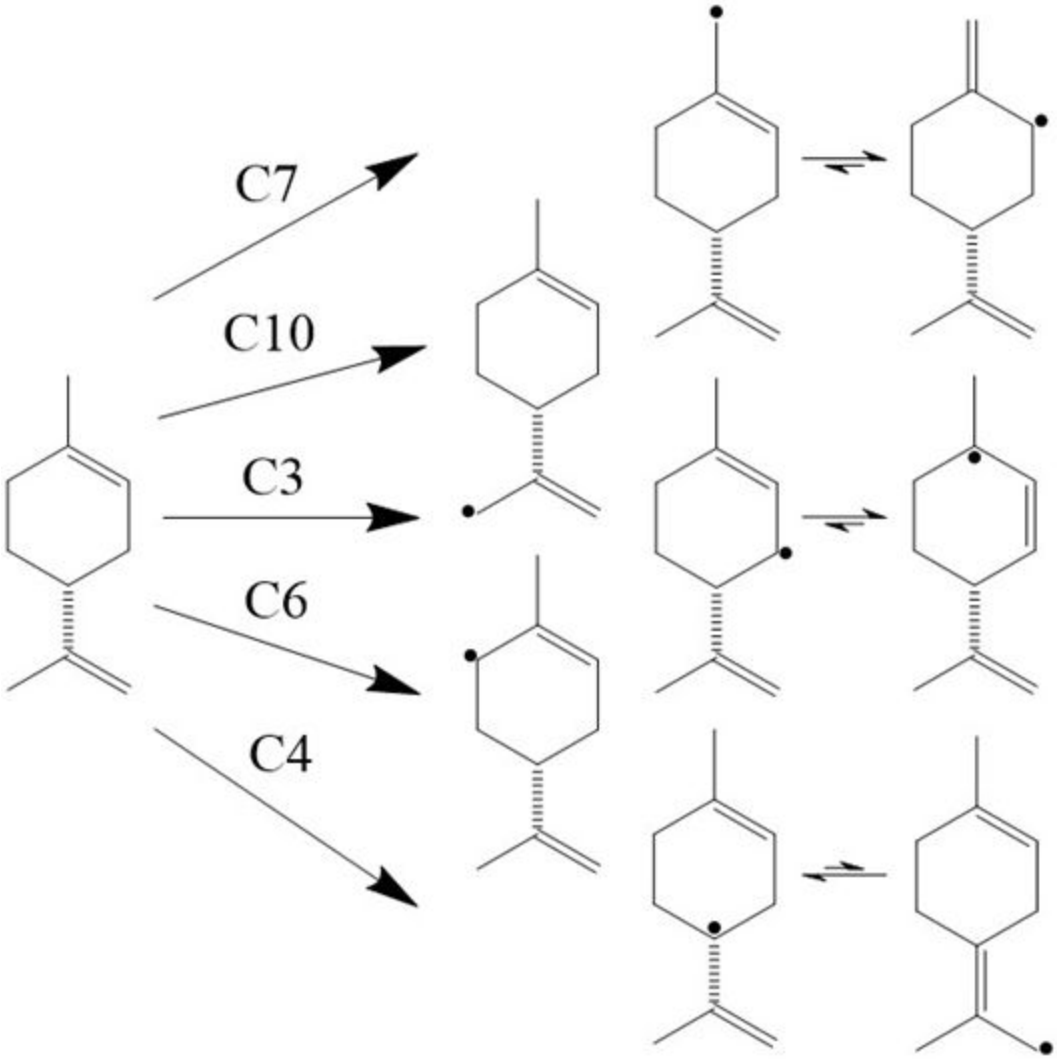

Figure 4.2 Potential limonene based allylic radical species [160-164, 167].

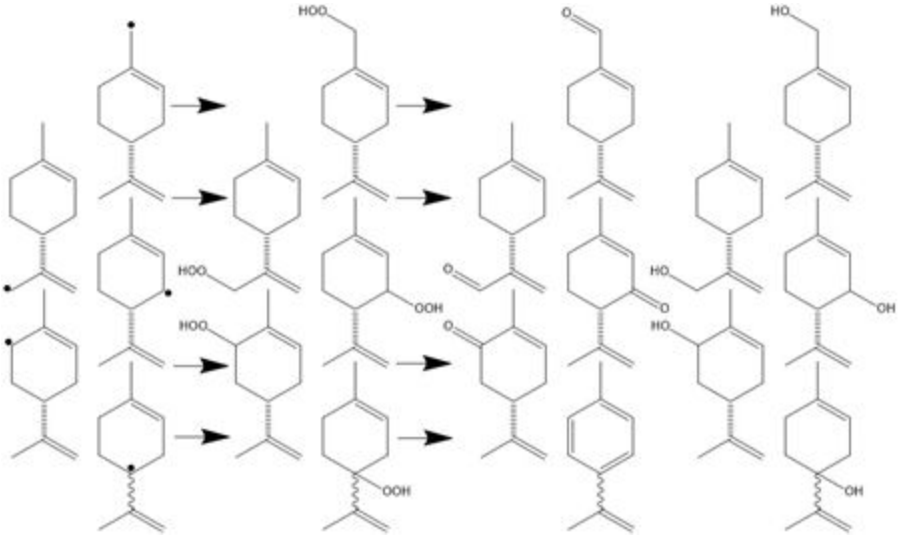

Figure 4.3 Limonene hydroperoxides and their observed monomolecular or bimolecular decomposition products [160-164, 167]. Note that multiple oxidation steps occur to obtain the sturene derivative product shown for the C4 hydroperoxide.

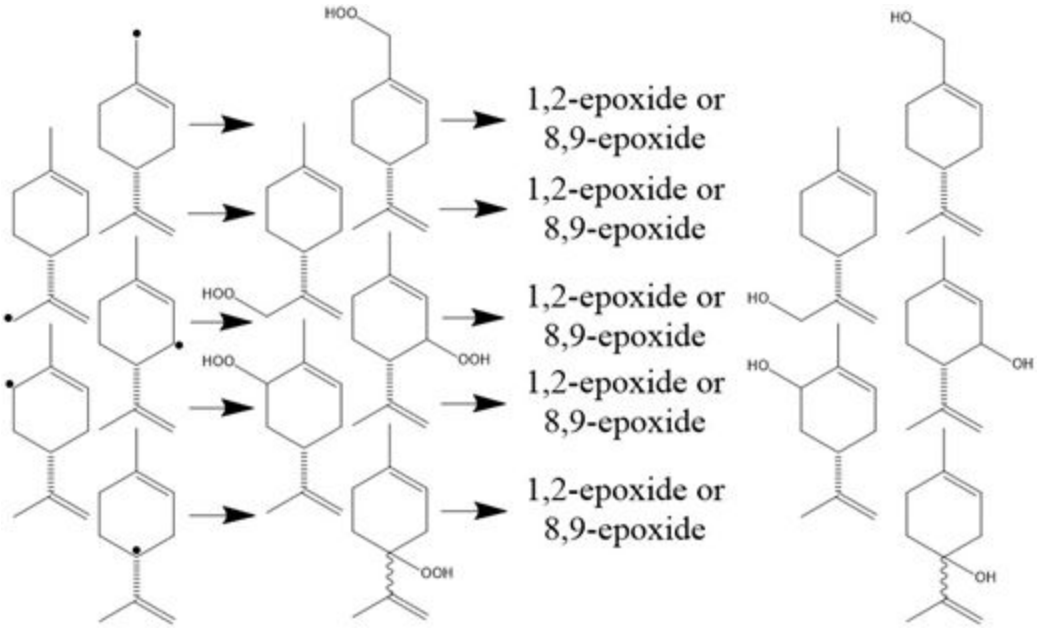

Figure 4.4 Limonene hydroperoxides and their Lewis acid catalyzed limonene oxidation products [160-164]. The direct selectivity mass balance was not modified to account for epoxides obtained via this pathway. These secondary reactions were assumed to have low prevalence at differential conversion.

Section 4.5 Results and Discussion

Section 4.5.1 Catalyst Characterization

Wide pore SiO_2 was used as the catalyst support instead of typical mesoporous silicas because its open pore geometry allows us to eliminate intrapore secondary reactions and for the SiO_2 overcoating process to occur. Table 4.1 shows characterization results of the synthesized catalysts and wide pore SiO_2 support. Surface areas were all ~375 m^2/g with mesopore diameters of 9 ± 1 nm, large enough to accommodate bulky metal precursors and to pose no diffusion restrictions on limonene (0.67 nm kinetic diameter). Mesopore volume decreased by ~10 % after grafting and calcination which confirms that the pore structure is stable up to 550 ^oC. The volume decreases further upon SiO_2 deposition for SiO_2 overcoated Ti-SiO_2 catalysts as expected. Ti-SBA-15 has a surface area of 829 m^2/g with smaller mesopore diameters with a tight distribution centered at 6 nm. Ti-Beta has a surface area of 683 m^2/g and possesses a regular crystalline microporous structure with a 0.67 nm pore size. Since this is approximately equal to the limonene kinetic diameter, one would expect this material to enact oxidation regioselectivity to the limonene 8,9-oxide.

Table 4.1 Catalyst and wide pore SiO_2 physical and active site properties.

Catalyst	Total surface area (m^2/g)	Surface density (M/nm^2)	M loading (wt.%)
SiO_2	374	<0.001	nil
Ti-SiO_2	375	0.21	0.60
Nb-SiO_2	375	0.19	1.16
Ta-SiO_2	375	0.22	2.25
Ti-2cFO	369	0.21	0.51
Ti-10cFO	193	0.24	0.32

Ti-SBA-15	829	0.05	0.31
Ti-Beta	683	0.14	0.77

Catalyst metal loadings were determined by ICP-OES and used to calculate metal surface densities. All synthesized catalysts have low metal loadings between 0.19-0.22 M/nm^2, Ti-SBA-15 and Ti-Beta have significantly lower loadings with these metals nominally contained within the SiO_2 framework. These loadings are < 5 % of the expected 4.6 M/nm^2 geometric monolayer coverage, and metal cations are statistically likely to be site isolated [168-170]. Powder XRD shows no diffraction lines associated with bulk TiO_2, Nb_2O_5, or Ta_2O_5 which indicates the absence of bulk crystallites > 3 nm in size. Characterization by DRUV-vis was used to gain further insights into surface oxide structure. DRUV-vis spectroscopy gives valuable insight into metal oxide dispersion and coordination geometry.

Figure 4.5 shows normalized DRUV-vis spectra of freshly calcined M-SiO_2 catalysts. Non crystalline Ti^{4+}, Nb^{5+}, and Ta^{5+} species exhibit an $O_{2p} \rightarrow M_d$ ligand to metal charge transfer (LMCT) band in the range of 220-350 nm. These low loading catalysts have DRUV-vis spectra with peaks centered at 245 nm (Ti-SiO_2, 4.0 eV edge), 240 nm (Nb-SiO_2, 4.0 eV edge), and 220 nm (Ta-SiO_2, 4.5 eV edge). Ti-SBA-15 and Ti-Beta have peaks centered at 220 nm (4.5 eV edge) and 260 nm (3.5 eV edge) respectively. These LMCT bands largely agree with prior literature references for isolated extraframework Lewis acid sites and isolated framework Ti for Ti-SBA-15 [32, 61]. The spectra of SiO_2 overcoated materials 2cFO and 10cFO closely match the parent Ti-SiO_2. Ti-Beta interestingly has a wide DRUV-vis spectra, indicative of extraframework O_3TiOH present in a confined environment [171].

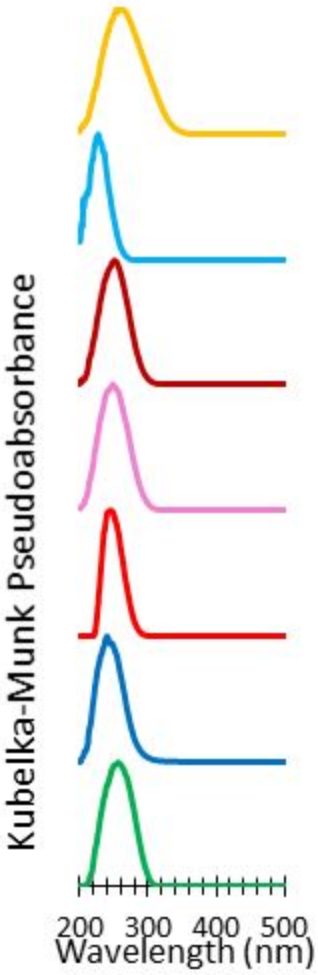

Figure 4.5 Ambient DRUV-vis spectra of freshly calcined M-SiO_2. Raw spectra were smoothed using a 6-point quadratic polynomial Savitzky-Golay filter [172]. Ti-SiO_2 (green), Nb-SiO_2 (blue), Ta-SiO_2 (red), 2cFO (pink), 10cFO (maroon), Ti-SBA-15 (cyan), and Ti-Beta (orange).

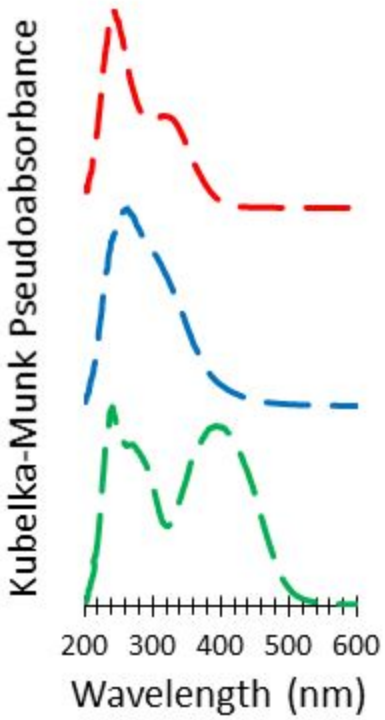

Figure 4.6 DRUV-vis of as-made Cp* (Ti, Ta) or Cp (Nb) based M-SiO_2 catalysts. Cp*Ti-SiO_2 (green), CpNb-SiO_2 (blue), and Cp*Ta-SiO_2 (red).

Section 4.5.2 Influence of Metal Cation Identity

Catalytic tests were performed to determine how differences in SiO_2 support structure, metal cation identity, reaction conditions, and reactant sterics affect limonene oxidation performance. Ti-SBA-15 and Ti-Beta catalysts were tested to compare the effects of changing both local sterics (framework vs extraframework Ti) and structural sterics (microporous vs mesoporous materials). The major products were typically limonene 1,2-oxide and 8,9-oxide at low conversion. The two types of selectivity are defined in equations 4.4 and 4.5 as direct epoxidation rate divided by limonene consumption rate and external epoxidation rate divided by direct epoxidation rate. All given rates and selectivity are initial rates and selectivity extrapolated back to t = 0 from data points taken before 10 % conversion of the limiting reagent. Rates are

calculated as the rate of limonene consumption divided by total metal content (1/h, rate per metal) or active metal content as determined by in-situ titration with phosphonic acids (1/h, turnover frequency, TOF).

Initial rates per metal, direct selectivity, and external regioselectivity as a function of metal cation are shown in Figure 4.7 using either aqueous H_2O_2 or anhydrous TBHP as the oxidant. Titania and niobia catalysts exhibit high initial rates as compared to the tantala catalyst. The rates follow the same metal cation trend observed in prior studies of cyclohexene oxidation systems [32]. As mentioned, aqueous H_2O_2 is known to deactivate Ti-SiO_2 catalysts, and we did a regeneration test which verifies that this phenomenon does occur. Likewise TBHP is somewhat incompatible with Group V catalysts due to their penchant for peroxide decomposition and need for the secondary hydroxyl during peroxide activation [49, 173-174]. Ti-SiO_2 maintains > 90 % direct selectivity with TBHP as the oxidant. Nb-SiO_2 achieves 55 % direct selectivity with H_2O_2 as the oxidant and Ta-SiO_2 has the lowest activity but 85 % direct selectivity with H_2O_2. Both Nb and Ta-SiO_2 catalysts have > 45 % regioselectivity to external epoxide, more than Ti-SiO_2 which performs at 25 % regioselectivity, typical for nonporous Ti-SiO_2. This indicates that metal cation identity, oxidant selection, and synergy between them have large impacts on direct selectivity and regioselectivity.

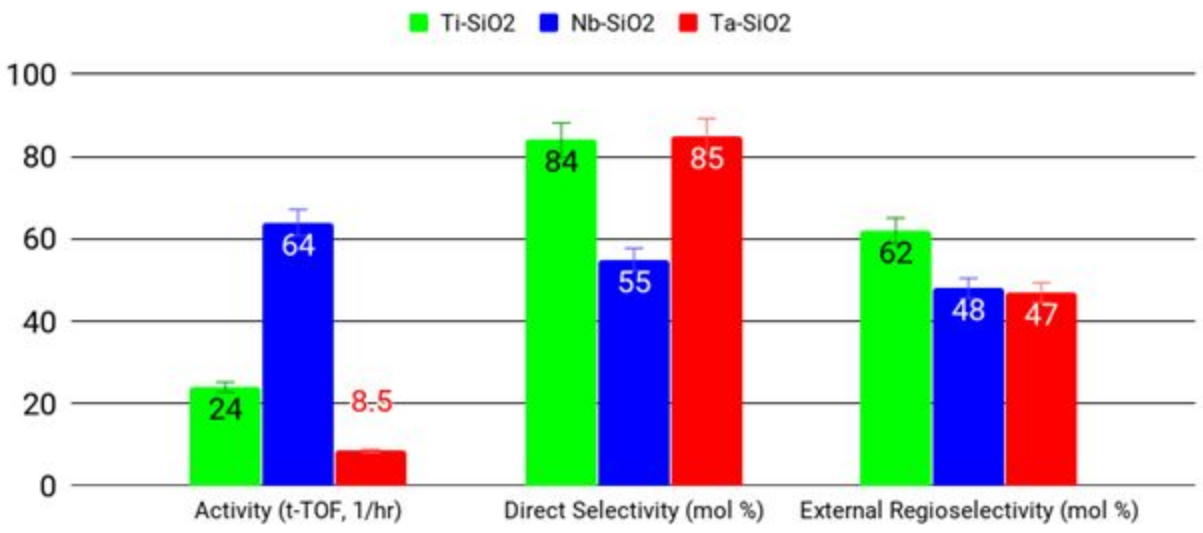

Figure 4.7 Effects of varying metal cation identity on limonene oxidation activity, epoxide selectivity, and external epoxide regioselectivity. Reaction conditions were 2 mmol H_2O_2, 1 mmol limonene, 4.6 mL acetonitrile, 30 mg catalyst, 65 ºC, 0-15 min.

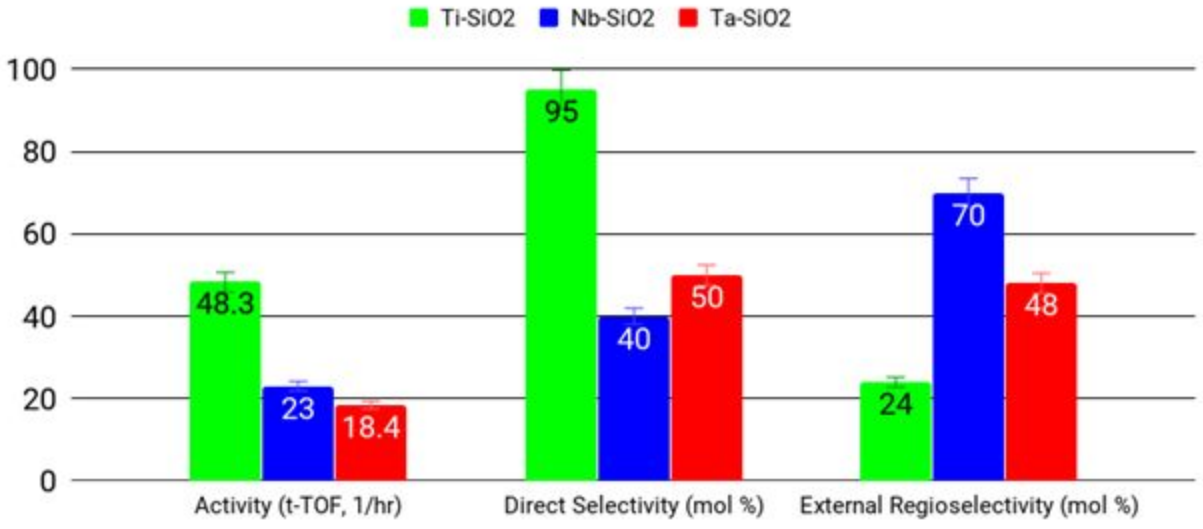

Figure 4.8 Effects of varying metal cation identity on limonene oxidation activity, epoxide selectivity, and external epoxide regioselectivity. Reaction conditions were 1.1 mmol TBHP, 1 mmol limonene, 4.6 mL acetonitrile, 30 mg catalyst, 65 ºC, 0-15 min.

Table 4.2 Comparison of fresh and spent/recalcined Ti-SiO_2 in limonene oxidation with H_2O_2. Reaction conditions were 2 mmol H_2O_2, 1 mmol limonene, 4.6 mL acetonitrile, 30 mg catalyst, 65 ^oC, 0-6 h.

Catalyst	Rate per metal (1/hr)	Direct selectivity (mol %)	External regioselectivity (mol %)
Ti-SiO_2	23.7	84.1	61.8
S/R Ti-SiO_2	3.5	88.8	57.3

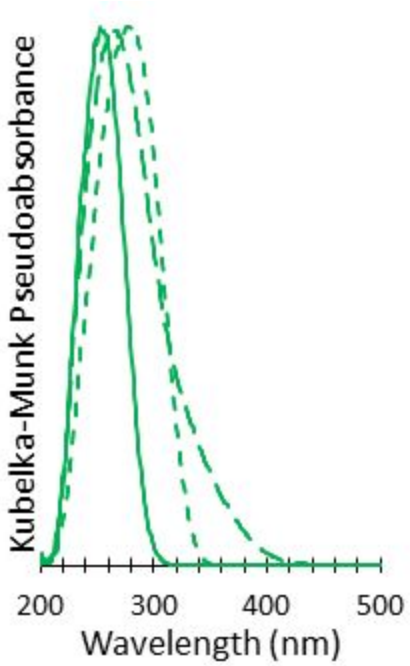

Figure 4.9 Ambient DRUV-vis spectra of freshly calcined Ti-SiO_2 (solid), Ti-SiO_2 recovered after 6 h of limonene oxidation with aq. H_2O_2 (long dash), and reclacined Ti-SiO_2 (short dash).

Section 4.5.3 SiO_2 Support Steric Effects

Since the Ti-SiO_2 catalysts offered the most room for improvement in terms of external regioselectivity, Ti-SBA-15, Ti-Beta, and the SiO_2 overcoated materials were tested to investigate whether changing the SiO_2 support sterics has a large influence on oxidation behavior. Catalysts with different structures were tested with 10 % excess TBHP as compared to

limonene. Wide pore SiO_2 supported catalysts are slightly less active than their framework molecular sieve counterparts. The potential origin of differences in TOF include (i) local electronic or steric effects on the active site or (ii) mass transfer or diffusion limitations. Internal diffusion limitations were assessed by calculating the Weisz-Prater criterion for Ti-SiO_2, Ti-SBA-15, and Ti-Beta. If Equation 5.1 is satisfied, then pore diffusion limitations are negligible [64]:

$$N = \frac{Rox\ x\ Dp}{Cs\ x\ Deff} < 0.3 \qquad (5.1)$$

Here, R_{ox} is the measured rate of limonene consumption per volume catalysts, Dp is the catalyst particle diameter, Cs is the reactant concentration at the surface, and Deff is the effective diffusivity. Dp is 4-6 micron for Ti-SBA-15 and 0.5-2 micron for Ti-Beta based on prior SEM. An effective diffusivity of 1 x 10^{-5} to 1 x 10^{-7} cm^2/s was used for limonene in acetonitrile, based on prior calculations by other researchers as a function of catalyst porosity [175]. Although catalyst geometries vary, this order of magnitude estimate should be sufficient for diffusion limitation checks. The Weisz-Prater criterion ranges between 0.027 to 0.060 for Ti-SBA-15 and between 0.069 and 0.120 for Ti-Beta. This indicates that pore diffusion limitations may be ignored for these catalysts. Internal diffusion limitations were tested for Ti-SiO_2 using experimental testing, namely, comparing the freshly calcined catalyst to a fraction of the material finely ground to < 0.7 micron. The results shown in Figure 4.10 demonstrate that pore diffusion limitations may also be ignored for Ti-SiO_2 because the rate per metal varies by only 1 % between the two materials which is well within run to run error.

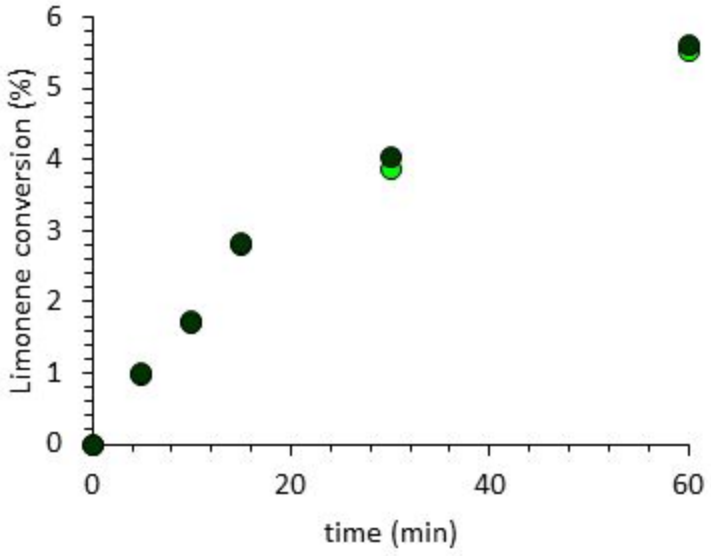

Figure 4.10 Experimental internal diffusion testing for Ti-SiO_2. Ti-SiO_2 (solid) was compared with a fraction of Ti-SiO_2 crushed down to < 0.7 micron (dashed). Reaction conditions were 1.1 mmol TBHP, 1 mmol limonene, 4.6 mL acetonitrile, 30 mg catalyst, 65 ^{o}C, 0-6 h.

Electronic and steric effects were assessed by obtaining the apparent activation enthalpy for each Ti catalyst based on the overall rate of limonene consumption. The results are plotted in Figure 4.11 over a temperature range of 35-65 ^{o}C. Interestingly, the catalysts break down into three groups with different apparent activation enthalpies. Ti-SiO_2, Ti-SBA-15, and 10cFO all have a ΔEa, app ~20 kJ/mol whereas 2cFO has a significantly lower value of 12 kJ/mol. Conversely, Ti-Beta has a much higher apparent activation enthalpy of 34 kJ/mol. Others have previously observed large variations in apparent activation enthalpy with support sterics, and have labeled this phenomenon the confinement effect [13]. 2cFO has a lower apparent enthalpy so SiO_2 deposition on the active site has imparted confinement during limonene adsorption or oxidation. This difference in mechanism can explain the difference in rate between 2cFO and the other Ti catalysts.

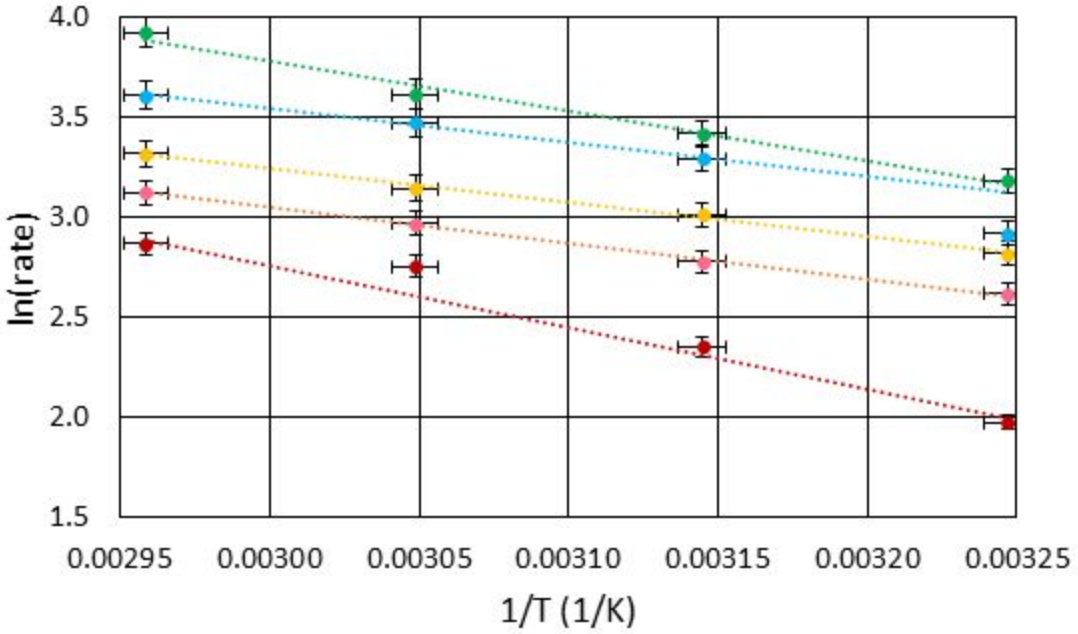

Figure 4.11 Arrhenius plots for all Ti based catalysts. Reaction conditions were 1.1 mmol TBHP, 1 mmol limonene, 4.6 mL acetonitrile, 25-55 mg catalyst, 65 ºC, 0-15 min. Ti-SiO_2 (green), Ti-SBA-15 (cyan), Ti-Beta (orange), 2cFO (pink), and 10cFO (maroon).

As seen in Figure 4.13, surprisingly all Ti catalysts converge on nearly identical direct selectivity and external regioselectivity values, indicating that limonene oxidation selectivity is insensitive to catalyst sterics at the local and structural level at 65 ºC. This conclusion runs counter to many previous studies but this is only the fourth study to the best of our knowledge where different catalyst structures are compared experimentally under identical reaction conditions [101]. These three prior studies largely agree with our results and found that external regioselectivity is 10-15 mol % with excess TBHP, regardless of the nature of the support [101]. Other reports that do claim shape selectivity do so mostly by inference, connecting increased steric constraints around the active site with regioselective behavior without (i) thoroughly vetting the mechanism, (ii) extrapolating down to low conversion, and (iii) providing product

analysis spectra (GC-FID, NMR) demonstrating the absence of other confounding mechanisms [10, 51]. Direct selectivity decreases slightly for all Ti catalysts as conversion increases, likely due to active site poisoning or deactivation with TBOH or limonene diols. In addition, external regioselectivity decreases as conversion increases, reaching 10-20 mol % regardless of sterics. Initial selectivity towards the external epoxide may be the result of initial allylic oxidation behavior, as observed for cyclohexene oxidation over similar materials [32, 62].

To more closely examine reactive differences and the effects of support sterics, we evaluated our Ti catalysts with an in-situ titration technique. Our group has previously demonstrated phenylphosphonic acid (PPA) to be a selective, irreversible titrant for poisoning Lewis acidic surface TiOx and NbOx sites during cis-cyclooctene oxidation with H_2O_2 [49, 61]. In a typical titration, variable amounts of PPA solution are added at parallel batch reactors at 65 ^{o}C prior to starting the oxidation reaction. Titrant loadings span 0-2 equiv PPA per total Ti metal loaded in the reactor. Initial rates are evaluated and decrease monotonically as a function of PPA added as shown in Figure 4.14. We assume PPA titrates active Ti in a 1:1 fashion and estimate the fraction of active Ti by extrapolating a linear fit of limonene oxidation rate as a function of PPA down to 0 rate. The determined value for these catalysts ranges from 49 to 104 % active Ti with a standard error of 10 %. Initial TOF ranges from 28 to 60 hr^{-1}, which demonstrates some convergence to a single TOF but not quite the level of agreement seen in previous work [61]. The residual rate, which is a proxy for measuring sites inaccessible to PPA, is high for Ti-Beta with 50 % of its original activity.

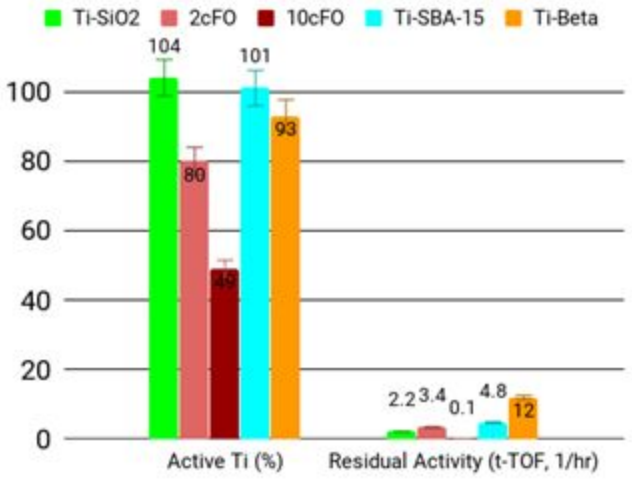

Figure 4.12 Percent active Ti and residual activity for freshly calcined catalysts determined with in-situ PPA titration. Reaction conditions were 1.1 mmol TBHP, 1 mmol limonene, 4.6 mL acetonitrile, 25-55 mg catalyst (4.0 micromol Ti), 0-2 equiv. PPA, 65 ºC, 0-15 min.

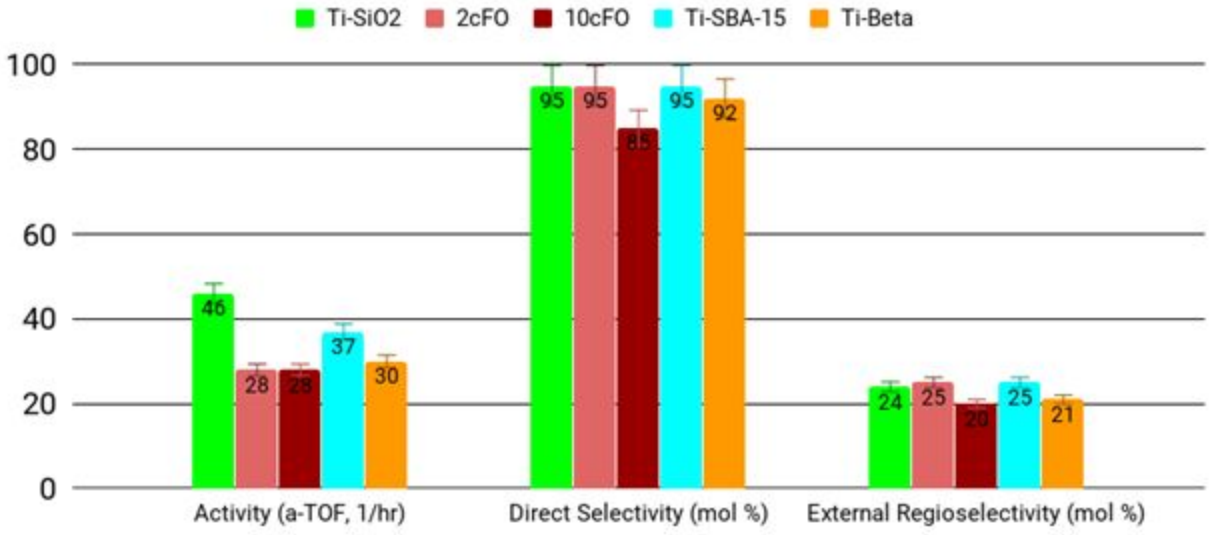

Figure 4.13 Effects of varying support sterics on limonene oxidation activity, epoxide selectivity, and external epoxide regioselectivity. Reaction conditions were 1.1 mmol TBHP, 1 mmol limonene, 4.6 mL acetonitrile, 30 mg catalyst, 65 ºC, 0-15 min.

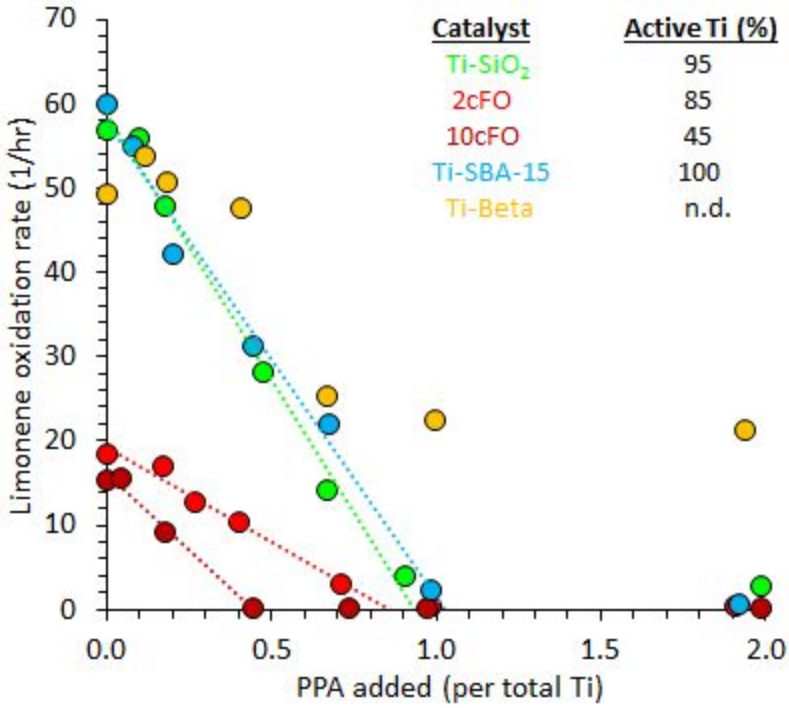

Figure 4.14 PPA titration curves for supported TiOx catalysts. Reaction conditions were 1.1 mmol TBHP, 1 mmol limonene, 4.4-4.6 mL acetonitrile, 25-55 mg catalyst (4.0 micromol Ti), 0-2 equiv. of PPA delivered from a 50 mM mesitylene solution, 0-15 min.

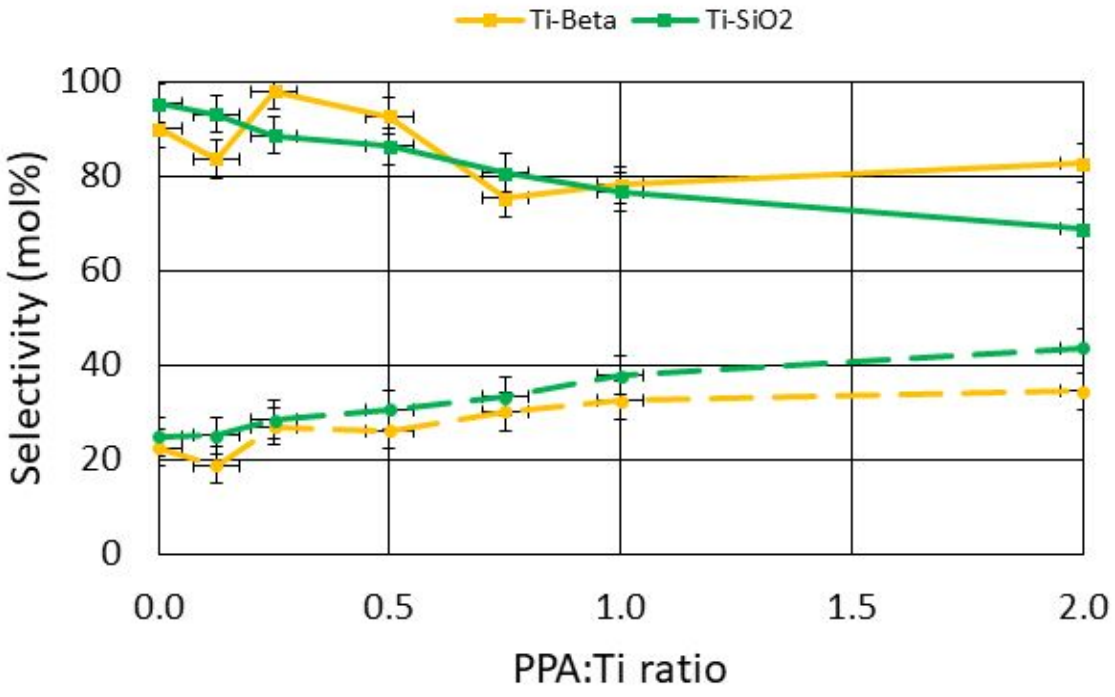

Figure 4.15 Effects of PPA titration on epoxide selectivity (solid) and external epoxide regioselectivity (dashed). Reaction conditions were 1.1 mmol TBHP, 1 mmol limonene, 4.6 mL acetonitrile, 25-30 mg catalyst (4.0 micromol Ti), 0-2 equiv. PPA, 65 ^{o}C, 0-15 min.

The data for PPA titration runs on Ti-SiO_2 and Ti-Beta catalysts was further analyzed to assess the effects of PPA poisoning on direct selectivity and external regioselectivity. Samples with increasing loadings of titrant have lower direct selectivity, with values decreasing down to 75-80 mol %. Surprisingly, highly poisoned samples were more selective to the external epoxide, with regioselectivity reaching 35-45 mol %. This demonstrates that a correlation between allylic oxidation activity and external epoxidation holds for active site poisoning. In addition, the regioselectivity for titrated Ti-Beta is similar to the unpoisoned catalyst, meaning that the source of residual activity lies with pore restrictions in the Beta framework or pore blocking by PPA.

Finally, reaction conditions were varied widely and all Ti catalysts were tested to investigate whether a regioselective regime could be found for limonene oxidation at high relative oxidant or alkene concentration. Interestingly, as the oxidant:limonene ratio is increased from 1.1:1 to 11:1 for TBHP, all catalysts identically approach 80 % selectivity to the kinetically unfavored limonene 8,9-oxide as seen in Figure 4.16. At the same time, direct epoxidation plummets to < 25 %, suggesting that external epoxidation may be the result of allylic oxidation rather than direct epoxidation. It is well known that radical C-H abstraction preferentially occurs at tertiary > secondary > primary bonds [176-177]. This is somewhat borne out in the limonene oxidation product distribution which consists primarily of secondary products carveol, carvone, and isostructural species at the C3 position. Since the internal double bond is more reactive for allylic oxidation and direct epoxidation, it follows that external epoxidation regioselectivity increases due to undesired side reactions. Studies on cyclohexene oxidation show that radical

oxidation occurs via cyclohexyl hydroperoxide intermediates [32]. A metal catalyzed epoxidation step between the formed hydroperoxide and reactant cyclohexene lead to the most of the observed radical products.

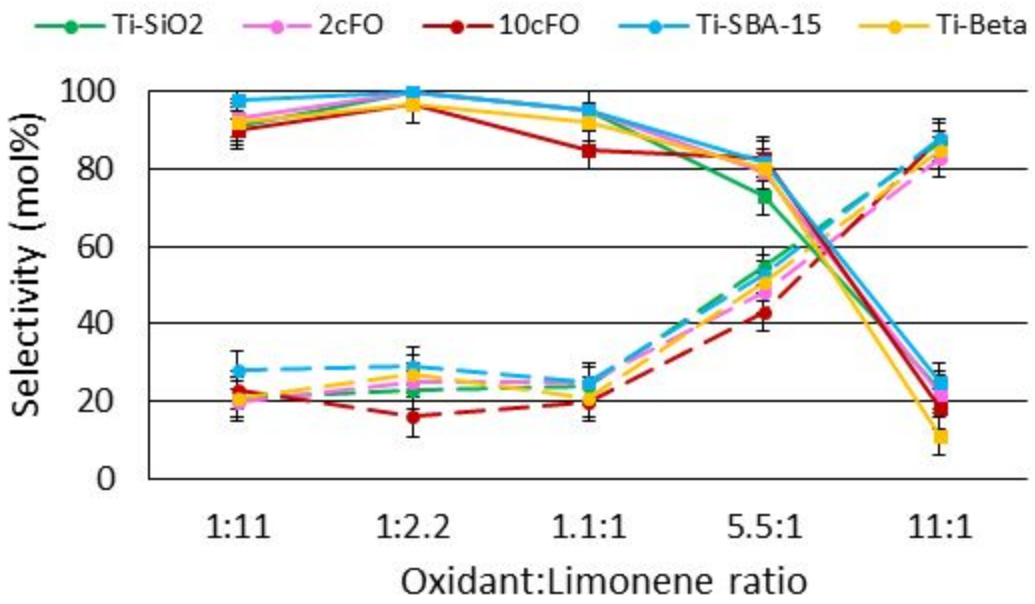

Figure 4.16 Effects of reaction conditions on epoxide selectivity (solid) and external epoxide regioselectivity (dashed). Reaction conditions were 1.1-11 mmol TBHP, 1-10 mmol limonene, 4.96 mL total volume, 25-55 mg catalyst, 65 ºC, 0-15 min.

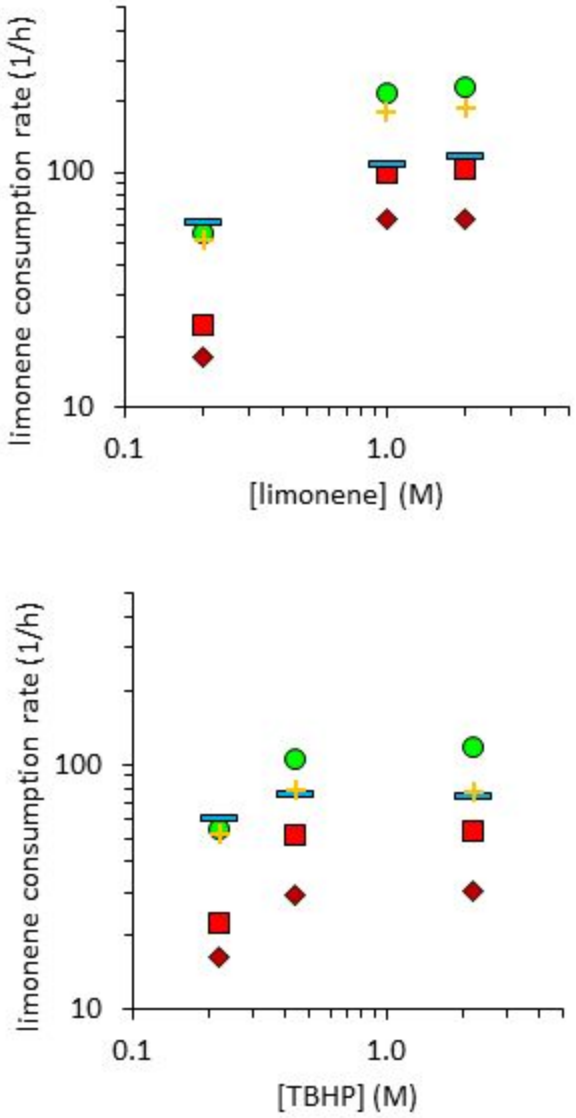

Figure 4.17 Rate order plot for limonene oxidation rate as a function of [limonene] (top) and [TBHP] (bottom). Reaction conditions were 1.1-11 mmol TBHP, 1-10 mmol limonene, 4.96 mL total volume, 25-55 mg catalyst, 65 ºC, 0-15 min.

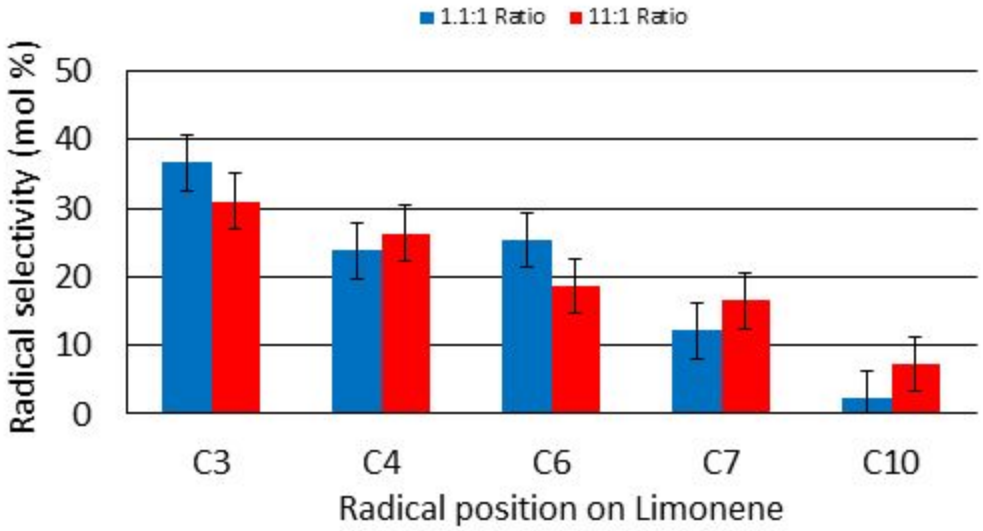

Figure 4.18 Limonene oxidation radical product selectivity over Ti-SiO_2. Reaction conditions were 1.1-11 mmol TBHP, 1 mmol limonene, 4.96 mL total volume, 30 mg Ti-SiO_2, 65 ºC, 0-15 min.

The observed radical reactivity trend of C3 > C6 ≅ C4 > C7 > C10 may be partially explained by assessing the relevant kinetic steps occurring in the mechanism: radical formation and disproportionation. Primary peroxide radicals typically do not play a significant part in liquid phase oxidation of hydrocarbons due to the high bond dissociation energy (BDE) of primary C-H bonds [176]. However, since all C-H abstraction steps are exothermic in the case of participation by oxidant radicals, the activation barriers for the reaction are likely 0-2 kcal/mol and disproportionation is the rate limiting step [176-177].

Generally, the disproportionation rate constant for secondary hydroperoxides (C3, C6) is 1000x greater than tertiary hydroperoxides (C4) [176]. The disproportionation of secondary hydroperoxides has been extensively studied using ethylbenzene hydroperoxide and cyclohexyl hydroperoxide reactants [176]. Based on the observed products in prior reports, limonene C6-hydroperoxide and limonene C3-hydroperoxide likely disproportionate to yield ketone,

alcohol, and epoxide products. C3 may react faster than C6 because it is in resonance with C1. This stable radical may undergo HOO* addition and form a highly stable C1 hydroperoxide that undergoes disproportionation at a very slow rate (Figure 4.2) to form a styrene derivative. The actual radical product distribution is shown for oxidation with 10 mol % and 1000 mol % excess TBHP.

On aggregate, limonene oxidation external regioselectivity is conclusively found to be strongly inversely correlated with direct epoxidation selectivity, irrespective of Lewis acidity or SiO_2 support sterics. This suggests that radical oxidation is possible and likely occurs at the internal and external double bonds but leads to limonene 8,9-oxide rather than the aldehyde. The possibility of epoxide formation through radical oxidation mechanisms has been previously suggested for limonene oxidation, observed in cyclohexene oxidation, and suspected for cyclooctene oxidation [32, 160-164, 61].

Section 4.5.4 Consequences of Limonene Stereochemistry

Applying the proposed radical mechanism to limonene oxidation, we suggest that the apparent stability of external alkene oxidation is a result of molecule sterics on disproportionation. Molecules that are sterically hindered at the radical react slowly as primary and secondary radicals are much more effective acceptors than tertiary radicals. Even if a radical is formed at the C4 position in limonene, as shown in Figure 4.2, the homo disproportionation reaction to form external radical products such as p, α-dimethylstyrene and 1, 8-menthadien-4-ol is likely slow. These products may be formed however if limonene C4-hydroperoxide instead disproportionates with a primary hydroperoxide. Since limonene molecular sterics are highly influential on the radical pathway, the effects of stereochemistry on product distribution were

assessed by substituting in the uncommon S-(-)-limonene and performing alkene oxidation with Ti catalysts over a wide range of [TBHP]. A similar inverse correlation between direct selectivity and external regioselectivity is observed for the S isomer, but it is more resistant to radical activation under similarly high oxidant concentrations. The reactivity at 10 mol % excess TBHP is identical for the two isomers but radical disproportionation reactions must proceed at a slower rate for the S isomer because direct selectivity remains > 80 mol %.

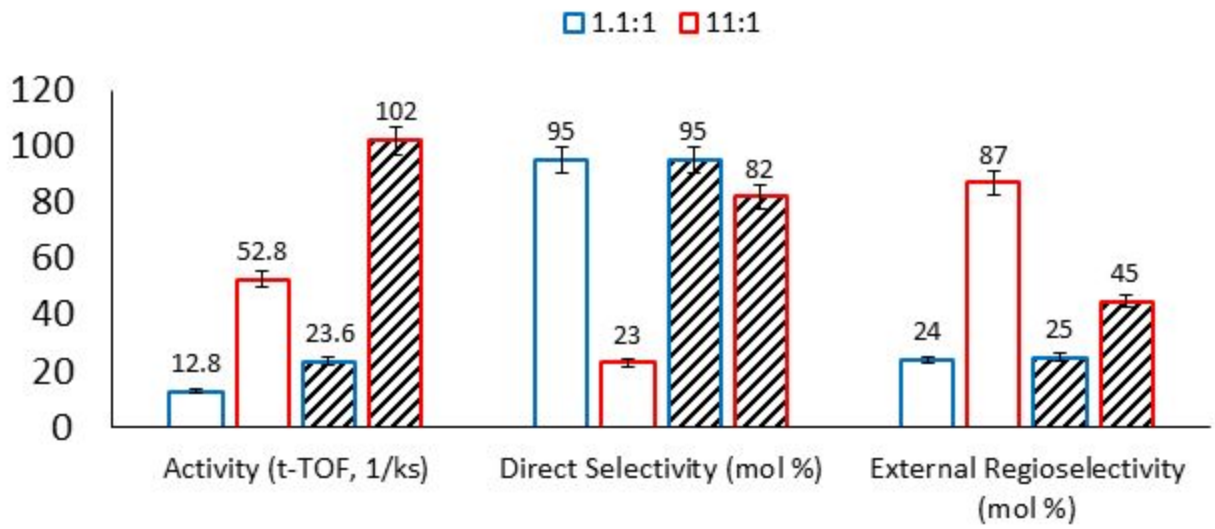

Figure 4.19 Effects of reaction conditions on oxidation of R-(+)-limonene (empty) and S-(-)-limonene (dashed). Reaction conditions were 1.1-11 mmol TBHP, 1 mmol limonene, 4.96 mL total volume, 25-55 mg catalyst, 65 ºC, 0-15 min.

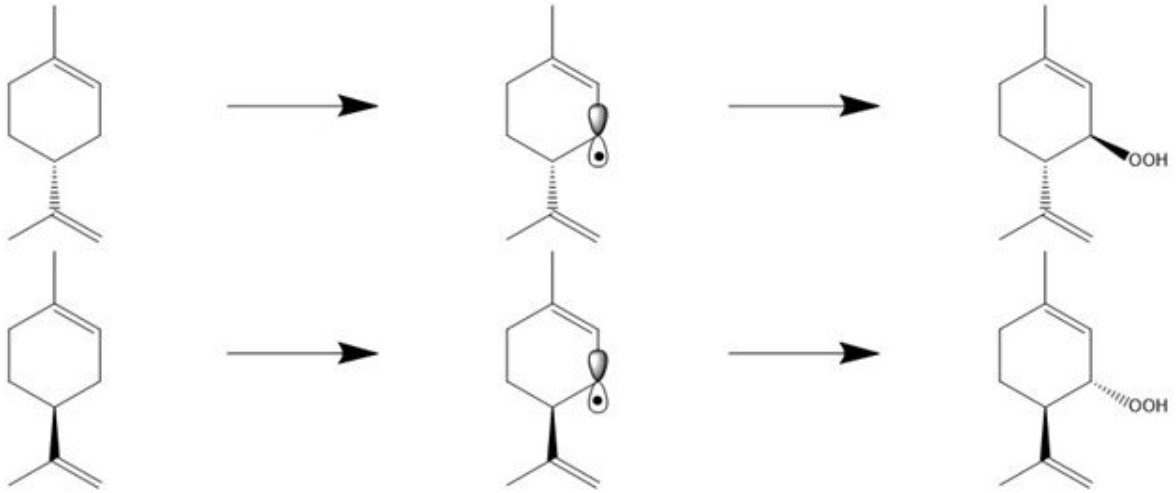

Figure 4.20 Potential differences in allylic oxidation behavior for R-(+)-limonene and S-(-)-limonene. The C3 position is predominantly affected by changes in stereochemistry.

The direct comparison of site isolated Lewis acid catalysts in limonene oxidation over a wide range of reaction conditions allows us to elucidate the importance of the radical mechanisms in determining external regioselectivity. Since limonene oxidation regioselectivity is insensitive to local and structural sterics we suggest that this reaction be avoided when assessing shape selectivity. The platform of catalyst and kinetics understanding here may be used to further assess shape selectivity sensitivity of candidate reactions such as competitive alkene or sulfide oxidation.

Section 4.6 Conclusions on Limonene Oxidation Kinetics

Here, we detail one of the first comprehensive reports on the effects of oxide support structure, metal cation identity, reaction conditions, and reactant sterics on limonene oxidation over M-SiO_2 catalysts. DRUV-vis spectroscopy of freshly calcined catalysts shows that catalysts synthesized in this work are predominately site isolated, extraframework MOx supported on SiO_2 [32, 61]. These species are identified by LMCT bands at 245 nm (Ti), 240 nm (Nb), and 220 nm (Ta). SiO_2 overcoated Ti-SiO_2 materials 2cFO and 10cFO have bands nearly identical to their

parent Ti-SiO_2. The high fraction of isolated sites is likely due to the use of Cp* and calixarene templates which enforce a minimum distance between deposited Lewis acid cations. Nominally framework Ti-SBA-15 and Ti-Beta materials have LMCT bands at 220 nm and 260 nm respectively. This indicates that Ti in Ti-SBA-15 is fully incorporated into its SiO_2 walls but Ti-Beta contains open O_3TiOH sites as framework defects.

External regioselectivity was seemingly a function of the relative kinetics of internal and external direct epoxidation as shown in Figures 4.7 and 4.8 based solely on the catalytic performance of Ti, Nb, and Ta-SiO_2. Regioselectivity is insensitive to sterics modifications at the local (framework vs extraframework Ti) and structural (pore size) level at 65 ^{o}C, in stark contrast with conclusions reached in prior reports. This is consistent with recent publications from our group that used in-situ phosphonic acid titration to demonstrate that M-SiO_2 with different support structures only possess different numbers of sites and not intrinsically different sites for oxidation. Most importantly, kinetic studies over a range of [limonene] and [TBHP] reveal that external regioselectivity is highly correlated with allylic oxidation. Allylic oxidation preferentially reacts with the internal double bond and this behavior is mixed in with selective formation of the external epoxide. This unfortunately casts the reaction in doubt as a useful shape selectivity probe for Lewis acid catalysts. The link between allylic oxidation behavior and limonene 8,9-oxide production will need to be overcome if this monomer is needed for polymer and plastics production. Potential methods to mitigate radical oxidation behavior is via the addition of additives (i.e. BHT) or chemically passivating surface hydroxyls with silylation agents (i.e. TMCS) [76, 178]. Additional studies on shape selective reactions, surface modified catalysts, and the radical oxidation mechanism are underway.

Chapter 5. SiO_2 Deposition on Ti-SiO_2: Transport Limitations Free Confinement Effects

The research presented in this chapter is in preparation for submission to JACS with Daniel T. Bregante, David W. Flaherty, and Justin M. Notestein.

Section 5.1 Confinement Effects on Lewis Acid Catalysts

Steric effects on catalyst reaction behaviors have been known since the first industrial applications of zeolites in the 1960s. Zeolites have significantly faster reaction rates than their amorphous mesoporous analogs for conventional feedstock molecules such as petroleum and light gases found in shale gas reserves. However, as industry looks to utilize cyclic compounds or bulky feedstocks, highly constrained active site environments may no longer be beneficial for catalysis. Mesoporous materials seem like a reasonable alternative but these catalyst often underperform in terms of both activity and selectivity. Nonporous materials could also work but they suffer from low activity due to apparently weaker acid sites. The implementation of shape selectivity without pore limitations is a grand challenge to move catalysis forward and design a new class of materials that allow for facile diffusion to the active site and high selectivity.

This work was inspired in part by prior research on shape selective photocatalysts. Our group modified a originally nonselective nonporous TiO_2 photocatalysts with calixarene and ACA in order to template the deposition of an inactive oxide over the surface [124]. ALD with trimethylaluminum (TMA) was used in order to cover most of the surface excluding the templates. The templates were removed with ozone in order to reexpose the underlying TiO_2

surface and provide limited access to the photocatalyst. Competitive photooxidation and photoreduction show that sterically bulky reactant molecules were limited in reaction as compared to the unhindered molecules [124]. This template, overcoat, template removal idea can be furthered to supported Lewis acid catalysts by employing templates similar to the metallocalixarenes our group has used [31-32].

This work covers the effects of confinement on limonene oxidation with TBHP over Ti-SiO_2 catalysts. DRUV-vis, Ti K-edge XANES, and ICP-OES were used to determine that Ti active sites on all studied catalysts are similar. N_2 physisorption was used to discern differences in SiO_2 support sterics amongst the catalysts. Templated surface modified catalysts were compared with in framework mesoporous or microporous Ti-SiO_2. Limonene oxidation was run with varying reactant concentrations in order to assess the mechanism and assign a MASI. Then, limonene oxidation apparent barriers, heat of adsorption, and intrinsic activation barriers were obtained. The intrinsic activation enthalpy converged on 45 ± 3 kJ/mol for all catalysts. Limonene adsorption isotherms were obtained to further show that activation entropies also converged on a single value. Expected effects on oxidation regioselectivity are shown to be negligible but classical confinement effects are observed for an SiO_2 overcoated catalyst.

Section 5.2 Catalyst Characterization

N_2 physisorption isotherms at -196 ^{o}C were collected for all catalysts using a Micromeritics ASAP 2010 instrument. The Rouquerol consistency criteria were applied to the BET method used on the adsorption branch of the isotherm [117-118]. Micropore surface areas were separated out from external surface areas using the t-plot (Ti-SiO_2, Ti-SBA-15, Ti-Beta) or the α_s plot (2cFO, 2cPO, 10cFO, 10cPO). The BJH method was applied to the desorption branch

of the isotherm to obtain the mesopore size distribution for each material. Ti content was obtained using ICP-OES on all catalysts. 20-50 mg of each solid was dissolved using 2-3 drops of concentrated HF. Then, all samples were diluted to ~11 mL using a 1 wt % HNO_3 solution. Dissolved samples were compared to Ti standards made by diluting a Ti standard down to make 5 standards and 1 blank between 0-75 ppm Ti content. ICP-OES was conducted on a Thermo iCAP 7600 instrument in the QBIC facility at Northwestern university.

Active site identity was partially discerned using ambient DRUV-vis. Powders were crushed with a mortar and pestle, then diluted by a factor of ~20 with perfect reflector and background material PTFE. Spectra were obtained from 200-800 nm. Edge energies for each material were calculated from the corresponding indirect Tauc plot for each material's DRUV-vis spectrum. Ti K-edge XANES was performed at DND-CAT Sector 5 of the Advanced Photon Source at Argonne National Laboratory. The K-edge was set using a pure Ti foil (Sigma-Aldrich, 99.7 % trace metals basis). All powder samples were dried at 150 ^{o}C under vacuum for 1 h before XANES spectra were obtained. Reported data are the average of 2 scans taken from 4,700-5,700 eV. The spectra are normalized by the average value from 5,000-5,200 eV. Spectra were obtained in fluorescence mode due to the low wt % content of Ti on the samples. Data for 4, 5, and 6-coordinate standards Ba_2TiO_4, Fresnoite, and anatase TiO_2 (Sigma-Aldrich, nanopowder, < 25 nm particle size, 99.7 % trace metals basis) were used from prior group publications [61]. The average peak position and a gaussian peak fitting routine from prior literature were used to estimate the coordination number for each sample [61, 179].

Limonene adsorption isotherms were obtained from 25-55 ^{o}C. Low concentration limonene solutions were made via serial dilution of 0.1, 0.3, 0.5, and 0.7 M standards. Limonene

was filtered over a column of neutral Al_2O_3 immediately before use. Limonene solutions from 5 x 10^{-6} to 1 x 10^{-3} M were used to construct adsorption isotherms. An initial 0.2 mL sample was taken using a Whatman syringe filter (0.7 micron, GF/F). Then, ~30 mg of each material was added to separate vials and the solutions were mixed on the Glas-Col digital mixer for 2 h at the desired temperature. 2 h was found to be adequate for equilibration over both Ti-SiO_2 based catalysts and Ti-Beta. The linear regime for adsorption was found to occur between 5 x 10^{-6} and 3 x 10^{-5} M for most catalysts. Langmuir isotherms were fitted to the data using a nonlinear least squares fitting routine in excel to find Kc and Vmax at 40 ^{o}C. The isosteric heat of adsorption of limonene was obtained using identical 7 x 10^{-6} M solutions from 25-55 ^{o}C.

Vmax was assumed to be invariant or weakly dependent on temperature. Therefore, adsorbed limonene values can be used to calculate the heat of adsorption in the linear regime. The adsorption isotherm for wide pore SiO_2 was obtained to check the linear regime and compare the bare support to the Ti grafted material. It should be noted that experiments performed in this section assess competitive adsorption between the solvent acetonitrile and limonene. A Shimadzu GCMS-QP2010 instrument was used to quantify low concentration limonene solutions. Selective ion monitoring (SIM) mode was employed to track the 67, 68, and 93 m/z ions and generate a new limonene calibration curve each day [5]. Run to run reproducibility was tested by obtaining duplicate isotherms for some catalysts. Standard error for these runs is 20 % for data points from 5 x 10^{-6} to 3 x 10^{-5} M limonene and 5 % for higher concentration data.

Section 5.3 Limonene Oxidation Energetics

Limonene oxidation was conducted in 20 mL glass vials with heating and shaking provided by a Glas-Col digital mixer. Runs between 0-65 ^{o}C were conducted with 800 rpm shaking speed. Subambient runs were conducted with the assistance of a recirculating chiller using propylene glycol refrigerant. 20-350 mg of catalyst were loaded into the vial, followed by 4.6 mL of acetonitrile in a typical run. Then, 0.16 mL limonene was added and the catalyst was allowed to adsorb the alkene for 30 min at 800 rpm. Finally, 0.2 mL TBHP was added and the timer was started upon TBHP addition. Time points were taken at 0, 5, 10, 15, 30, 60, 120, 360, and 1440 min. Some initial runs were performed with [limonene] and [TBHP] varying between 0.2 and 2.2 M. In the case of increased concentration, less acetonitrile solvent was used such that the total volume remained constant at 4.96 mL. Initial rates were taken as the concentration decrease in limonene observed through 15 min of reaction time. Batch to batch triplicate runs resulted in a standard error of ~15 % for initial rates.

In some runs, phosphonic acid titrants phenylphosphonic acid (PPA, Sigma-Aldrich, 98 %) or methylpohosphonic acid (MPA, Sigma-Aldrich, 98 %) were added in order to perform in-situ titration and count active Ti sites. In these cases, 50 mM solutions of PPA or MPA were created in Mesitylene (Sigma-Aldrich, 98 %) or 1,2-Dimethoxyethane (Sigma-Aldrich, anhydrous, 99.5 %, inhibitor-free) respectively. Then, 0-0.16 mL of solution were added with some acetonitrile removed in order to keep the total volume constant at ~4.96 mL. The titrant was allowed to adsorbed for 30 min competitively with the alkene and acetonitrile. Initial rates were obtained as a function of added titrant and this relationship was extrapolated down to 0 rate in order to obtain the amount of active Lewis sites for each catalyst.

Mass balances typically closed within 95-103 % comparing total products to the limone consumed by quantifying limonene, limonene 1,2-oxide, limonene 8,9-oxide, limonene dioxide, limonene 1,2-diol, limonene 8,9-diol, dihydrocarvone, carveol, carbone, perillyl alcohol, peryllil aldehyde, and several structural isomers. A Shimadzu GC-2010 equipped with an FID and β-CD column was used to analyze product mixtures for these runs. A Shimadzu GCMS QP-2010 was used with a ZB-624 column to verify product identity and help identify structural isomer products. Calibration curves were constructed spanning 0-0.2 M with authentic standards of known products from Sigma-Aldrich. Calibration factors for structural isomers discovered using GCMS were assumed to be equal to that of known structural isomers.

Section 5.4 Results and Discussion

Section 5.4.1 Catalyst Characterization

Some catalysts from Chapter 4 were used in this study, so refer to Section 4.5.1 for some of the characterization results. N_2 physisorption was used to assess the pore structure and surface morphology of SiO_2 overcoated Ti-SiO_2 (see Figures 5.1 and 5.2). SiO_2 deposition leads to a per gram decrease in total surface area (Table 5.1). However, when these values are normalized per gram original support, the primary consequence of overcoating is revealed to be the formation of a microporous SiO_2 layer on the material. Two cycles of overcoating introduces 25 and 45 m^2/g microporosity for 2cPO and 2cFO respectively. Ten cycles results in 30 and 75 m^2/g for 10cFO and 10cPO respectively. Added microporosity has previously been observed in overcoated materials by us and other groups. This is due to the thin oxide layer density being significantly less than that of the bulk oxide. Changes in the average pore diameter indicate the formation of a

new SiO_2 layer 0.3 nm thick for 2 cycles and 0.5-1 nm thick for 10 deposition cycles. Ti-SBA-15 and Ti-Beta from Chapter 4 were used in this study.

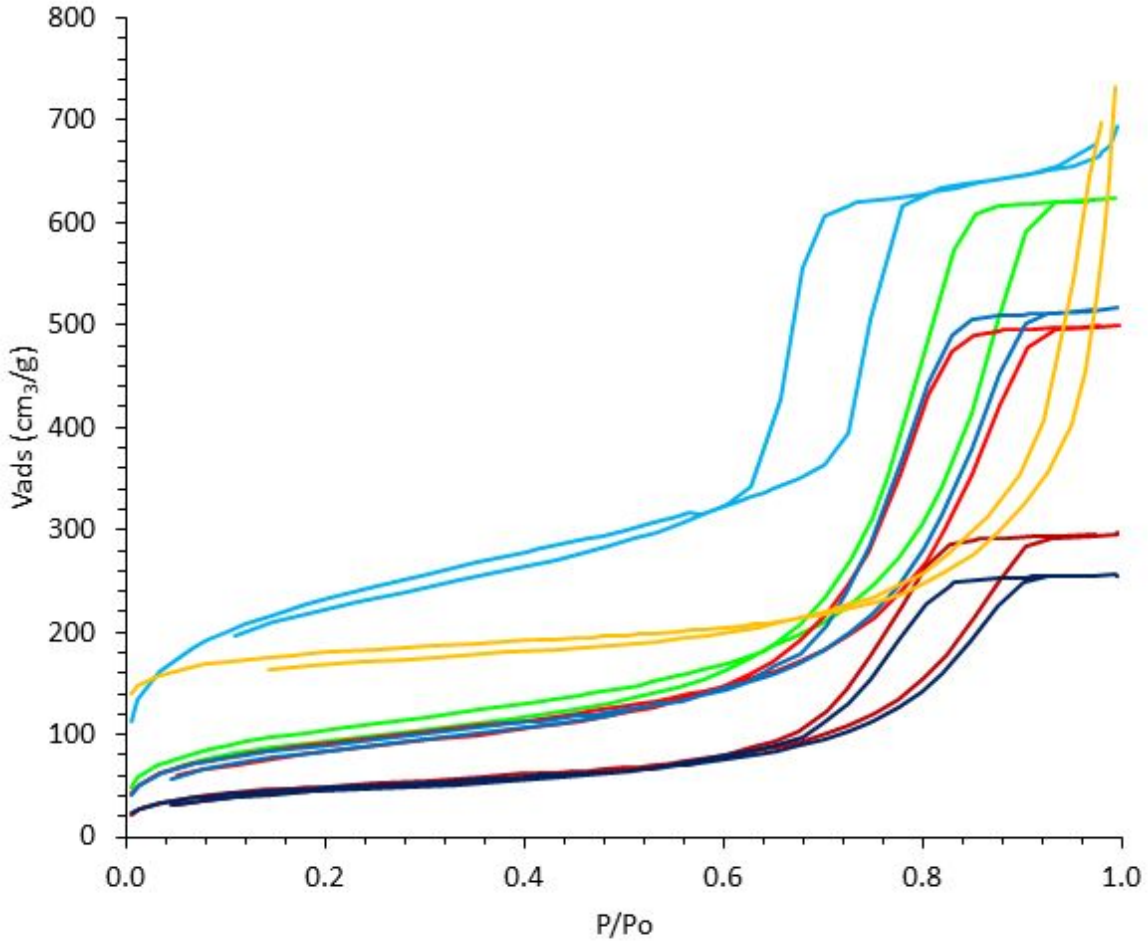

Figure 5.1 N_2 physisorption isotherm obtained at -196 ºC for Ti-SiO_2 (green), 2cPO (blue), 2cFO (red), 10cPO (dark blue), 10cFO (maroon), Ti-SBA-15 (cyan), and Ti-Beta (orange).

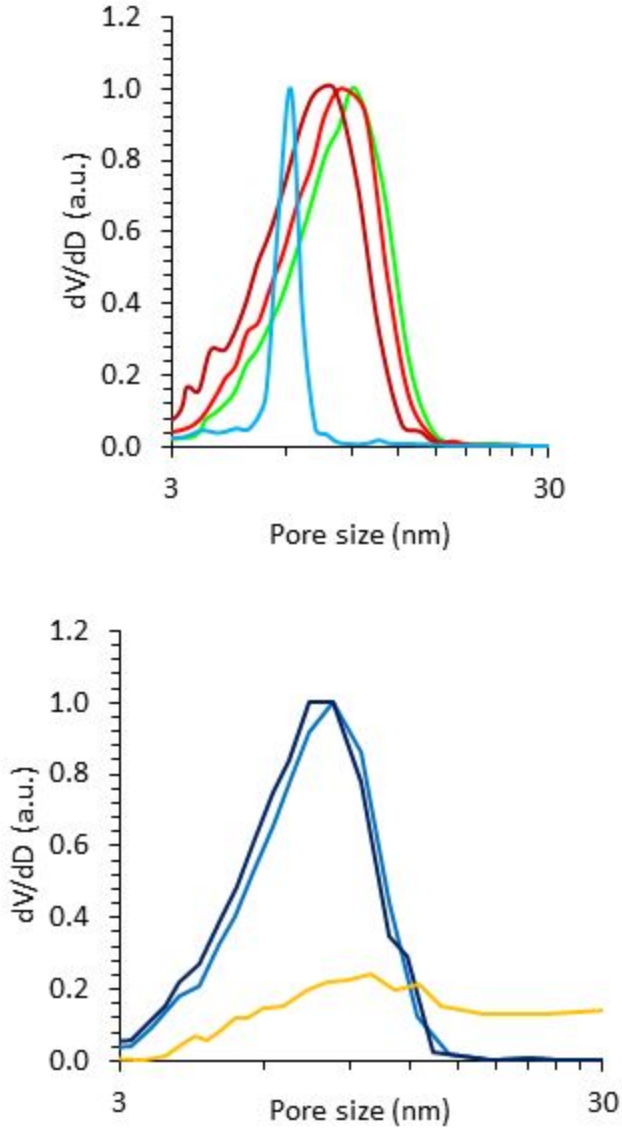

Figure 5.2 BJH mesopore size distributions obtained from the desorption branch of N_2 physisorption isotherms obtained at -196 ºC. Distributions are normalized to their highest peak feature. Ti-SiO2 (green), 2cFO (red), 10cFO (maroon), Ti-SBA-15 (cyan), 2cPO (blue), 10cPO (dark blue), and Ti-Beta (orange). Note that Beta has a regular crystalline micropore structure with 0.67 nm pore size.

The parent Ti-SiO_2 catalyst was synthesized to have a Ti surface density of 0.21 Ti/nm^2 and the framework reference materials possess < 1 wt % metal. These low loadings and surface

densities, especially given the bulky Cp*$TiCl_3$ precursor used here, are generally considered to form highly dispersed TiOx sites [32]. DRUV-vis spectroscopy shows an indirect edge energy of 4.0-4.2 eV for Ti-SiO_2 based materials, consistent with very highly dispersed extraframework O_3TiOH [32, 61]. Critically, DRUV-vis indicates that there is no significant aggregation of the TiOx sites after SiO_2 overcoating. Incidentally, materials derived from other bulky precursors such as 4-tert-Butylcalix[4]arene-TiCl were not resistant to decomposition under the highly alkaline SiO_2 deposition conditions. Ti-SBA-15 and Ti-Beta have indirect energies of 4.5 eV and 3.5 eV respectively as reported before.

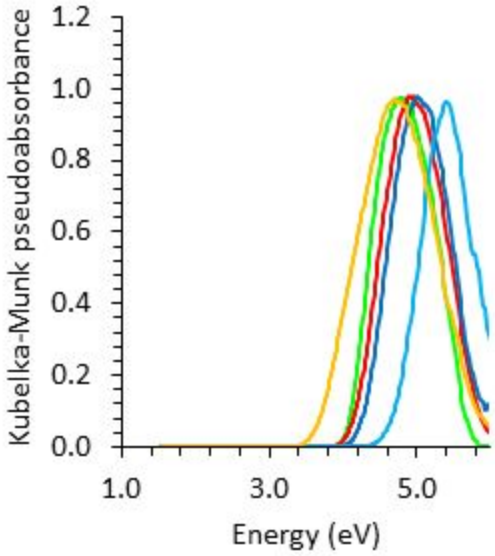

Figure 5.3 Representative ambient DRUV-vis spectra of Ti-SBA-15 (cyan), 2cPO (blue), 2cFO (red), Ti-SiO_2 (green), and Ti-Beta (orange). 10cPO and 10cFO spectra are indistinguishable from 2cPO and 2cFO respectively.

Table 5.1 Physical and active site characterization for supported TiOx catalysts.

Catalyst	Ti loading[a]			Edge[b]	CN[c]	Active Ti	Total SA	Micropore SA	Pore diameter[d]
	mol/g	/nm^2	wt%	(eV)		(%)	(m^2/g)	(m^2/g)	(nm)
Ti-SiO_2	0.13	0.21	0.63	4.0	4.2	103	374	nil	9.0
2cFO	0.11	0.21[e]	0.54	4.1	4.3	82	326	37	8.5
10cFO	0.07	0.24[e]	0.34	4.1	4.3	35	178	16	8.1
2cPO	0.11	0.21[e]	0.54	4.2	4.3	89	324	21	8.3
10cPO	0.07	0.24[e]	0.34	4.2	4.4	79	173	40	7.9
Ti-SBA-15	0.07	0.05	0.31	4.5	4.5	100	829	331	6.2
Ti-Beta	0.16	0.14	0.77	3.5	4.6	72	683	618	0.67

[a]From Ti ICP-OES and are within 5 % of expected values from synthesis for Ti-SiO_2 based materials

[b]From DRUV-vis and indirect transition Tauc plots

[c]Apparent coordination number (CN) from Ti K-edge XANES using the pre-edge peak position and decomposition into Gaussian features [9, 179]

[d]From the BJH method applied to the N_2 physisorption desorption branch

[e]From the total surface areas after SiO_2 deposition

Ti K-edge XANES directly measures Ti 3d orbital availability and therefore the average Ti coordination number for each sample. Pre-edge peak intensity and position have previously been correlated with the average Ti-O coordination number using 4, 5, and 6-coordinate standards [9, 179]. Figure 5.4 shows the Ti K-edge XANES spectra for Ti-SiO_2, 2cPO, Ti-SBA-15, and Ti-Beta along with reference materials Ba_2TiO_4 and Fresnoite. The spectra of

Ti-SiO_2, 2cFO, 2cPO, 10cFO, and 10cPO are essentially indistinguishable to the naked eye, and the remaining spectra are given in Figure 5.4. The pre-edge features were fitted to four Gaussians following established methods and the resulting pre-edge "sharpness" and average pre-edge peak position were compared to the standards to calculate a Ti coordination number, reported in Table 5.1.

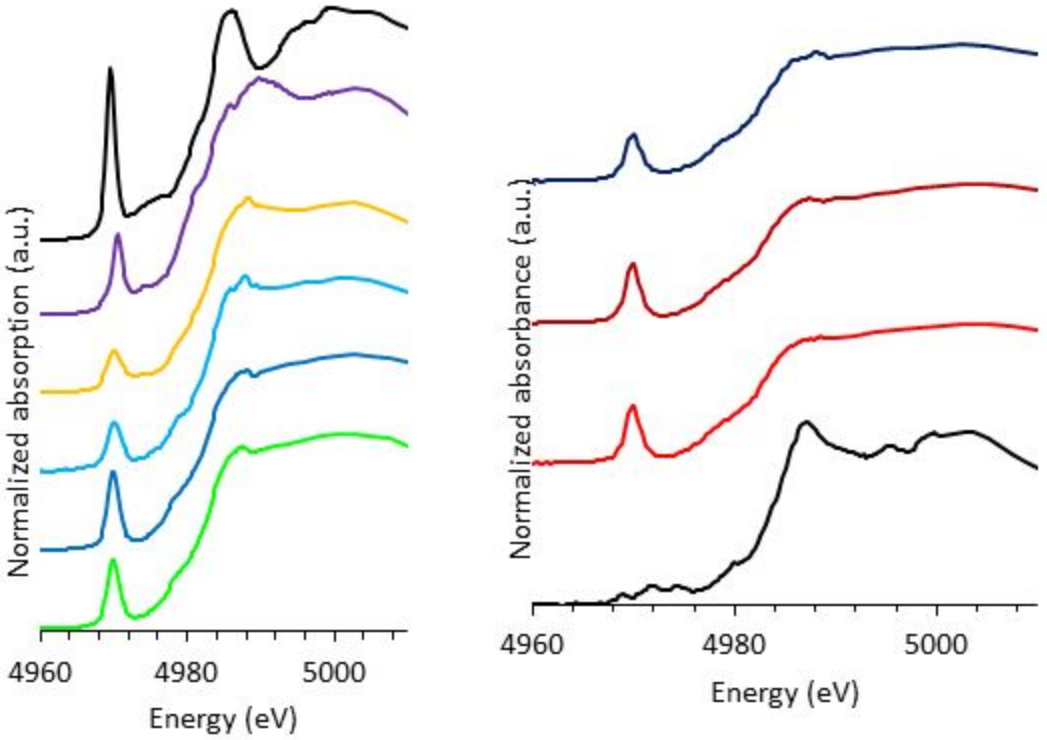

Figure 5.4 Ti K-edge XANES spectra for **left, a)** 4-coordinate standard Ba_2TiO_4 (black), 5-coordinate standard Fresnoite (purple), Ti-Beta (orange), Ti-SBA-15 (cyan), 2cPO (blue), and Ti-SiO_2 (green) **right, b)** 10cPO (dark blue), 10cFO (maroon), 2cFO (red), and 6-coordinate standard anatase TiO_2 (black).

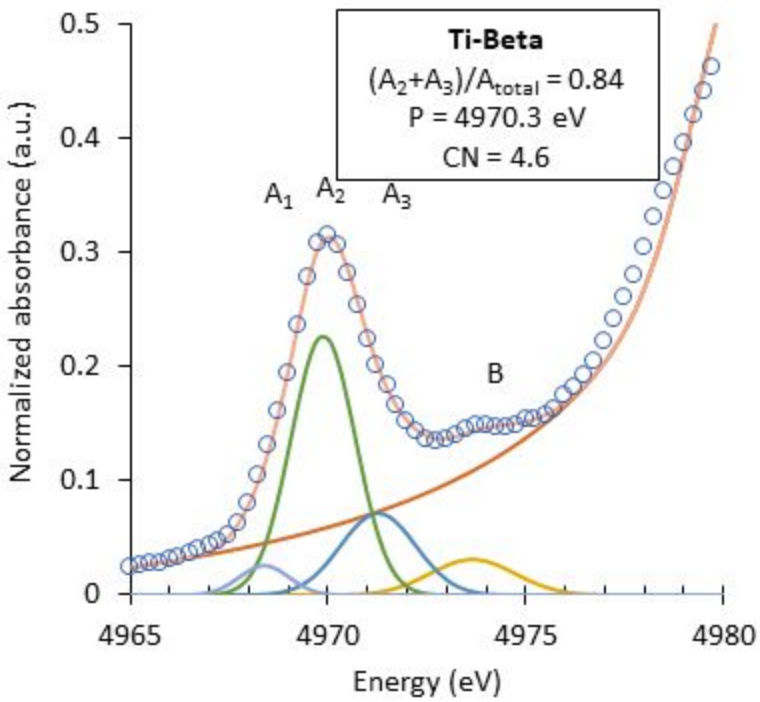

Figure 5.5 Example of the Ti K-edge XANES pre edge peak fitting routine. An arctan baseline and four Gaussian peaks were fitted according to prior literature methods [9, 179].

Pre-edge features were sharp for Ti-SiO_2 and the overcoated materials and centered at 4970.1 eV, characteristic of 4-coordinate Ti. However, their normalized absorption is significantly weaker than that for Ba_2TiO_4, meaning that the active sites are distorted from perfect tetrahedral symmetry. The average coordination numbers fall between 4.2-4.4, confirming their assignment from DRUV-vis as site isolated, extraframework sites. Ti-SBA-15 possesses a similar XANES spectra to these materials. The corresponding feature for Ti-Beta is less sharp, potentially indicating a small degree of oligomerization, and consistent with a lower DRUV-vis derived indirect edge energy for this material. Considering speciation results from XANES and DRUV-vis along with ICP-OES and N_2 physisorption derived active site densities

on these materials, their supported Ti sites are expected to be undercoordinated, highly dispersed Ti active for alkene oxidation.

Section 5.4.2 Revisiting Limonene Oxidation Kinetics over Ti Catalysts

Limonene is a bulky reactant that others have used to probe epoxidation selectivity and confinement effects [160-164]. For example, when new larger pore materials Ti-Beta and Ti-MCM-41 were first synthesized, they were tested against benchmark TS-1 and Ti-SiO_2 catalysts for limonene epoxidation regioselectivity to the ring (limonene 1,2-oxide) or external (limonene 8,9-oxide) epoxide. Typical regioselectivity values for Ti catalysts range from 75-80 mol % in favor of the ring epoxide [160-164]. Catalytic performance at 65 ^{o}C is shown in Figure 5.6 for the materials in this study, and it is expressed in terms of limonene consumption rate divided by total metal content. Materials were made free from diffusion limitations by repetitive grinding with mortar and pestle followed by sieving below 325 mesh using a screen. The normalized rates range from 14-60 hr^{-1} which are relatively typical for alkene oxidation under these conditions. SiO_2 exhibits no epoxide production and negligible formation of allylic oxidation products under these conditions. As a negative control, microporous TS-1 (Enichem, 0.53 nm diameter pores) showed negligible epoxide production, consistent with its pores being markedly smaller than the limonene kinetic diameter.

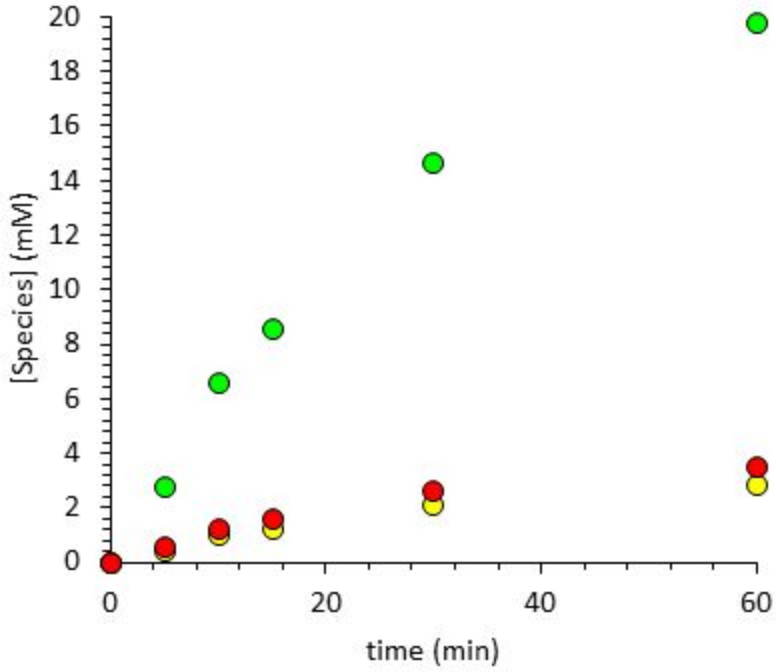

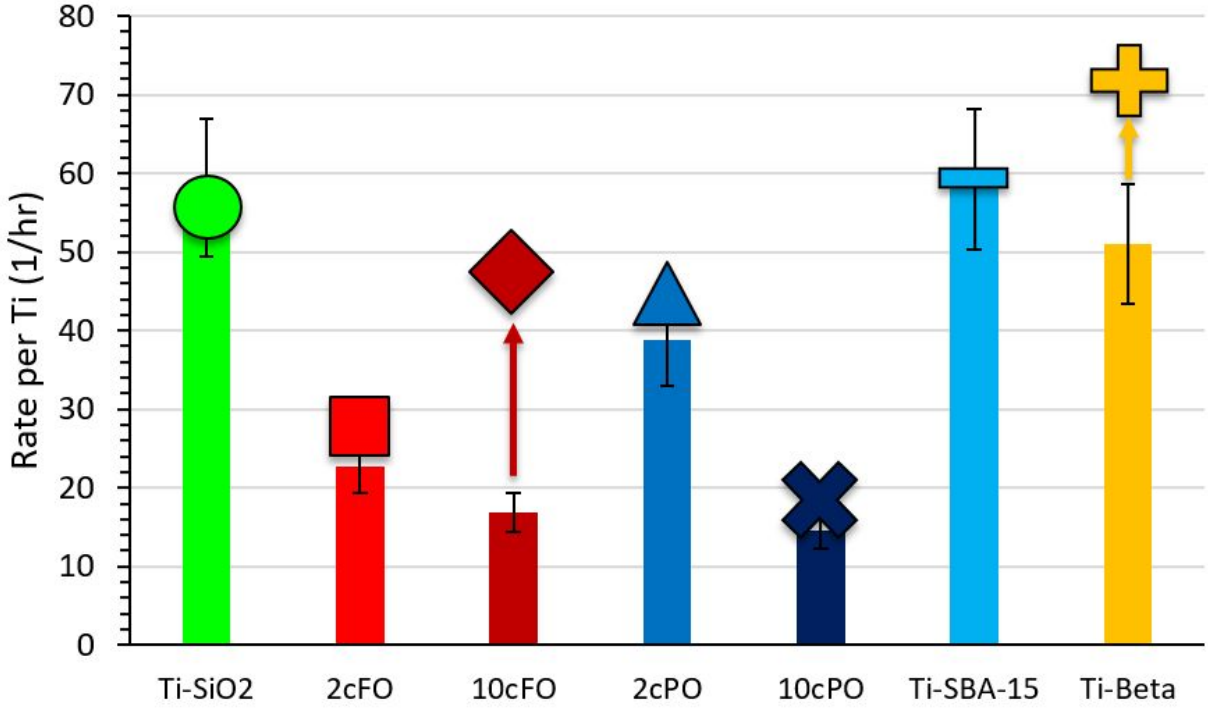

Figure 5.6 top, a) Example concentration vs. time plot for limonene oxidation products with Ti-SiO2. Limonene 1,2-oxide (green), limonene 8,9-oxide (yellow), and allylic oxidation products (red) are shown. 10 mmol corresponds to 5 % conversion under these conditions. Reaction conditions were 1.1 mmol TBHP, 1 mmol limonene, 4.6 mL acetonitrile, 30 mg catalyst, 65 ^{o}C, 800 rpm, 0-6 h. **bottom, b)** summary of initial limonene oxidation rates with

TBHP at 65 ºC. Bars show rates per total Ti metal and symbols show TOF with active site counting using in-situ MPA titration.

Ti-SiO_2, Ti-SBA-15, and Ti-Beta perform essentially identically under these conditions, while the rates for SiO_2 overcoated materials are lower in the order Ti-SiO_2 > 2cPO > 2cFO > 10cFO ≅ 10cPO. These initial rates are consistent with the naive view that SiO_2 deposition blocks Ti sites as the amount of SiO_2 deposition increases i.e. 2cFO vs 10cFO and in the absence of a protecting template, i.e. 2cPO vs 2cFO. Ti site counting using in-situ phosphonic acid titration was used to assess this assumption.Typical titration curves with PPA and MPA (0.65 and 0.54 nm kinetic diameters respectively) are shown in Figure 5.7 for the wide pore Ti-SiO_2 catalyst. For that material, regardless of titrant, the initial rate per metal decreases linearly with added phosphonic acid and the x intercept corresponds to 100 ± 10 % active Ti. Ti-SBA-15 has a similarly high dispersion consistent with large pores accessible to reactants and titrants and consistent with highly dispersed TiOx. In contrast, PPA fails to titrate away some activity for Ti-Beta, presumably because the PPA kinetic diameter is comparable to the Beta pore size and thus only titrates external surface sites.

The smaller titrant MPA gives a linear titration curve for Ti-Beta and 72 % active Ti. It should be emphasized that this active site count is specific for limonene as a reactant because other researchers demonstrated that ~100 % of the sites are active for cyclohexene oxidation with H_2O_2 [63]. By MPA titration, the fully overcoated materials 2cFO and 10cFO have 82 and 35 % active Ti, showing significant site blockage at higher SiO_2 loadings. Indeed, 10cFO was removed from further study because such a large fraction of its Ti is inactive for limonene oxidation. In contrast, 2cPO and 10cPO were shown to have 89 and 79 % active Ti respectively, and improved

site accessibility for these materials even with SiO_2 deposition demonstrates the positive effects of keeping the Cp* template in place to prevent SiO_2 from burying Ti active sites. At this point, rates in Figure 5.6 can be recomputed per active Ti to give TOF. In contrast to prior studies by our group comparing different grafted precursors on relatively large pore materials, here this renormalization does not eliminate differences between catalysts [61]. Therefore, a more detailed investigation was carried out into the kinetics and adsorption behavior at the active sites on these materials.

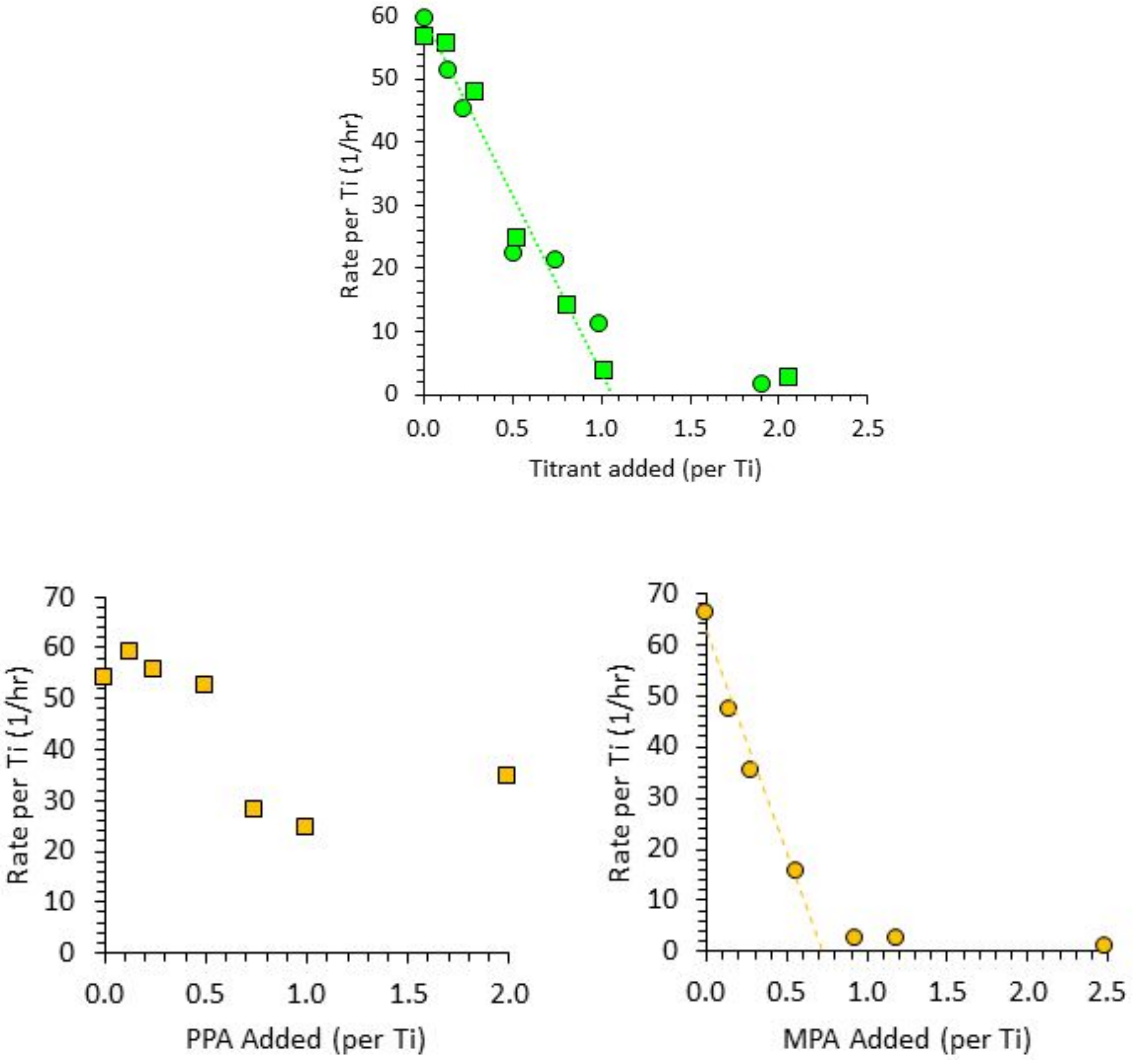

Figure 5.7 top, a) Initial limonene oxidation rates as a function of added PPA (squares) or MPA (circles). Reaction conditions were 1.1 mmol TBHP, 1 mmol limonene, 4.6 mL acetonitrile, 30 mg Ti-SiO_2, 65 ^oC, 800 rpm, 0-15 min. The x-intercept gives 103 % active Ti. **bottom, b)** PPA (squares) and MPA (circles) titration curves for Ti-Beta. Identical reaction conditions were used with 25 mg of the zeolite catalyst.

Section 5.4.3 Limonene Oxidation Energetics and Entropies

To assess limonene oxidation energetics, a catalytic cycle and mechanism based on prior alkene oxidation literature are proposed as shown in Figure 5.8. TBHP is reversibly adsorbed at

TiOR sites (K_T), then activated irreversibly to form TiOOtBu (k_A), followed by by electrophilic, rate limiting attack at limonene (k_E) [10, 63, 160-164]. Limonene is generally assumed to not adsorb directly on TiOx during kinetically relevant steps but here it is assumed to adsorb in the local vicinity (K_L) prior to rate limiting O transfer. The formed epoxide product then reversibly desorbs (K_{LO}). For this hypothesized catalytic cycle and rate limiting step, initial rates (negligible product formation) should follow a rate law:

$$r = \frac{k_A K_T [Ti][TBHP]}{1+\frac{k_A K_T [TBHP]}{k_E K_L [limonene]}} \tag{5.2}$$

Consistent with the rate law, TOFs were zero order in limonene for 1.0 M < [limonene] < 2.0 M with [TBHP] = 0.22 M and zero order in TBHP for 0.44 M < [TBHP] < 2.2 M with [limonene] = 0.2 M. For [limonene] = 0.2 M and [TBHP] = 0.22 M all catalysts examined are nearly zero order in TBHP and positive order in limonene, corresponding to the case where $k_A K_T$[TBHP] >> $k_E K_L$[limonene] and the rate law simplifies to $k_E K_L$[limonene] or k_{app}[limonene]. According to transition state theory and the Eyring equation, the apparent activation enthalpy ($\Delta H^{\ddagger}$app) can be found via equations 5.3 and 5.4 according to Figure 5.8.

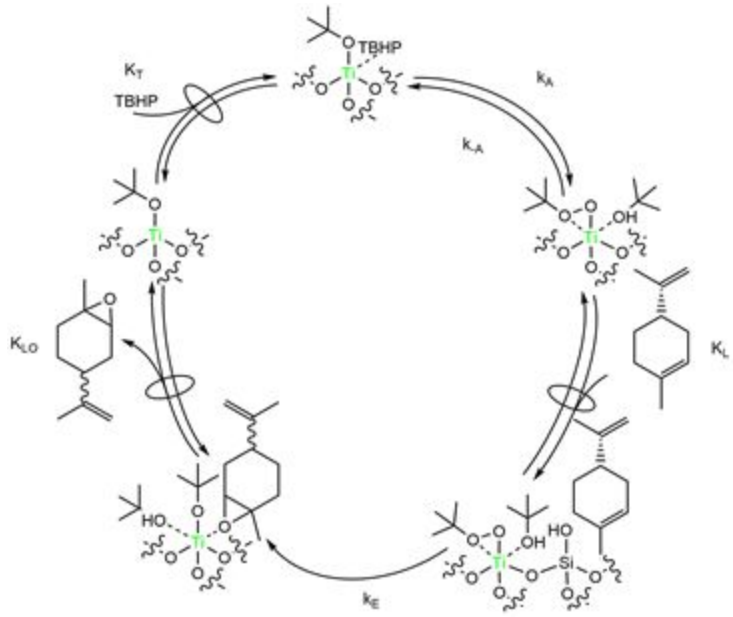

Figure 5.8 Limonene oxidation mechanism with TBHP over M-SiO_2 catalysts [10, 63, 160-164]. Solvent acetonitrile and other spectator molecules are omitted for clarity and brevity.

$$TOF = \frac{k_B T}{h} K_E^{\ddagger} [TBHP][limonene] \tag{5.3}$$

$$K_E^{\ddagger} = e^{\Delta H_E^{\ddagger}/RT} e^{\Delta S_E^{\ddagger}/R} \tag{5.4}$$

Limonene oxidation was run for all Ti catalysts over a temperature range of 35-65 ^{o}C to obtain the apparent activation enthalpy as detailed in Chapter 4. The midpoint of the observed activation enthalpies agrees with typical literature values for limonene oxidation which are between 16-25 kJ/mol. Surprisingly, Ti-Beta has the highest value, 15 kJ/mol higher than Ti-SiO_2 and Ti-SBA-15, when it shows lower apparent activation enthalpies for oxidation reactions with cyclohexene and styrene [63]. In contrast, SiO_2 overcoated materials 2cFO and 2cPO show a significant decrease in $\Delta H^{\ddagger}$app, 6 and 9 kJ/mol lower than the parent Ti-SiO_2 respectively. The apparent activation enthalpies and entropies are collected in Table 5.2.

Apparent activation entropies range from -165 to -240 J/mol-K, indicative of severe entropy loss in the transition state, which must be due to the loss of translational entropy [180-183].

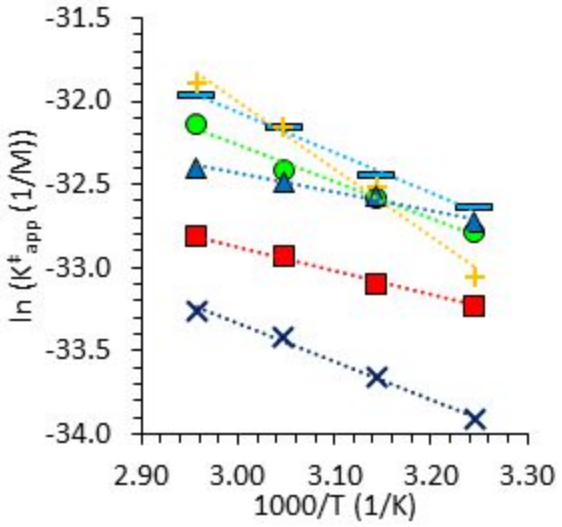

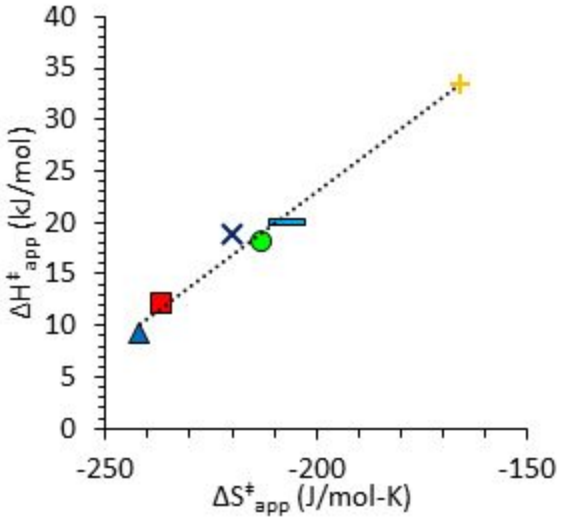

Figure 5.9 top, a) relationship between $K^{\ddagger}_{app}$ and 1/T for Ti-Beta (orange), Ti-SBA-15 (cyan), Ti-SiO_2 (green), 2cPO (blue), 2cFO (red), and 10cPO (dark blue). **bottom, b)** observed compensation effect between activation enthalpies and entropies obtained from Eyring plot.

Figure 5.9 shows a strong compensation effect between apparent activation entropy and enthalpy, with low activation enthalpies being correlated with more negative activation entropy.

The compensation effect occurs because catalysts with lower apparent activation enthalpy typically have stronger adsorption of the reactant, leading to lower apparent activation entropy as the reactant loses more degrees of freedom [181-183]. This is shown in Figure 5.9 for Ti-SiO_2 and 2cPO catalysts. The apparent activation entropy is least negative for Ti-Beta, likely because limonene is larger than its zeolite pores. Here, 2cFO and 2cPO show the strongest evidence for reactant confinement. To remove the compensation effect and parse out contributions from limonene adsorption near the active site vs the intrinsic rate of O transfer, limonene adsorption experiments were performed to obtain zero coverage adsorption entropies and enthalpies.

Equilibrium adsorption isotherms were collected for Ti-SiO_2, 2cFO, 2cPO, Ti-Beta, and SiO_2 at 40 ^{o}C using a literature GC-MS SIM mode analysis that enable the tracking of limonene concentration in acetonitrile precisely even at values on the order of 10^{-7} M [5]. All isotherms showed adsorption uptake linearly depend on concentration below 3 x 10^{-5} M limonene. Langmuir adsorption isotherms were fitted to experimental data using nonlinear least squares fitting for Kads (1/M) and Nmax (mmol/g). Equilibrium adsorption constants were then calculated in the linear regime for all materials between 25 and 55 ^{o}C and the results are shown in Figure 5.10. The strength of limonene adsorption (ΔHads) decreases in the order Ti-SiO_2 > Ti-SBA-15 > Ti-Beta. It is presumed that the ordering is significantly influenced by the increasing difficulty of displacing one or more acetonitrile solvent molecules from the smaller pore materials [63, 184].

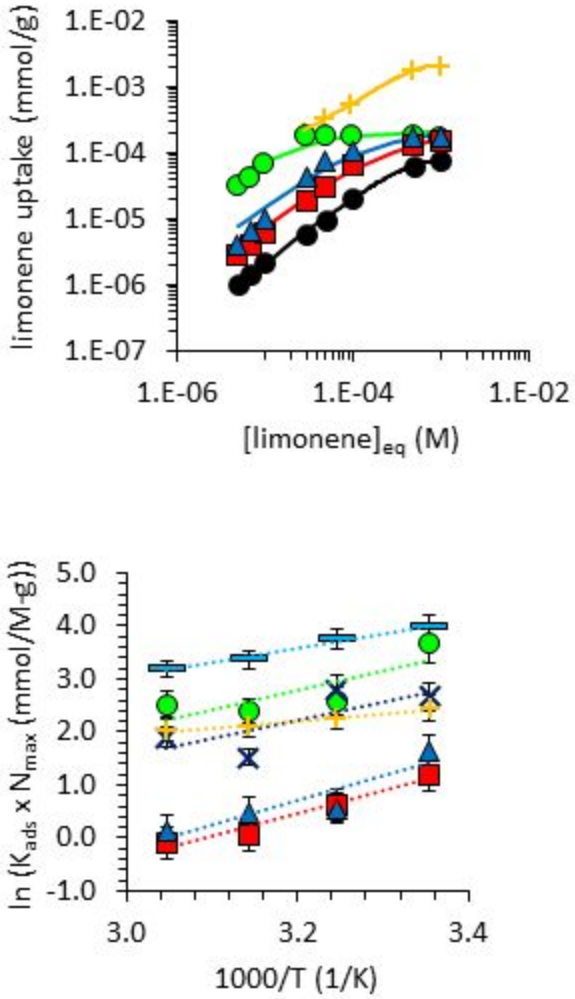

Figure 5.10 top, a) limonene adsorption isotherms obtained at 40 ºC for Ti-Beta (orange), Ti-SiO_2 (green), 2cPO (blue), 2cFO (red), and SiO_2 (black). **bottom, b)** relationship between Henry's law constants and 1/T for Ti-SBA-15 (cyan), Ti-SiO_2 (green), 10cPO (dark blue), Ti-Beta (orange), 2cPO (blue), and 2cFO (red).

The SiO_2 overcoated materials 2cFO and 2cPO demonstrate significantly stronger limonene adsorption than conventional materials, 2cFO and 2cPO materials have 6-9 kJ/mol higher heat of adsorption than their parent Ti-SiO_2 suggesting some level of confinement due to microporous surface SiO_2 domains. Confinement effects have thus far been exclusively observed for materials with an extended pore structure [13, 63]. However, these experiments show that

adsorption stabilization can be imparted by very local effects. This can be compared to modifications where surface silylation was used to increase hydrophobicity [76, 178]. These methods typically involve capping of hydroxyls with $-Si(CH_3)_3$ moieties. Silylated Ti-SiO_2 and Ti-MCM-41 catalyst showed increased stability and activity in alkene oxidation with aqueous H_2O_2, likely because of enhanced adsorption of hydrophobic alkene reactants [76]. Since $\Delta H^{\ddagger}$app is really $\Delta H^{\ddagger}$int plus ΔHads, we should find that these catalyst converge to an identical $\Delta H^{\ddagger}$int once adsorption is accounted for. The adjusted activation enthalpy values are shown in Table 5.2 and all six Ti catalysts tested converge on an intrinsic activation enthalpy of 45 ± 3 kJ/mol. This value agrees well with several DFT models of limonene oxidation with TS-1 and Ti-SiO_2 [186-186].

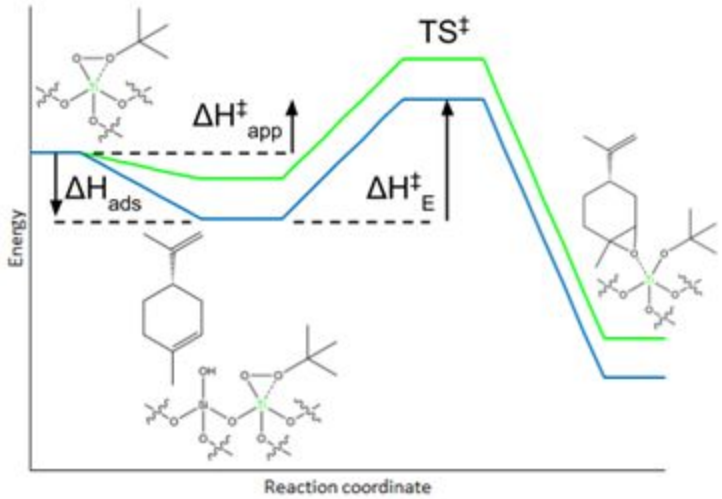

Figure 5.11 limonene oxidation free energy diagram showing four states: (i) activated TBHP with limonene in solution, (ii) physisorbed limonene near activated TBHP, (iii) limonene oxidation transition state, and (iv) limonene oxide chemisorbed on TiOx. This diagram demonstrates that $\Delta H^{\ddagger}$int is the sum of $\Delta H^{\ddagger}$app and ΔHads.

Table 5.2 limonene oxidation and adsorption energies and entropies.

Catalyst	K_{ads}[1] (1/M)	N_{max} (mmol/g)	ΔH_{ads} (kJ/mol)	ΔS_{ads} (J/mol-K)	$\Delta H^{\ddagger}_{app}$ (kJ/mol)	$\Delta S^{\ddagger}_{app}$ (J/mol-K)	$\Delta H^{\ddagger}$[2] (kJ/mol)	$\Delta S^{\ddagger}$ (J/mol-K)
SiO_2	1830	1.27×10^{-4}	n.d.	n.d.	n.d.	n.d.	n.d.	n.d.
Ti-SiO_2	53900	2.08×10^{-4}	-30.1 ± 9	-5.6	18.3	-213	48.4 ± 9	-207
2cFO	3740	2.01×10^{-4}	-36.1 ± 7	-46.8	12.1	-237	48.2 ± 7	-190
10cFO	n.d.	n.d.	n.d.	n.d.	n.d.	n.d.	n.d.	n.d.
2cPO	7500	2.10×10^{-4}	-38.7 ± 12	-49.5	9.2	-242	47.9 ± 12	-193
10cPO	n.d.	n.d.	-29.0 ± 9	n.d.	18.9	-220	47.9 ± 9	n.d.
Ti-SBA-15	n.d.	n.d.	-22.9 ± 5	n.d.	19.9	-207	42.8 ± 5	n.d.
Ti-Beta	2440	3.10×10^{-3}	-11.3 ± 2	28.8	33.5	-166	44.8 ± 7	-195

[1] K_{ads} and N_{max} are calculated from fitted Langmuir isotherms at 40 °C

[2] Relative errors are much higher for heat of adsorption values than apparent activation enthalpies due to the nature of the liquid phase adsorption experiment

Concerning entropies, ΔSads for limonene in Ti-SiO_2 was essentially 0, which follows logically because the nominal 15 nm pore size is far larger than both limonene and acetonitrile, rendering competitive adsorption unimportant. 2cFO and 2cPO have large negative ΔSads indicative of greater steric confinement for limonene than acetonitrile on these surfaces. This provides further evidence that partial SiO_2 surface pores are sufficient to stabilize limonene adsorption. Since these surface structures preferentially stabilize large molecules, they could find use in contaminant removal applications. Once the apparent activation enthalpies are added to the enthalpy of adsorption the intrinsic activation entropy converges on -200 ± 10 J/mol-K. All six Ti catalysts tested converge to identical activation enthalpies and entropies, indicating that

they all have the same active site, and that differences in catalytic performance are related to preferential stabilization of limonene adsorption via steric confinement.

Section 5.4.4 Impacts on Industrial Limonene Oxidation

The studies shown above support the conclusion that fundamentally all the Ti catalysts have the same intrinsic activation enthalpy for oxidation. Although 2cPO has the lowest apparent activation enthalpy due to confinement effects, the entropic penalty it pays means that at 65 ^{o}C, the intrinsic rate of oxidation remains higher for Ti-Beta. However, it should be recalled that these rates are observed for < 2 micron crystallites, and that any industrial scale processing, i.e. to feed bioplastics manufacturing, will require the particles to be pressed into much larger aggregates to ease recovery by filtration or minimize pressure drop through the packed bed [187-188]. Moreover, because epoxides are intrinsically unstable, it is desirable to run reactions at low temperature to minimize side reactions including hydrolysis/alcoholysis, oligomerization, and overoxidation [31-32, 63, 160-164, 187-188]. Therefore, Ti-Beta was pelletized and crushed to 75-150 micron aggregates and compare with high performing 2cPO and benchmark Ti-SiO_2 catalysts at 0 and 65 ^{o}C. The latter catalysts already possess particles in that size range. Limonene oxidation rates for these three catalysts are shown in Figure 5.12 on a per gram basis. When Ti-Beta is pressed to a larger particle size, its activity decreases by a factor of ~ 3.2 because internal diffusion limitations become prevalent.

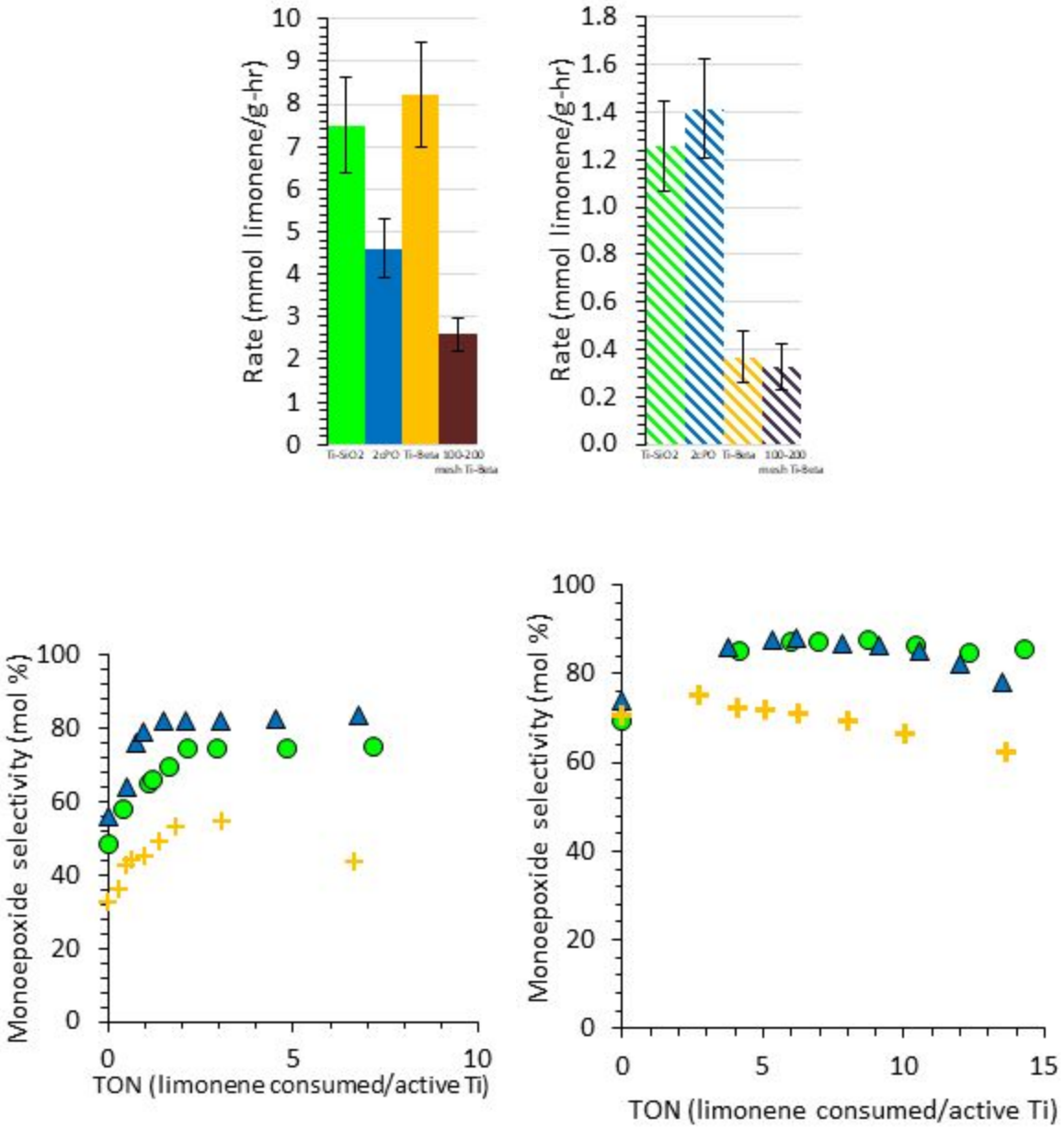

Figure 5.12 top, a) summary of initial limonene oxidation rates at 65 ºC (solid) and 0 ºC (dashed). Particle size was increased for Ti-Beta by pressing into a pellet, crushing with mortar and pestle, and sieving to 100-200 mesh particle size. **bottom, b)** selectivity to limonene monoepoxides (1,2-oxide and 8,9-oxide) for 2cPO (blue), Ti-SiO_2 (green), and Ti-Beta (orange) at 65 ºC (right) and 0 ºC (left).

This makes it significantly slower than the 2cPO and Ti-SiO_2 catalysts. One feature of imparting confinement via SiO_2 deposition is that transport limitations issues are avoided because the active sites remain accessible to the fluid phase at large particle sizes. This can be expressed in terms of an effectiveness factor which compares the observed rate to the intrinsic rate at bulk solution concentrations. Ti-Beta has an effectiveness factor of ~ 0.3 once its particle size is increased to 75-150 micron, while differences between 2cPO and Ti-SiO_2 have been shown to be due to intrinsic differences in adsorption behavior rather than diffusion limitations. This demonstrates the advantage from a mass transport perspective of imparting confinement effects via oxide deposition on nonporous or macroporous catalysts because extended zeolite pore structures inevitably lead to diffusion limitations at industrial particle sizes.

Additionally, industrial applications will demand that conversion is increased to 20-50 % and beyond while maintaining high selectivity to the desired epoxide products that can be polymerized to produce plastics. Selectivity plots as a function of catalyst turnover (TON, mol limonene consumed/mol active Ti) show that Ti-Beta is 20 % less selective to monoepoxides than 2cPO at 65 ^{o}C. 2cPO maintains > 85 mol % selectivity even as conversion increases beyond 50 %. Furthermore, experiments were conducted at 0 ^{o}C to test catalytic performance over a wide range of temperatures. Below RT, 2cPO has the highest TOF because it has the lowest apparent activation enthalpy. More importantly, 2cPO maintains selective performance to monoepoxides with ~85 mol % selectivity at similar TON at 65 ^{o}C and 0 ^{o}C. This catalyst far outperforms Ti-SiO_2 and Ti-Beta which both have lower selectivity at low temperature. These two suffer from undesired activity to allylic oxidation products and these radical mediate processes become prevalent over Ti-Beta at 0 ^{o}C. Higher epoxidation selectivity for 2cPO is directly attributable to

its higher affinity for limonene adsorption. This conclusively demonstrates that SiO_2 overcoated Ti-SiO_2 has unique performance over a wide range of temperature relevant to the industrial alkene oxidation process. Sol gel SiO_2 deposition provides a transport limitation free synthesis handle to tune reactant adsorption on M-SiO_2 catalysts.

Section 5.5 Conclusions on Steric Effects on Limonene Oxidation

A set of supported Ti catalysts with varying support structures and pore sizes were tested in the liquid phase oxidation of biomass derived limonene. DRUV-vis and XANES results reveal the presence of predominantly site isolated, extraframework O_3TiOH, facilitating comparison between the 7 catalysts used here. A modified version of previously established in-situ titration with phosphonic acids was used to obtain active Ti counts and normalize rates per active site (TOF). MPA, with a kinetic diameter ~0.54 nm, showed it was able to titrate active sites located within microporous zeolite environments unlike bulkier PPA. Ti-SBA-15 and Ti-SiO_2 had essentially 100 % catalytically competent TiOx. Partial overcoating of Ti-SiO_2 resulted in 80-90 % active Ti if the template was kept during overcoating or if limited SiO_2 deposition was performed. Conversely, Ti-Beta only had 72 % active Ti even though this material was previously shown to be fully active for cyclohexene oxidation [63]. This means that the limonene reactant significantly exceeds the pore limiting diameter in Beta and cannot access some TiOx contained within micropores.

Limonene oxidation energetics were assessed over temperatures ranging 35-65 ^{o}C and SiO_2 overcoated materials 2cPO and 2cFO had the lowest activation enthalpies of 9 and 12 kJ/mol respectively. These values are 6-9 kJ/mol lower than that for their parent Ti-SiO_2. Conversely, the apparent activation enthalpy for Ti-Beta is 15 kJ/mol higher than that for

Ti-SiO_2. Severe internal diffusion limitations were ruled out for Ti-SiO_2 and the overcoated materials, instead the lower apparent activation enthalpies are due to strong adsorption of limonene. Specifically, the high isosteric heat of adsorption for 2cPO and 2cFO are presumably related to the inclusion of thin, hydrophilic SiO_2 domains surrounding TiOx active sites.

Once the heat of adsorption was added to the apparent activation enthalpy for all supported Ti catalysts, the intrinsic $\Delta H^{\ddagger}_{E}$ for the 6 materials tested converged to 45 ± 3 kJ/mol. This convergence confirms that the catalysts have identical TiOx active sites from the perspective of limonene oxidation, consistent with their similar DRUV-vis and XANES spectra. In addition, a similar convergence was observed between Ti-SiO_2 and Ti-Beta in styrene oxidation with H_2O_2 [63]. From a practical perspective, 2cPO outperforms the fundamentally best catalyst Ti-Beta in terms of direct selectivity and 2cPO has consistent performance over a wide range of temperatures spanning 0-65 ^{o}C. Unlike silylated materials, 2cPO is synthesized in such a way that it can maintain its unique reaction behavior even after multiple regeneration cycles. These materials are suited for future applications including continuous flow conversion or adsorption of bulky substrates, low boiling alkenes, and temperature sensitive reactants.

In future work, the selectivity and activity of styrene oxidation over various SiO_2 supported Ti catalysts should be explored with TBHP as the oxidant. Direct epoxide selectivity and relative rates of epoxidation between various styrenes are highly dependent on active site sterics. Zeolite Ti-Beta is expected to be inactive for 4-benzhydryl styrene oxidation but very selective for styrene oxidation as shown previously in the literature. SiO_2 overcoated Ti-SiO_2 using different templates (i.e. calixarene, Cp*) can maximize epoxide selectivity and activity for certain substituted styrenes. Trimethyl styrene (0.85 nm) should fit well in the templated

overcoat left behind by Cp* decomposition during calcination. Competitive adsorption between acetonitrile and each styrene should be performed for high performing catalyst/styrene pairs to demonstrate how adsorption behavior affects catalytic performance. Styrene adsorption has previously been shown to be more enthalpically favorable in zeolite Beta than in amorphous, mesoporous SiO_2.

Bulky substrate adsorption should be performed on all materials to obtain isotherms at 40 ^{o}C. The isosteric heat of adsorption should also be assessed from 25-55 ^{o}C using a modified GCMS SIM mode method for each reactant. If there are changes in the linear adsorption regime then the isosteric heat of adsorption experiment will need to be adjusted. Low concentration solutions of 5×10^{-6} to 1×10^{-3} M can be easily prepared using the same methodology as section 5.2.

N_2 physisorption, DRUV-vis, ICP-OES, TGA, DRIFTS, and H_2O adsorption should be performed on the silylated catalysts. TGA can be run using the same method as Section 3.2 and desorption of the silylating agents will likely occur between 400-550 ^{o}C based on prior literature. TGA was attempted for use to determine H_2O content but catalyst mass loss was irregular and too low for accurate quantification using the instrument. DRIFTS studies are useful to determine the number of hydroxyls covered by silylation groups. Studies should be performed on the Thermo Nicolet 6700 FT-IR in the CleanCat core facility at Northwestern university. Pretreatment can be conducted for 1 h at 120 ^{o}C in order to remove physisorbed water. Then, spectra can be obtained at 100 ^{o}C with KBr (Sigma-Aldrich, FT-IR grade, ≥ 99 % trace metals basis) serving as the background for the spectrum. Hydroxyl content present at 3745 cm^{-1} can be compared across different samples by normalization using the Si-O-Si overtone band at 670 cm^{-1}.

Hydrophilicity can be determined quantitatively be obtaining H_2O adsorption isotherms at 25 ºC on the Micromeritics 3Flex instrument in the CleanCat core facility at Northwestern university. Pretreatment can be conducted overnight at 120 ºC under vacuum to remove physisorbed water. Nanopure H_2O (18.2 MΩ) can be used as the adsorbate after 3-4 freeze pump thaw cycles on the instrument. The instrument heater allows the water source to be heated to 40 ºC during adsorption experiments. The vapor pressure for water at 40 ºC is 55.3 torr and at 25 ºC is 23.8 torr [197]. Then, water isotherms can be obtained, holding the catalyst at 25 ºC during adsorption. Data points should be collected from P/Po = 10^{-3} to P/Po = 0.5 using a geometric progression to capture the linear regime, monolayer formation, and multilayer formation. The BET equation can be used to fit the isotherm and obtain Vml along with c, which is quantitatively related to the heat of adsorption of water on the surface [197]. Terpineol adsorption isotherms need to be obtained at 40 ºC along with the isosteric heat of adsorption from 25-55 ºC. Solutions of concentrations between 5 x 10^{-6} and 1 x 10^{-3} can be made in acetonitrile using a similar method to Section 5.2. Isotherm equilibration testing and linear regime assessment need to be done for terpineol over Ti-SiO_2 and Ti-Beta to check for differing behaviors from limonene.

Chapter 6. Explorations Using SiO_2 Overcoated Oxides

The research presented in chapter 6.1 is in preparation for submission to Journal of Catalysis with Justin M. Notestein.

Section 6.1 Niobia Silicates as Solid Acid Catalysts

Section 6.1.1 Tetrahydropyranylation with Nb_2O_5-SiO_2

Solid acid catalysts for the production of fine chemicals are continually being developed due to changing industry demands. There is a large need for reactions that selectively protect functional groups while allowing for modifications to be made to other parts of the molecule [189]. Dihydropyran is one such protecting group that selectively caps alcohol groups and functionalities on complex molecules. Typical industrial processes use homogeneous Brønsted acid catalysts for this reaction step, which makes the process very fast but leads to excess disposable waste and hazardous liquid acid waste [190]. Some zeolites and ASAs have been tested for tetrahydropyranylation and have been shown to be fast catalysts [191-192]. However, zeolites have size restrictions for the molecules that can enter the pores. Some large pharmaceutical molecules approaching the size of cholesterol (1-1.5 nm) need capping of select alcohol functional groups. Researchers have found alternatives such as delaminated zeolites or sulfonic acid catalysts that can readily process bulky alcohols.

Separately, niobium silicates have consistently demonstrated promising reactivity and selectivity in many Lewis acid, Brønsted acid, and redox probe reactions [174]. They have proven useful in alcohol dehydration, alkene oxidation, and alkylation. However, their activity and surface structure are still poorly understood. For example, although isolated Lewis acidic Nb

supported on SiO_2 and in zeolite frameworks has shown to be useful for alkene oxidation with H_2O_2, it is not clear where Brønsted acidity originates for these catalysts [49, 174]. A probe reaction that tests specifically for Lewis or Brønsted acidity will provide insight into the speciation of Nb on the surface of different catalysts.

Therefore, in this mini study tetrahydropyranylation was used to interrogate the surface of core-shell Nb_2O_5 @ SiO_2 and SiO_2 @ Nb_2O_5 catalysts. Both systems are model systems for the mixed niobia silicates that have been extensively studied. These materials were analyzed with in-situ pyridine titration in the liquid phase in order to count active sites. Si and Nb content were separately measured so that rates at 70 ^{o}C could be related to the number of interfacial sites. Finally, tentative conclusions were made about surface NbOx and SiOx speciation. Correlations were obtained for DRUV-vis edge energy vs reaction rate for SiO_2 supported NbOx materials with oligomeric species being most active.

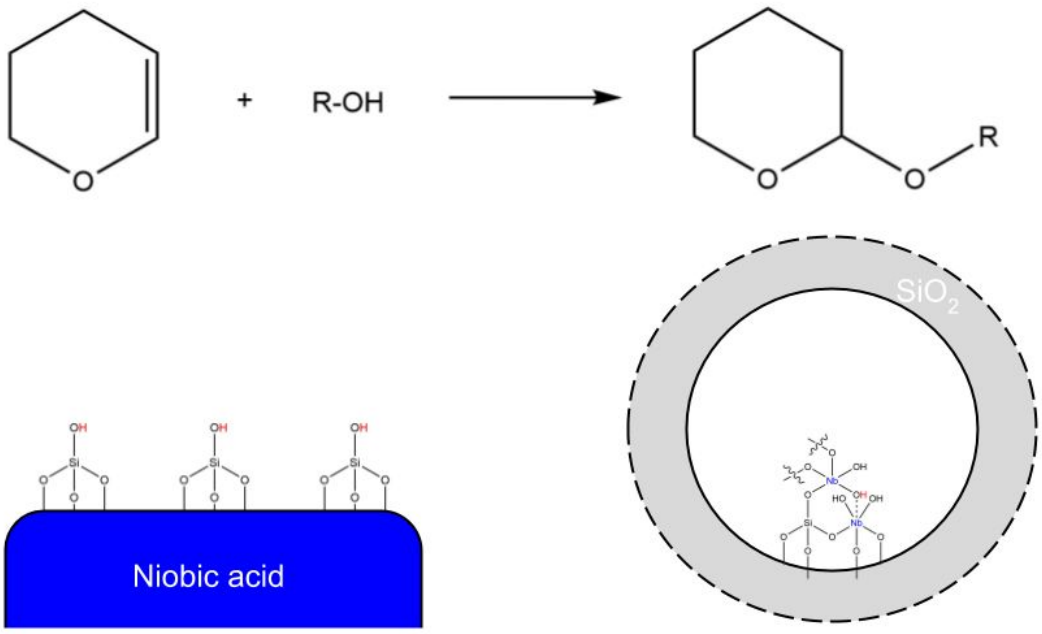

Figure 6.1 Alcohol tetrahydropyranylation using Brønsted acid catalysts. Core-shell niobia silicates include SiO_2 overcoated niobic acid and NbO_5 supported on mesoporous SiO_2.

Section 6.1.2 Catalyst Characterization

N_2 physisorption isotherms were obtained at -196 ºC on the Micromeritics ASAP 2010 instrument for SiO_2 and Niobic acid supported materials. SiO_2 supported materials were dried overnight at 450 ºC under vacuum and niobic acid supported materials were dried at 120 ºC. The Rouquerol consistency criteria were applied and the BET method was used on the adsorption branch of the isotherm to obtain the total surface area. The t-plot method was used to separate out micropore and external surface areas. The BJH method was applied to the desorption branch of the isotherm to assess the mesopore size distribution. Si and Nb content were obtained by ICP-OES. Samples were dissolved with 2-3 drops of concentrated HF, however, calcined Nb_2O_5 was not able to be dissolved using this method. Dissolved solids were then diluted to ~11 mL total. ICP-OES experiments were performed on the Thermo iCAP 7600 instrument in the QBIC facility at Northwestern university. DRUV-vis spectra were obtained under ambient conditions for Nb_2O_5 and SiO_2 supported materials. Edge energies were reported as obtained from the indirect Tauc plot for each material corresponding to their DRUV-vis spectra.

Table 6.1 ICP-OES results for $SiOx/Nb_2O_5$ and $NbOx/SiO_2$ catalysts.

Catalyst	Si content (wt %)	Si content (M/nm^2)	Nb content (wt %)	Nb content (M/nm^2)
SiO_2			<0.01	<0.001
Niobic acid	0.02	n.d.		
Nb_2O_5	0.02	0.04		
1cFO	2.1	4.7		
3cFO	7.0	14		
5cFO	11	24		
1cPO	2.3	5.3		
3cPO	7.9	16		
5cPO	12	27		
0.15 Nb-SiO_2			1.3	0.14
0.30 Nb-SiO_2			2.5	0.29
0.60 Nb-SiO_2			4.8	0.57
1.2 Nb-SiO_2			8.8	1.1
2.3 Nb-SiO_2			16	2.2
4.6 Nb-SiO_2			29	4.5
9.2 Nb-SiO_2			44	8.9
Nb-SBA-15			0.93	0.05

Section 6.1.3 Alcohol Tetrahydropyranylation

Tetrahydropyranylation was run in heptane (Sigma-Aldrich, ReagentPlus, 99 %) solvent at 70 ^{o}C on a Glas-Col digital mixer. 10 mg of catalyst was added to a 20 mL glass vial with 7

mL of heptane. Then, the reactant alcohol was added and the solution was allowed to stir at 500 rpm for 30 min. 1-octanol (Sigma-Aldrich, ACS Reagent, ≥ 99 %), 2-octanol (Sigma-Aldrich, 97 %), cyclooctanol (EMD Millipore, for synthesis), cholesterol (Sigma-Aldrich, Sigma Grade, ≥ 99 %), ethylene glycol (Sigma-Aldrich, ReagentPlus, ≥ 99 %), propylene glycol (Sigma-Aldrich, ≥ 99.5 %, FCC, FG), 1,3-butanediol (Sigma-Aldrich, 98 %), 1,4-butanediol (Sigma-Aldrich, ReagentPlus, 99 %), cis-1,2-cyclohexane diol (Sigma-Aldrich, 99 %), cis-1,2-cyclooctane diol (Sigma-Aldrich, 99 %), and limonene 1,2-diol (Sigma-Aldrich, ≥ 97.0 %) were tested.

After 30 min, dihydropyran (DHP, Sigma-Aldrich, 97 %) was added and the timer was started upon DHP addition. Time points were taken at 0, 5, 10, 15, 30, 60, 120, and 360 min. Initial rates were found to be consistent within 5-10 % error for duplicate trials with different catalysts. Products were identified using a ZB-624 column equipped on a Shimadzu GC-2010 instrument with a FID. Product standards were created by reacting the alcohol to completion with ASA for 24 h. The Shimadzu GCMS QP-2010 was used with a ZB-624 column to identify the two possible products for diols or confirm product ID for mono alcohols. Oligomers of the alcohol and THP ethers were observed to arise over zeolite catalysts at short times due to strong acidity.

Positive controls ASA (Sigma-Aldrich, catalyst support, Grade 135, 6.5 % Al, 100 mesh particle size), amberlyst 15 (Sigma-Aldrich, dry, moisture ≤ 1.5 %), and calcined zeolite ZSM-5 (Zeolyst, CBV 3024E, SiO_2/Al_2O_3 = 30, 405 m^2/g) were used to assess acid strength via rate per H^+. Recycle tests were conducted by recovering spent catalysts after 6 h, washing with 2 x 50 mL of methanol, and drying overnight in an oven at 120 ^oC. Mass balances closed to within 85-105 % by quantifying the reactant alcohol and the product THP ether. In some cases the

GC-MS was used to quantify the DHP reactant, the DHP water ether, and the desired DHP alcohol ether. In some runs, in-stu titration with substituted pyridines was used to count active sites for tetrahydropyranylation. 50 mM solutions of pyridines were created using heptane as the solvent. Pyridine (Sigma-Aldrich, anhydrous, 99.8 %), 2,6-lutidine (Sigma-Aldrich, ReagentPlus, 98 %), and 2,6-di tert butylpyridine (Sigma-Aldrich, ≥ 97 %) were used as titrants. 0-0.16 mL of pyridine solutions were added after the reactant alcohol and allowed to scavenge catalyst protons for 30 min at 500 rpm. Initial rates were obtained for pyridine titrated materials and the active sites were calculated by extrapolating rate vs pyridine added down to 0 rate.

Section 6.1.4 Results and Discussion

Section 6.1.4.1 Catalyst Characterization

Oxide supports Selecto SiO_2 and HY-340 niobic acid were analyzed using N_2 physisorption and trace elemental ICP-OES to assess their morphology and impurity content. SiO_2 contains negligible Nb and has a total surface area of 570 m^2/g with a 6 nm pore size, meaning that confinement effects are not expected. Unlike SiO_2, niobic acid is known to change surface area rapidly via particle sintering during heat treatment. The as-received powder from CBMM was analyzed using TGA up to 800 ^oC to identify crystallization or particle sintering steps. There was a noticeable sharp mass loss at 525 ^oC which cannot be attributed to hydroxyl condensation and desorption. N_2 physisorption of a sample treated at 500 ^oC for 4 h measured 100-110 m^2/g but samples treated at temperatures > 550 ^oC have a low surface area ~5 m^2/g. Unfortunately, niobic acid from CBMM can contain many trace metal contaminants because the powder is not subjected to typical quality control. Trace elemental ICP revealed the presence of 0.03 wt % SiO_2 on the material. This Si may be active for Brønsted acid probe reactions.

Calixarene grafting was performed on niobic acid to template the SiO_2 overcoat and maintain access to interfacial sites between niobic acid and SiO_2. TGA of the grafted material and bare Nb_2O_5 support was measured to show that 0.20 calixarene/nm^2 can be grafted at 80 ^oC. Si ICP-OES was performed on SiO_2 overcoated variants 1cPO, 3cPO, 5cPO, 1cFO, 2cFO, 3cFO, and 5cFO. The effects of including a calixarene template were observed as the Si content for the PO materials was consistently higher than the amount on FO materials even though the same amount of TEOS precursor was used. TEOS grafting efficiency was found to be 87-89 % for PO catalysts and 78-79 % for FO catalysts. Calixarene is known to be a good adsorption site for hydrophobic molecules from aqueous mixtures so the TEOS precursor may have a higher uptake on calixarene grafted materials. DRUV-vis spectra were obtained for these samples to test for changes to surface Nb coordination, however no changes were observed in the spectra as expected. The signal from the Nb_2O_5 bulk can also drown out changes in surface Nb.

Niobium ethoxide was grafted onto SiO_2 at varying surface loadings spanning 0.14-9.2 Nb/nm^2 support. Nb showed quantitative grafting up to 4.6 Nb/nm^2 with a decreased grafting efficiency for the 2 ML material. These varying loadings were used to analyze changes in Lewis and Brønsted acidity as a function of Nb surface nuclearity and oligomerization. DRUV-vis spectra were obtained for all catalysts and the corresponding indirect Tauc plots were used to obtain edge energies. The series spanned between 4.5 eV down to 3.1 eV which is similar to bulk niobic acid [174]. SiO_2 supported Nb species with an edge of 4.0 eV correspond to site isolated, extraframework O_3NbO species [32, 49]. Edge energies between 4.0 and 3.1 eV indicate dimers, oligomers, and 2D chains of NbOx across the surface. Others have claimed that oligomeric species can possess significant Brønsted acidity due to the presence of hydroxyls bridging two

Nb atoms [174]. Nb-SBA-15 was used as a framework Nb reference material and its edge was significantly higher than the others at 4.5 eV. This material possesses O_4NbOH species fully incorporated into the SiO_2 walls and it will act as a purely Lewis acid catalyst.

Section 6.1.4.2 n-Octanol Tetrahydropyanylation Activity

Initial testing was performed using n-octanol with mesitylene as the internal standard. Most alcohols of interest for protection reactions are linear because upgrading reactions are desirable for linear alcohols which are readily obtained from biomass or petroleum processing. Standard catalysts SiO_2, Nb_2O_5, ASA, zeolite Y, and zeolite ZSM-5 were tested using reaction conditions from the literature. SiO_2, as-received niobic acid, and Nb_2O_5 had negligible alcohol conversion even after 6 h of reaction time. This is surprising for Nb_2O_5 because this catalyst has been shown to be active for gas phase reactions including alcohol dehydration. However, this may be because DHP cannot be protonated by Nb_2O_5 and that its Lewis acid sites are responsible for alcohol dehydration. Regardless, ASA steadily converted n-octanol and reached 100 % conversion within 1 h. This moderate solid acid catalyst had high selectivity >97 mol % to the desired THP octyl ether. Stronger Brønsted acid catalysts zeolite Y and zeolite ZSM-5 were tested to observe their behavior and selectivity. Both catalysts convereted n-octanol to 100 % within a few short minutes, however oligomeric byproducts started to form at 5 min and 30 min respectively. Oligomers can be comprised of octanol ethers or ring opened THP octyl ether.

Based on these preliminary results, this reaction is best suited for a moderate or mild Brønsted acid catalyst. Therefore, the first set of catalysts tested were SiO_2 overcoated niobic acid. One, three, and five deposition cycle variants were synthesized with or without the calixarene template. N-octanol capping activity was measured between 0-60 min and the only

observed product for SiO_2 overcoated catalysts was the desired THP ether. Surprisingly, SiO_2 deposition activated the underlying Nb_2O_5 and the overcoated catalysts perform much better than the bare support. Unlike the earlier work on catalytic cracking with SiO_2 overcoated Al_2O_3, tetrahydropyranylation activity trended inversely as a monotonic function of added SiO_2. One cycle variants performed very highly and reached activities of ~10 mmol/g-h for secondary alcohols like 2-octanol and 3-octanol and ~50-80 mmol/g-h for primary alcohols like 1-octanol. These catalysts reached 100 % conversion before 6 h of reaction. However, three deposition cycle variants performed at significantly lower rates than the one deposition cycle variants. This immediately indicated that Brønsted site formation occurs close to the Nb_2O_5 surface. This is not too surprising because Nb should activate silanols by induction similar to Al via Nb-O-Si-OH linkages. Finally, five overcoat cycles was found to kill activity and return the catalyst to SiO_2 like behavior. This shows that the active site region for SiO_2 @ Nb_2O_5 core-shell catalysts is limited to < 2 nm off the surface, with most sites being formed in the monolayer.

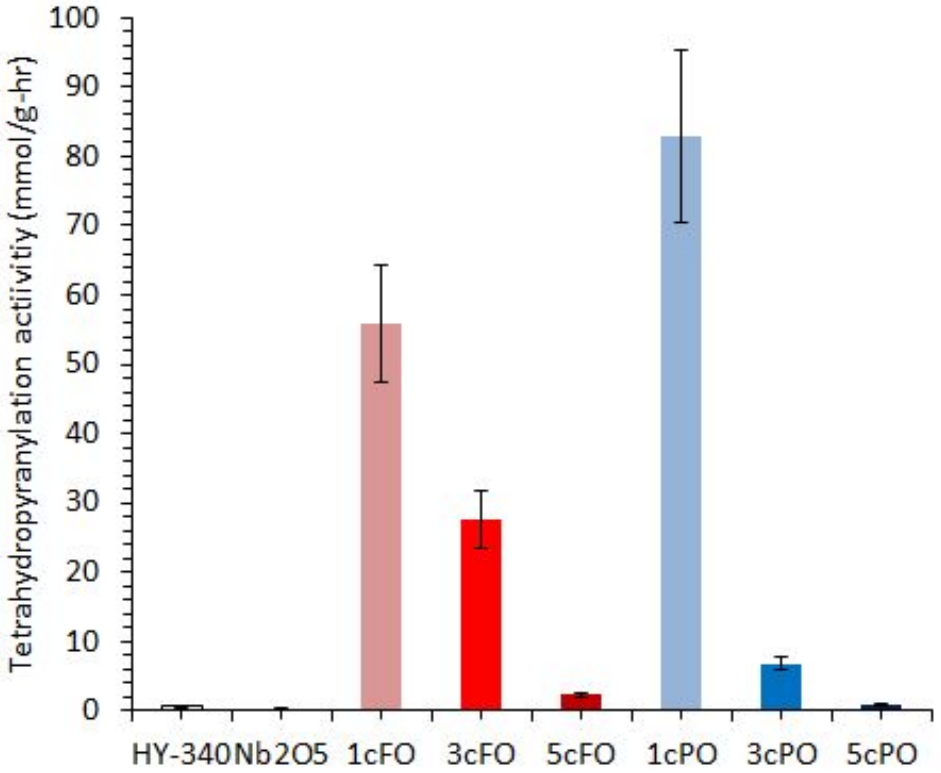

Figure 6.2 n-octanol tetrahydropyranylation activity over SiO_2 overcoated niobic acid. Reaction conditions: 10 mg catalyst, 7 mL heptane, 70 ºC, 0.6 mmol n-octanol, 1.2 mmol DHP, and 0.6 mmol mesitylene. Rates are calculated via linear regression of conversion data from 0-15 min.

Nb_2O_5 @ SiO_2 core-shell catalysts had somewhat different behavioral trends than SiO_2 @ Nb_2O_5. Site isolated NbOx supported on SiO_2 is expected to be strongly Lewis acidic and inactive for the reaction. Consequently, framework Nb in Nb-SBA-15 showed very low activity for n-octanol tetrahydropyranylation even though it has previously been demonstrated to be a fast and selective catalyst for alkene oxidation [49]. A moderately low surface density of 0.30 Nb/nm^2 on SiO_2 had high performance with a conversion rate of 43 mmol/g-h for primary alcohols. Its indirect edge energy is ~3.5 eV which suggests that the active sites are small oligomers of NbOx. This backs up prior claims of Brønsted acidity in small chain oligomers of

Group IV and V oxides. As further Nb is deposited and the Nb surface density increases, the rate decreases drastically with bulk-like materials having low conversion. This is a different active site formation mechanism than SiO_2 @ Nb_2O_5 as the lowest surface loading of Nb on SiO_2 results in an inactive catalyst for tetrahydropyranylation. It is clear that smaller clusters on the order of dimers and trimers can be specifically Brønsted acidic.

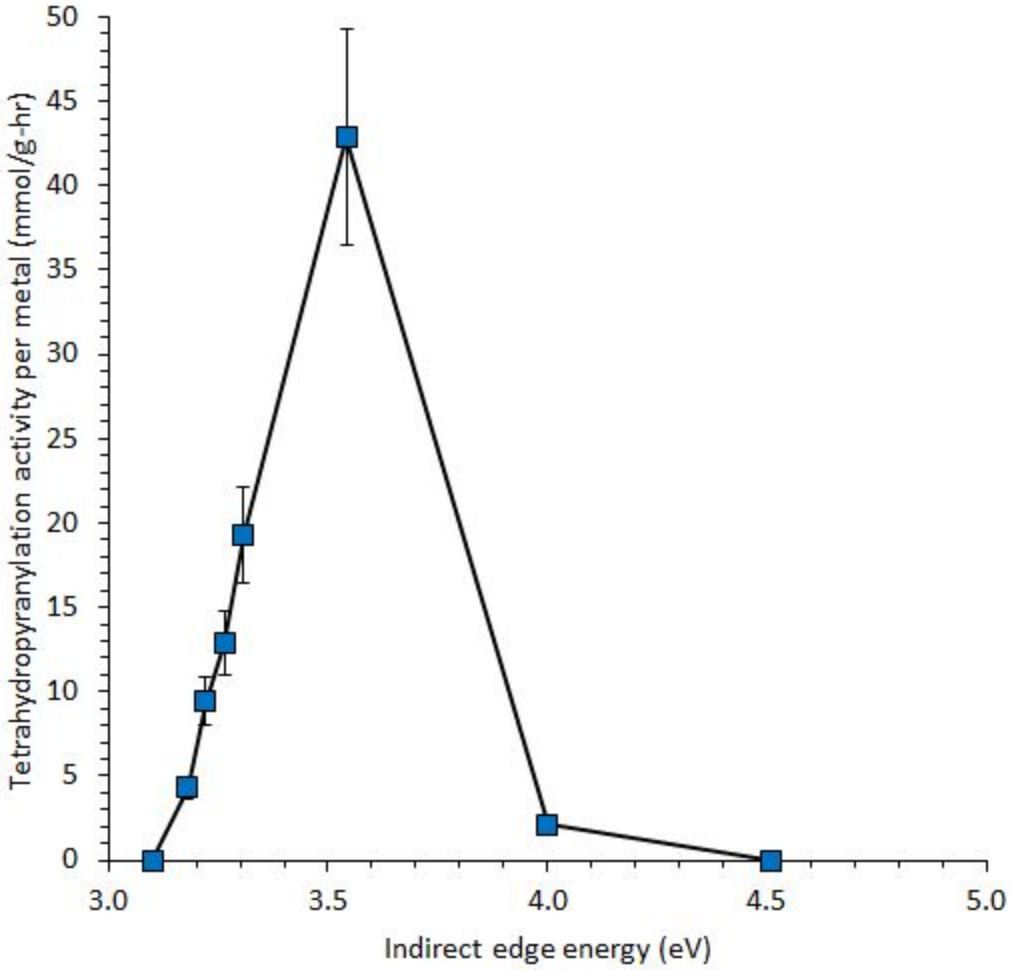

Figure 6.3 n-octanol tetrahydropyranylation activity over SiO_2 supported NbOx. Reaction conditions: 10 mg catalyst, 7 mL heptane, 70 ^{o}C, 0.6 mmol n-octanol, 1.2 mmol DHP, and 0.6 mmol mesitylene.

Section 6.1.4.3 Competitive Tetrahydropyranylation

After assessing the activity and active site requirements for n-octanol tetrahydropyranylation, different alcohols were assessed to measure steric and electronic effects on the reaction. Benzyl alcohol and trimethylbenzyl alcohol were tested over control catalysts to see if added steric bulk leads to decreased activity. Zeolites Y and ZSM-5 surprisingly did not show significant shape selectivity between these two alcohols. This may be due to very high intrinsic rates of reaction which make differential selectivity impossible to quantify. In addition, the presence of strong Brønsted sites on the external surface of the zeolite can preclude shape selective behavior. ASA was selective towards the conversion of benzyl alcohol with a factor of 2.5 higher activity than trimethyl benzyl alcohol. Since ASA is not expected to be shape selective due to its large pore size, this results indicates that steric inductive effects are important since the trimethyl groups decrease the reactivity of the alcohol. We also tried to use the SiO_2 overcoated Lewis acid catalysts from Chapter 5 to see if support sterics could affect the selectivity. Unfortunately, all Ti-SiO_2 based catalysts were 2.1-2.5 x more selective to benzyl alcohol then trimethylbenzyl alcohol. This selectivity is similar to that of ASA.

Another shape selective test used was to probe linear 2-octanol vs cyclic cyclooctanol. One would expect different site strength or different site sterics to affect selectivity between the two alcohols. The series of SiO_2 overcoated niobic acid catalysts were tested using this competitive reaction setup. All catalysts were 67 % selective to cyclooctanol conversion except for 3cFO which was 55 % selective. It is unclear why its active site distribution was different but this suggests the formation of stronger sites or higher adsorption for the linear alcohol as compared to the cyclooctanol. The final test was to try regioselective tetrahydropyranylation

with various diols. Ethylene glycol, propylene glycol, 1,2-butanediol, 1,3-butanediol, and 1,4-butanediol were tested for this. Various SiO_2 overcoated niobic acid catalysts were used to observe differences in regioselectivity. Interestingly, there was a big difference in regioselectivity depending on diol structure. Ethylene glycol, propylene glycol, and 1,2-butanediol were converted at a factor of 2.5 x higher to the primary alcohol ether but 1,3-butanediol was only 1.25 x higher. 1,4-butanediol conversion stopped at the monoether even though 2 equiv. of DHP are present initially in the reaction mixture.

Section 6.1.5 Conclusions on Nb_2O_5-SiO_2 Brønsted Acidity

Two series of core-shell Nb_2O_5-SiO_2 catalysts were synthesized to study catalyst speciation and acidity in probe reactions. SiO_2 deposition on niobic acid occurred readily and the SiO_2 shell prevented Nb_2O_5 particle sintering at high temperature (> 800 ºC). Grafted calixarene templates led to a bright orange powder with a maximum loading of 0.20 calix/nm^2 possible on niobic acid at 80 ºC. The presence of the calixarene template during SiO_2 deposition led to enhanced grafting efficiency with > 90 % of added Si ending up in the final material. Nb_2O_5 deposition on mesoporous SiO_2 was achieved using reactive niobium ethoxide precursors under nominally anhydrous conditions. Surface loadings from 0.14-9.2 Nb/nm^2 were grafted onto the support with nearly 100 % Nb grafting efficiency below 4.6 Nb/nm^2. DRUV-vis spectra of calcined Nb_2O_5 @ SiO_2 demonstrates gradual 2D polymerization and 3D crystallization at high Nb content. Edge energies measured varied between 3.2-4.5 eV depending on dispersion.

Tetrahydropyranylation of primary alcohols (i.e. n-octanol) proceeded quickly over conventional Brønsted acid catalysts ASA, zeolite Y, and zeolite ZSM-5. Lewis acidic and weakly acidic control materials SiO_2, TiO_2, and niobic acid were shown to be inactive for the

reaction. Although the reaction proceeds at the highest rate over zeolites, milder Brønsted acid catalysts were shown to have higher selectivity to the desired tetrahydropyranyl ether. SiO_2 @ Nb_2O_5 catalysts were active for the reaction and activity per g-Nb_2O_5 decreased superlinearly as a function of added Si. This result shows that interfacial sites between Nb_2O_5 and SiO_2 are key to Brønsted acidity on these core-shell catalysts. Further studies using NH_3 and pyridine chemisorption or DNP ^{29}Si NMR will provide insight into the geometry and speciation of these Brønsted sites. Nb_2O_5 @ SiO_2 catalysts were largely inactive for the reaction except at intermediate surface coverages of Nb (i.e. 0.30-1.2 Nb/nm^2). This results indicates that short chain oligomers of NbOx such as dimers and trimers likely possess adequate Brønsted acidity to facilitate tetrahydropyranylation. In-situ titration with substituted pyridines will help quantify active Nb on these catalysts to identify active species.

Tetrashydropyranylation with these core-shell catalysts was attempted on various diols and competitive alcohols to assess whether regioselectivity or shape selectivity can be implemented with these systems. Calixarene grafted variants of SiO_2 @ Nb_2O_5 did not show unique selectivity, ruling out the calixarene template as ineffective at implementing shape selectivity here. Use of smaller template molecules or wide pore zeolites may be prove useful. However, tetrahydropyranylation of symmetric diols (i.e. 1,4-butanediol) show that mild Brønsted acid catalysts allow conversion to stop at the monosubstituted ether. This occurred in spite of the availability of 2 equiv. DHP during the reaction. Future work will be performed to improve the process and potentially upgrade biomass derived diols to platform chemicals such as n-butanol [192-193]. These mild acid catalysts can find use in dehydration, isomerization, and cracking reactions where strong acidity leads to byproduct formation.

Section 6.2 Shape Selective Alkene Oxidation

Section 6.2.1 Shape Selective Catalysis

In many oxidation reactant streams, several components of the mixture are prevalent and the molecules are differently sized. Therefore, zeolites were synthesized to keep out larger contaminant molecules and allow for their facile separation from desired products. However, a more ideal approach is to design each catalyst to work for a specific range of reactant sizes. Prior research on zeolites and mesoporous materials demonstrates that material-reactant pairings are well known for linear and monocyclic molecules. An example of this is alkene oxidation where linear molecules are processed using ZSM-5 (MFI) based catalysts whereas cyclohexyl or benzyl alkenes have higher oxidation rates over Beta (BEA) framework materials [56, 63]. Industry is looking to expand materials development towards materials that show enhanced catalytic activity for bulky reactant molecules such as cyclooctyl and polycyclic compounds.

Homogeneous manganese porphyrin catalysts have been developed to address shape selective applications for alkene oxidation [194-195]. In prior research, the commercially available porphyrin was substituted with bulkier chelating agents to enact steric blockage around the Mn active sites [194-195]. When limonene and other dienes were oxidized with H_2O_2 over these catalysts, the kinetically disfavored but sterically favored oxide product was produced in excess [194]. Regioselectivity shifts were seen from 3:1 in favor of the sterically hindered limonene 1,2-oxide to 4:1 in favor of the less hindered terminal limonene 8,9-oxide. Furthermore, the oxidation of various substituted styrene molecules were tested over sterically hindered porphyrin catalysts [195]. Many styrene variants are available due to their abundant use as polystyrene polymer precursors. Researchers found that bulky 2,6-di tert butyl styrene and

4-benzhydryl styrene were more reactive than styrene over the control catalysts due to more reactive double bonds. However, once steric bulk was added to the manganese site, standard styrene oxide was formed more readily than the bulkier styrene oxides [195].

Therefore, future work on supported Lewis acid catalysts can focus on the design and investigation of shape selective catalysts for the oxidation of substituted styrene molecules. A catalysts class including Ti-SiO_2, Ti-Beta, and a Ti mesoporous material allows us to demonstrate shape selective regimes for each catalyst. A templated SiO_2 overcoated version of Ti-SiO_2, 2cPO is hypothesized to have enhanced shape selectivity for molecules above 0.65 nm and below 0.9 nm. This size range is bigger than the zeolite Beta pore size but lower than the size of the cavity left behind by the Cp* template. Kinetic regimes and reaction pathways are developed for all substituted styrenes to quantify direct epoxidation and allylic oxidation. Finally, ratios of rates can be taken and heat of adsorption can be obtained to understand why alkene oxidation is faster for certain pairs of reactants-materials.

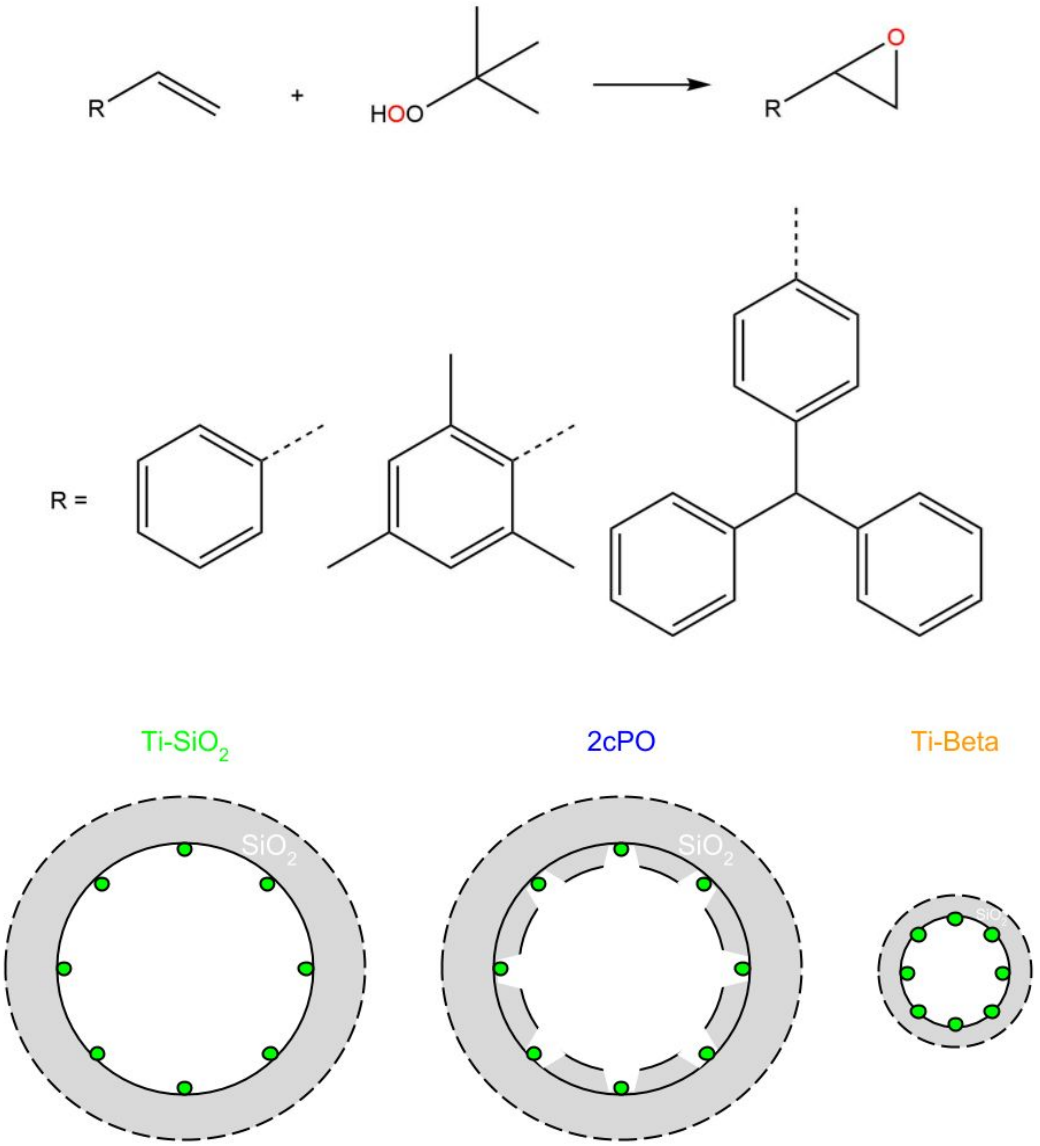

Figure 6.4 epoxidation of substituted styrene reactants with TBHP. Example SiO_2 supported TiOx catalysts, from Chapter 5, with varying sterics at the local and structural level. Various materials are expected to perform highly for differently sized styrenes.

Section 6.2.2 Catalyst Characterization

Catalysts from Chapter 5 should be used further to explore shape selective alkene oxidation. See Section 5.2 for details on physical and active site characterization.

Section 6.2.3 Substituted Styrenes Oxidation

Styrene oxidation was performed in the liquid phase at 65 ^{o}C on a Glas-Col digital mixer shaking at 800 rpm. ~30 mg of Ti-SiO_2 catalyst as loaded into a 20 mL glass vial with 4.6-4.7 mL of acetonitrile. 0.12 mL of styrene (Sigma-Aldrich, ReagentPlus, contains 4-tert-butylcatechol as stabilizer, ≥ 99 %), 0.16 mL of 2,4,6-tri methyl styrene (Sigma-Aldrich, 95 %, < 0.05 % tert-butylcatechol as inhibitor), or 270 mg of 4-benzhydryl styrene (Sigma-Aldrich, 96 %) were added to the vial. All liquid substituted styrenes were filtered over a column of neutral Al_2O_3 immediately before use to remove oxidation inhibitors. The mixture was then shaken for 30 min to allow for styrene adsorption onto the catalysts. 0.2 mL of TBHP in decane or 0.11 mL of 50 wt % aqueous H_2O_2 was added and the timer was started after oxidant addition. Time points were taken at 0, 5, 10, 15, 30, 60, 120, 360, and 1440 min. Mass balances closed to 93-100 % for all substituted styrenes oxidation. The standard styrene mass balance consisted of measuring styrene consumed vs the formation of styrene oxide, phenylacetaldehyde, benzaldehyde, styrene diol, and benzoic acid. Calibration factors for styrene and its products were obtained using calibration curves and authentic standards of each product purchased from Sigma-Aldrich.

2,4,6-tri methyl styrene oxide and 4-benzhydryl styrene oxide were synthesized as standards by reacting the parent styrene with 1 equiv of m-CPBA (Sigma-Aldrich, ≤ 77 %) in acetonitrile for 24 h at RT. Other products were identified on the Shimadzu GCMS QP-2010 and their calibration factors were assumed to be equal to that of the substituted styrene oxide multiplied by the ratio of the unknown products carbon number to that of the styrene oxide. Typical reaction runs were analyzed using a Shimadzu GC-2010 equipped with a FID and a

ZB-624 column for product separation. Nonpolar column TR-1 was found to be inadequate for product analysis due to severe peak tailing. Kinetic fitting was performed in excel according to an alkene oxidation mechanism based on the compilation of prior literature. Concentration profiles of the reactant and products were used to fit effective rate constants. Elementary steps considered are detailed here and the reaction network is shown below:

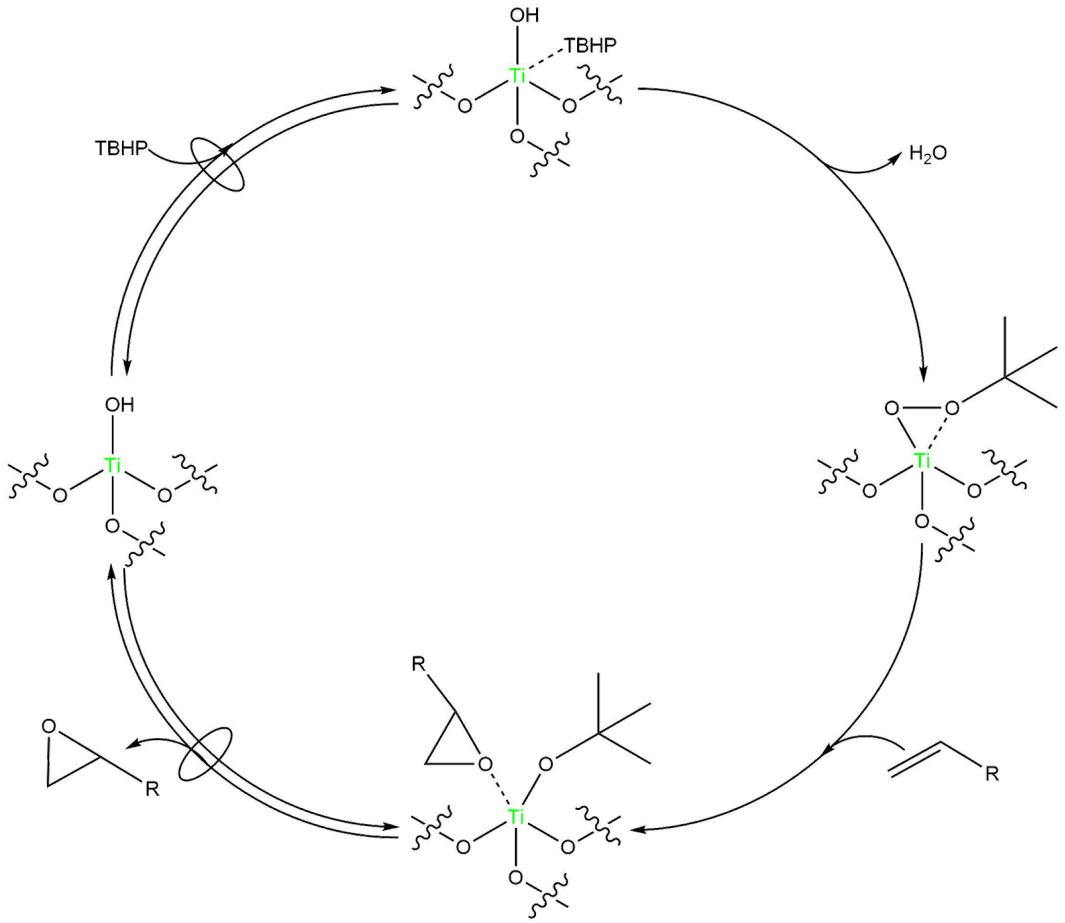

Figure 6.5 proposed styrene epoxidation mechanism with TBHP over extraframework Ti-SiO_2 catalysts. Epoxidation occurs in four steps: (i) reversible adsorption of TBHP, (ii) irreversible TBHP activation with water desorption, (iii) irreversible rate limiting alkene epoxidation, and (iv) reversible epoxide product desorption to generate tert-butoxy capped active site.

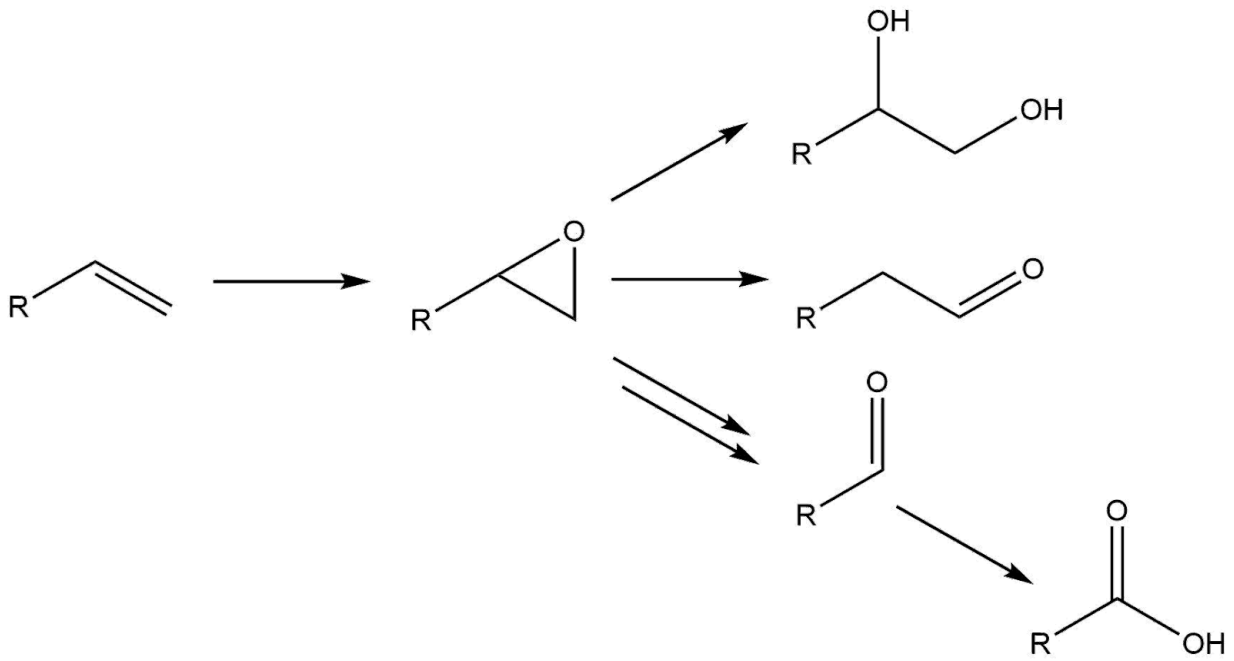

Figure 6.6 substituted styrene epoxidation reaction network. The primary product for styrene oxidation is styrene oxide. Undesired subsequent reactions (i) ring opening, (ii) isomerization, and (iii) decarboxylation lead to (i) styrene diol, (ii) phenylacetaldehyde, and (iii) benzaldehyde. Aldehydes can undergo further oxidation to their respective carboxylic acids.

Section 6.2.4 Results and Discussion

Section 6.2.4.1 Screening Reaction Conditions

The reaction conditions were initially screened to choose which oxidant to use and choose catalyst loading to maximize selectivity to desired epoxide products. Catalysts from Chapter 5 were used without further modification. Ti-SiO_2 was tested for styrene oxidation using either 1.1 equiv. of TBHP or 2 equiv. of aqueous H_2O_2 as done in Chapter 4. Catalytic styrene oxidation rates were similar between the two oxidants with a TOF of 8.1 hr^{-1}. However, the selectivity profiles were very different due to interactions between the oxidant and the TiOx active site. Use of aqueous H_2O_2 led to the formation of undesired benzaldehyde at 55 mol % selectivity, which is believed to be formed via radical mediated allylic oxidation. This follows

the observation from Chapter 4 where Ti-SiO_2 used with aqueous H_2O_2 led to the production of allylic oxidation products carveol, carvone, perillyl alcohol, and perillaldehyde. TBHP use on the other hand leads to > 85 mol % selectivity to direct epoxidation products styrene oxide and phenylacetaldehyde. This is a similar selectivity number to that observed for limonene oxidation in Chapter 5 over the top performing catalysts. Phenylacetaldehyde may be an undesired product but its formation is primarily due to isomerization of the highly reactive styrene oxide primary product [32]. Therefore, TBHP was used as the oxidant for the studies in this section on oxidation of substituted styrene molecules.

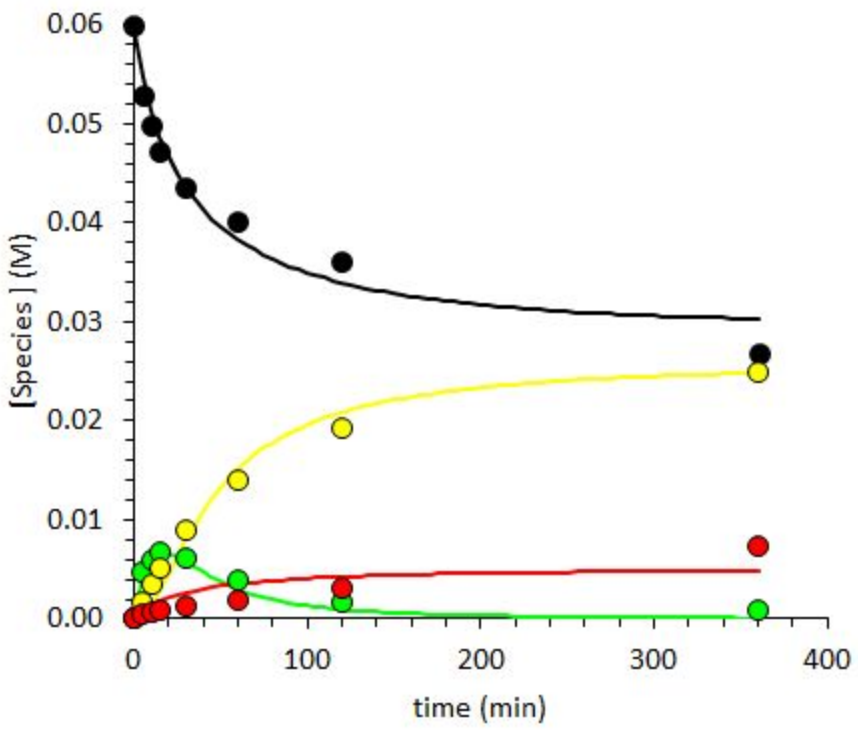

Figure 6.7 Example styrene oxidation selectivity vs. time plot. Reaction conditions were 100 mg Ti-SiO_2, 0.3 mmol styrene, 0.9 mmol TBHP, 4.7 mL acetonitrile, 65 ^oC, 0-6 h. Reactant styrene (black) and products phenylacetaldehyde (yellow), styrene oxide (green), and benzaldehyde (red) are shown.

Then, benzaldehyde formation was analyzed and its rate was compared to the heterogeneous direct epoxidation rate obtained using different masses of catalysts. Comparing runs with 20, 50, and 400 mg of Ti-SiO_2, we observed that benzaldehyde yield is independent of catalyst loading. This suggests that autooxidation of styrene proceeds under these conditions and catalyzed by homogeneous allylic oxidation chemistry [32, 63]. 50 mg catalyst was used to ensure that the benzaldehyde fraction of activity was less than 10 % of the observed initial reactivity. These two tests allowed us to decide on the oxidant and molar concentration of Ti. Future work will involve testing Ti, Nb, and Ta-SiO_2 with H_2O_2 or TBHP to choose the best catalyst/oxidant pairing for styrene oxidation. Group V metals are known to be more active and selective with aqueous H_2O_2 as the oxidant which would be preferred as H_2O_2 use results in the production of H_2O as the byproduct. Efforts to decrease autooxidation to benzaldehyde can be pursued via two routes, (i) decrease the reaction temperature to one with minimum observable rate (~40 ^{o}C) or (ii) add preservatives or radical scavengers to decrease allylic oxidation pathway contributions.

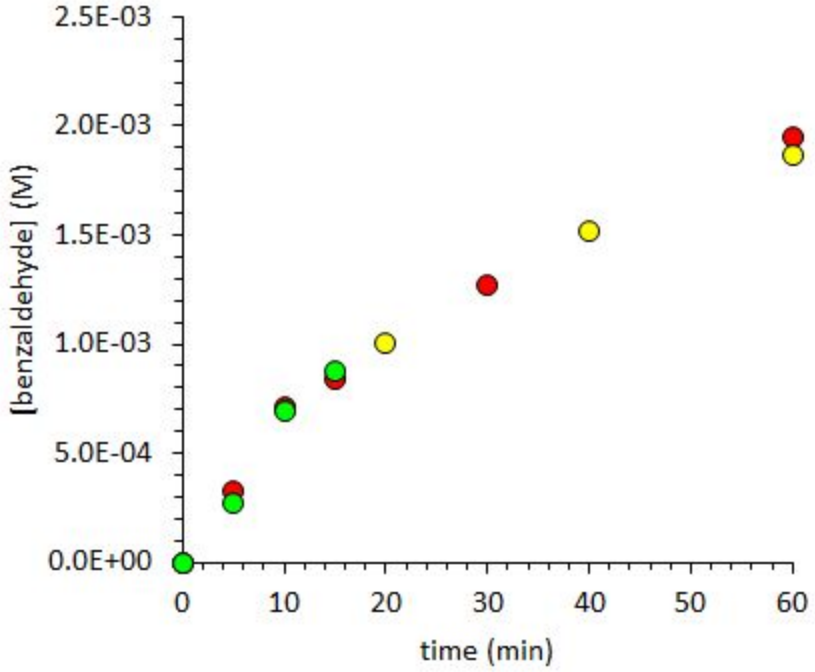

Figure 6.8 benzaldehyde production vs. time plot for varying catalyst weight loadings. Reaction conditions were 20-400 mg of catalyst, 0.3 mmol styrene, 0.9 mmol TBHP, 4.7 mL acetonitrile, 65 ºC, 0-60 min.

Section 6.2.4.2 Substituted Styrene Oxidation Kinetic Fitting

After choosing the appropriate catalyst loading and oxidant, the styrene oxidation reaction network was mapped out for use with Ti-SiO_2 and TBHP. Product selectivity and styrene conversion were tracked for separate runs using 20 mg or 400 mg of catalyst for 24 h. Styrene conversion leveled out around 35 % and 58 % respectively. Benzaldehyde production was observed to increase linearly with time irrespective of catalyst loading, confirming that the catalyst does not perform this chemistry. Styrene oxide production occurred quickly initially but eventually it was consumed in the 400 mg case. Phenylacetaldehyde yield was observed to increase slowly and then further increase past the maximum concentration observed for styrene

oxide. This led to the initial hypothesis that the oxidation proceeds in two steps from styrene to styrene oxide to phenylacetaldehyde. We then fitted a microkinetic model to the observed concentration vs time of products and the styrene reactant using Excel.

Three competing pathways were constructed for TBHP consumption: (i) bimolecular decomposition to produce TBOH, (ii) direct epoxidation to styrene oxide, and (iii) allylic oxidation to benzaldehyde. TBHP concentration was not measured in most runs but the decomposition step was included in the model and assessed using styrene concentration. The model found that TBHP utilization was only 30 % which is typical for styrene oxidation with Ti as styrene is difficult to oxidize using d^0 metals. This reaction network analysis was extended to trimethyl styrene and 4-benzhydryl styrene to quantify effects of reactant inductive electronics on oxidation activity and selectivity.

Surprisingly, trimethyl styrene conversion was slower but much more selective to the desired epoxide. Its fitted rate constants show > 90 % initial selectivity to the epoxide product with very little isomerization to trimethyl phenylacetaldehyde. This selectivity difference is likely due to reactant steric bulkiness because isomerization mechanisms have stricter site requirements as isomerization takes place directly on the metal cation. TBHP utilization for this reaction is lower than for styrene with only 17-20 % of the TBHP going towards direct epoxidation. 4-benzhydryl styrene conversion is slightly faster than trimethyl styrene and still highly selective to 4-benzhydryl styrene oxide. Its epoxide selectivity is nearly 90 % and its TBHP utilization is 35 % which is higher than that for styrene. Regardless of substituents etc. there are both benzaldehyde and phenyl acetaldehyde analogs for substituted styrenes. In

addition, 4-benzhydryl styrene has a unique allylic oxidation position at the carbon between the three benzyl groups and oxidation occurs there to form an alcohol product.

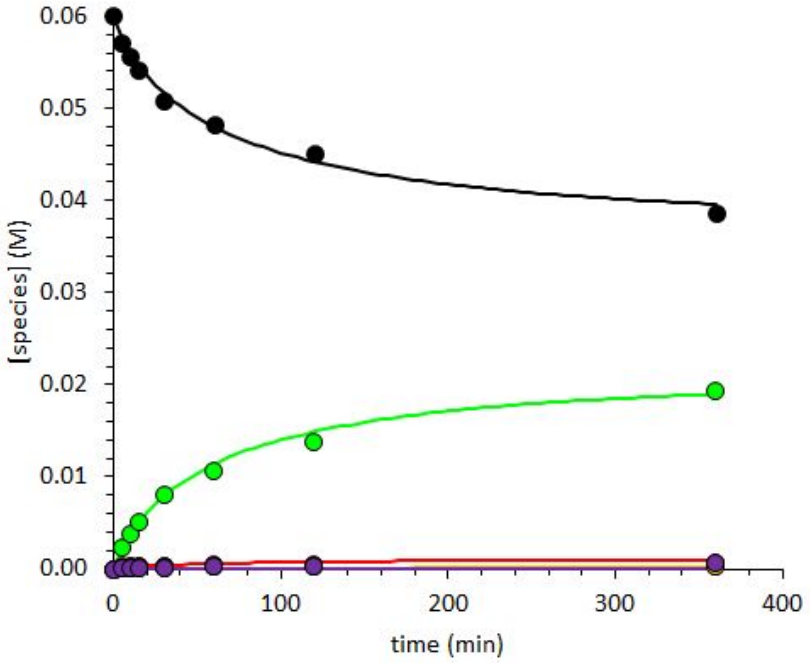

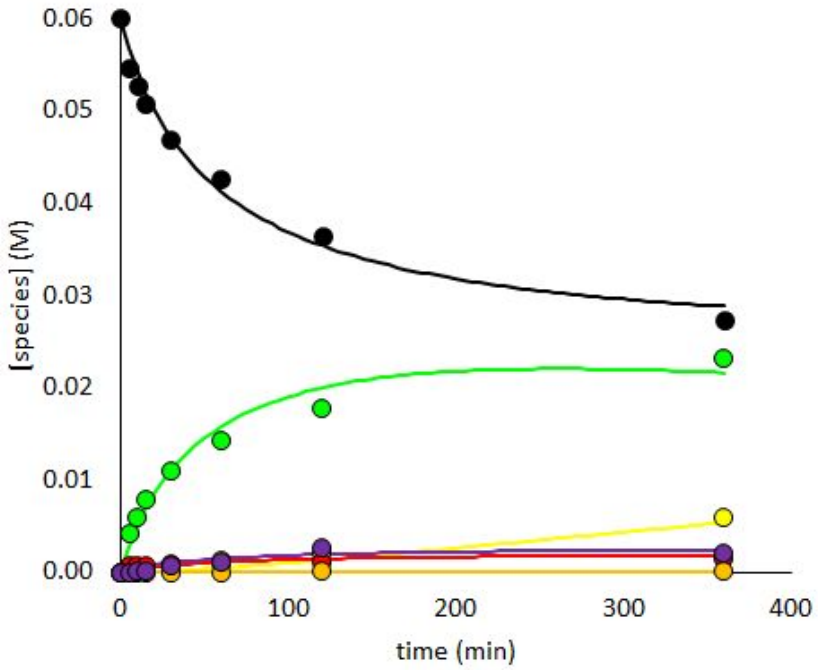

Figure 6.9 substituted styrene oxidation selectivity vs. time plot. Reaction conditions were 100 mg Ti-SiO_2, 0.3 mmol substituted styrene, 0.9 mmol TBHP, 4.7 mL acetonitrile, 65 ^oC, 0-6 h. Reactant substituted styrene (black) and products phenylacetaldehyde (yellow), styrene oxide (green), and benzaldehyde (red) are shown. The top figure is for 2, 4, 6-trimethyl- and the bottom is for 4-benzhydryl- styrene respectively.

Section 6.2.5 Conclusions on Styrene Oxidation with TBHP

Ti-SiO_2 from Chapters 4 and 5 was used to investigate styrene oxidation behavior. Substituted styrenes including 2,4,6-trimethyl styrene and 4-benzhydryl styrene were also assessed for later use as shape selectivity probes. Styrene oxidation was found to proceed via competing allylic oxidation and direct epoxidation pathways similar to those observed for cyclohexene and limonene oxidation. The combination of aqueous H_2O_2 and Ti-SiO_2 led to high allylic oxidation selectivity with 65 mol % to benzaldehyde, use of TBHP led to ~ 85 mol % direct epoxidation products. Benzaldehyde production from styrene with TBHP occurs linearly regardless of catalyst content so at least 6 micromol metal was required to minimize side reaction contributions under these conditions. Styrene oxide was found to be very unstable with phenylacetaldehyde appearing as its isomerization product. Lower reaction temperatures or more hydrophobic catalysts may be used to prevent over conversion of styrene oxide. Substituted styrene molecules did not show the same isomerization behavior and their oxides were stable beyond 50 % reactant conversion. Selectivity to the epoxide product was > 85 mol % for Ti-SiO_2.

Future work will involve the comparison of the catalysts from Chapter 5 in oxidation of various substituted styrene molecules. Direct epoxidation rate constants at 65 ^oC can be compared to identify optimal reactant-catalyst pairings for enhanced activity and selectivity. These trends will be rationalized using liquid phase styrene adsorption measurements to assess

reactant affinity for each catalyst's steric environment. The hypothesis proposes that the best reactant-catalyst pairings will have agreement between kinetic diameter and material pore size.

Section 6.3 Hydrophobic vs Hydrophilic Confinement Effects

Section 6.3.1 Hydrophobic Lewis Acid Catalysts

Bulk oxide materials are known to be highly hydrophilic due to their abundant surface hydroxyls [168]. Zeolites and fumed oxides may be hydrophobic or hydrophilic depending on their synthesis method. Unfortunately, hydrophilicity is an undesirable trait from the standpoint of reactant adsorption during alkene oxidation. Alkenes are significantly less polar and less hydrophilic than the typical reaction solvents acetonitrile and methanol. Therefore, the catalyst design idea that researchers have had is to modify the surface such that the surface becomes hydrophobic. This was crudely and effectively achieved in the 1950s and 1960s by boiling the catalyst in heavy oils or alcohols to cap the surface or plug zeolite pore mouths with nonpolar molecules. These catalysts were found to have higher performance in reaction conditions where water or other polar catalysts poisons were present because adsorption was less favorable.

In the late 1990s and early 2000s, silylation became widely used to cap surface hydroxyl groups with hydrophobic Si containing moieties [76, 178]. This treatment method works for both bulk and mixed oxides. When applied to mesoporous materials such as Ti-SBA-15 and Ti-MCM-41, hydrophobicity was demonstrated by comparing water adsorption values with the original catalyst using TGA at 150 ^{o}C [196]. These catalysts were tested in the liquid phase oxidation of cyclohexene with aqueous H_2O_2. Unlike the original Ti-mesoporous materials, the hydrophobic variants were stable under aqueous conditions and could be recycled for further oxidation reactions [76, 178, 196]. The researchers postulated that this is because H_2O could not

effectively poison Ti active sites with attached silyl groups. They also postulated that the reaction proceed faster due to preferred adsorption of the alkene onto the hydrophobic surface near the active sites.

A developing and wide open line of research involves the use of confined hydrophobic spaces to conduct catalytic reactions. There is much experience in this area for hydrophobic beta zeolites substituted with Sn, Zr, and Ti in Lewis acid probe reactions [33, 76, 171, 178]. These catalysts have found use in biomass conversion as sugar isomerization catalysts because they maintain high activity even in the presence of H_2O solvent. When these materials are made defective or when commercially available hydrophilic zeolites are used in the reactions, rates are lower and deactivation of the active site is observed. In this way, hydrophobic modification to the catalyst surface enables adsorption control and can enhance catalytic activity.

In order to bring hydrophobic confinement effects to a nonporous surfaces, the surface voids provided by a carbonaceous template are needed. Once nanocavities are formed on the surface using a Cp* or Calixarene template, hydrophobic groups can be grafted on surface silanols in order to make the surface hydrophobic. Any voids or surface pores will be stronger adsorption sites for reactant alkenes due to confinement and the increased hydrophobic due to hydrophobic surface groups in close proximity. Therefore, the proposed project is just one step further from the work in Chapter 5. All studied SiO_2 supported Ti catalysts are made hydrophobic by grafting alkylsilane groups onto the surface from an anhydrous alkane solution. Hydrophobic variants of Ti-Beta were provided by the Flaherty group at the University of Illinois Champaign-Urbana. Hydrophobicity is quantifiable by using H_2O adsorption isotherms at

25 ºC to assess adsorption quantity and heat of adsorption. Effects on alkene oxidation can be studied by varying the hydrophilicity of the reactant alkene.

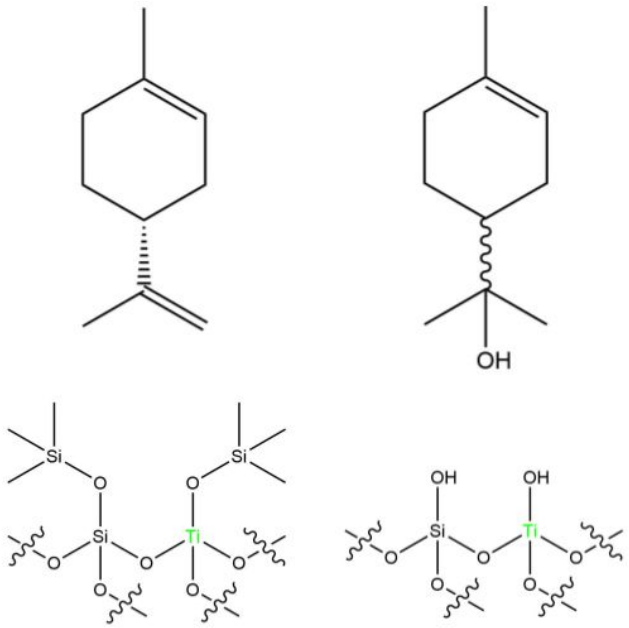

Figure 6.10 hydrophobic (limonene) and hydrophilic (terpineol) alkenes as epoxidation reactants. Conventional Ti-SiO_2 catalysts consist of hydrophilic O_3TiOH active sites but these can be silylated with various silylating agents to add hydrophobicity via attached methyl groups.

Section 6.3.2 Catalyst Characterization

Catalysts were used from Chapter 5 so they were all characterized according to chapter 5.2.

Section 6.3.3 Hydrophilic Alkene Oxidation

Since extensive testing has been performed where the hydrophobic catalysts is exposed to different oxidants, a more unique study is on alkenes of varying hydrophilicity. A stark comparison will be between limonene (hydrophobic) and terpineol (Sigma-Aldrich, mixture of isomers, ≥ 96 %, FG, hydrophilic). Terpineol is somewhat soluble in water whereas limonene is

immiscible with water. ~30 mg of catalyst was added to a 20 mL glass vial along with 4.6 mL of acetonitrile. Then, 0.16 mL of limonene or terpineol is added and the mixture is shaken at 800 rpm on a Glas-Col digital mixer for 30 min. Finally, 0.2 mL of TBHP in decane is added and the timer is started. Time points are taken at 0, 5, 10, 15, 30, 60, 120, 360, and 1440 min. In order to ensure that alkene oxidation is the rate limiting step, the rate order is determined by varying [alkene] and [TBHP] from 0.2-2.2 M while keeping the other reactant constant. Alkene oxidation rates at 65 ^{o}C can be compared, with the hypothesis being that hydrophobic silylated 2cPO has the highest ratio of (kT/kL)/(kT/kL) as compared to the hydroxylated hydrophilic variant. Care will need to be taken in assessing terpineol oxidation as side reactions can occur including allylic oxidation and epoxidation of the terminal double bond. If terpineol caps the surface or binds too strongly, an alternative hydrophilic alkene will need to be tested.

Section 6.3.4 Results and Discussion

H_2O adsorption on the 3Flex instrument was used to assess hydrophilicity of SiO_2 supports with varying pore size between 0.67-9 nm. Prior literature suggests that hydrophilicity is a complex function of pore size, surface area, and synthesis method. SiO_2, MCM-41, SBA-15, and Si-Beta were tested for water adsorption at RT. We found that the adsorption curves for H_2O follow a BET isotherm rather than langmuir as limonene did. The BET equation was used to fit the data and this allowed us to use the BET constant c to calculate the heat of adsorption for water onto the surface. Wide pore SiO_2 was found to be the most hydrophilic with a heat of adsorption around 56 kJ/mol. SBA-15 was second most hydrophilic followed by MCM-41 and Si-Beta. This method can then be extended to hydrophobic zeolites, hydrophobic silylated Ti-SiO_2 catalysts, and other surface modified oxides. We propose that hydrophobic materials are

stronger adsorbents of the alkene reactant limonene so the relative oxidation of limonene vs terpineol will be higher over hydrophobic catalysts.

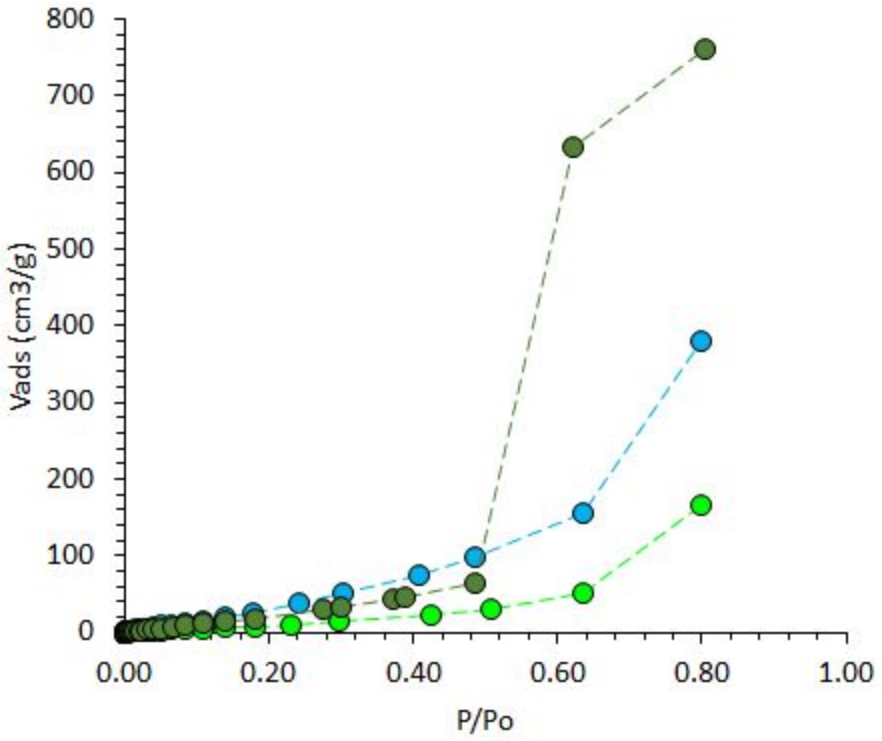

Figure 6.11 H_2O physisorption isotherms on SiO_2 (green), SBA-15 (cyan), and MCM-41 (olive) obtained at 25 ºC. The adsorption branch was fitted using the BET equation to find c and Vml.

Future work can focus on obtaining H_2O and acetonitrile adsorption isotherms for SiO_2 supported Ti catalysts with varying pore sizes and hydrophobicity. Then, we can compare liquid phase alkene adsorption isotherms depending on the hydrophobicity of the alkene. Here we will show that we are tuning adsorption properties to change reaction selectivity and allow SiO_2 overcoated catalysts to have enhanced hydrophobicity around the Ti active sites.

6.3.5 Conclusions on Hydrophobic Confinement Effects

In this preliminary study, catalysts from Chapter 4 and Chapter 5 were used to assess confinement effects on alkenes of varying hydrophilicity. Surface silylation with HMDS was shown to proceed using an anhydrous solution but Lewis acid poisoning was observed by shoulder formation in its DRUV-vis spectra. Method development will be needed to effectively cap all hydroxyl groups without leaving behind catalyst poisons on the surface. Potential silylating agents include those with hindered amines and ethoxy substituents. H_2O and n-hexane physisorption isotherms obtained at RT were used to separately assess catalyst hydrophilicity and hydrophobicity. Hydrophilicity, as measured by the heat of adsorption of H_2O, was found to be inversely dependent on pore size with wide pore SiO_2 > SBA-15 > MCM-41. Alkene oxidation with varying hydrophilic alkenes will be done to assess hydrophobic effects on hydrophilic alkenes with alcohol functionality. Typical substrates such as limonene, styrene, cyclohexene, and cyclooctene will likely adsorb more strongly on hydrophobic surfaces. Overall epoxidation rates and selectivities of these model compounds will be increased due to stronger adsorption. The liquid phase heat of adsorption from acetonitrile can be measured on various hydrophobic catalysts, with the locally confined O_3TiO-Si on 2cPO expected to enact strong hydrophobic confinement effects on alkene reactants.

Chapter 7. Conclusions on SiO_2 Overcoated Oxides

Section 7.1 Recap of Thesis Objectives and Progress

The primary goals for this thesis work were to (i) develop a controlled, liquid-phase deposition method for SiO_2 on bulk metal oxides, (ii) expand SiO_2 deposition to supported Lewis acid catalysts previously studied in the group, and (iii) demonstrate enhanced alkene oxidation behavior with SiO_2 overcoated catalysts. SiO_2 deposition was developed using NanoDur Al_2O_3 to assess the synthesis method and identify levers for tunable deposition. NanoDur was chosen because its regular spherical morphology makes it easy to use TEM for imaging studies. SiO_2-Al_2O_3 core-shell materials are interesting in their own right as moderate Brønsted acid catalysts for alcohol dehydration, catalytic cracking, and alkene isomerization [24-26]. SiO_2 deposition was found to be highly dependent on (i) the number of deposition cycles, (ii) the presence of carbonaceous templates (i.e. calixarenes) on the surface, and (iii) the heating rate used for calcination. TEM imaging revealed a 0.4 nm/deposition cycle growth rate of SiO_2 on the Al_2O_3 support. This can be brought down to the expected monolayer growth rate of 0.3 nm/cycle by using the size of the TEOS precursor to determine the amount of TEOS to add per cycle rather than assuming all hydroxyls are available for grafting.

N_2 physisorption results showed the effects of all three variables on overcoat morphology and density. As more SiO_2 deposition cycles are performed, the relative amounts of external and micropore surface area change drastically. Materials with low SiO_2 content have indiscernible overcoats by TEM or N_2 physisorption but a large microporous SiO_2 shell was observed in samples with high SiO_2 content. The presence of calixarene templates during the overcoat

process leads to the formation of increased external surface area, representing contributions from nanocavity walls. Finally, higher calcination ramp rates during posttreatment led to SiO_2 shell cracking and increased microporosity. These catalysts were characterized with NH_3 TPD, NH_3 DRIFTS, pyridine DRIFTS, and ^{27}Al solid state NMR to identify and quantify accessible Brønsted and Lewis acid sites. The cracked overcoat material showed high activity in TIPB dealkylation comparable to standard ASA and higher than zeolite Y [4]. However, the zeolite had much higher selectivity to deep cracking products cumene and benzene. This core-shell material is active due to its strong acid sites and potential restructuring of the underlying Al_2O_3.

Then, the SiO_2 deposition process was extended to metallocalixarene M-SiO_2 catalysts possessing site isolated Ti, Nb, or Ta atoms supported on mesoporous SiO_2. The deposition was changed to adjust for difficulty in suspending SiO_2 in the ethanol solvent. Overcoating was found to proceed similarly on these materials; N_2 physisorption and M ICP-OES was used to infer changes to catalyst morphology and SiO_2 content. N_2 physisorption shows the emergence of microporosity on the surface with increasing amounts seen on samples with high SiO_2 content. M ICP-OES was then used to infer dilution of the original M-SiO_2 with added SiO_2. These amounts revealed nearly quantitative grafting of TEOS onto the support, as expected from prior Stöber sol-gel synthesis results. DRUV-vis and XANES were used to assess the metal speciation on the surface and identify whether it maintained site isolation or oligomerized during deposition. Both methods confirmed that the M present was predominately site isolated, extraframework $O_3MO(H)$ supported on SiO_2 [32, 61].

Liquid phase limonene oxidation with TBHP was used to assess active site sterics for SiO_2 overcoated Ti-SiO_2. Previous researchers suggested that we could use epoxidation

regioselectivity as a handle for shape selective behavior [10, 51]. Limonene consumption rates at 65 ºC were obtained over 7 supported Ti catalysts and the rate per metal was found to vary widely between 14-60 hr^{-1}. In-situ titration with phosphonic acids per some of the group's previous work measured active Ti content spanning 35-104 % but renormalization per active Ti did not close the gap in rates. TOF values remained between 18-71 hr^{-1} with Ti-Beta as the top performer. Liquid phase limonene adsorption isotherms and enthalpies were obtained using a literature GCMS SIM mode method by tracking ions with m/z = 68, 93, and 67 [5]. SiO_2 overcoated Ti-SiO_2 was found to adsorb limonene strongly (ΔH_{ads} = -39 kJ/mol) and this led to a lower apparent activation enthalpy for limonene oxidation. Its lower apparent $\Delta H^{\ddagger}_{E}$ means that the SiO_2 overcoated catalyst is high performing at desirable low temperature conditions, making it a candidate for deployment in the industrial conversion of biomass alkenes.

Section 7.2 Potential Future Studies in Brief

As with any relatively new field of research, the possibilities for study with SiO_2 overcoated metal oxides are nearly endless. The author wishes that further investigation is done on the preliminary research conducted in Chapter 6. However, there are other larger areas of research that can be explored in terms of materials development, reaction development, characterization into interfacial active sites.

The first class of materials that may be explored is SiO_2 @ MOx core-shell catalysts with the MOx support being Lewis acid oxides comprised of metal cations from Groups IV, V, VI, XIII, and XIV. SiO_2-Al_2O_3 catalysts are well known but it is not clear whether other Lewis acid metals can activate or interact with thin layers of SiO_2. One promising candidate is ZrO_2 as modified versions of ZrO_2 (i.e. sulfated, tungstated) have been shown to possess superacid sites

and be highly active Brønsted acid catalysts [198]. There is potential then to modify these mixed ZrO_2 oxide catalysts with SiO_2 or deposit SiO_2 on bare ZrO_2 to generate interfacial Zr-O-Si-OH sites. In this way the relative acidity can be tuned to change selectivity for reactions where coking and oligomerization proceed over strong acid sites.

Another class of materials to be explored is SiO_2 @ M-SiO_2 expanding beyond the metallocalixarenes containing Group IV and V metals. The synthesis of templated Al or Sn sites on SiO_2 followed by overcoating can bring in interesting comparison with microporous zeolites. Al and Sn-zeolites hold distinction as strong Brønsted and Lewis acid catalysts respectively for industrial consideration [13, 33]. The thought is to incorporate these heteroatoms as extraframework species on SiO_2 and enact confinement around the active site using SiO_2 overcoating. Extraframework O_3AlOH and O_3SnOH can offer different activity and selectivity than the framework species expected for co-gelation synthesis of zeolites. These materials can link up well with advanced characterization being done currently on Sn-Beta to assess extraframework site contribution to various reactions of interest [33, 59].

In terms of reaction development and relevant probe reactions for use with SiO_2 overcoated materials, there are many options from prior literature. Alcohol dehydration, tetrahydropyranylation, and catalytic cracking have been shown to be sensitive to the strength of Brønsted acidity on the catalyst [24-26]. Brønsted acidity can be tuned by changing the underlying MOx support or by using carbonaceous templates to leave behind confined support regions. Future work can focus on tuning catalyst morphology and interfacial site strength to fit reaction requirements. In the three reactions mentioned, product selectivity is sensitive to the pore channel structure in zeolites, leading to coking, oligomerization, and overoxidation. Surface

modified oxides offer interesting combinations of atomic composition unlike that available with current zeolite synthesis technology. Esterification or dimerization reactions proceed at higher rates on the external surface of bulk oxides. Biomass conversion reactions such as furfuryl alcohol dimerization can proceed selectively with the correct active site environment [199].

The second class of reactions to expand for the SiO_2 overcoated Lewis acidic M-SiO_2 includes MPV reduction, aldol condensation, and Baeyer villiger oxidation. Reactions which are more sensitive to sterics, via the entropy term in the rate constant, will show more selectivity differences than the muted differences shown for limonene oxidation. One can imagine for aldol condensation that we can enact transition state selectivity by varying the void space on the surface or by varying the template kinetic diameter. These reactions have been only shown to work for bulk oxides or framework sites in zeolites [200]. This means that we can try different combinations of support MOx and supported M to tune for adsorption and active site requirements for the reaction. The use of Lewis basic oxides as support can encourage adsorption of oxygenates onto the surface. Reaction can then proceed in confined environments at high rate on extraframework active sites unless there are intrinsic restrictions on coordination environment.

References

[1] *La roca magica*: Uses of natural zeolites in agriculture and industry, Frederick A. Mumpton, Proceedings of the National Academy of Sciences, Mar 1999, 96 (7) 3463-3470; DOI: 10.1073/pnas.96.7.3463

[2] Wulff, H. P.; Wattimena, F. Olefin epoxidation, May 3, 1977

[3] Taramasso, M.; Perego, G.; Notari, B. Preparation of porous crystalline synthetic material comprised of silicon and titanium oxides, October 18, 1983

[4] Depositing SiO_2 on Al_2O_3: a route to tunable Brønsted acid catalysts, M. Alexander Ardagh, Zhenyu Bo, Scott L. Nauert, and Justin M. Notestein, ACS Catalysis, 2016, 6 (9) 6156-6164; DOI: 10.1021/acscatal.6b01077

[5] Determination of d-limonene in adipose tissue by gas chromatography–mass spectrometry, Jessica A. Miller, Iman A. Hakim, Cynthia Thomson, Patricia Thompson, H.-H. Sherry Chow, Journal of Chromatography B, 2008, 870 (1) Pages 68-73; DOI: 10.1016/j.jchromb.2008.06.002

[6] Richardson, J. T. *Principles of Catalyst Development*; Springer, 2013

[7] Atomic Description of the Interface between Silica and Alumina in Aluminosilicates through Dynamic Nuclear Polarization Surface-Enhanced NMR Spectroscopy and First-Principles Calculations, Maxence Valla, Aaron J. Rossini, Maxime Caillot, Céline Chizallet, Pascal Raybaud, Mathieu Digne, Alexandra Chaumonnot, Anne Lesage, Lyndon Emsley, Jeroen A. van Bokhoven, and Christophe Copéret, Journal of the American Chemical Society, 2015, *137* (33), 10710-10719; DOI: 10.1021/jacs.5b06134

[8] Chemical and Technical Aspects of Propene Oxide Production via Hydrogen Peroxide (HPPO Process), V. Russo, R. Tesser, E. Santacesaria, and M. Di Serio, Industrial & Engineering Chemistry Research, 2013, *52* (3), 1168-1178; DOI: 10.1021/ie3023862

[9] Quantifying accessible sites and reactivity on titania–silica (photo)catalysts: Refining TOF calculations, Todd R. Eaton, Michael P. Campos, Kimberly A. Gray, Justin M. Notestein, Journal of Catalysis, 2014, *309,* 156-165; DOI: https://doi.org/10.1016/j.jcat.2013.09.015

[10] Molecularly Imprinted Ru Complex Catalysts Integrated on Oxide Surfaces, Satoshi Muratsugu and Mizuki Tada, Accounts of Chemical Research, 2013, *46* (2), 300-311; DOI: 10.1021/ar300142p

[11] Surface Organometallic and Coordination Chemistry toward Single-Site Heterogeneous Catalysts: Strategies, Methods, Structures, and Activities; Christophe Copéret, Aleix Comas-Vives, Matthew P. Conley, Deven P. Estes, Alexey Fedorov, Victor Mougel, Haruki Nagae, Francisco Núñez-Zarur, and Pavel A. Zhizhko, Chemical Reviews, 2016, *116* (2), 323-421; DOI: 10.1021/acs.chemrev.5b00373

[12] Anti-Markovnikov alkene oxidation by metal-oxo–mediated enzyme catalysis, Stephan C. Hammer, Grzegorz Kubik, Ella Watkins, Shan Huang, Hannah Minges, Frances H. Arnold; Science, 2017, 215-218

[13] Compensation between activation entropy and enthalpy in reactions of aromatic hydrocarbons catalyzed by solid acids, Koshiro Nakamura, Ryo Mizuta, Satoshi Suganuma, Etsushi Tsuji, Naonobu Katada, Catalysis Communications, 2017, 102, 103-107; DOI: https://doi.org/10.1016/j.catcom.2017.08.033

[14] The Catalytic Cracking of Cumene, A. Corma & B. W. Wojciechowski, Catalysis Reviews, 2007, 24 (1), 1-65; DOI: 10.1080/03602458208079649

[15] The role of diffusion in alkyl-benzenes catalytic cracking, S. Al-Khattaf, H. de Lasa, Applied Catalysis A: General, 2002, 226 (1–2), 139-153; DOI: https://doi.org/10.1016/S0926-860X(01)00895-X

[16] Synergetic effects of Y-zeolite and amorphous silica-alumina as main FCC catalyst components on triisopropylbenzene cracking and coke formation, N. Hosseinpour, Y. Mortazavi, A. Bazyari, A.A. Khodadadi, Fuel Processing Technology, 2009, 90 (2), 171-179; DOI: https://doi.org/10.1016/j.fuproc.2008.08.013

[17] The effect of crystal size of SAPO-34 on the selectivity and deactivation of the MTO reaction, De Chen, Kjell Moljord, Terje Fuglerud, Anders Holmen, Microporous and Mesoporous Materials, 1999, 29 (1-2), 191-203; DOI: https://doi.org/10.1016/S1387-1811(98)00331-X

[18] Sulfuric acid: Pumping up the volume, Kiefer, D. M. https://pubs.acs.org/subscribe/archive/tcaw/10/i09/html/09chemch.html

[19] http://ostseis.anl.gov/guide/tarsands

[20] PAH distributions in sediments in the oil sands monitoring area and western Lake Athabasca: Concentration, composition and diagnostic ratios, Marlene Evans, Martin Davies, Kim Janzen, Derek Muir, Rod Hazewinkel, Jane Kirk, Dirk de Boer, Environmental Pollution, 2016, 213, 671-687; DOI: https://doi.org/10.1016/j.envpol.2016.03.014

[21] Klaus, J. W.; George, S. M. *Journal of The Electrochemical Society* **2000**, *147* (7), 2658

[22] Ferguson, J. D.; Smith, E. R.; Weimer, A. W.; George, S. M. *Journal of The Electrochemical Society* **2004**, *151* (8)

[23] The chemical vapour and liquid deposition of tetraethoxysilane on ZSM-5, mordenite and beta, R.W. Weber, K.P. Möller, C.T. O'Connor, Microporous and Mesoporous Materials, 2000, 35–36, 533-543; DOI: https://doi.org/10.1016/S1387-1811(99)00248-6

[24] Inorganic Solid Acids and Their Use in Acid-Catalyzed Hydrocarbon Reactions, A. Corma, Chemical Reviews, 1995, *95* (3), 559-614; DOI: 10.1021/cr00035a006

[25] Industrial application of solid acid–base catalysts, Kozo Tanabe, Wolfgang F. Hölderich, Applied Catalysis A: General, 1999, 181 (2), 399-434; DOI: https://doi.org/10.1016/S0926-860X(98)00397-4

[26] Thin silica layer on alumina: evidence of the acidity in the monolayer, Miki Niwa, Naonobu Katada, and Yuichi Murakami, The Journal of Physical Chemistry, 1990, *94* (16), 6441-6445; DOI: 10.1021/j100379a052

[27] Ammonia IRMS-TPD Study on the Distribution of Acid Sites in Mordenite
Miki Niwa, Katsuki Suzuki, Naonobu Katada, Tomonori Kanougi, and Takashi Atoguchi, The Journal of Physical Chemistry B, 2005, *109* (40), 18749-18757; DOI: 10.1021/jp051304g

[28] Acidity Characterization of Amorphous Silica–Alumina, Emiel J.M. Hensen, Dilip G. Poduval, Volkan Degirmenci, D.A J. Michel Ligthart, Wenbin Chen, Françoise Maugé, Marcello S. Rigutto, and J.A. Rob van Veen, The Journal of Physical Chemistry C, 2012, *116* (40), 21416-21429; DOI: 10.1021/jp309182f

[29] Quantification of Strong Brønsted Acid Sites in Aluminosilicates, Emiel J. M. Hensen, Dilip G. Poduval, D. A. J. Michel Ligthart, J. A. Rob van Veen, and Marcello S. Rigutto, The Journal of Physical Chemistry C, 2010, *114* (18), 8363-8374; DOI: 10.1021/jp9106348

[30] State of the art and future challenges of zeolites as catalysts, Avelino Corma, Journal of Catalysis, 216 (1–2), 2003, 298-312; DOI: https://doi.org/10.1016/S0021-9517(02)00132-X

[31] Grafted Metallocalixarenes as Single-Site Surface Organometallic Catalysts, Justin M. Notestein,Enrique Iglesia, and Alexander Katz, Journal of the American Chemical Society, 2004, *126* (50), 16478-16486; DOI: 10.1021/ja0470259

[32] Periodic Trends in Highly Dispersed Groups IV and V Supported Metal Oxide Catalysts for Alkene Epoxidation with H_2O_2, Nicholas E. Thornburg, Anthony B. Thompson, and Justin M. Notestein, ACS Catalysis, 2015, *5* (9), 5077-5088; DOI: 10.1021/acscatal.5b01105

[33] Improved Postsynthesis Strategy to Sn-Beta Zeolites as Lewis Acid Catalysts for the Ring-Opening Hydration of Epoxides, Bo Tang, Weili Dai, Guangjun Wu, Naijia Guan,

Landong Li, and Michael Hunger, ACS Catalysis, 2014, *4* (8), 2801-2810; DOI: 10.1021/cs500891s

[34] Lewis Acids as Catalysts in Oxidation Reactions: From Homogeneous to Heterogeneous Systems, Avelino Corma and and Hermenegildo García, Chemical Reviews, 2002, *102* (10), 3837-3892; DOI: 10.1021/cr010333u

[35] Thomas, J. M.; Raja, R.; Lewis, D. W. Angewandte Chemie International Edition 2005, 44 (40), 6456–6482

[36] Heteroatom-Substituted Delaminated Zeolites as Solid Lewis Acid Catalysts, Xiaoying Ouyang, Son-Jong Hwang, Dan Xie, Thomas Rea, Stacey I. Zones, and Alexander Katz, ACS Catalysis, 2015, *5* (5), 3108-3119; DOI: 10.1021/cs5020546

[37] Williams, C.; Hillmyer, M. *Polymer Reviews* **2008**, *48* (1), 1–10

[38] ***Polym. Chem.***, 2015,**6**, 4497-4559

[39] *Nature* volume 540, pages 354–362 (15 December 2016) doi:10.1038/nature21001

[40] The promise of plastics from plants, Marc A. Hillmyer, *Science,* 17 NOV 2017, 868-870

[41] Aigner, M.; Grosso-Giordano, N. A.; Okrut, A.; Zones, S.; Katz, A. *Reaction Chemistry & Engineering* **2017**, *2* (6), 842–851

[42] Heterogeneous Catalysts for Liquid-Phase Oxidations: Philosophers' Stones or Trojan Horses? Roger A. Sheldon, Martin Wallau, Isabel W. C. E. Arends, and and Ulf Schuchardt, Accounts of Chemical Research, 1998, *31* (8), 485-493; DOI: 10.1021/ar9700163

[43] Activities and stabilities of heterogeneous catalysts in selective liquid phase oxidations: recent developments, I.W.C.E. Arends, R.A. Sheldon, Applied Catalysis A: General, 2001, 212 (1–2), 175-187; DOI: https://doi.org/10.1016/S0926-860X(00)00855-3

[44] Oxidative dehydrogenation of short chain alkanes on supported vanadium oxide catalysts, T. Blasco, J.M.López Nieto, Applied Catalysis A: General, 1997, 157 (1–2), 117-142; DOI: https://doi.org/10.1016/S0926-860X(97)00029-X

[45] Critical Literature Review of the Kinetics for the Oxidative Dehydrogenation of Propane over Well-Defined Supported Vanadium Oxide Catalysts, C. A. Carrero, R. Schloegl, I. E. Wachs, and R. Schomaecker, ACS Catalysis, 2014, *4* (10), 3357-3380; DOI: 10.1021/cs5003417

[46] Enhanced Two-Dimensional Dispersion of Group V Metal Oxides on Silica, Joseph T. Grant, Carlos A. Carrero, Alyssa M. Love, René Verel, and Ive Hermans, ACS Catalysis, 2015, *5* (10), 5787-5793; DOI: 10.1021/acscatal.5b01679

[47] Metal-Catalyzed Epoxidations of Alkenes with Hydrogen Peroxide, Benjamin S. Lane and and Kevin Burgess, Chemical Reviews, 2003, *103* (7), 2457-2474; DOI: 10.1021/cr020471z

[48] Lee, J.; Farha, O. K.; Roberts, J.; Scheidt, K. A.; Nguyen, S. T.; Hupp, J. T. *Chemical Society Reviews* 2009, *38* (5), 1450

[49] Synthesis−Structure–Function Relationships of Silica-Supported Niobium(V) Catalysts for Alkene Epoxidation with H_2O_2, Nicholas E. Thornburg, Scott L. Nauert, Anthony B. Thompson, and Justin M. Notestein, ACS Catalysis, 2016, *6* (9), 6124-6134; DOI: 10.1021/acscatal.6b01796

[50] Maschmeyer, T.; Rey, F.; Sankar, G.; Thomas, J. M. *Nature* **1995**, *378* (6553), 159–162

[51] Niobium metallocenes deposited onto mesoporous silica via dry impregnation as catalysts for selective epoxidation of alkenes, Alessandro Gallo, Cristina Tiozzo, Rinaldo Psaro, Fabio Carniato, Matteo Guidotti, Journal of Catalysis, 2013, 298, 77-83; DOI: https://doi.org/10.1016/j.jcat.2012.11.015

[52] Why are some titanium silicalite-1 samples active and others not? A.J.H.P. van der Pol, A.J. Verduyn, J.H.C. van Hooff, Applied Catalysis A: General, 1992, 92 (2), 113-130; DOI: https://doi.org/10.1016/0926-860X(92)80310-9

[53] Corma, A.; Navarro, M. T.; Pariente, J. P. R. *Journal of the Chemical Society, Chemical Communications* **1994**, No. 2, 147

[54] Zeolite titanium beta as a selective catalyst in the epoxidation of bulky alkenes, J.C. van der Waal, M.S. Rigutto, H. van Bekkum, Applied Catalysis A: General, 1998, 167 (2), 331-342; DOI: https://doi.org/10.1016/S0926-860X(97)00323-2

[55] Hydrothermal and Postsynthesis Surface Modification of Cubic, MCM-48, and Ultralarge Pore SBA-15 Mesoporous Silica with Titanium, Mark S. Morey, Stephen O'Brien, Stephan Schwarz, and Galen D. Stucky, Chemistry of Materials, 2000, *12* (4), 898-911; DOI: 10.1021/cm9901663

[56] Synthesis, Characterization, and Catalytic Activity of Ti-MCM-41 Structures, T. Blasco, A. Corma, M.T. Navarro, J.P. Pariente, Journal of Catalysis, 1995, 156 (1), 65-74; DOI: https://doi.org/10.1006/jcat.1995.1232

[57] Turnover Rates in Heterogeneous Catalysis, M. Boudart, Chemical Reviews, 1995, *95* (3), 661-666; DOI: 10.1021/cr00035a009

[58] Abdelrahman, O. A.; Vinter, K. P.; Ren, L.; Xu, D.; Gorte, R. J.; Tsapatsis, M.; Dauenhauer, P. J. *Catalysis Science & Technology* **2017**, *7* (17), 3831–3841

[59] Distinguishing Active Site Identity in Sn-Beta Zeolites Using 31P MAS NMR of Adsorbed Trimethylphosphine Oxide, Jennifer D. Lewis, Michelle Ha, Helen Luo, Alexandra Faucher, Vladimir K. Michaelis, and Yuriy Román-Leshkov, ACS Catalysis, 2018, *8* (4), 3076-3086; DOI: 10.1021/acscatal.7b03533

[60] Selective Surface Modification of SiO_2−TiO_2 Supports with Phosphonic Acids, P. Hubert Mutin, Vincent Lafond, Aurelian F. Popa, Michel Granier, Laurent Markey, and Alain Dereux, Chemistry of Materials, 2004, *16* (26), 5670-5675; DOI: 10.1021/cm035367s

[61] Eaton, T. R.; Boston, A. M.; Thompson, A. B.; Gray, K. A.; Notestein, J. M. *ChemCatChem* **2014**, *6* (11), 3215–3222

[62] Thornburg, N. E.; Notestein, J. M. *ChemCatChem* **2017**, *9* (19), 3714–3724

[63] Consequences of Confinement for Alkene Epoxidation with Hydrogen Peroxide on Highly Dispersed Group 4 and 5 Metal Oxide Catalysts, Daniel T. Bregante, Nicholas E. Thornburg, Justin M. Notestein, and David W. Flaherty, ACS Catalysis, 2018, *8* (4), 2995-3010; DOI: 10.1021/acscatal.7b03986

[64] Interpretation of Measurements in Experimental Catalysis, P.B. Weisz, C.D. Prater, Advances in Catalysis, 6, 1954, 143-196; DOI: https://doi.org/10.1016/S0360-0564(08)60390-9

[65] Experimental criterion for the absence of artifacts in the measurement of rates of heterogeneous catalytic reactions, Rostam J. Madon and Michel Boudart, Industrial & Engineering Chemistry Fundamentals, 1982, *21* (4), 438-447; DOI: 10.1021/i100008a022

[66] Bell, A. T. *Science* **2003**, *299* (5613), 1688–1691

[67] Size control of SAPO-34 crystals and their catalyst lifetime in the methanol-to-olefin reaction, Norikazu Nishiyama, Masumi Kawaguchi, Yuichiro Hirota, Dung Van Vu, Yasuyuki Egashira, Korekazu Ueyama, Applied Catalysis A: General, 2009, 362 (1–2), 193-199; DOI: https://doi.org/10.1016/j.apcata.2009.04.044

[68] Olsbye, U.; Svelle, S.; Bjørgen, M.; Beato, P.; Janssens, T. V. W.; Joensen, F.; Bordiga, S.; Lillerud, K. P. *Angewandte Chemie International Edition* **2012**, *51* (24), 5810–5831

[69] Mechanisms of the Deactivation of SAPO-34 Materials with Different Crystal Sizes Applied as MTO Catalysts, Weili Dai, Guangjun Wu, Landong Li, Naijia Guan, and Michael Hunger, ACS Catalysis, 2013, *3* (4), 588-596; DOI: 10.1021/cs400007v

[70] Methylbenzenes Are the Organic Reaction Centers for Methanol-to-Olefin Catalysis on H-SAPO-34, Weiguo Song,†, James F. Haw, John B. Nicholas, and Catherine S. Heneghan, Journal of the American Chemical Society, 2000, *122* (43), 10726-10727; DOI: 10.1021/ja002195g

[71] Srivastava, R.; Choi, M.; Ryoo, R. *Chemical Communications* **2006**, No. 43, 4489

[72] Verboekend, D.; Pérez-Ramírez, J. *Catalysis Science & Technology* **2011**, *1* (6), 879

[73] Gueudré, L.; Milina, M.; Mitchell, S.; Pérez-Ramírez, J. *Advanced Functional Materials* **2013**, *24* (2), 209–219

[74] Kang, Z.; Fang, G.; Ke, Q.; Hu, J.; Tang, T. *ChemCatChem* **2013**, *5* (8), 2191–2194

[75] Detailed analysis of sulfur compounds in gasoline range petroleum products with high-resolution gas chromatography–atomic emission detection using group-selective chemical treatment, Árpád Stumpf, Krisztina Tolvaj, Miklós Juhász, Journal of Chromatography A, 1998, 819 (1–2), 67-74; DOI: https://doi.org/10.1016/S0021-9673(98)00444-0

[76] Postsynthesis, Characterization, and Catalytic Properties in Alkene Epoxidation of Hydrothermally Stable Mesoporous Ti-SBA-15, Peng Wu, Takashi Tatsumi, Takayuki Komatsu, and Tatsuaki Yashima, Chemistry of Materials, 2002, *14* (4), 1657-1664; DOI: 10.1021/cm010910v

[77] Controlled Postgrafting of Titanium Chelates for Improved Synthesis of Ti-SBA-15 Epoxidation Catalysts, François Bérubé, Bendaoud Nohair, Freddy Kleitz, and Serge Kaliaguine, Chemistry of Materials, 2010, *22* (6), 1988-2000; DOI: 10.1021/cm9030667

[78] Characterization of the Porous Structure of SBA-15, Michal Kruk, Mietek Jaroniec, Chang Hyun Ko, and Ryong Ryoo, Chemistry of Materials, 2000, *12* (7), 1961-1968; DOI: 10.1021/cm000164e

[79] Silica-Supported, Single-Site Titanium Catalysts for Olefin Epoxidation. A Molecular Precursor Strategy for Control of Catalyst Structure, Jonggol Jarupatrakorn and and T. Don Tilley, Journal of the American Chemical Society, 2002, *124* (28), 8380-8388; DOI: 10.1021/ja0202208

[80] Design and synthesis of heterogeneous catalysts: the thermolytic molecular precursor approach, Kyle L. Fujdala, T. Don Tilley, Journal of Catalysis, 2003, 216 (1–2), 265-275; DOI: https://doi.org/10.1016/S0021-9517(02)00106-9

[81] Grafted Ta–calixarenes: Tunable, selective catalysts for direct olefin epoxidation with aqueous hydrogen peroxide, Natalia Morlanés, Justin M. Notestein, Journal of Catalysis, 2010, 275 (2), 191-201; DOI: https://doi.org/10.1016/j.jcat.2010.07.010

[82] Finding the Rate-Determining Step in a Mechanism: Comparing DeDonder Relations with the “Degree of Rate Control”, Charles T Campbell, Journal of Catalysis, 2001, 204 (2), 520-524; DOI: https://doi.org/10.1006/jcat.2001.3396

[83] A Combined Kinetic−Quantum Mechanical Model for Assessment of Catalytic Cycles: Application to Cross-Coupling and Heck Reactions, Sebastian Kozuch and and Sason Shaik, Journal of the American Chemical Society, 2006, *128* (10), 3355-3365; DOI: 10.1021/ja0559146

[84] Degree of rate control approach to computational catalyst screening, Christopher A. Wolcott, Andrew J. Medford, Felix Studt, Charles T. Campbell, Journal of Catalysis, 2015, 330, 197-207; DOI: https://doi.org/10.1016/j.jcat.2015.07.015

[85] The Brønsted–Evans–Polanyi Relation and the Volcano Plot for Ammonia Synthesis over Transition Metal Catalysts, A Logadottir, T.H Rod, J.K Nørskov, B Hammer, S Dahl, C.J.H Jacobsen, Journal of Catalysis, 2001, 197 (2), 229-231; DOI: https://doi.org/10.1006/jcat.2000.3087

[86] Fernández, E. M.; Moses, P. G.; Toftelund, A.; Hansen, H. A.; Martínez, J. I.; Abild-Pedersen, F.; Kleis, J.; Hinnemann, B.; Rossmeisl, J.; Bligaard, T.; Nørskov, J. K. *Angewandte Chemie International Edition* **2008**, *47* (25), 4683–4686

[87] Norskov, J. K.; Abild-Pedersen, F.; Studt, F.; Bligaard, T. Proceedings of the National Academy of Sciences 2011, 108 (3), 937–943

[88] Simancas, R.; Dari, D.; Velamazan, N.; Navarro, M. T.; Cantin, A.; Jorda, J. L.; Sastre, G.; Corma, A.; Rey, F. Science 2010, 330 (6008), 1219–1222

[89] Preparation of RTH-type zeolites with the amount and/or kind of organic structure-directing agents (OSDA): Are OSDAs indispensable for the crystallization? Masato Yoshioka, Toshiyuki Yokoi, Ming Liu, Hiroyuki Imai, Satoshi Inagaki, Takashi Tatsumi, Microporous and Mesoporous Materials, 2012, 153, 70-78; DOI: https://doi.org/10.1016/j.micromeso.2011.12.024

[90] Pophale, R.; Daeyaert, F.; Deem, M. W. *Journal of Materials Chemistry A* **2013**, *1* (23), 6750

[91] Synthesis and stabilization of small Pt nanoparticles on TiO_2 partially masked by SiO_2, Zhenyu Bo, Sol Ahn, M. Alexander Ardagh, Neil M. Schweitzer, Christian P. Canlas, Omar K. Farha, Justin M. Notestein, Applied Catalysis A: General, 2018, 551, 122-128; DOI: https://doi.org/10.1016/j.apcata.2017.11.017

[92] Adsorption of n-Butanol from Dilute Aqueous Solution with Grafted Calixarenes, Anthony B. Thompson, Sydney J. Cope, T. Dallas Swift, and Justin M. Notestein, Langmuir, 2011, *27* (19), 11990-11998; DOI: 10.1021/la202508q

[93] Size-Selective Synthesis and Stabilization of Small Silver Nanoparticles on TiO_2 Partially Masked by SiO_2, Zhenyu Bo, Todd R. Eaton, James R. Gallagher, Christian P. Canlas, Jeffrey T. Miller, and Justin M. Notestein, Chemistry of Materials, 2015, *27* (4), 1269-1277; DOI: 10.1021/cm504243f

[94] Shear-Thickening Response of Fumed Silica Suspensions under Steady and Oscillatory Shear, Srinivasa R. Raghavan, Saad A. Khan, Journal of Colloid and Interface Science, 1997, 185 (1), 57-67; DOI: https://doi.org/10.1006/jcis.1996.4581

[95] Dehydration of ethanol over zeolites, silica alumina and alumina: Lewis acidity, Brønsted acidity and confinement effects, Thanh Khoa Phung, Loriana Proietti Hernández, Alberto Lagazzo, Guido Busca, Applied Catalysis A: General, 2015, 493, 77-89; DOI: https://doi.org/10.1016/j.apcata.2014.12.047

[96] Selectivity improvement in xylene isomerization, Frank Bauer, Wen-Hua Chen, Horst Ernst, Shing-Jong Huang, Annette Freyer, Shang-Bin Liu, Microporous and Mesoporous Materials, 2004, 72 (1–3), 81-89; DOI: https://doi.org/10.1016/j.micromeso.2004.04.007

[97] Xylene isomerization with surface-modified H-ZSM-5 zeolite catalysts: An in situ IR study, Shourong Zheng, Andreas Jentys, Johannes A. Lercher, Journal of Catalysis, 2006, 241 (2), 304-311; DOI: https://doi.org/10.1016/j.jcat.2006.04.026

[98] Selective formation of para-xylene over H-ZSM-5 coated with polycrystalline silicalite crystals, Dung Van Vu, Manabu Miyamoto, Norikazu Nishiyama, Yasuyuki Egashira, Korekazu Ueyama, Journal of Catalysis, 2006, 243 (2), 389-394; DOI: https://doi.org/10.1016/j.jcat.2006.07.028

[99] Infrared and gravimetric study of an aerosil and a precipitated silica using chemical and hydrogen/deuterium exchange probes, B. A. Morrow and A. J. McFarlan, Langmuir, 1991, *7* (8), 1695-1701; DOI: 10.1021/la00056a022

[100] Titania-Silica Mixed Oxides: I. Influence of Sol-Gel and Drying Conditions on Structural Properties, D.C.M. Dutoit, M. Schneider, A. Baiker, Journal of Catalysis, 1995, 153 (1), 165-176; DOI: https://doi.org/10.1006/jcat.1995.1118

[101] Titania Silica Mixed Oxides: II. Catalytic Behavior in Olefin Epoxidation, R. Hutter, T. Mallat, A. Baiker, Journal of Catalysis, 153 (1), 177-189; DOI: https://doi.org/10.1006/jcat.1995.1119

[102] Effect of polymorphic phase transformations in Al_2O_3 film on oxidation kinetics of aluminum powders, Mikhaylo A. Trunov, Mirko Schoenitz, Xiaoying Zhu, Edward L. Dreizin, Combustion and Flame, 2005, 140 (4), 310-318; DOI: https://doi.org/10.1016/j.combustflame.2004.10.010

[103] Relationship between acid amount and framework aluminum content in mordenite, Masahiko Sawa, Miki Niwa, Yuichi Murakami, Zeolites, 1990, 10 (6), 532-538; DOI: https://doi.org/10.1016/S0144-2449(05)80308-2.

[104] Controlling the Isolation and Pairing of Aluminum in Chabazite Zeolites Using Mixtures of Organic and Inorganic Structure-Directing Agents, John R. Di Iorio and Rajamani Gounder, Chemistry of Materials, 2016, *28* (7), 2236-2247; DOI: 10.1021/acs.chemmater.6b00181

[105] Periodic Trends in Olefin Epoxidation over Group IV and V Framework-Substituted Zeolite Catalysts: A Kinetic and Spectroscopic Study, Daniel T. Bregante and David W. Flaherty, Journal of the American Chemical Society, 2017, *139* (20), 6888-6898; DOI: 10.1021/jacs.7b01422

[106] Koval, C. A. *Basic Research Needs for Catalysis Science;* US Department of Energy, Office of Basic Energy Sciences: Gaithersburg, MD, 2017; 1-76

[107] Structure and Properties of Amorphous Silicoaluminas. II. Lewis and Brønsted Acid Sites, J. J. Fripiat, A. Léonard, and J. B. Uytterhoeven, The Journal of Physical Chemistry, 1965, *69* (10), 3274-3279; DOI: 10.1021/j100894a009

[108] Haag, W. O.; Lago, R. M.; Weisz, P. B. *Nature* **1984**, *309* (5969), 589–591

[109] Dealumination of zeolites III. Effect of extra-framework aluminum species on the activity, selectivity, and stability of Y zeolites in n-heptane cracking, Q.L. Wang, G. Giannetto, M. Guisnet, Journal of Catalysis, 1991, 130 (2), 471-482; DOI: https://doi.org/10.1016/0021-9517(91)90129-R

[110] Coutanceau, C.; Silva, J. D.; Alvarez, M.; Ribeiro, F.; Guisnet, M. *Journal de Chimie Physique* **1997**, *94*, 765–781

[111] Comparison of the dealumination of zeolites beta, mordenite, ZSM-5 and ferrierite by thermal treatment, leaching with oxalic acid and treatment with SiCl4 by 1H, 29Si and 27Al MAS NMR, M Müller, G Harvey, R Prins, Microporous and Mesoporous Materials, 2000, 34 (2), 135-147; DOI: https://doi.org/10.1016/S1387-1811(99)00167-5

[112] Decomposition of 2-propanol over alkali cation exchanged zeolites, Tatsuaki Yashima, Hisashi Suzuki, Nobuyoshi Hara, Journal of Catalysis, 1974, 33 (3), 486-492; DOI: https://doi.org/10.1016/0021-9517(74)90295-4

[113] Measurement of the acidity of various zeolites by temperature-programmed desorption of ammonia, Carmela V. Hidalgo, Hirofumi Itoh, Tadashi Hattori, Miki Niwa, Yuichi Murakami, Journal of Catalysis, 1984, 85 (2), 362-369; DOI: https://doi.org/10.1016/0021-9517(84)90225-2

[114] Formation of acid sites in amorphous silica-alumina, E.J.M. Hensen, D.G. Poduval, P.C.M.M. Magusin, A.E. Coumans, J.A.R. van Veen, Journal of Catalysis, 2010, 269 (1), 201-218; DOI: https://doi.org/10.1016/j.jcat.2009.11.008

[115] Mouat, A. R.; George, C.; Kobayashi, T.; Pruski, M.; Van Duyne, R. P.; Marks, T. J.; Stair, P. C. *Angewandte Chemie* **2015**, *127* (45), 13544–13549

[116] Direct Spectroscopic Evidence for Isolated Silanols in SiOx/Al2O3 and Their Formation Mechanism, Aidan R. Mouat, Takeshi Kobayashi, Marek Pruski, Tobin J. Marks, and Peter C. Stair, The Journal of Physical Chemistry C, 2017, *121* (11), 6060-6064; DOI: 10.1021/acs.jpcc.6b11196

[117] Is the bet equation applicable to microporous adsorbents? J. Rouquerol, P. Llewellyn, F. Rouquerol, Studies in Surface Science and Catalysis, 2007, 160, 49-56; DOI: https://doi.org/10.1016/S0167-2991(07)80008-5

[118] Application of Consistency Criteria To Calculate BET Areas of Micro- And Mesoporous Metal–Organic Frameworks, Diego A. Gómez-Gualdrón, Peyman Z. Moghadam, Joseph T. Hupp, Omar K. Farha, and Randall Q. Snurr, Journal of the American Chemical Society, 2016, *138* (1), 215-224; DOI: 10.1021/jacs.5b10266

[119] http://adsorption.org/awm/ads/meso/plots/MCM-16.htm#alfa-s (accessed May 16, 2018)

[120] Calculation of Flame Ionization Detector Relative Response Factors Using the Effective Carbon Number Concept, Scanlon; T.Willis, J.; E., D. Journal of Chromatographic Science, Oxford Academic; DOI: https://doi.org/10.1093/chromsci/23.8.333

[121] Morphological and electronic properties of ultrathin crystalline silica epilayers on a Mo(112) substrate, Schroeder, T. and Giorgi, J. B. and Baumer, M. and Freund, H.-J. Phys. Rev. B, 2002, 66 (16), 165422; DOI: 10.1103/PhysRevB.66.165422

[122] Catalyst stabilization by stoichiometrically limited layer-by-layer overcoating in liquid media, Florent Héroguel, Benjamin P. Le Monnier, Kristopher S. Brown, Juno C. Siu, Jeremy S. Luterbacher, Applied Catalysis B: Environmental, 2017, 218, 643-649; DOI: https://doi.org/10.1016/j.apcatb.2017.07.006

[123] Controlled deposition of titanium oxide overcoats by non-hydrolytic sol gel for improved catalyst selectivity and stability, Florent Héroguel, Luca Silvioli, Yuan-Peng Du, Jeremy S. Luterbacher, Journal of Catalysis, 2018, 358, 50-61; DOI: https://doi.org/10.1016/j.jcat.2017.11.023

[124] Canlas, C. P.; Lu, J.; Ray, N. A.; Grosso-Giordano, N. A.; Lee, S.; Elam, J. W.; Winans, R. E.; Duyne, R. P. V.; Stair, P. C.; Notestein, J. M. *Nature Chemistry* **2012**, *4* (12), 1030–1036

[125] Alothman, Z. *Materials* **2012**, *5* (12), 2874–2902

[126] Aging of Silica-Alumina Cracking Catalyst. I. Kinetics of Structural Changes by Heat and Steam, W. G. Schlaffer, C. Z. Morgan, and J. N. Wilson, The Journal of Physical Chemistry, 1957, *61* (6), 714-722; DOI: 10.1021/j150552a003

[127] Effect of Boehmite Crystallite Size and Steaming on Alumina Properties, M. L. Guzmán-Castillo, X. Bokhimi, A. Toledo-Antonio, J. Salmones-Blásquez, and F. Hernández-Beltrán, The Journal of Physical Chemistry B, 2001, *105* (11), 2099-2106; DOI: 10.1021/jp001024v

[128] Exploring Pore Formation of Atomic Layer-Deposited Overlayers by in Situ Small- and Wide-Angle X-ray Scattering, Tao Li, Saurabh Karwal, Bachir Aoun, Haiyan Zhao, Yang Ren, Christian P. Canlas, Jeffrey W. Elam, and Randall E. Winans, Chemistry of Materials, 2016, *28* (19), 7082-7087; DOI: 10.1021/acs.chemmater.6b03222

[129] Surface Acidity of Solid Catalysts, H.A. Benesi, B.H.C. Winquist, Advances in Catalysis, Academic Press, 1979, 27, 97-182; DOI: https://doi.org/10.1016/S0360-0564(08)60055-3

[130] Microcalorimetric study of the acidity and basicity of metal oxide surfaces Aline Auroux and Antonella Gervasini, The Journal of Physical Chemistry, 1990, *94* (16), 6371-6379; DOI: 10.1021/j100379a041

[131] Coking, aging, and regeneration of zeolites: II. Deactivation of H-Y zeolite during n-heptane cracking, P. Magnoux, P. Cartraud, S. Mignard, M. Guisnet, Journal of Catalysis, 1987, 106 (1), 235-241; DOI: https://doi.org/10.1016/0021-9517(87)90227-2

[132] Barzetti, T.; Selli, E.; Moscotti, D.; Forni, L. *Journal of the Chemical Society, Faraday Transactions* **1996**, *92* (8), 1401

[133] H-ZSM-5 Zeolites with Different SiO_2/Al_2O_3 Ratios. Characterization and NH_3 Desorption Kinetics, Abdullah S. Al-Dughaither, and Hugo de Lasa, Industrial & Engineering Chemistry Research, 2014, 53 (40), 15303-15316; DOI: 10.1021/ie4039532

[134] Characterization of Catalytically Active Sites on Aluminum Oxides, Hydroxyfluorides, and Fluorides in Correlation with Their Catalytic Behavior, A. Hess, E. Kemnitz, Journal of Catalysis, 1994, 149 (2), 449-457; DOI: https://doi.org/10.1006/jcat.1994.1311

[135] Aluminum incorporation into high silica zeolites, R.M. Dessau, G.T. Kerr, Zeolites, 1984, 4 (4), 315-318; DOI: https://doi.org/10.1016/0144-2449(84)90005-8

[136] Role of the acid-base properties of aluminas, modified γ-alumina, and silica-alumina in 1-butanol dehydration, P. Berteau, S. Ceckiewicz, B. Delmon, Applied Catalysis, 1987, 31 (2), 361-383; DOI: https://doi.org/10.1016/S0166-9834(00)80702-2

[137] Cracking Activity and Hydrothermal Stability of MCM-41 and Its Comparison with Amorphous Silica-Alumina and a USY Zeolite, A. Corma, M.S. Grande, V. Gonzalez-Alfaro,

A.V. Orchilles, Journal of Catalysis, 1996, 159 (2), 375-382; DOI: https://doi.org/10.1006/jcat.1996.0100

[138] FTIR study of the silanol groups in dealuminated HY zeolites: Nature of the extraframework debris, A. Janin, M. Maache, J.C. Lavalley, J.F. Joly, F. Raatz, N. Szydlowski, Zeolites, 1991, 11 (4), 391-396; DOI: https://doi.org/10.1016/0144-2449(91)80308-M

[139] An investigation of the surface acidity of mesoporous Al-containing MCM-41 and of the external surface of ferrierite through pivalonitrile adsorption, Marcella Trombetta, Guido Busca, Maurizio Lenarda, Loretta Storaro, Massimo Pavan, Applied Catalysis A: General, 1999, 182 (2), 225-235; DOI: https://doi.org/10.1016/S0926-860X(99)00005-8

[140] An FT-IR study of the internal and external surfaces of H-ZSM5 zeolite, Marcella Trombetta, Tiziana Armaroli, Aìda Gutièrrez Alejandre, Jorge Ramirez Solis, Guido Busca, Applied Catalysis A: General, 2000, 192 (1), 125-136; DOI: https://doi.org/10.1016/S0926-860X(99)00338-5

[141] Poduval, D. G.; Veen, J. A. R. V.; Rigutto, M. S.; Hensen, E. J. M. *Chemical Communications* **2010**, *46* (20), 3466

[142] Thermal conductivity and particle agglomeration in alumina nanofluids: Experiment and theory, Timofeeva, Elena V.; Gavrilov, Alexei N.; McCloskey, James M.; Tolmachev, Yuriy V.; Sprunt, Samuel; Lopatina, Lena M.; and Selinger, Jonathan V. Phys. Rev. E, 2007, 76 (6), 061203; DOI: 10.1103/PhysRevE.76.061203

[143] IR spectroscopic detection of Lewis acid sites on alumina using adsorbed carbon monoxide. Correlation with aluminum-hydroxyl group removal, Todd H. Ballinger and John T. Yates, Langmuir, 1991, 7 (12), 3041-3045; DOI: 10.1021/la00060a022

[144] Concentration of surface hydroxyl groups on MCM-41, A Jentys, K Kleestorfer, H Vinek, Microporous and Mesoporous Materials, 1999, 27 (2–3), 321-328; DOI: https://doi.org/10.1016/S1387-1811(98)00265-0

[145] FT-IR Study of Water Adsorption on Aluminum Oxide Surfaces, Hind A. Al-Abadleh and V. H. Grassian, Langmuir, 2003, *19* (2), 341-347; DOI: 10.1021/la026208a

[146] FTIR analysis of the hydroxyl region in US-Y zeolites, Marina A. Makarova and John Dwyer, The Journal of Physical Chemistry, 1993, *97* (24), 6337-6338; DOI: 10.1021/j100126a004

[147] Flocculation of Colloidal Silica with Hydrolyzed Aluminum: An 27Al Solid State NMR Investigation, B. S. Lartiges, J. Y. Bottero, L. S. Derrendinger, B. Humbert, P. Tekely, and H. Suty, Langmuir, 1997, *13* (2), 147-152; DOI: 10.1021/la951029x

[148] Solid-State NMR Detection, Characterization, and Quantification of the Multiple Aluminum Environments in US-Y Catalysts by 27Al MAS and MQMAS Experiments at Very High Field, Colin A. Fyfe, Jeremy L. Bretherton, and Lau Y. Lam, Journal of the American Chemical Society, 2001, *123* (22), 5285-5291; DOI: 10.1021/ja003210k

[149] Modification of H-ZSM-5 zeolites with phosphorus. 1. Identification of aluminum species by 27Al solid-state NMR and characterization of their catalytic properties, S.M. Cabral de Menezes, Y.L. Lam, K. Damodaran, M. Pruski, Microporous and Mesoporous Materials, 2006, 95 (1–3), 286-295; DOI: https://doi.org/10.1016/j.micromeso.2006.05.032

[150] Determination of Integrated Molar Extinction Coefficients for Infrared Absorption Bands of Pyridine Adsorbed on Solid Acid Catalysts, C.A. Emeis, Journal of Catalysis, 1993, 141 (2), 347-354; DOI: https://doi.org/10.1006/jcat.1993.1145

[151] Comprehensive Study of Surface Chemistry of MCM-41 Using 29Si CP/MAS NMR, FTIR, Pyridine-TPD, and TGA, X. S. Zhao, G. Q. Lu, A. K. Whittaker, G. J. Millar, and H. Y. Zhu, The Journal of Physical Chemistry B, 1997, 101 (33), 6525-6531; DOI: 10.1021/jp971366+

[152] In situ FTIR spectra of pyridine adsorbed on SiO_2–Al_2O_3, TiO_2, ZrO_2, and CeO_2: general considerations for the identification of acid sites on surfaces of finely divided metal oxides, Mohamed I Zaki, Muhammad A Hasan, Fakhryia A Al-Sagheer, Lata Pasupulety, Colloids and Surfaces A: Physicochemical and Engineering Aspects, 2001, 190 (3), 261-274; DOI: https://doi.org/10.1016/S0927-7757(01)00690-2

[153] Influence of external surface area of rare-earth containing Y zeolites on the cracking of 1,3,5-triisopropylbenzene, Eduardo Falabella S. Aguiar, M.L. Murta^Valle, Marcos P. Silva, Débora F. Silva, Zeolites, 1995, 15 (7), 620-623; DOI: https://doi.org/10.1016/0144-2449(95)00069-I

[154] Is the catalytic activity of Al-MCM-41 sufficient for hydrocarbon cracking? Heico Koch, Wladimir Reschetilowski, Microporous and Mesoporous Materials, 1998, 25 (1–3), 127-129; DOI: https://doi.org/10.1016/S1387-1811(98)00184-X

[155] Zhang, Z.; Han, Y.; Zhu, L.; Wang, R.; Yu, Y.; Qiu, S.; Zhao, D.; Xiao, F.-S. *Angewandte Chemie* **2001**, *113* (7), 1298–1302

[156] Mesoporous Y zeolite with homogeneous aluminum distribution obtained by sequential desilication–dealumination and its performance in the catalytic cracking of cumene and 1,3,5-triisopropylbenzene, Zhengxing Qin, Baojian Shen, Xionghou Gao, Feng Lin, Baojie Wang, Chunming Xu, Journal of Catalysis, 2011, 278 (2), 266-275; DOI: https://doi.org/10.1016/j.jcat.2010.12.013

[157] Hauenstein, O.; Reiter, M.; Agarwal, S.; Rieger, B.; Greiner, A. *Green Chemistry* **2016**, *18* (3), 760–770

[158] Hauenstein, O.; Agarwal, S.; Greiner, A. *Nature Communications* **2016**, *7*, 11862

[159] Rachma Wikandari, Huong Nguyen, Ria Millati, Claes Niklasson, and Mohammad J. Taherzadeh, "Improvement of Biogas Production from Orange Peel Waste by Leaching of Limonene," BioMed Research International, vol. 2015, Article ID 494182, 6 pages, 2015. https://doi.org/10.1155/2015/494182

[160] Alumina-catalyzed alkene epoxidation with hydrogen peroxide, Dalmo Mandelli, Michiel C.A van Vliet, Roger A Sheldon, Ulf Schuchardt, Applied Catalysis A: General, 2001, 219 (1–2), 209-213; DOI: https://doi.org/10.1016/S0926-860X(01)00693-7

[161] Kinetics of limonene epoxidation by hydrogen peroxide on PW-Amberlite, Aída Luz Villa de P, Farlán Taborda A, Consuelo Montes de Correa, Journal of Molecular Catalysis A: Chemical, 2002, 185 (1–2), 269-277; DOI: https://doi.org/10.1016/S1381-1169(02)00077-8

[162] "Clean" limonene epoxidation using Ti-MCM-41 catalyst, M.V. Cagnoli, S.G. Casuscelli, A.M. Alvarez, J.F. Bengoa, N.G. Gallegos, N.M. Samaniego, M.E. Crivello, G.E. Ghione, C.F. Pérez, E.R. Herrero, S.G. Marchetti, Applied Catalysis A: General, 2005, 287 (2), 227-235; DOI: https://doi.org/10.1016/j.apcata.2005.04.001

[163] Limonene epoxidation with H_2O_2 promoted by Al_2O_3: Kinetic study, experimental design, Anderson J. Bonon, Yuriy N. Kozlov, Juliana O. Bahú, Rubens Maciel Filho, Dalmo Mandelli, Georgiy B. Shul'pin, Journal of Catalysis, 2014, 319, 71-86; DOI: https://doi.org/10.1016/j.jcat.2014.08.004.

[164] Wróblewska, A. *Molecules* **2014**, *19* (12), 19907–19922

[165] Toward understanding the unusual reactivity of mesoporous niobium silicates in epoxidation of CC bonds with hydrogen peroxide, Irina D. Ivanchikova, Igor Y. Skobelev, Nataliya V. Maksimchuk, Eugenii A. Paukshtis, Mikhail V. Shashkov, Oxana A. Kholdeeva, Journal of Catalysis, 2017, 356, 85-99; DOI: https://doi.org/10.1016/j.jcat.2017.09.011

[166] Reactive sputter deposition of titanium dioxide, Rand Dannenberg, Phil Greene, Thin Solid Films, 2000, 360 (1–2), 122-127; DOI: https://doi.org/10.1016/S0040-6090(99)00938-4

[167] Epoxidation of limonene over low coordination Ti in Ti- SBA-16, Luc Charbonneau, Serge Kaliaguine, Applied Catalysis A: General, 2017, 533, 1-8; DOI: https://doi.org/10.1016/j.apcata.2017.01.001

[168] The surface chemistry of amorphous silica. Zhuravlev model, L.T. Zhuravlev, Colloids and Surfaces A: Physicochemical and Engineering Aspects, 2000, 173 (1–3), 1-38; DOI: https://doi.org/10.1016/S0927-7757(00)00556-2

[169] Boronat, M.; Corma, A.; Renz, M.; Viruela, P. M. *Chemistry - A European Journal* **2006**, *12* (27), 7067–7077

[170] Rascón, F.; Wischert, R.; Copéret, C. *Chemical Science* **2011**, *2* (8), 1449

[171] Tang, B.; Dai, W.; Sun, X.; Guan, N.; Li, L.; Hunger, M. *Green Chem.* **2014**, *16* (4), 2281–2291

[172] Smoothing and Differentiation of Data by Simplified Least Squares Procedures. Abraham Savitzky and M. J. E. Golay, Analytical Chemistry, 1964, *36* (8), 1627-1639; DOI: 10.1021/ac60214a047

[173] Allison, K.; Sparke, M. B. Decomposition of Hydroperoxides, April 7, 1970

[174] Niobium Compounds: Preparation, Characterization, and Application in Heterogeneous Catalysis, Izabela Nowak and and Maria Ziolek, Chemical Reviews, 1999, *99* (12), 3603-3624; DOI: 10.1021/cr9800208

[175] Limonene Epoxidation: Diffusion and Reaction over PW-Amberlite in a Triphasic System, R. Barrera Zapata, A. L. Villa, and C. Montes de Correa, Industrial & Engineering Chemistry Research, 2006, *45* (13), 4589-4596; DOI: 10.1021/ie060098b

[176] Absolute rate constants for hydrocarbon autoxidation. VI. Alkyl aromatic and olefinic hydrocarbons, J. A. Howard, K. U. Ingold, *Canadian Journal of Chemistry*, 1967, 45:793-802; DOI: https://doi.org/10.1139/v67-132

[177] Recent Advances in Transition Metal Catalyzed Oxidation of Organic Substrates with Molecular Oxygen, T. Punniyamurthy, Subbarayan Velusamy, and Javed Iqbal, Chemical Reviews, 2005, *105* (6), 2329-2364; DOI: 10.1021/cr050523v

[178] Oldroyd, R. D.; Thomas, J. M.; Maschmeyer, T.; Macfaul, P. A.; Snelgrove, D. W.; Ingold, K. U.; Wayner, D. D. M. *Angewandte Chemie International Edition in English* **1996**, *35* (2324), 2787–2790

[179] Ti K-edge XANES studies of Ti coordination and disorder in oxide compounds: Comparison between theory and experiment, Farges, Fran; Brown, Gordon E.; and Rehr, J. J. Phys. Rev. B, 1997, 56 (4), 1809-1819; DOI: 10.1103/PhysRevB.56.1809

[180] Notestein, J. M.; Katz, A. *Chemistry - A European Journal* **2006**, *12* (15), 3954–3965

[181] Geoffrey C. Bond, Mark A. Keane, Hans Kral, and Johannes A. Lercher (2007) Compensation Phenomena in Heterogeneous Catalysis: General Principles and a Possible Explanation, Catalysis Reviews,42:3, 323-383, DOI: 10.1081/CR-100100264

[182] Teschner, D.; Novell-Leruth, G.; Farra, R.; Knop-Gericke, A.; Schlögl, R.; Szentmiklósi, L.; Hevia, M. G.; Soerijanto, H.; Schomäcker, R.; Pérez-Ramírez, J.; López, N. *Nature Chemistry* **2012**, *4* (9), 739–745

[183] The Entropies of Adsorbed Molecules, Charles T. Campbell and Jason R. V. Sellers, Journal of the American Chemical Society, 2012, *134* (43), 18109-18115; DOI: 10.1021/ja3080117

[184] Recovery of Dilute Aqueous Acetone, Butanol, and Ethanol with Immobilized Calixarene Cavities, Anthony B. Thompson, Rachel C. Scholes, and Justin M. Notestein, ACS Applied Materials & Interfaces, 2014, *6* (1), 289-297; DOI: 10.1021/am404182m

[185] Neurock, M.; Manzer, L. E. *Chemical Communications* **1996**, No. 10, 1133

[186] A DFT Study on Peroxo-Complex in Titanosilicate Catalyst: Hydrogen Peroxide Activation on Titanosilicalite-1 Catalyst and Reaction Mechanisms for Catalytic Olefin Epoxidation and for Hydroxylamine Formation from Ammonia, Hiroaki Munakata, Yasunori Oumi, and Akira Miyamoto, The Journal of Physical Chemistry B, 2001, *105* (17), 3493-3501; DOI: 10.1021/jp0022196

[187] The Production of Propene Oxide: Catalytic Processes and Recent Developments, T. Alexander Nijhuis, Michiel Makkee, Jacob A. Moulijn, and Bert M. Weckhuysen, Industrial & Engineering Chemistry Research, 2006, *45* (10), 3447-3459; DOI: 10.1021/ie0513090

[188] Direct Gas-Phase Epoxidation of Propene with Hydrogen Peroxide on TS-1 Zeolite in a Microstructured Reactor, Elias Klemm, Enrico Dietzsch, Thomas Schwarz, Thomas Kruppa, Armin Lange de Oliveira, Frank Becker, Georg Markowz, Steffen Schirrmeister, Rüdiger Schütte, Karl J. Caspary, Ferdi Schüth, and Dieter Hönicke, Industrial & Engineering Chemistry Research, 2008, *47* (6), 2086-2090; DOI: 10.1021/ie071343+

[189] Heterogeneous Catalysts for the One-Pot Synthesis of Chemicals and Fine Chemicals, Maria J. Climent, Avelino Corma, and Sara Iborra, Chemical Reviews, 2011, *111* (2), 1072-1133; DOI: 10.1021/cr1002084

[190] Pyridinium p-toluenesulfonate. A mild and efficient catalyst for the tetrahydropyranylation of alcohols, Masaaki Miyashita, Akira Yoshikoshi, and Paul A. Grieco, The Journal of Organic Chemistry, 1977, *42* (23), 3772-3774; DOI: 10.1021/jo00443a038

[191] Use of delaminated zeolites (ITQ-2) and mesoporous molecular sieves in the production of fine chemicals: Preparation of dimethylacetals and tetrahydropyranylation of alcohols and phenols, I. Rodriguez, M.J. Climent, S. Iborra, V. Fornés, A. Corma, Journal of Catalysis, 2000, 192 (2), 441-447; DOI: https://doi.org/10.1006/jcat.2000.2861

[192] Narender, N., Suresh Kumar Reddy, K., Arun Kumar, M. et al. Catal Lett (2010) 134: 175. https://doi.org/10.1007/s10562-009-0205-7

[193] Werpy, T. and Petersen, G. *Top Value Added Chemicals from Biomass;* US Department of Energy, 2004, 22-26

[194] Suslick, K. S.; Cook, B. R. *Journal of the Chemical Society, Chemical Communications* **1987**, No. 3, 200

[195] A Self-Assembled Molecular Cage for Substrate-Selective Epoxidation Reactions in Aqueous Media, Petrus F. Kuijpers, Matthias Otte, Maximilian Dürr, Ivana Ivanović-Burmazović, Joost N. H. Reek, and Bas de Bruin, ACS Catalysis, 2016, *6* (5), 3106-3112; DOI: 10.1021/acscatal.6b00283

[196] Corma, A.; Domine, M.; Gaona, J. A.; Jordá, J. L.; Navarro, M. T.; Rey, F.; Pérez-Pariente, J.; Tsuji, J.; Mcculloch, B.; Nemeth, L. T. *Chemical Communications* **1998**, No. 20, 2211–2212

[197] Speight, J.; Lange, N. A.; Dean, J. A. *Langes handbook of chemistry*; McGraw-Hill: New York, NY, 2005

[198] Biodiesel fuel production with solid superacid catalysis in fixed bed reactor under atmospheric pressure, Satoshi Furuta, Hiromi Matsuhashi, Kazushi Arata, Catalysis Communications, 2004, 5 (12), 721-723; DOI: https://doi.org/10.1016/j.catcom.2004.09.001

[199] Lange, J.-P.; Van De Graaf, W. D.; Haan, R. J. *ChemSusChem* **2009**, *2* (5), 437–441

[200] Aldol Condensation of Acetaldehyde over Titania, Hydroxyapatite, and Magnesia, Zachary D. Young, Sabra Hanspal, and Robert J. Davis, ACS Catalysis, 2016, *6* (5), 3193-3202; DOI: 10.1021/acscatal.6b00264